

# Ultra Low-Power Biomedical Signal Processing

An Analog Wavelet Filter Approach for Pacemakers

## PROEFSCHRIFT

ter verkrijging van de graad van doctor  
aan de Technische Universiteit Delft,  
op gezag van de Rector Magnificus Prof.dr.ir. J.T. Fokkema  
voorzitter van het College voor Promoties,  
in het openbaar te verdedigen op dinsdag 12 december 2006 om 10:00 uur

door

Sandro Augusto PAVLÍK HADDAD

Engenheiro Eletricista, Universidade de Brasília, UnB (Brasil)  
geboren te Anápolis, Goiás, Brasil

Dit proefschrift is goedgekeurd door de promotor:  
Prof.dr.ir. J.R. Long

Toegevoegd promotor:  
Dr.ir. W.A. Serdijn

Samenstelling promotiecommissie:

|                                 |  |
|---------------------------------|--|
| Rector Magnificus               | Technische Universiteit Delft, voorzitter          |
| Prof.dr.ir. J.R. Long           | Technische Universiteit Delft, promotor            |
| Dr.ir. W.A. Serdijn             | Technische Universiteit Delft, toegevoegd promotor |
| Prof.dr.ir. A.H.M. van Roermund | Technische Universiteit Eindhoven                  |
| Prof.dr.ir. I.M. Filanovsky     | University of Alberta, Canada                      |
| Prof.dr.ir. P.J. French         | Technische Universiteit Delft                      |
| Prof.dr.ir. M.H.G. Verhaegen    | Technische Universiteit Delft                      |
| Dr.ir. R.L.M. Peeters           | Universiteit Maastricht                            |

Reservelid:  
Prof.dr.ir. G.C.M. Meijer                                  Technische Universiteit Delft

## ULTRA LOW-POWER BIOMEDICAL SIGNAL PROCESSING *An Analog Wavelet Filter Approach for Pacemakers*

Keywords: Biomedical systems, pacemakers, wavelet transform, analog signal processing, analog wavelet filters, low-power analog integrators, translinear circuits, log-domain filters,  $G_m - C$  filters, Class-AB Sinh integrators, analog integrated circuits, electronics.

ISBN-10: 90-9021237-X  
ISBN-13: 978-90-9021237-1

Copyright ©2006 by Sandro Augusto Pavlik Haddad

All rights reserved.  
No part of the material protected by this copyright notice may be reproduced or utilized in any form or by any means, electronic or mechanical, including photocopying, recording or by any information storage and retrieval system, without the prior written permission of the author.

Printed in The Netherlands by PrintPartners IPSKamp.

*To my beloved wife,  
Carolina*



# Contents

|          |  |           |
|----------|--|-----------|
| <b>1</b> | <b>Introduction</b>  | <b>7</b>  |
| 1.1      | Biomedical signal processing . . . . .   | 8         |
| 1.2      | Biomedical applications of the wavelet transform . . . . .   | 8         |
| 1.3      | Analog versus digital circuitry - a power consumption challenge<br>for biomedical front-ends . . . . . | 10        |
| 1.3.1    | Power consumption in analog sense amplifiers . . . . .   | 11        |
| 1.3.2    | Power consumption in digital sense amplifiers . . . . .  | 12        |
| 1.4      | Objective and scope of this thesis . . . . .   | 14        |
| 1.5      | Outline of the thesis . . . . .  | 16        |
| <b>2</b> | <b>The Evolution of Pacemakers: An Electronics Perspective</b>   | <b>21</b> |
| 2.1      | The Heart . . . . .  | 22        |
| 2.2      | Cardiac Signals . . . . .  | 23        |
| 2.2.1    | Surface Electrocardiogram . . . . .  | 23        |
| 2.2.2    | Intracardiac electrogram (IECG) . . . . .  | 25        |
| 2.2.3    | Cardiac Diseases - Arrhythmias . . . . .   | 25        |
| 2.3      | The history and development of cardiac pacing . . . . .  | 26        |
| 2.3.1    | What is an artificial pacemaker? . . . . .   | 26        |
| 2.3.2    | Hyman's Pacemaker . . . . .  | 27        |
| 2.3.3    | Dawn of the Modern Era - Implantable Pacemakers . . . . .  | 28        |
| 2.4      | New Features in Modern Pacemakers . . . . .  | 34        |
| 2.5      | Summary and Conclusions . . . . .  | 37        |
| <b>3</b> | <b>Wavelet versus Fourier analysis</b>   | <b>41</b> |
| 3.1      | Introduction . . . . .   | 41        |
| 3.2      | Fourier transform . . . . .  | 42        |
| 3.3      | Windowing function . . . . .   | 42        |
| 3.4      | Wavelet transform . . . . .  | 43        |
| 3.4.1    | Continuous-time wavelet bases . . . . .  | 47        |
| 3.4.2    | Complex continuous wavelet bases . . . . .   | 48        |
| 3.5      | Signal Processing with Wavelet Transform . . . . .   | 50        |
| 3.5.1    | Singularity detection - Wavelet Zoom . . . . .   | 51        |
| 3.5.2    | Denoising . . . . .  | 54        |
| 3.5.3    | Compression . . . . .  | 55        |

|          |  |            |
|----------|--|------------|
| 3.6      | Low-power analog wavelet filter design . . . . .                             | 55         |
| 3.7      | Conclusions . . . . .  | 57         |
| <b>4</b> | <b>Analog Wavelet filters: the need for approximation</b>                    | <b>61</b>  |
| 4.1      | Introduction . . . . .   | 61         |
| 4.2      | Complex First Order filters . . . . .  | 62         |
| 4.3      | Padé Approximation in the Laplace domain . . . . .                           | 66         |
| 4.4      | $L_2$ Approximation . . . . .  | 71         |
| 4.5      | Other approaches for Wavelet bases approximation . . . . .                   | 75         |
| 4.5.1    | Bessel-Thomson filters - a quasi-Gaussian impulse response . . . . .         | 75         |
| 4.5.2    | Filanovsky's filter approach [15] . . . . .                                  | 76         |
| 4.5.3    | Fourier-series method . . . . .  | 78         |
| 4.6      | Discussion . . . . .   | 81         |
| 4.7      | Conclusions . . . . .  | 82         |
| <b>5</b> | <b>Optimal State Space Descriptions</b>                                      | <b>85</b>  |
| 5.1      | State space description . . . . .  | 85         |
| 5.2      | Dynamic Range . . . . .  | 87         |
| 5.2.1    | Dynamic Range Optimization . . . . .   | 88         |
| 5.3      | Sparsity . . . . .   | 89         |
| 5.3.1    | Orthogonal transformations . . . . .   | 90         |
| 5.3.2    | Canonical form representations . . . . .                                     | 92         |
| 5.3.3    | Biquad Structure . . . . .   | 95         |
| 5.3.4    | Diagonal controllability gramian - an Orthonormal Ladder Structure . . . . . | 96         |
| 5.3.5    | Sparsity versus Dynamic Range comparison . . . . .                           | 99         |
| 5.3.6    | New Sparsity Figure-of-Merit (SFOM) . . . . .                                | 100        |
| 5.4      | Sensitivity . . . . .  | 101        |
| 5.4.1    | New Dynamic Range-Sparsity-Sensitivity Figure-of-Merit (DRSS) . . . . .      | 103        |
| 5.5      | Conclusion . . . . .   | 105        |
| <b>6</b> | <b>Ultra Low-power Integrator Designs</b>                                    | <b>109</b> |
| 6.1      | $G_m$ -C filters . . . . .   | 109        |
| 6.1.1    | nA/V CMOS Triode-Transconductor . . . . .                                    | 110        |
| 6.1.2    | New pA/V Delta-Gm ( $\Delta - G_m$ ) Transconductor . . . . .                | 113        |
| 6.2      | Translinear (Log-domain) filters . . . . .                                   | 114        |
| 6.2.1    | Static and Dynamic Translinear principle . . . . .                           | 115        |
| 6.2.2    | Log-domain integrator . . . . .  | 116        |
| 6.3      | Class-A log-domain filter design examples . . . . .                          | 119        |
| 6.3.1    | Bipolar multiple-input log-domain integrator . . . . .                       | 119        |
| 6.3.2    | CMOS multiple-input log-domain integrator . . . . .                          | 120        |

|          |   |            |
|----------|---|------------|
| 6.3.3    | New high-frequency log-domain integrator in CMOS technology . . . . .                                   | 121        |
| 6.4      | Low-power Class-AB <i>Sinh</i> Integrators . . . . .  | 125        |
| 6.4.1    | A State-Space formulation for Class-AB Log-domain integrator . . . . .                                  | 126        |
| 6.4.2    | New Class-AB <i>Sinh</i> integrator based on State-Space formulation using single transistors . . . . . | 128        |
| 6.4.3    | Companding <i>Sinh</i> Integrator . . . . .   | 129        |
| 6.4.4    | New Ultra Low-power Class-AB <i>Sinh</i> Integrator . . . . .   | 132        |
| 6.5      | Discussion . . . . .  | 141        |
| 6.6      | Conclusions . . . . .   | 142        |
| <b>7</b> | <b>Ultra Low-power Biomedical System Designs</b>  | <b>147</b> |
| 7.1      | Dynamic Translinear Cardiac Sense Amplifier for Pacemakers . . . . .                                    | 148        |
| 7.1.1    | Differential voltage to single-ended current converter . . . . .  | 150        |
| 7.1.2    | Bandpass filter . . . . .   | 150        |
| 7.1.3    | Absolute value and RMS-DC converter circuits . . . . .  | 152        |
| 7.1.4    | Detection (Sign function) circuit . . . . .   | 154        |
| 7.2      | QRS-complex wavelet detection using CFOS . . . . .  | 156        |
| 7.2.1    | Filtering stage - CFOS wavelet filter . . . . .   | 158        |
| 7.2.2    | Decision stage - Absolute value and peak detector circuits  | 160        |
| 7.2.3    | Measurement results . . . . .   | 161        |
| 7.3      | Wavelet filter designs . . . . .  | 166        |
| 7.3.1    | Gaussian filters . . . . .  | 166        |
| 7.3.2    | Complex Wavelet filter implementation . . . . .   | 172        |
| 7.4      | Morlet Wavelet Filter . . . . .   | 177        |
| 7.4.1    | Circuit design . . . . .  | 179        |
| 7.4.2    | Measurement results of the Morlet wavelet filter [18] . . . . .   | 183        |
| 7.5      | Conclusions . . . . .   | 186        |
| <b>8</b> | <b>Conclusions and Future Research</b>  | <b>191</b> |
| 8.1      | Future Research . . . . .   | 193        |
| <b>A</b> | <b>High-Performance Analog Delays</b>   | <b>197</b> |
| A.1      | Bessel-Thomson approximation . . . . .  | 197        |
| A.2      | Padé approximation . . . . .  | 198        |
| A.3      | Comparison of Bessel-Thomson and Padé approximation delay filters . . . . .                             | 200        |
| A.4      | Gaussian Time-domain impulse-response method . . . . .  | 201        |
| <b>B</b> | <b>Model reduction - the Balanced Truncation method</b>   | <b>205</b> |
| <b>C</b> | <b>Switched-Capacitor Wavelet Filters</b>   | <b>209</b> |

|  |            |
|--|------------|
| <b>D Ultra-Wideband Circuit Designs</b>                      | <b>215</b> |
| D.1 Impulse Generator for Pulse Position Modulator . . . . . | 215        |
| D.2 A Delay Filter for an UWB Front-End . . . . .            | 217        |
| D.3 A FCC Compliant Pulse Generator for UWB Communications   | 219        |
| <b>Summary</b>   | <b>221</b> |
| <b>Samenvatting</b>  | <b>225</b> |
| <b>Acknowledgements</b>                                      | <b>229</b> |
| <b>Biography</b>   | <b>231</b> |
| <b>Publications</b>  | <b>233</b> |

# Chapter 1

## Introduction

*“Reading, after a certain age, diverts the mind too much from its creative pursuits. Any man who reads too much and uses his own brain too little falls into lazy habits of thinking.”* - Albert Einstein

Around 40% of all human deaths are attributed to cardiovascular diseases. A practical way to decrease the overall cardiac mortality and morbidity is to supply patients at risk with an implantable device, known as artificial pacemaker, that is designed to monitor the cardiac status and to regulate the beating of the heart. Cardiac pacing has become a therapeutic tool used worldwide with over 250.000 pacemaker implants every year.

Cardiac pacemakers include real-time sensing capacities reflecting the state of the heart. Current pacemaker detection circuitry can be interpreted as a cardiac electrical signal compression algorithm squeezing the time signal information into a single event representing the cardiac activity. Future cardiac pacing algorithms, however, are believed to take advantage of the morphological aspects of the sensed cardiac signal, improving the analysis and the recording of relevant cardiac activity data via implantable sensors. This will provide, for instance, a new opportunity for monitoring and managing infarct-threatened patients and post-infarction patients outside of the hospital.

In implantable medical devices, such as pacemakers, power consumption is critical, due to the limited power density and the longevity of currently available portable batteries. This implies that the design of such devices has to be optimized for very low power dissipation.

The purpose of this thesis is to detail the significant advances in cardiac pacing systems and to develop novel signal processing methodologies and analog integrated circuit techniques for low-power biomedical systems.

## 1.1 Biomedical signal processing

Biomedical signal processing centers on the acquisition of vital signals extracted from biologic and physiologic systems. These signals permit us to obtain information about the state of living systems, and therefore, their monitoring and interpretation have significant diagnostic value for clinicians and researchers to obtain information related to human health and diseases.

The processing of biomedical signals strongly depends on the knowledge about the origin and the nature of the signal and poses many special properties, which usually presents some unique problems. The reason for this is mainly due to the complexity of the underlying biologic structures and their signals, and the need to perform indirect, noninvasive measurements. In addition, the detected signals are commonly corrupted with noise, and thus, the relevant information is not “visible” and cannot be readily extracted from the raw signal. For such reasons, advanced signal processing is usually required.

Another important aspect of biomedical signals is that the information of interest is often a combination of features that are well localized temporally (e.g., spikes) and others that are more diffuse (e.g., small oscillations) [6]. This requires the use of analysis methods sufficiently versatile to handle events that can be at opposite extremes in terms of their time-frequency localization. In this thesis, we will investigate the ability of the Wavelet analysis to extract information from a biomedical signal.

## 1.2 Biomedical applications of the wavelet transform

Physiological signals are mostly non-stationary, such as the electrocardiogram (ECG), the electroencephalogram (EEG) and the electromyogram (EMG). Those signals represent the electrical activity of the heart, the brain and the muscles, respectively. The main difficulty in dealing with biomedical signal processing is the extreme variability of the signals and the necessity to operate on a case by case basis [6]. The Wavelet transform (WT) has been extensively used in biomedical signal processing, mainly due to the versatility of the wavelet tools. The WT has been shown to be a very efficient tool for local analysis of nonstationary and fast transient signals due to its good estimation of time and frequency (scale) localizations [13] [14]. The wavelet transform is a linear operation that decomposes a signal into components that appear at different scales (or resolutions). The transform is based on the convolution of the signal with a dilated filter, thereby mapping the signal onto a two-dimensional function of time and frequency.

The uses of the WT in biomedical applications are extremely diverse. Signal analysis methods derived from wavelet analysis [13] carry large potential to support a wide range of biomedical signal processing applications including

noise reduction [4], feature recognition [6] and signal compression [7]. The discussion here shall deal with wavelet techniques for cardiac signals analysis.

### Cardiac signal analysis

In the past few years, many new approaches to cardiac signal analysis have been proposed [5], e.g., algorithms based on filter banks [7], artificial neural networks [8], nonlinear transformations [9] and the wavelet transform [10]. In Fig.1.1, one can compare the numbers of publications in the IEEE online database related to electrocardiogram (ECG) signal detection for three different types of algorithms, being filter-based, wavelet transform and neural networks. Besides the fact that wavelet analysis is still relatively new, the wavelet-based signal processing methods have been evolving very rapidly and the rate of publication keeps increasing steadily.

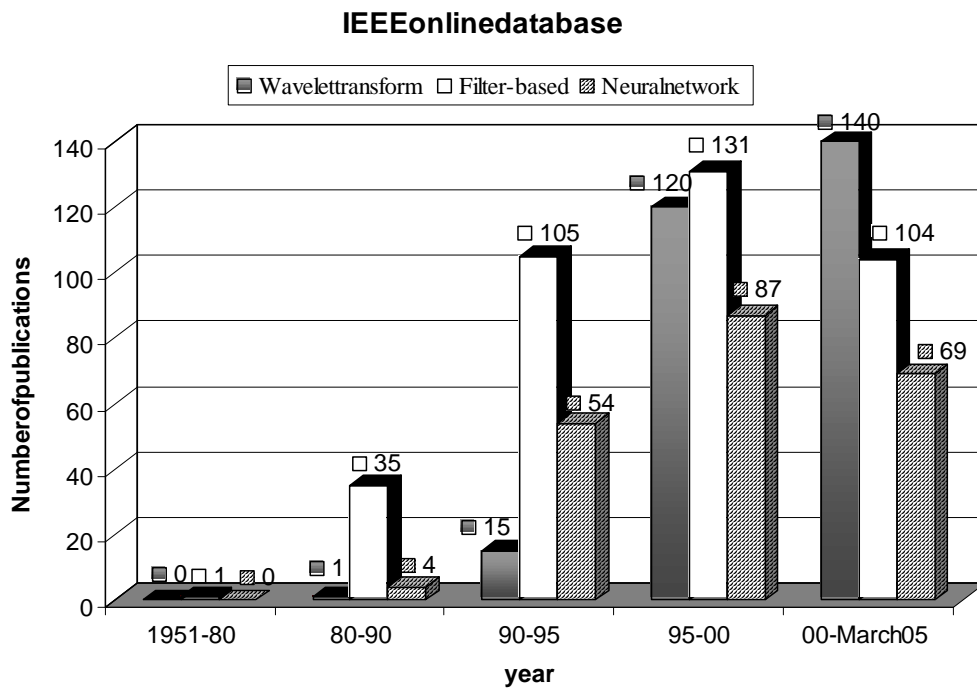


Figure 1.1: IEEE online database publications of cardiac signal detection for different types of algorithms

There are reasons for the growing number of algorithms using wavelets. Since usually cardiac signal and noise components share the same spectral bands, the scope of linear signal processing methods (linear filtering) is rather limited. Therefore, signal analysis methods improving discrimination of signals from noise and interference are of great importance. Several approaches [5] have demonstrated the potential of wavelet-based feature extraction for discriminating between normal and abnormal cardiac patterns.

Being a multiscale analysis technique, wavelets allow analysis of the electrogram focusing on the signal at various levels of detail, in analogy with inspection of a sample with a microscope at various levels of magnification. As one can see in Fig.1.2, at very fine scales (smaller values of scale  $a$ ), details of the electrogram, e.g., the QRS-complex (most striking waveform within the ECG), are revealed while unimpaired by the overall structure of the signal. At coarse scale (larger values of the scale factor  $a$ ), the overall structure of the electrogram can be studied while overlooking the details. Note that by this global view, both the QRS-complex and the T-wave can be detected.

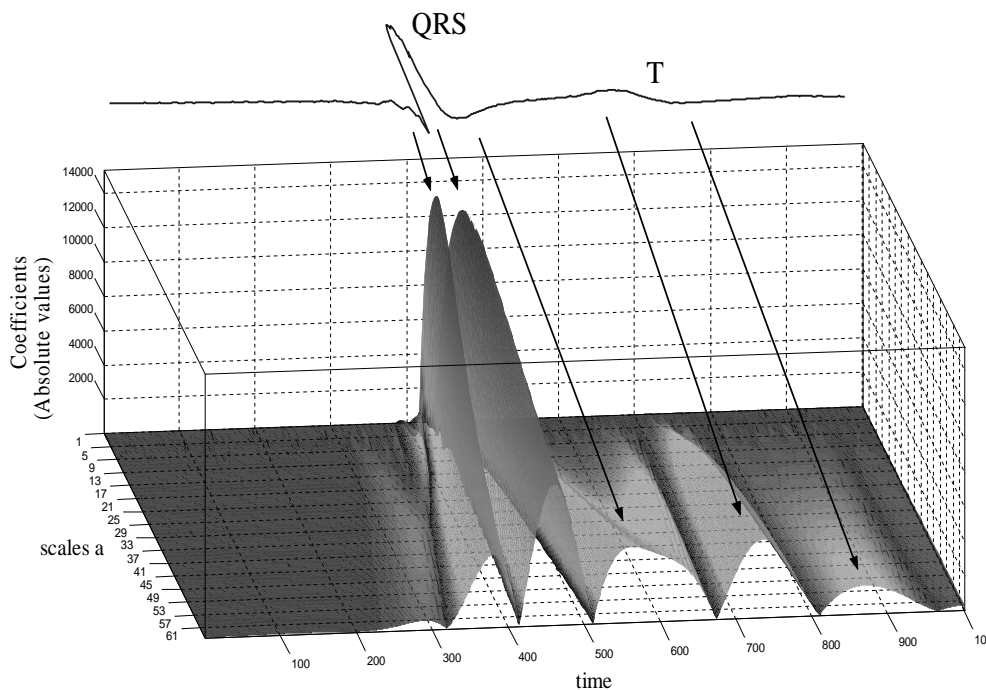


Figure 1.2: Wavelet analysis of an intracardiac signal (IECG). For small values of scale  $a$ , the QRS-complex information is dominant, whereas for large values of  $a$  both QRS and T waves are well localized.

### 1.3 Analog versus digital circuitry - a power consumption challenge for biomedical front-ends

A modern pacemaker consists of a telemetry system to receive and transmit data, a sense amplifier (analog or digital) consisting of passive/active filters, an amplifier and a comparator, analog output circuitry (also known as pulse generator) which stimulates the heart, and a microprocessor acting as a controller for all the settings of the pacemaker system. Moreover, an algorithm in

the microprocessor determines whether pacing is needed or not. Nevertheless, the longevity of a pacemaker must not be shortened by new improved features, so, reliable detection performance as well low power consumption is one of the most challenging design constraints.

The sense amplifier plays a fundamental role in providing information about the current state of the heart. State of the art implantable pulse generators or cardiac pacemakers include real-time sensing capabilities that are designed to detect and monitor intracardiac signal events (e.g., R-waves in the ventricle). A sense amplifier and its subsequent detection circuitry, together called the front-end, are shown in the block diagram in Fig.1.3. As one can see in Fig.1.3, the signal processing block of the front-end can be implemented with analog or digital circuitry and in the subsections that follow we will compare the minimum power required for both analog and digital implementations.

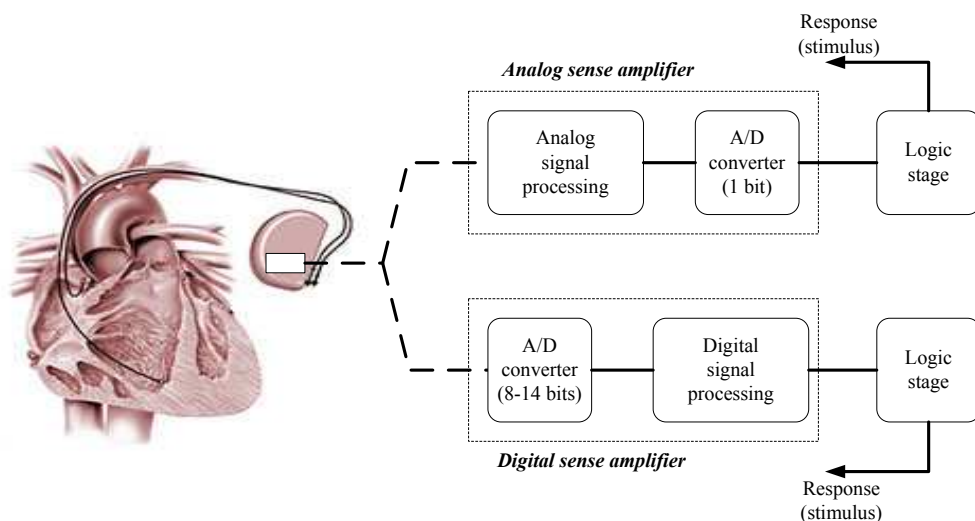


Figure 1.3: Analog and digital sense amplifiers for pacemakers

### **1.3.1 Power consumption in analog sense amplifiers**

Generally, the detection of the electrical activity of the heart requires filtering, where there is a discrimination between cardiac signals and noise based on differences in energy spectra, and comparison to determine if a heart beat has occurred. Therefore, an analog sense amplifier derives only a single event (characterized by a binary pulse from the 1-bit A/D converter) and feeds this to a micro-controller (logic stage) that decides upon the appropriate pacing therapy to be delivered by the stimulator. The system consists of an analog signal processing unit, usually a bandpass filter, and a 1-bit comparator circuit. The bandpass filter is used to specifically select intra-cardiac signals and to minimize the effect of the noise and interference. Normally, an integrated continuous-time filter is realized as a network of integrators and this

integration is exclusively performed by capacitive elements. The power per pole figure of merit [11] gives an indication of the power dissipation associated with the elementary signal processing operation of integration (filtering).

### Power per pole for analog filters

From this figure of merit, the minimum power dissipation ( $P_{an}$ ) of an integrator, connected as a first-order low-pass filter and driven by a sinusoidal input signal, can be expressed in terms of the dynamic range (DR)

$$P_{an} = 8fkT\xi DR \quad (1.1)$$

where  $f$  is the cut-off frequency,  $kT$  is the thermal energy and  $\xi$  is the excess noise factor of the (trans)conductance element [12].  $\xi$  is fundamentally greater than  $\frac{1}{2}$ . Thus, a large value for the noise factor translates directly to a proportionate disadvantage in terms of power dissipation. For a linearized transconductor, for instance a  $G_m - C$  structure, the excess noise factor can be significantly larger, with common values of  $\xi_{lin} \approx 3$  to 8 [13]. Whereas, for log-domain integrators, the noise factor can be approximated as  $\xi_{log} \approx \frac{3}{2}$  [13]. This means that log-domain filter allows a substantial power saving compared to more traditional continuous-time filters. This can be partially explained by the fact that log-domain filters do not require any local linearization as traditional filters do [12].

### 1.3.2 Power consumption in digital sense amplifiers

Digital information is different from its continuous counterpart in two important respects: it is sampled, and it is quantized. In order to interface digital circuitry with the physical world, analog-to-digital converters (ADC's) are required, which convert the continuous-time signals to discrete-time, binary-coded form.

### Power consumption in A/D converters

The resolution of the converter indicates the number of discrete values it can produce. The signal-to-noise ratio (SNR) of an ideal ADC is given by

$$SNR_{dB} = 6.02N - 1.25 + 10 \cdot \log \frac{f_s}{f_{sig}} \quad (1.2)$$

where  $N$  is the stated number of bits,  $f_s$  is the sampling frequency and  $f_{sig}$  is the highest frequency of the input signal. It can be noticed that for a Nyquist converter, where sampling frequency is defined as  $f_s = 2f_{sig}$ , the  $SNR_{dB}$  is now given by

$$SNR_{dB} = 6.02N + 1.76. \quad (1.3)$$

In [14], a figure of merit ( $F$ ) has been defined that emphasizes efficiency with respect to power dissipation and signal-to-noise-and-distortion ratio SNDR

$$F = \frac{2^N f_s}{P} \quad (1.4)$$

where  $P$  is the power dissipation. Here we will consider an optimistic case where SNDR is equal to the Dynamic Range (DR). By this, one can quantify the ADC power consumption performance ( $P_{ADC}$ ), which can be related to the correspondent DR by

$$P_{ADC} = \frac{2^{ENOB} f_s}{F} = \frac{2^{\frac{DR_{dB}-1.76}{6.02}} f_s}{F} \quad (1.5)$$

In this analysis, we will consider  $F$  equal to  $1.2 \cdot 10^{12}$ , which represents the present-day state-of-the-art A/D according to Walden in [14]. Another figure of merit known as the quantization energy ( $E_Q$ ) per conversion step [15], is based on the effective resolution bandwidth ( $F_{BW}$ ) instead of the sampling rate. This is defined as

$$E_Q = \frac{P_{ADC}}{2^N 2 F_{BW}} \quad (1.6)$$

where for Nyquist ADC,  $F_{BW}$  is equal to  $f_s$ . As one can see, this quantity is nearly the inverse of the figure of merit suggested by Walden. Again, the analysis for minimal power consumption will be based on recently published papers, where the lowest reported number for  $E_Q$  is 2.8pJ [16].

Finally, the fundamental limit for the quantization energy can be calculated based on the minimum thermal noise per pole (single capacitor) and the quantization-noise [17]. This absolute lower bound on the quantization energy  $E_Q$  for an ADC of a given resolution  $N$  at any speed is given by [17]

$$E_{Qmin} > 48kT2^N \quad (1.7)$$

Thus, the absolute minimum power per cycle for an analog-to-digital converter can be defined from Eq. 1.6 and Eq.1.7, resulting in

$$P_{min,ADC} > 48kT2^{2N} \quad (1.8)$$

The following analysis relates consumed power to the function of the number of bits ( $N$ ) representing the filtered information inside the digital filter. In the case of pacemakers, for instance, proper cardiac signal characterization would require at least 8-12 bits A/D conversion, at a sample rate of 1kHz [18].

### Power consumption in digital filters

To have a fair comparison of the minimal power needed in analog and digital filters, we will assume that the only noise source presented in the circuit

is the thermal noise integrated on the capacitor, which presents a Gaussian distribution. Note that in a digital filter, the signal is represented by a sequence of bits, rather than a voltage or current. Then, for digital signals, we can consider the associated noise in terms of probability that a bit-error will occur.

The bit-error function  $P_{bit,error}$  is defined by the probability of having an instantaneous noise amplitude exceeding a certain threshold, so that the wrong decision about the logic level will be made. It is known that the power consumed by the digital filter and its correspondent dynamic range depend on the probability of the error we can allow in the logic gates [19], [20]. Hence, the function  $P_{bit,error}$  can be defined as [19]

$$P_{bit,error} = \frac{1}{4} \left( \frac{1}{DR} - \frac{1}{2^{2N-1}} \right) = \frac{1}{2} \operatorname{Erfc} \left( \frac{1}{2} \sqrt{\frac{P_{dig}}{fkTN}} \right) \quad (1.9)$$

where  $\operatorname{Erfc}$  represents the error function given by  $\operatorname{Erfc}(x) = 1 - \frac{2}{\sqrt{\pi}} \int_0^x e^{-t^2} dt$ . Note that from Eq.1.9, we can relate the dynamic range (DR) with the corresponding power dissipation ( $P_{dig}$ ) in a digital filter.

Fig.1.4 shows minimal power consumption per cycle,  $(\frac{P_{an}}{f})$ ,  $(\frac{P_{ADC}}{f})$  ( $\frac{P_{dig}}{f}$ ), for the analog (analog filter) and digital (digital filter plus A/D converter) sense amplifiers, respectively, as a function of the DR achieved in the system. One can see that a digital filter presents lower power consumption than the equivalent analog filter. Nevertheless, due to the huge amount of power required for the analog-to-digital conversion, application of a fully digital signal processing in implantable devices like pacemakers is not feasible yet.

As a prediction of the power consumption related to the A/D converters over the years, we can use the  $E_Q$  figure of merit described before. Fig.1.4 also shows how much the lowest reported quantization energy, and the corresponding  $\frac{P_{ADC}}{f}$ , decrease yearly [17]. One can see, that  $E_Q$  decreases almost linearly, from 29.3Jp in 1995 [17] to 2.8pJ in 2004 [16], with only a factor of ten improvement over nine years.

Then, we conclude that the power efficiency of A/D converters needs to improve considerably in order to have the power dissipation of the digital sense amplifier comparable to the analog signal processing and, due to its power constraints, implantable devices will still be implemented using analog signal processing for many years to come.

## 1.4 Objective and scope of this thesis

The main objective of this thesis is the design of a novel signal processing system for ultra low-power real-time sensing of cardiac signals in pacemakers. Given the advantages in previous sections, the system will be based on wavelet transform using continuous-time analog circuitry.

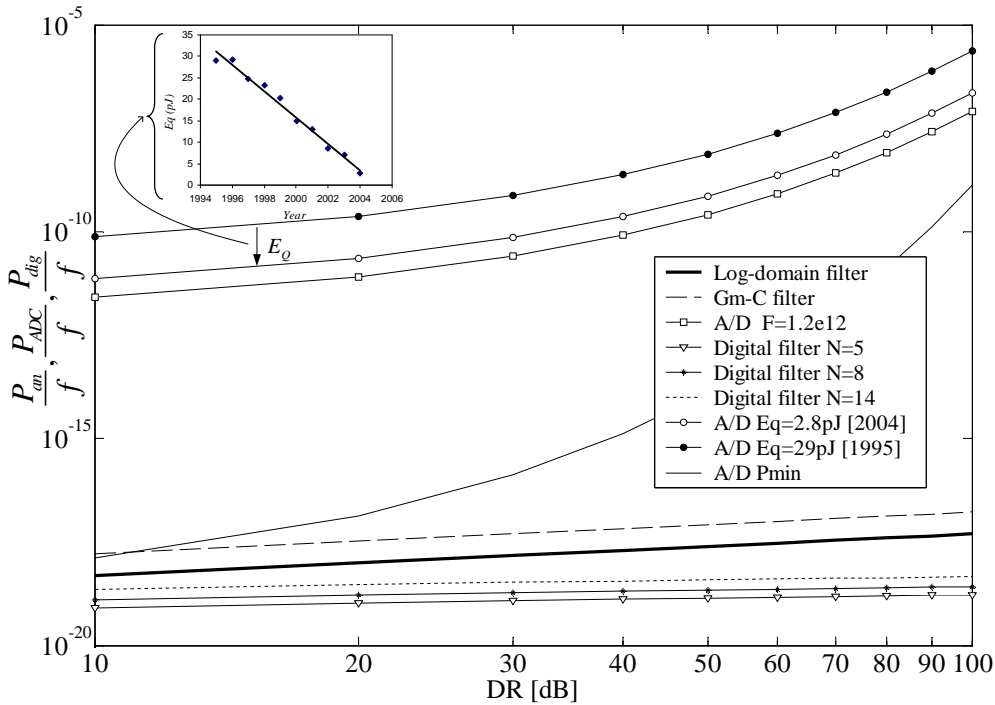


Figure 1.4: Comparison of the analog and digital sense amplifiers' power consumption

The Wavelet Transform (WT) has been shown to be a very efficient tool for analysis of non-stationary signals, like cardiac signals. Being a multiscale analysis technique, it offers the possibility of selective noise filtering and reliable parameter estimation.

Low-power analog realization of the wavelet transform enables its application *in vivo*, e.g., pacemakers. In this application, the wavelet transform provides a means to extremely reliable cardiac signal detection. A promising technique for the design of ultra low power analog integrated circuits is Dynamic Translinear (DTL) circuits. The DTL principle can be applied to the implementation of functions described by linear and nonlinear polynomial differential equations. Another suitable technique for low-power filters design is based on CMOS triode  $nA/V$  transconductor for linear  $g_m - C$  filters.

In this thesis we propose a method for implementing the novel signal processing based on WT in an analog way. The methodology will focus then on the development of ultra low-power analog integrated circuits that implement the required signal processing, taking into account the limitations imposed by an implantable device.

## 1.5 Outline of the thesis

A brief overview of the history and development of circuit designs applied in pacemakers is presented in Chapter 2. The advances in integrated circuit designs have resulted in increasingly sophisticated pacing circuitry, providing, for instance, diagnostic analysis, adaptive rate response and programmability. Also, based on future trends for pacemakers, some features and improvements for modern cardiac sensing systems are described.

Chapter 3 deals with the properties of the WT as well as the definition of some wavelet bases. In addition, an example is given to illustrate the advantages and limitations of the frequency (Fourier transform), time (windowing function) and time-frequency (wavelet transform) representations.

From the wavelet definition, we can state that a wavelet filter implementation is based on a bandpass filter design which presents an impulse response equal to a wavelet base. In order to obtain the transfer function of certain wavelet filter, mathematical approximation techniques are required. Some of those approximation methods, i.e., Complex first order system (CFOS), Padé and least mean square ( $L_2$ ) approaches, will be presented in Chapter 4.

In Chapter 5, one will see that there are many possible state space descriptions, and, of course, different filter topologies that implement a particular transfer function. By this, we are able to achieve the required low-power specifications. Some of the requirements treated in this chapter are dynamic range, sensitivity and sparsity.

The trend towards lower power consumption, lower supply voltage and higher frequency operation has increased interest in new design techniques for analogue integrated filters. The class of translinear (TL) filters, also known as log-domain filters, has emerged in recent years as a promising approach to face these challenges and it will be presented in Chapter 6. In addition, new Class-A log-domain and Class-AB *Sinh* integrator designs will be presented. In the field of medical electronics, active filters with large time constants are often required to design low cutoff-frequency filters (in the Hz and sub-Hz range), necessitating the use of large capacitors or very low transconductances. To limit capacitors to practical values, a transconductor with an extremely small transconductance  $g_m$  (typically a few nA/V) is needed. Ultra low-power CMOS triode nano-A/V and pico-A/V transconductors for low-frequency  $g_m - C$  filters are also introduced in this chapter.

In Chapter 7, the methodology presented in the previous chapter is now employed in the design of several ultra low-power biomedical systems. First, a benchmark cardiac sense amplifier, i.e., a standard pacemaker front-end, based on the Dynamic Translinear (DTL) circuit technique is presented. Then, an analog QRS complex detection circuit, based on the Wavelet Transform (WT) is described. The system uses an CFOS structure to approximate the Gaussian wavelet base and the decision stage detects the wavelet modulus maxima of the QRS complex. Two convenient methods to provide the transfer function of

the wavelet filter are given by the Padé and  $L_2$  approximations and, thus, some designs based on these approaches, for Gaussian and Morlet wavelet bases, will also be presented. In addition, a complex wavelet filter design, based on the combination of the real and the imaginary state-space descriptions is described. To fulfill the low-power requirement, the filter's state space description will be optimized. Simulations and measurement results of the various systems are also presented in this chapter.

Finally, Chapter 8 presents the conclusions and suggestions for further research in this area.



# Bibliography

- [1] M. Unser and A. Aldroubi, *A review of wavelets in biomedical applications*, Proceeding of the IEEE, vol. 84, no. 4, pp.626-638, April, 1996.
- [2] I. Daubechies, *Ten Lectures on Wavelets*, Society for Industrial and Applied Mathematics, Philadelphia, 1992.
- [3] S. Mallat, *A Wavelet Tour of Signal Processing*, Academic Press, 2001.
- [4] M. Jansen, *Noise reduction by wavelet thresholding*, Springer Verlag, 2001.
- [5] S. Mallat and W. L. Hwang, *Singularity Detection and Processing with Wavelets*, IEEE Transactions on Information Theory, vol.38, no. 2, pp.617-643, March, 1992.
- [6] B. U. Kohler, C. Hennig and R. Orglmeister, *The principles of software QRS detection*, IEEE Engineering in Medicine and Biology, pp.42-57, February, 2002.
- [7] V. X. Afonso, W. J. Tompkins, T. Q. Nguyen and S. Luo, *ECG beat detection using filter banks*, IEEE Trans. Biomed. Eng., vol. 46, pp. 192-202, 1999.
- [8] Y. H. Hu, W. J. Tompkins, J. L. Urrusti and V. X. Afonso, *Applications of artificial neural networks for ECG signal detection and classification*, J. Electrocardiology, vol. 26, pp.66-73, 1993.
- [9] S. Suppappola and Y. Sun, *Nonlinear transforms of ECG signals for digital QRS detection: A quantitative analysis*, IEEE Trans. Biomed. Eng., vol. 41, pp. 397-400, 1994.
- [10] J. S. Sahambi and S. N. Tandon and R. K. P. Bhatt, *Using Wavelet Transform for ECG Characterization*, IEEE Engineering in Medicine and Biology, pp.77-83, February, 1997.
- [11] E. A. Vittoz, *Future of analog in the VLSI environment*, In Proc. IEEE Int. Symp. on Circuits and Systems, vol.2, pp.1372-1375, 1990.

- [12] C. Enz, M. Punzenberger and D. Python, *Low-Voltage Log-Domain Signal Processing in CMOS and BiCMOS*, IEEE Transactions of Circuits and Systems II, vol. 46, no. 3 p. 279-289, March 1999.
- [13] Y. Tsividis, *Externally linear, time-invariant systems and their applications to companding signal processors*, IEEE Transactions of Circuits and Systems II, vol. 44, p. 65-85, February 1997.
- [14] R. H. Walden, *Analog-to-digital converter survey and analysis*, IEEE Journal on Selected Areas in Communication, 17(4):539-550, April, 1999.
- [15] G. Geelen, *A 6b 1.1GSample/s CMOS A/D converter*, IEEE International Solid-State Circuits Conference, Digest of Technical Papers, pp.128-129, February, 2001.
- [16] G. Geelen and E. Paulus, *An 8b 600MS/s 200mV CMOS Folding A/D Converter Using an Amplifier Preset Technique*, IEEE International Solid-State Circuits Conference, Digest of Technical Papers, pp.254-255, February, 2004.
- [17] K. H. Lundberg, *High-Speed Analog-to-Digital Converter Survey*, Lecture notes found at <http://web.mit.edu/klund/www/papers/>.
- [18] L. S. Y. Wong, S. Hossain, A. Ta, J. Edvinsson, D. H. Rivas and H. Naas, *A Very Low-Power CMOS Mixed-Signal IC for Implantable Pacemaker Applications*, IEEE Journal of Solid-State Circuits, vol.39, no.12, pp.2446-2456, December, 2004.
- [19] D. P. W. M. Rocha, *Optimal Design of Analogue Low-power Systems, A strongly directional hearing-aid adapter*, PhD thesis, Delft University of Technology, April, 2003.
- [20] M. Djurica, *Design of Low power Analog to Digital Converter*, PhD thesis, Delft University of Technology, April, 2001.

## Chapter 2

# The Evolution of Pacemakers: An Electronics Perspective

*"The heart is the only broken instrument  
that works." - T. E. Kalem*

Since the first artificial pacemaker was introduced in 1932, much has changed and will continue to change in the future [1], [2], [3]. The complexity and reliability in modern pacemakers has increased significantly, mainly due to developments in integrated circuit design. Early pacemakers merely paced the ventricles asynchronously, not having the capability of electrogram sensing. Later devices, called demand mode pacemakers, included a sense amplifier measuring cardiac activity, thereby avoiding competition between paced and intrinsic rhythms. By the introduction of demand pacemakers, also the longevity increased since pacing stimuli were only delivered when needed. In 1963 pacemakers were introduced having the capability to synchronize ventricular stimuli to atrial activation. Since that time, clinical, surgical and technological developments have proceeded at a remarkable pace providing highly reliable, extensive therapeutic and diagnostic devices that we know today.

Modern pacemaker topologies are extremely sophisticated and include an analog part (comprising the sense amplifier and a pacing output stage) as well as a digital part (consisting of a micro controller, and some memory), implementing diagnostic analysis of sensed electrograms, adaptive rate response and device programmability. Pacemakers have become smaller and lighter over the years. Early devices weighed more than 180g, whereas today devices are available weighting no more than 25g [4]. This weight reduction has occurred partly due to the development of high energy-density batteries. Finally, there have been remarkable advances in cardiac lead technology. Novel electrode tip materials and configurations have provided extremely low stimulation thresholds and low polarization properties [5]. In this chapter, we will concentrate on the evolution of analog circuit designs applied in cardiac pacemakers.

## 2.1 The Heart

In order to better understand why some patients require pacemakers and how these devices work, it is worth briefly discussing how the heart and its electrical system work. In a global view one can think of the heart as a pumping station which pumps the blood through the body. In order to do so, the heart is divided into four chambers: two atria and two ventricles, as shown in Fig. 2.1. The two atria act as collecting reservoirs (primer pump) for blood returning to the heart while the two ventricles act as pumps to eject the blood to the body. Deoxygenated blood returning from the body via the superior and inferior vena cava, enters the right atrium and passes through the tricuspid valve to the right ventricle, which expels it through the pulmonary artery to the lungs. Oxygenated blood returning from the lungs enters the left atrium via the pulmonary veins, passes via the mitral valve to the left ventricle and is pumped out through the aorta back to the body. The tricuspid and the mitral valves are important to prevent the back flow of blood from the respective ventricle to the atrium [6].

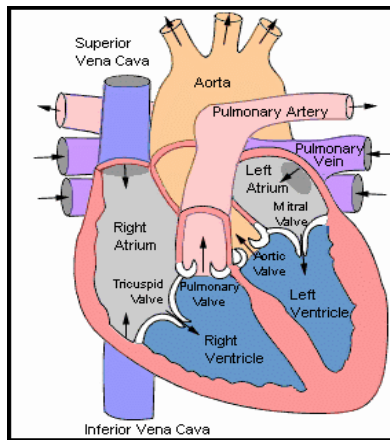


Figure 2.1: The heart

The pumping action starts with the simultaneous contraction of the two atria, called "diastole". This contraction serves to give an added push to get the blood into the ventricles. Shortly after that, the ventricles contract virtually in unison, making the beginning of "systole". Therefore, from electrical point of view the heart can, in most instances, be treated as just two chambers.

### Excitation and Conduction system

The heart is composed basically by three types of cardiac muscle: the atrial muscle, the ventricle muscle and the specialized fibers (which can be further subdivided into excitation and conduction fibers). Both the atrial and the

ventricle muscles, which make up the myocardium, each have a similar form of contraction to other muscles of the body, but with a larger period of contraction time. On the other hand, the excitation and conduction fibers have very weak contractions, but do have rhythmicity and variable conduction speed. Once an electrical activation has occurred, contraction of the muscle follows. An orderly sequence of activation of the cardiac muscle in a regularly timed manner is critical for the normal functioning of the heart.

The excitation and conduction system of the heart, responsible for the control of the regular pumping of the heart, is presented in Fig.2.2. It consists of the sinoatrial node (SA node), internodal tracks and Bachmann's bundle, the atrioventricular node (A-V node), the bundle of His, bundle branches and Purkinje fibers. A heart pacemaker is a device that exhibits automaticity, i.e. generates electrical impulses (known as action potentials) via automatic self activation, and delivers them to the muscles of the heart in such a way to contract those muscles and the heart to beat. Several cells in the heart are able to generate inherent impulses (inherent rate in A-V node is about 50 beats per minute and in Purkinje fibers about 40 beats per minute), but with lower rate than the SA node (about 60-80 beats per minute). The normal rhythm of the heart, between 60 and 100 beats per minute, is controlled by the discharges from the SA node, unless the SA node is nonfunctional. The Internodal tracks and Bachmann's bundle transmit this excitation throughout the atria and initiate a coordinated contraction of the atrial walls. Meanwhile, the impulse reaches the A-V node, which is the only electrical connection between atria and ventricles. The A-V node introduces an effective delay, allowing the contraction of the atria to finish before ventricular concentration begins. By this delay, an optimal ventricular filling is achieved. Subsequently, the electrical impulses are conducted very rapidly through the His-Purkinje system (comprising the bundle of His, bundle branches and Purkinje fibers). Once the bundle of His activates, its signal splits into the right bundle branch, which goes to the right ventricle, and the left bundle branch which leads to the left ventricle. Both bundle branches terminate in Purkinje fibers. The Purkinje fibers are responsible for spreading the excitation throughout the two ventricles and causing a coordinated ventricular contraction [6].

## 2.2 Cardiac Signals

### 2.2.1 Surface Electrocardiogram

The electrocardiogram (ECG) is the recording on the body surface of the electrical activity generated by heart. It was originally observed by Waller in 1899 [7]. In 1903, Einthoven introduced some concepts still in use today, including the labelling of the various waves. He chose the letters from P to U to label the waves and to avoid conflict with other physiologic waves being studied at that time [7]. Fig. 2.3 depicts a typical ECG signal.

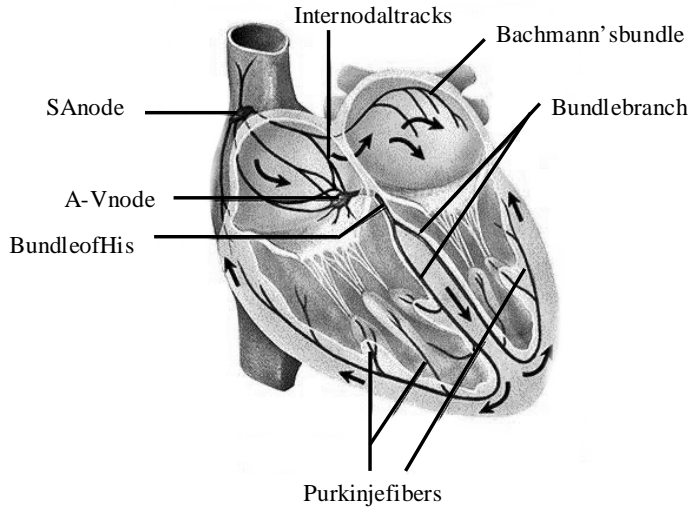


Figure 2.2: The cardiac conduction system

ECG signals are typically in the range of 2 mV peak-to-peak and occupy a bandwidth of 0.05 to 150 Hz. The character of the body surface waves depends on the amount of tissue activating at one time and the relative speed, direction of the activation waveform (action potentials) and the position of the electrodes. Therefore, the pacemaker potentials, i.e. the SA node potentials, that are generated by a small tissue mass are not seen on the ECG. The first ECG wave of the cardiac cycle is the P wave, and it represents the depolarization of the atria. Conduction of the cardiac impulse proceeds from the atria through a series of specialized cardiac cells (the A-V node and the His-Purkinje system) which was explained in the previous section. Again the total mass is too small to generate a signal large enough to be seen on the ECG. There is a short relatively isoelectric segment following the P wave. This is the P-Q interval which is defined by the propagation delay time of the specialized cells and, usually, is 0.2 s. Once the large muscle mass of the ventricles is excited, a rapid and large deflection is seen on the body surface. This ventricles' depolarization waveform is generically called the QRS complex. Following the QRS complex is another isoelectric segment, the S-T interval. The S-T interval represents the duration of the action potential, normally about 0.25s to 0.35s. After this short segment, the ventricles return to their electrical resting state, and a wave of repolarization is seen as a low-frequency signal known as the T wave. In some individuals, a small peak occurs at the end or after the T wave and is called the U wave. Its origin has never been fully established, but it is believed to be a repolarization potential [8].

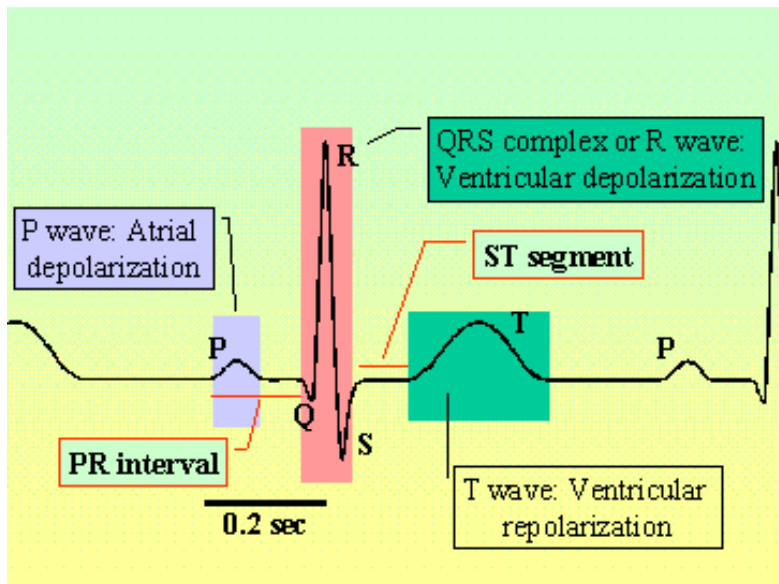


Figure 2.3: Typical Electrocardiogram

### 2.2.2 Intracardiac electrogram (IECG)

An intracardiac electrogram (IECG) is a recording of changes in electric potentials of specific cardiac locations measured by electrodes placed within or onto the heart by using cardiac catheters. The IECG can be recorded between one electrode and an indifferent electrode, usually more than 10 cm apart (unipolar electrogram) or between two more proximate electrodes (< 15 mm) in contact with the heart (bipolar electrogram). Sensing the intrinsic activity of the heart depends on many factors related to the cardiac source and the electrode-tissue interface where complex electrochemical reactions take place. In most situations it is desirable that the IECG does not contain signals from other more distant cardiac chambers. Bipolar lead systems are much less sensitive to far-field potentials and electromagnetic interference (EMI) sources obscuring the cardiac signal.

### 2.2.3 Cardiac Diseases - Arrhythmias

Arrhythmias (or dysrhythmias) are due to cardiac problems producing abnormal heart rhythms. In general arrhythmias reduce hemodynamic performance including situations where the heart's natural pacemaker develops an abnormal rate or rhythm or when normal conduction pathways are interrupted and a different part of the heart takes over control of the rhythm. An arrhythmia can involve an abnormal rhythm increase (tachycardia; > 100 bpm) or decrease (bradycardia; < 60 bpm), or may be characterized by an irregular

cardiac rhythm, e.g. due to asynchrony of the cardiac chambers. An "artificial pacemaker" can restore synchrony between the atria and ventricles.

## 2.3 The history and development of cardiac pacing

### 2.3.1 What is an artificial pacemaker?

An artificial pacemaker is a device that delivers a controlled, rhythmic electric stimulus to the heart muscle in order to maintain an effective heartbeat for long periods of time and thereby ensures the pumping capacity of the heart. Indication for permanent pacemaker implantation and the selection of the appropriate pacemaker mode are based mainly on the cardiac diseases such as failure of impulse formation (sick sinus syndrome) and/or conduction (A-V block). Functionally, a pacemaker comprises at least three parts: a electrical pulse generator, a power source (battery) and an electrode (lead) system, as we can see in Fig. 2.4 [9].

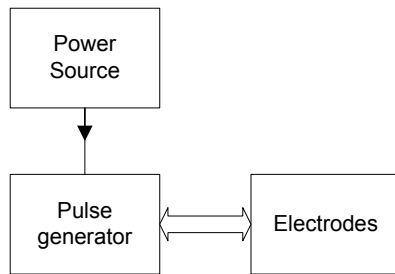


Figure 2.4: Basic pacemaker functional block diagram

Different types of output pulses (monophasic, biphasic, etc.) can be used to stimulate the heart. The output stimulus provided by the pulse generator is the amount of electrical charge transferred during the stimulus (current). For effective pacing, the output pulse should have an appropriate width and sufficient energy to depolarize the myocardial cells close to the electrode. Generally, a pacemaker can provide a stimulus in both chambers of the heart. During AV-block, ventricular pacing is required because the seat of disease is in the AV-node or His-Purkinje system. However, in case of a sick sinus syndrome, the choice of pacemaker will be one that will stimulate the right atrium. A pacemaker utilizes the energy stored in batteries to stimulate the heart. Pacing is the most significant drain on the pulse generator power source. The battery capacity is commonly measured in units of charge (ampere-hours). Many factors will affect the longevity of the battery, including primary device settings like pulse amplitude and duration and pacing rate. An ideal pulse generator battery should have a high energy density, low self-discharge rate and sufficient energy reserve between early signs of depletion and full depletion to allow for safe replacement of the device. The electrical connection between

the heart and the implanted pulse generator is provided by an implantable electrode catheter called 'lead'. In an implantable pulse generator system, commonly two types of lead systems are used. A unipolar lead system has a single isolated conductor with an electrode located at the tip. A bipolar lead has two separate and isolated conductors connecting the two electrodes, i.e. the anode and cathode, usually not more than 12 mm apart. The cathode refers to the electrode serving as the negative pole for delivering the stimulation pulse and the anode to the positive pole. For unipolar pacing-sensing systems, the distance between anode and cathode easily exceeds 10 cm. Its cathode is typically located at the lead tip whereas the pulse generator housing, usually located in the pectoral region, is used as anode. Several types of bipolar leads exist, including the coaxial lead allowing a diameter in the range of 4 to 5 F (French = 0.33 mm), which is comparable to state-of-the-art unipolar leads. The sensing behavior of bipolar lead systems outperform their unipolar counterparts by providing a better signal to interference ratio. Especially for sensing atrial activation, bipolar electrodes are less sensitive to far-field potentials generated by the ventricles. Moreover, bipolar leads are less sensitive to electromagnetic interference (EMI) sources and skeletal muscle potentials. However, owing to their construction, bipolar leads are stiffer and more complex from a mechanical construction point of view.

### 2.3.2 Hyman's Pacemaker

In the early nineteenth century, many experiments such as drug therapy and electrical cardiac pacing had been conducted for stimulating heart arrest. Previous methods employed in electrically stimulating the heart were performed by applying the same current that would cause contraction of the muscle tissue of the heart. Whereas in the latter theory, Albert S. Hyman stated that "the introduced electric impulse serves no other purpose than to provide a controllable irritable point from which a wave of excitation may arise normally and sweep over the heart along its accustomed pathways." Hyman designed the first experimental heart pacemaker in 1932 [10], shown in Fig. 2.5.

Hyman's pacemaker was powered by a hand-wound, spring-driven generator that provided 6 minutes of pacemaking without rewinding. The operation is as follows: The hand crank (F) winds the spring motor (D) which drives the magneto-generator (A) at a controlled speed (E and H) and causes the interrupter disc (not shown) to rotate. The magneto-generator supplies current to a surface contact on the interrupter disc. The companion magnet pieces (B' and B") provides the magnetic flux necessary to generate current in the magneto-generator. Subsequently, the interrupter disc produces a pulsed current at 30 60 or 120 beats per minute, regulated by the impulse controller (G), which represents the periodic pacing waveform delivered to the electrode needle (L). The neon lamp (C) is illuminated when a stimulus is interrupted. In Fig.2.6 a suitable block diagram of the Hyman's pacemaker is given [11].

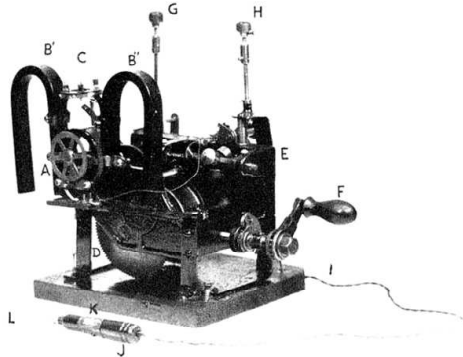


Figure 2.5: The first artificial pacemaker. A, magneto-generator; B' and B'', companion magnet pieces; C, neon lamps; D, spring motor; E, ballistic governor; F, handle; G, impulse control; H, speed control; I, flexible electric cord; J, insulated handle; K, handle switch, and L, electrode needle.

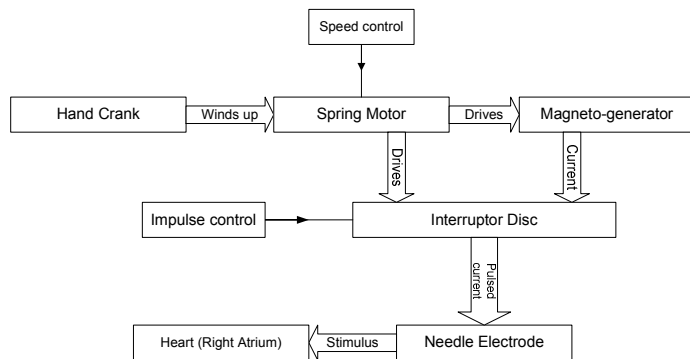


Figure 2.6: Block diagram of Hyman pacemaker

### 2.3.3 Dawn of the Modern Era - Implantable Pacemakers

The origin of modern cardiac pacing is defined as the time when the first pacemaker was implanted without the need for opening the chest. The first pacemaker, developed by Dr. Rune Elmquist, was used in a patient in 1958 by Dr. Ake Senning [12]. In 1959 the engineer Wilson Greatbatch and the cardiologist W.M. Chardack developed the first fully implantable pacemaker [13]. This device was essentially used to treat patients with complete A-V block caused by Stokes-Adams diseases delivering a single-chamber ventricular pacing. It measured 6 cm in diameter by 1.5 cm thick and the total weight of the pacemaker was approximately 180g. The pacemaker circuit delivered to the electrode pulses 1ms wide, pulse amplitude of 10mA and a repetition rate of 60 beats per minute. The average current drain of the circuit under these conditions was about  $12\mu\text{A}$  which, energized by 10 mercury-zinc cells, gave a

continuous operation life estimated at 5 years. The schematic of the implanted pacemaker is shown in Fig.2.7 and consists of a pulse forming (square pulse) oscillator and an amplifier.

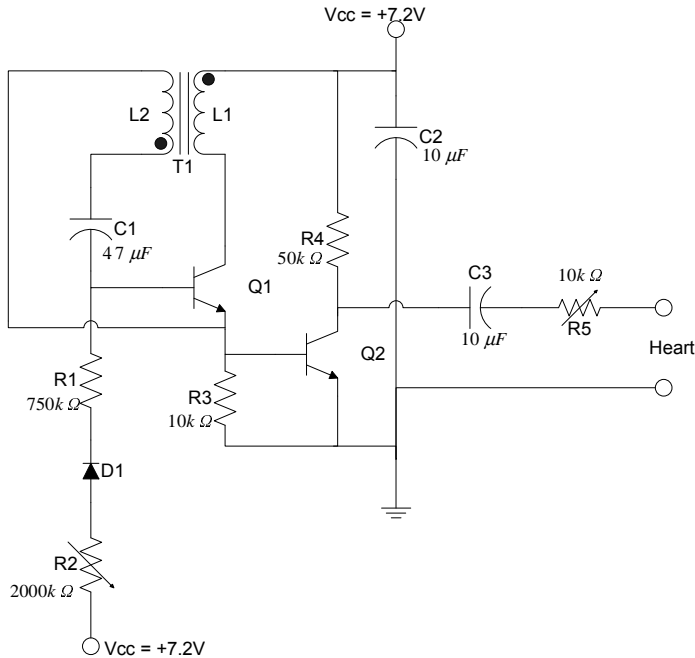


Figure 2.7: Schematic of the first implanted pacemaker [13]

Basically, the cardiac pacemaker includes a blocking oscillator [14], which is a special type of wave generator used to produce a narrow pulse. The blocking oscillator is closely related to the two-transistor astable circuit, except that it uses only one amplifying device. The other is replaced by a pulse transformer, which provides inductive regenerative positive feedback. The transistor of the blocking oscillator is normally cut off between pulses and conducting during the time that a pulse is being generated. The operation of a blocking oscillator during a single cycle may be divided into three parts: the turn-on period, the pulse period and the time interval between adjacent pulses (relaxation period). The turn-on period ( $t_0$ ) occurs when  $V_{cc}$  is applied to the circuit,  $R1$  and  $R2$  provide forward bias and transistor  $Q1$  conducts. Current flow through  $Q1$  and the primary ( $L1$ ) of  $T1$  induces a current through the secondary ( $L2$ ), increasing the voltage across  $C1$  and thus across the base-emitter junction of  $Q1$ . The positive voltage of  $L2$  is coupled to the base of the transistor through  $C1$ . This provides more collector current and consequently more current through  $L1$ . Very rapidly, sufficient voltage is applied to saturate the base of  $Q1$ . Once the  $Q1$  becomes saturated, the circuit can be defined as a series RL (resistance-inductance) circuit and the current increase in  $L1$  is determined by the time constant of  $L1$  and the total series resistance. From

$t_0$  to  $t_1$  (pulse period) the voltage across  $L1$  will be approximately a constant value as long as the current increase through  $L1$  is linear. The pulse width depends mainly on the time constant  $\tau_C = L1/R3$ . At time  $t_1$ ,  $L1$  saturates. At this time,  $C1$ , which has charged during the pulse period, will now discharge through  $R1$  and cut off  $Q1$ . This causes collector current to stop, and the voltage across  $L1$  returns to 0. The length of time between  $t_1$  and  $t_2$  is the relaxation period.

### Demand Pacemaker

As was shown in previous section, the early pacing devices simply delivered a fixe-rate pulse to the ventricle at a preset frequency, regardless of any spontaneous activity of the heart. These pacemakers, called asynchronous or fixed rate, compete with the natural heart activity and can sometimes induce arrhythmias or ventricular fibrillation. By adding a sensing amplifier to the asynchronous pacemaker in order to detect intrinsic heart activity and thus avoid this competition, one obtains a demand pacemaker, which provides electrical heart-stimulating impulses only in the absence of natural heartbeat. The other advantage of the demand pacemaker compared to the fixed rate system is that now the battery life of the system is prolonged because it is only activated when pacing stimuli are needed.

Berkovits introduced in June 1964 the demand concept, which is the basis of all modern pacemakers. In Fig.2.8 a suitable block diagram of a demand pacemaker is given. Intracardiac electrodes of conventional demand pacemakers serve two major functions, namely pacing and sensing. Pacing is achieved by the delivery of a short, intense electrical pulse to the myocardial wall where the distal end of the electrode is attached, similarly as in the early pacing devices. However the same electrode is used to detect the intrinsic activity of the heart (e.g., R-waves in the ventricle). The electrical pulse generator consists of the following components: a sense amplifier circuit, a timing control circuit and an output driver circuit (electrical impulse former).

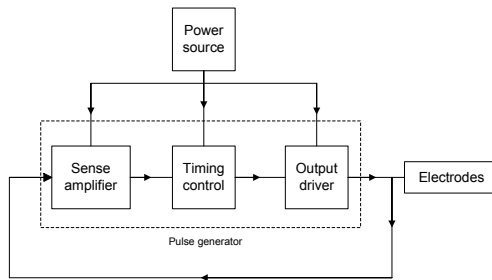


Figure 2.8: Basic demand pacemaker functional block diagram

The schematic of the pulse generator designed by Berkovits is given in Fig. 2.9 [15]. The general function of this circuit was to make the timing circuit

responsive to cardiac activity. This allowed inhibition of the pacing pulse from the pulse generator whenever the heart beats on its own. To achieve such function the sense amplifier played a fundamental role. It was designed to amplify and normalize the cardiac signal. Also, the sense amplifier was configured to filter out the undesired signals such as P and T wave and 60 Hz stray signal. The electrical signals picked up by the electrodes are coupled across capacitor  $C_{c1}$  in the input of the sense amplifier. The first two transistors Q1 and Q2 are class A amplifiers. The maximum gain of this amplifier stage is above 50. AC signals at the collector of Q2 are coupled through capacitor  $C_{C2}$  to the bases of both transistors Q3 and Q4. The circuit is symmetrically responsive to negative or positive inputs, since signals of positive polarity turn on Q3 and signals of negative polarity turn on Q4. Either transistor momentarily turns on Q6 which is the timing capacitor ( $C_t$ ) discharge switch.

A bandpass filter with bandwidth of 20-30 Hz was incorporated in the sense amplifier. Three differentiators ( $R_{B1}$  and  $C_{C1}$ ,  $R_{E1}$  and  $C_{E1}$ , and  $R_{E2}$  and  $C_{E2}$ ) limited the low frequency response of the detecting circuit to discriminate against the P and T waves and any other frequencies well below 20 Hz. Two integrators ( $R_{I1}$  and  $C_{I1}$ , and  $R_{I2}$  and  $C_{I2}$ ) were designed to reduce high frequency noise components well above 30 Hz. However, these filters were not totally effective in preventing the triggering of Q6 by 60 Hz signals. For this reason, a rate discrimination circuit (including transistor Q3, Q4 and Q5, resistors  $R_{E5}$  and  $R_{UNI}$ , and capacitors  $C_{UNI}$  and  $C_{C3}$ ) was provided.

Then, the rate discrimination stage had two functions. First, to provide unipolar current pulse (rectifier) of constant magnitude independent of the amplitude of input signals above a threshold value (1 V at the bases of Q3 and Q4). A phase inverter circuit (Q5,  $R_{phi1}$  and  $R_{phi2}$ ) was provided to invert the polarity signal from transistor Q3. Second, to provide a rate discrimination which avoided triggering of Q6 by signals occurring at a rate greater than a minimum value. The 60 Hz signals have a rate of 120 pulses per second which is much greater than 72 pulses per minute. Each pulse fully charged  $C_{UNI}$  and the next pulse was delivered before the capacitor had an opportunity to discharge to any meaningful extent and the increase in the capacitor voltage was negligible. Consequently, steps of negligible magnitude were transmitted through capacitor  $C_{C3}$  to the base of transistor Q6.

The switch S was used only to define the operation mode of the system, free-running mode (switch closed) or demand mode (switch opened). In free-running mode, the switch had to be closed and, therefore, the transistor Q6 remained in cut-off condition. When the switch was opened, i.e., in the case of a pacer required to operate in the demand mode, each pulse transmitted through capacitor  $C_{C3}$  to the base of transistor Q6 caused the transistor to conduct. Capacitor  $C_T$  discharged through the collector-emitter circuit of the transistor. In such a case, the timing cycle was interrupted and the junction of capacitor  $C_T$  and resistor  $R_p$  did not increase in potential to the point where transistors Q7 and Q8 were triggered to conduction. After capacitor  $C_T$  had

discharged through transistor Q6, the transistor turned off. The capacitor then started charging once again and the new cycle began immediately after the occurrence of the last heartbeat. The free-running operation would take place were there no input to the base of transistor Q6. Transistor Q6 would remain non-conducting and would not affect the charging of capacitor  $C_T$ . The capacitor  $C_T$  would trigger, and discharge through transistors Q7 and Q8 to control the generation of a pulse. The timing control circuit which determines the pulse duration (1 ms) and the repetition rate (72 pulses per minute) of the pulse generator, is made up of the transistors Q7 and Q8, the capacitor  $C_T$  and the resistances  $R_p$ ,  $R_T$ ,  $R_8$  and  $R_9$ . The pulse duration is determined by the time constant  $\tau_p = C_T \times R_p$  and the rate mainly by  $\tau_T = C_T \times R_T$ . The capacitor charge current flows through the resistances. During the charging period both transistors are off. As the  $C_T$  charges, the emitter voltage of Q7 rises and eventually exceeds the 4.2V reference sufficiently to forward bias the transistor causing collector current to flow. This turns on Q8 raising its emitter voltage which in turn raises the potential on the lower plate of the capacitor. This creates a regenerative turn on of both Q7 and Q7 which is sustained as long as  $C_T$  can supply current, a time determined primarily by resistor  $R_p$ . During this discharge time, the output transistor Q9 is turned on, causing current to flow in the electrode circuit. The output driver comprises the transistor Q9, the resistor  $R_{out}$  and the capacitor  $C_{c4}$ . After 1 ms  $C_T$  is discharged, the transistors Q7, Q8 and Q9 turn off and the pulse is terminated.

Finally, to avoid damage to the circuit due to high voltage signals from the electrodes, a zener diode (Z1) was placed between the terminals of the electrode.

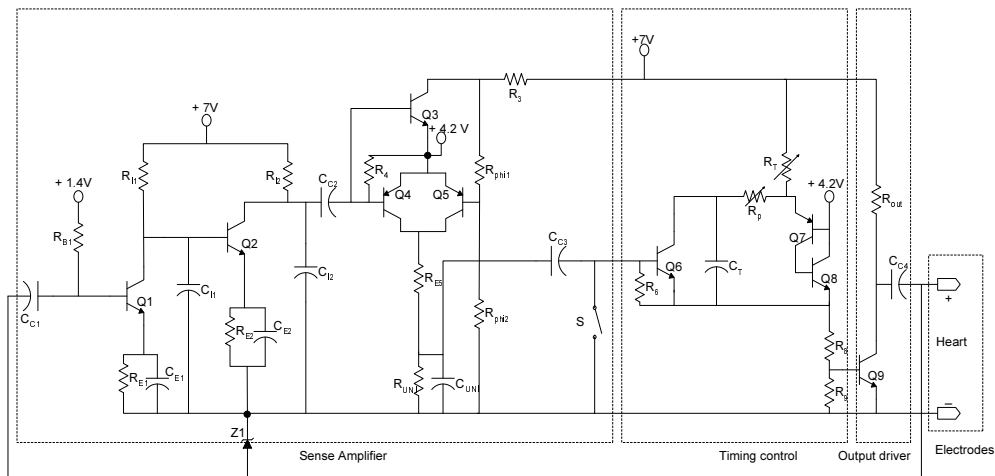


Figure 2.9: Schematic of the pulse generator of the first demand pacemaker

A variation of this concept is the demand-triggered pacemaker, which stimulates every time it senses intrinsic heart activity, i.e., the stimulus falls directly on the natural QRS.

### Dual-chamber Pacemaker

A dual-chamber pacemaker typically requires two pacing leads: one placed in the right atrium, and the other placed in the right ventricle. A dual-chamber pacemaker monitors (senses) electrical activity in the atrium and/or the ventricle to see if pacing is needed. When pacing is needed, the pacing pulses of the atrium and/or ventricle are timed so that they mimic the heart's natural way of pumping.

Dual-chamber pacemakers were introduced in the 1970's. One of the first description of a dual-chamber pacemaker was given by Berkovits in 1971. Berkovits announced a "bifocal" (AV sequential) pacer that sensed only in the ventricle but paced both chambers. In the presence of atrial standstill or a sinus node syndrome plus A-V block, the bifocal pacemaker could deliver a stimulus to the atrium and then, after an appropriate interval, to the ventricle. Berkovits improved on his original design given in Fig.2.9 with a dual-chamber demand pacemaker. An schematic of this design is given in Fig. 2.10 [16] . In accordance with the principles of the demand pacemaker design, a sense amplifier was provided to detect intrinsic ventricular activity. The timing control circuits determined both atrial and ventricular timeout stimulating period. However the atrial-stimulating impulse was generated first, and, after a predetermined time interval (200 ms), the ventricular-stimulating impulse was generated. Three electrodes were provided, a neutral electrode, an electrode for atrial stimulation and an electrode for ventricular pacing and sensing. The FET switch (S FET) was inserted in the feedback path of the ventricular electrode in order to avoid erroneous detection because of the atrial contraction. The FET switch was normally conducting. The negative pulse generated at the atrial electrode was transmitted through the diode  $D_a$ , charging the capacitor  $C_a$  and turning off the switch. When the atrial-stimulating terminated,  $C_a$  discharged through resistor  $R_a$  and turned on the switch again. In this manner, the sense amplifier was disabled during each atrial stimulation and for a short interval thereafter.

More Sophisticated dual-chamber pacemakers that sense intrinsic activity and pace in both chambers were developed, with the first use in late 1977.

### Rate-responsive Pacemaker

The latest innovations include the development of "rate-responsive" pacemakers in the early eighties, which could regulate their pacing rate based upon the output of a sensor system incorporated in the pacemaker and/or lead. A sensor system consists of a device to measure some relevant parameter from the body (body motion, respiration rate, pH, blood pressure and so forth)

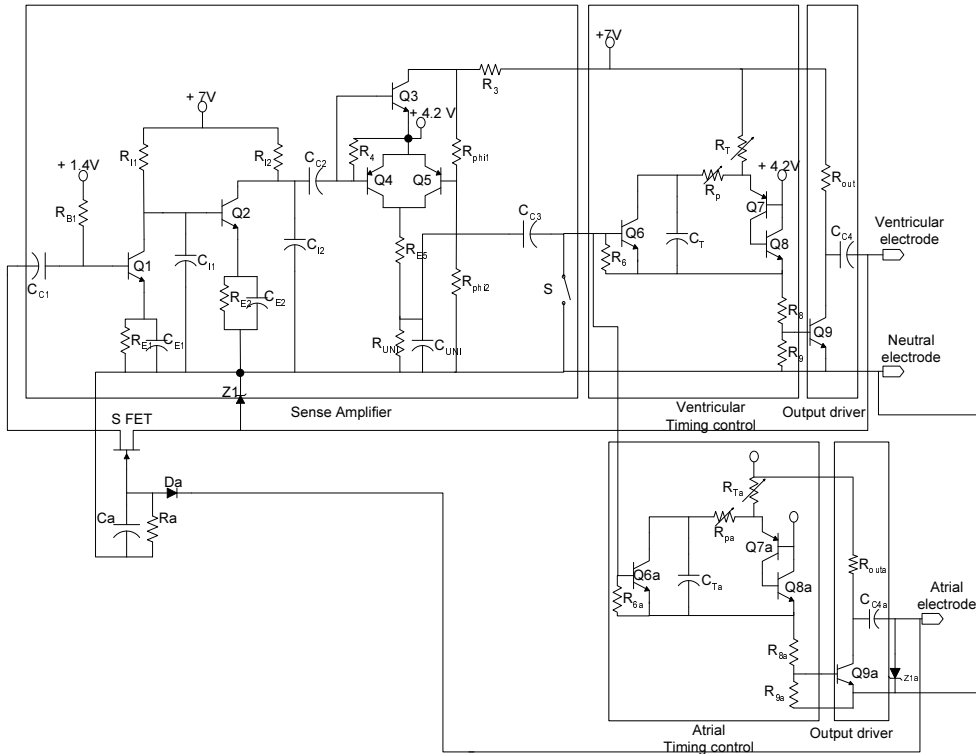


Figure 2.10: Schematic of the Dual-chamber demand pacemaker

and an algorithm in the pacemaker, which is able to adjust the pacemaker response in accordance with the measured quantity. Modern rate-responsive (also called frequency-response) pacemakers are capable of adapting to a wide range of sensor information relating to the physiological needs and/or the physical activity of the patient.

A block diagram of a rate-responsive pacemaker is given in Fig. 2.11. The system is based on a pacemaker having a demand pulse generator, which is sensitive to the measured parameter. Many rate-responsive pacemakers currently implanted are used to alter ventricular response in single-chamber ventricular systems. However, rate-responsive pacing can also be done with a dual-chamber pacing system.

## 2.4 New Features in Modern Pacemakers

A modern pacemaker consists of a telemetry system, an analog sense amplifier, analog output circuitry, and a microprocessor acting as a controller, as one can see in Fig. 2.12 [4].

Nevertheless, the sense amplifier plays a fundamental role in providing information about the current state of the heart. State of the art implantable

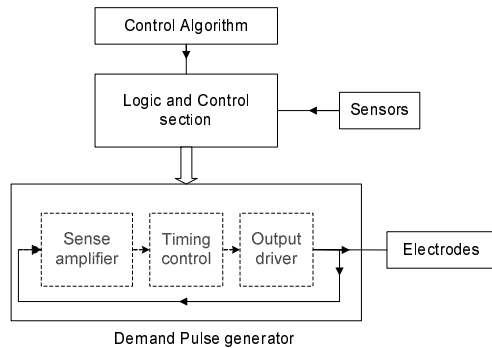


Figure 2.11: Block diagram of a rate-responsive pacemaker

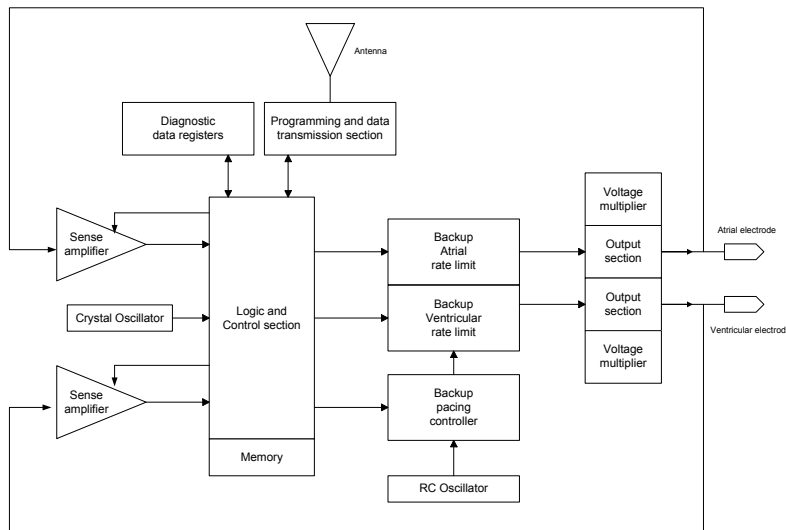


Figure 2.12: Block diagram of a typical modern pulse generator [4]

pulse generators or cardiac pacemakers include real-time sensing capabilities that are designed to detect and monitor intracardiac signal events (e.g. R-waves in the ventricle). A sense amplifier and its subsequent detection circuitry, together called the front-end, derive only a single event (characterized by a binary pulse) and feed this to a micro-controller that decides upon the appropriate pacing therapy to be delivered by the stimulator. Over the years, huge effort is put into the improvement of sense amplifier and detection circuitry. The dynamic range of the atrial and ventricular electrograms sensed by an endocardial lead typically lies between 0.5-7 mV and 3-20 mV respectively. Slew-rates of the signals range between 0.1 and 4 V/s. For the QRS complex, spectral power concentrates in the band from 10 to 30 Hz. The T wave is a slower signal component with a reduced amount of power in a band not exceeding 10 Hz. Amplification of intrinsic cardiac signals requires circuitry

that is robust against artifacts generated from non-cardiac electromagnetic sources located outside or inside the patient. Introduction of electronic article surveillance systems (EAS) has raised concerns with regard to the possible interaction between emitting field sources and the sense amplifiers of medical implantable devices like pacemakers [17], implantable cardioverter defibrillators and insertable loop recorders [18]. Other sources of electromagnetic interference (EMI) include cellular phones, airport metal detector gates, high voltage power lines [19], electro-cautery devices and MRI equipment [20]. Especially the more sensitive atrial-sensing channel of a brady-arrhythmia device is more prone to detection of EMI. Any type of EMI having sufficient amplitude could cause the pacemaker to react in a clinically undesirable way either inhibiting or triggering stimuli. Fortunately, noise reversion algorithms and circuits mostly provide reliable discrimination between EMI and intrinsic cardiac activity.

### Morphological analysis

In pacemakers, one of the challenges is the reduction of unnecessary therapies delivered to the patient's heart when the heart rate dynamics becomes comparable to that of lethal tachyarrhythmias like ventricular tachycardia (VT) or ventricular fibrillation (VF). This situation includes supraventricular tachycardia (SVT) that may occur as a result of atrial fibrillation. As heart rate does not discriminate between lethal tachyarrhythmias like VT/VF and SVT or atrial tachyarrhythmias, the morphology of the QRS complex, or more specifically, the R-wave morphology can be used for a more accurate discrimination between SVT and VT.

In addition, to ensure efficient use of the memory available in an implantable device, the incidence of false positives, erroneously triggering automatic storage, should be minimized. For insertable loop recorders (ILRs), promoting factors include the low amplitude electrogram signal as a result of the limited vector available for pseudo ECG measurement and the presence of muscle EMG and mechanical disturbance of the electrode tissue interface. Therefore, signal analysis methods improving discrimination of signals from noise are of great importance.

Since the information retrieved by the above front-end circuit is reduced to a single event, morphological attributes of the electrogram are completely suppressed. Recent research and clinical studies report details on how morphological aspects of the electrogram relate to various pathological states of the heart and on how the wavelet transform can contribute efficiently to analysis.

Analyzing the structure of the electrogram over multiple scales allows discrimination of electrogram features pertaining over all scales from those only seen at fine or coarse scales. Based on such observation, the presence or absence of electrogram features related to proximal or distal electrophysiological phenomena can be discriminated. The wavelet transform, being a multiscale analysis technique, offers the possibility of selective noise filtering and reliable

parameter estimation. An algorithm based on wavelet analysis that compares morphologies of baseline and tachycardia electrograms based on differences between corresponding coefficients of their wavelet transforms has been found highly sensitive for VT detection [21]. Whereas smoothing attenuates spectral components in the stop band of the linear filter used, wavelet-denoising attempts to remove noise and retain whatever signal is present in the electrogram.

Off-line ECG analysis, like Holter analysis, employs the discrete wavelet transform, implemented in the digital domain using multi-rate filter banks [22]. In these applications, the wavelet transform provides a means to reliably detect QRS-complexes. However, in patient worn external applications (e.g. intelligent Holter devices), it is not favourable to implement the WT by means of digital signal processing due to the high power consumption associated with A to D conversion and computation.

## 2.5 Summary and Conclusions

A brief overview of the history and development of circuit designs applied in pacemakers has been presented. The advances in integrated circuit designs have resulted in increasingly sophisticated pacing circuitry, providing, for instance, diagnostic analysis, adaptive rate response and programmability. Also, based on future trends for pacemakers, some features and improvements for modern cardiac sensing systems have been described.

In the next chapters we will investigate a fully integrated implementation of the analog WT circuit to be used in pacemakers. But, before that, the advantages of the wavelet over the Fourier analysis will be the subject of the following chapter.



# Bibliography

- [1] D. J. Woollons, *To beat or not to beat: the history and development of heart pacemakers*, Engineering Science and Education Journal, pp.259-268, Dec. 1995.
- [2] L. A. Geddes, *Historical Highlights in Cardiac Pacing*, IEEE Engineering in Medicine and Biology, pp.12-18, Jun. 1990.
- [3] W. Greatbatch and C. F Holmes, *History of Implantable Devices*, IEEE Engineering in Medicine and Biology, pp.38-49, Sep. 1991.
- [4] R. S. Sanders and M. T. Lee, *Implantable Pacemakers*, Proceedings of the IEEE, vol. 84, no.3, pp.480-486, Mar. 1996.
- [5] H. G. Mond, *Recent Advantages in Pacemaker Lead Technology*, Cardiac Electrophysiology Review, pp.5-9, 1999.
- [6] A. C. Guyton and J. E. Hall, *Textbook of Medical Physiology*, W B Saunders, 9<sup>th</sup> ed., Jan. 1996.
- [7] J. D. Bronzino, *The Biomedical Engineering Handbook*, CRC Press and IEEE Press, 2<sup>nd</sup> ed., vol.1, 2000.
- [8] R. Sutton and I. Bourgeois, *The foundations of cardiac pacing. Part I*, Futura Publishing Company, 1991.
- [9] M. Schaldach and S. Furman, *Advances in Pacemaker Technology*, Springer-Verlag, 1975.
- [10] A. A. Hyman, *Resuscitation of the stopped heart by intracardial therapy*, Arch Intern Med, 50:283.
- [11] [www.ep-history.org](http://www.ep-history.org).
- [12] R. Elmquist and A. Senning, *An Implantable Pacemaker for the Heart*, Tliffe & Sons, London, pp. 253-254, 1959.
- [13] W. Greatbatch, *Medical Cardiac Pacemaker*, US Patent 3,057,356, Oct. 1962.

- [14] *www.tpub.com.*
- [15] B. V. Berkovits, *Demand Pacer*, US Patent 3,528,428, Sep. 1970.
- [16] B. V. Berkovits, *Atrial and Ventricular Demand Pacer*, US Patent 3,595,242, Jul. 1971.
- [17] J. W. Harthorne, *Pacemakers and store security devices*, Cardiol. Rev., vol.9, no. 1, pp.10-17, 2001.
- [18] C. C. de Cock, H. J. Spruijt, L. M. van Campen, W. A. Plu and C. A. Visser *Electromagnetic interference of an implantable loop recorder by commonly encountered electronic devices*, Pacing Clin. Electrophysiol., vol.23, no. 10, pp.1516-1518, 2000.
- [19] T. W. Dawson, K. Caputa, M. A. Stuchly and R. Kavet *Pacemaker interference by 60-Hz contact currents*, IEEE Trans. Biomed. Eng., vol.49, no. 8, pp.878-886, 2002.
- [20] G. Lauck, A. von Smekal, S. Wolke, K. C. Seelos, W. Jung, M. Manz and B. Luderitz *Effects of nuclear magnetic resonance imaging on cardiac pacemakers*, Pacing Clin. Electrophysiol., vol.18, no. 8, pp.1549-1555, 1995.
- [21] C. D. Swerdlow, M. L. Brown, K. Lurie, J. Zhang, N. M. Wood, H. W. Olson and J. M. Gillberg *Discrimination of ventricular tachycardia from supraventricular tachycardia by a downloaded wavelet-transform morphology algorithm: a paradigm for development of implantable cardioverter defibrillator detection algorithms*, Pacing Clin. Electrophysiol., vol.13, no. 5, pp.432-441, 2002.
- [22] G. Strang and T. Nguyen *Wavelets and Filter Banks*, Wellesley Cambridge Press, 1996.

# Chapter 3

## Wavelet versus Fourier analysis

*“Concentrating on transients is probably a strategy for selecting important information from the overwhelming amount of data recorded by our senses.”* - Stéphane Mallat

### 3.1 Introduction

The Fourier transform, named after Jean Baptiste Joseph Fourier, is an integral transform that re-expresses a function in terms of sinusoidal basis functions, i.e. as a sum, possibly infinite, of sines and cosines functions multiplied by some amplitude coefficients. The Fourier transform can thus be defined as frequency-amplitude decomposition [1].

The big disadvantage of a Fourier expansion however is that it has only frequency resolution and no time resolution. This means that although we might be able to determine all the frequencies present in a signal, we do not know when they are present. To overcome this problem in the past decades several solutions have been developed which are able to represent a signal in the time and frequency domain at the same time. The wavelet transform or wavelet analysis is probably the most recent solution to overcome the shortcomings of the Fourier transform. The idea behind these time-frequency joint representations is to decompose the signal of interest into several parts and then analyze the parts separately. It will be clear from the next sections that analyzing a signal in this way will give more information about the 'when' and 'where' of different frequency components. In addition, one will see that in contrast to the Fourier filters, a wavelet filter is not exclusively defined by its frequency behavior and one of the most important design aspect for an wavelet filter is the impulse response definition in time-domain.

### 3.2 Fourier transform

The behavior of a linear, continuous-time, time-invariant system (LTI) with input signal  $x(t)$  and output signal  $y(t)$  is described by the convolution integral [8]

$$y(t) = \int_{-\infty}^{\infty} x(\tau)h(t - \tau)d\tau \quad (3.1)$$

where  $h(t)$  is the response of the system to a unit impulse input. Since complex sinusoidal waves  $e^{j\omega t}$  are eigenvectors of linear time-invariant operators (eigenvectors of convolution operators), the Fourier transform is widely used in LTI signal processing [14]. Another way to think of Fourier analysis is as a mathematical technique for transforming the signal from time-based to frequency-based. This is due to the fact that the Fourier transform of  $f(t) = e^{j\omega_0 t}$  is a Dirac function  $\hat{f}(\omega) = 2\pi\delta(\omega - \omega_0)$ .

The Fourier coefficients are obtained by correlating the input signal  $f(t)$  with a sinusoidal wave  $e^{j\omega t}$  given by the equation

$$\hat{f}(\omega) = \int_{-\infty}^{\infty} f(t)e^{-j\omega t}dt \quad (3.2)$$

The Fourier integral described in Eq. 3.2 measures the amplitude spectrum of  $f(t)$  at frequency  $\omega$ . Note that the Fourier basis functions are represented by periodic infinite duration functions (sinusoidal waves), giving information only in frequency domain. Hence, when the signal are periodic and sufficiently regular, the Fourier coefficients converge quickly. For nonperiodic signals, the Fourier integral gives a continuous spectrum. Hence, the Fourier transform is not satisfactory for analyzing signals whose spectra vary with time. In Fig. 3.1 one can see the Fourier Transform of a nonstationary signal. From the Fourier analysis, the signals' frequency content is easily detected. However the time information, i.e., when the change of the momentary frequency component took place, is lost, as can be seen from the inverse Fourier Transform.

To characterize the time information of  $f(t)$  (i.e., the discontinuity) it is necessary to decompose it over waveforms that are also well localized in time.

### 3.3 Windowing function

To characterize the time information of  $f(t)$  (i.e., discontinuities) it is necessary to decompose it over waveforms that are well localized in time. For instance, one can apply a rectangular (so-called Haar-basis) window function [1], which is well localized in time, to "zoom-in" on the singularity of the signal in the time domain. However, its Fourier transform is defined over the entire frequency axis (i.e., it has a poor resolution in frequency domain). As an example, we apply two signals with different frequency components, as depicted in Fig. 3.2.a and Fig. 3.2.b, respectively. The smaller the window we choose,

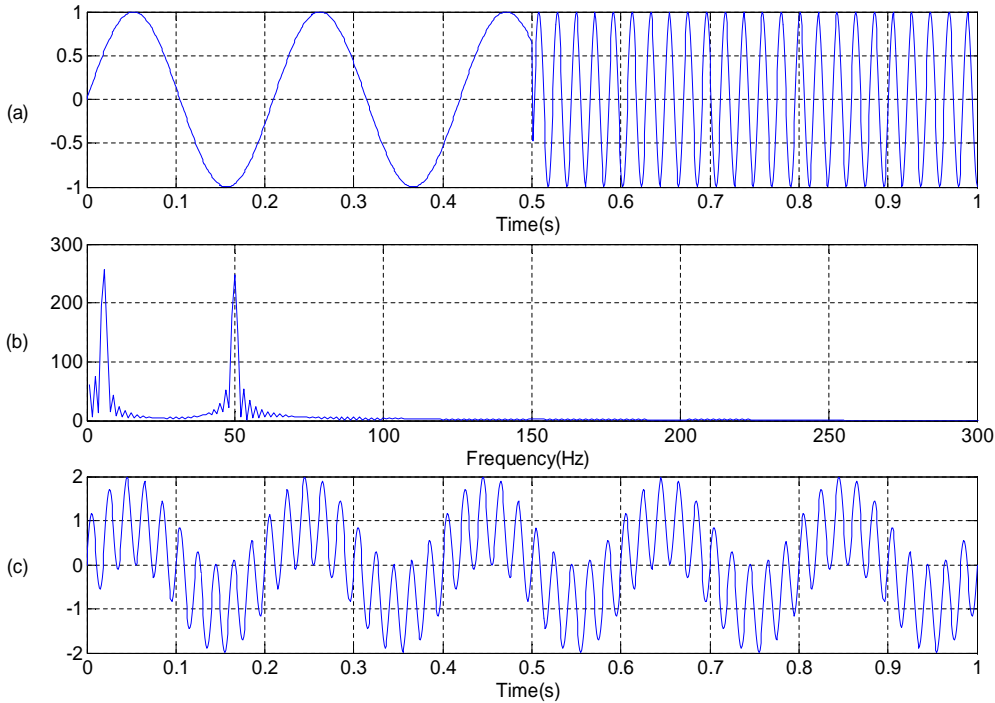


Figure 3.1: (a) Input signal with two frequency components with different instant in time (b) Fourier Transform (c) Inverse Fourier Transform

the better we can locate sudden changes, such as peak or discontinuities, but the "blinder" we become to the lower frequency components of both signals. The truncated analyzed signal and its Fourier transform are plotted respectively in Fig. 3.2.c and Fig. 3.2.d. It can be easily seen that the singularity of the signal is now better localized in time, but it is not well represented in frequency by its Fourier transform. Note that we cannot discriminate both input signals from their frequency components anymore.

## 3.4 Wavelet transform

The Fourier basis provides a very efficient representation of functions that exhibit long term oscillatory behavior whereas the Haar basis best represents functions that consist of sharp peaks and discontinuities. Unfortunately, these two representations are orthogonal to each other, meaning that it is not easy to extract frequency information from the time representation and vice versa. To overcome these limitations, we must decompose signals over basis functions that are well concentrated in time and frequency and the Wavelet Transform (WT) is well suitable for local time-frequency decomposition. As an example we can apply the WT to the signal in Fig. 3.1.a. The left side of the Fig. 3.3 shows the wavelet mapping of the input signal in the time domain (using

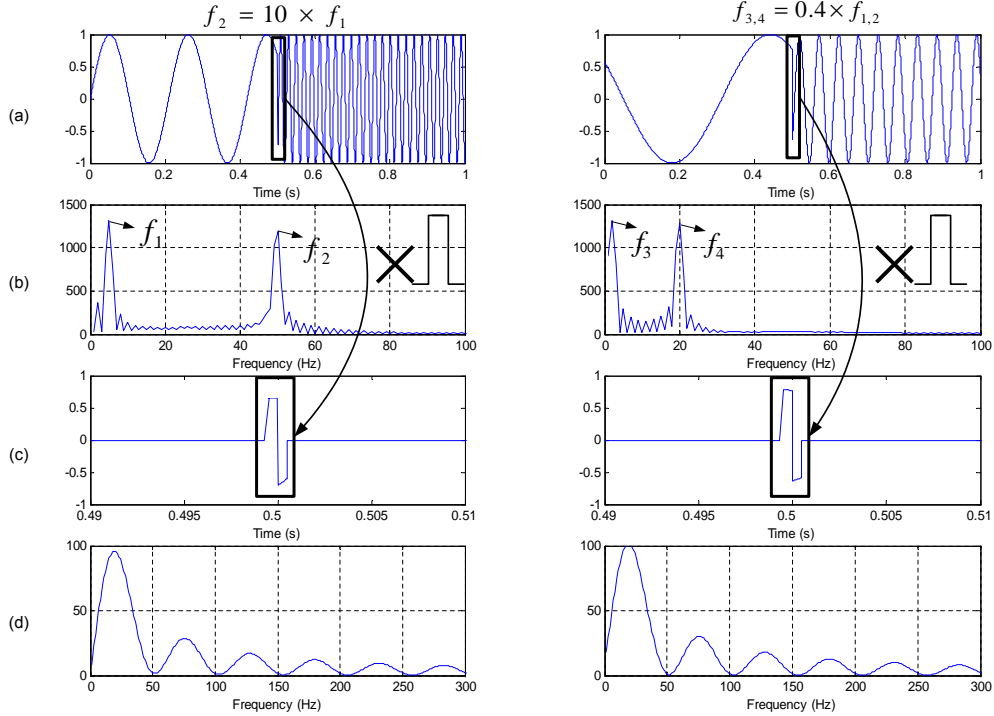


Figure 3.2: (a) Input signals with two frequency components with different instant in time ( $f_1 = 5$  Hz,  $f_2 = 50$  Hz,  $f_3 = 2$  Hz and  $f_4 = 20$  Hz) (b) Fourier Transform (c) Truncated signals in time domain (d) Fourier transform of the truncated signals

different scaling parameter  $a$ ), and their Fourier spectra are plotted on the right. Note that, depending on the value of  $a$ , one can zoom into the singularity or obtain a global view to preserve the frequency information. This is the zooming ability of wavelets that will be explained below.

For signal processing, the Wavelet Transform (WT) has been shown to be a very promising mathematical tool [13], [14], [4], particularly for local analysis of nonstationary and fast transient signals, due to its good estimation of time and frequency localizations. Fig. 3.4 shows an example of the WT analysis of an intracardiac signal (IECG). In Fig. 3.4.a, the WT is applied for QRS-complex detection using a typical IECG signal. As one can see, the maximum values of the WT correspond to the QRS-complex, and thus, the time position of the QRS-complex can be easily identified at several scales, i.e.,  $a$  varying from 2 to 32. Another important advantage of the WT compared to the Fourier analysis is given by Fig. 3.4.b, where a white Gaussian noise is added to an IECG. By definition, white Gaussian noise covers the whole frequency spectrum, so its frequency spectrum overlaps with the cardiac signal. Therefore, the in-band noise cannot be removed by applying a Fourier analysis. In addition, due to the large amplitude of the noise, one

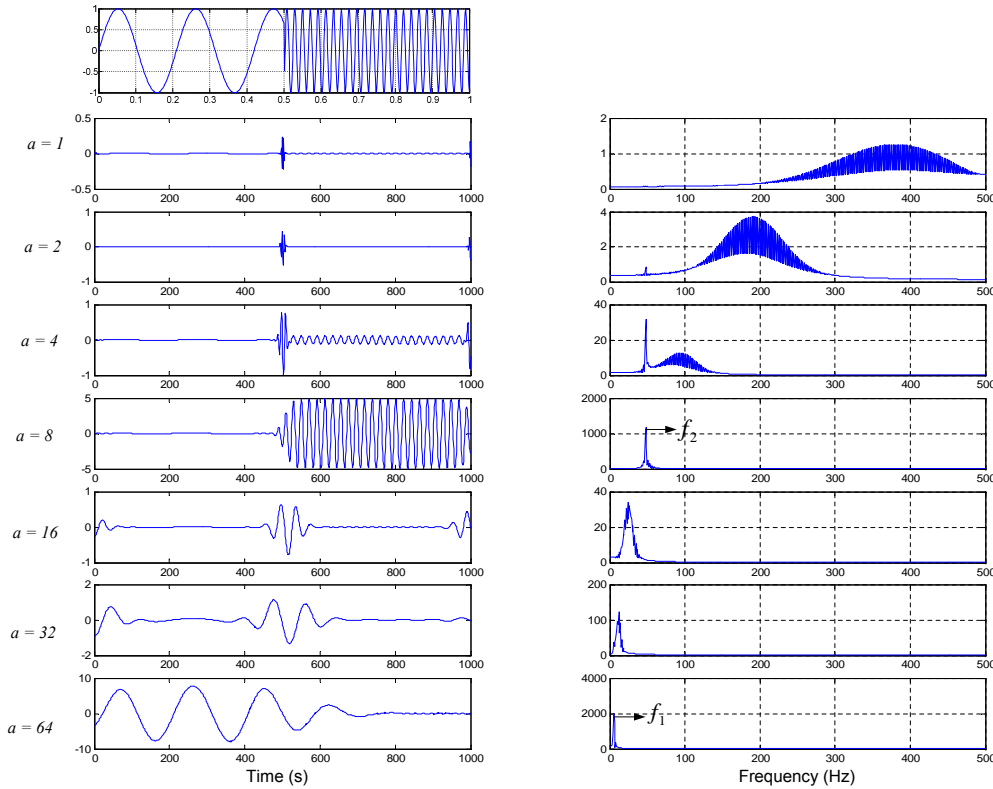


Figure 3.3: Morlet wavelet transform with 7 scales of the signal in Fig.3.1.a. Time-response is shown in the left side and the corresponding frequency-response is given in the right side

cannot discriminate the desired signal from the noise in time-domain (amplitude threshold). Nevertheless, for certain scale values, the WT can distinguish cardiac signal points from noise and the maxima of the QRS-complex can still be identified for  $a$  equals 8, 16 and 32, as seen from the wavelet analysis in Fig. 3.4.b. This denoising characteristic of the WT is based on correlation factor, and it will be explained later.

Wavelet literally means small wave. Wavelet analysis is performed using a prototype function called the wavelet base, which decomposes a signal into components appearing at different scales (or resolutions). Since the Wavelet Transform is a linear operation that decomposes a signal into components that appear at different scales (or resolutions)[14], the WT is a so-called constant-Q analysis (bandpass filters with constant relative bandwidth). The wavelet transform of a function  $f(t)$  at scale  $a$  and position  $\tau$  is given by

$$W_f(\tau, a) = \frac{1}{\sqrt{a}} \int_{-\infty}^{\infty} f(t)\psi^*(\frac{t-\tau}{a})dt \quad (3.3)$$

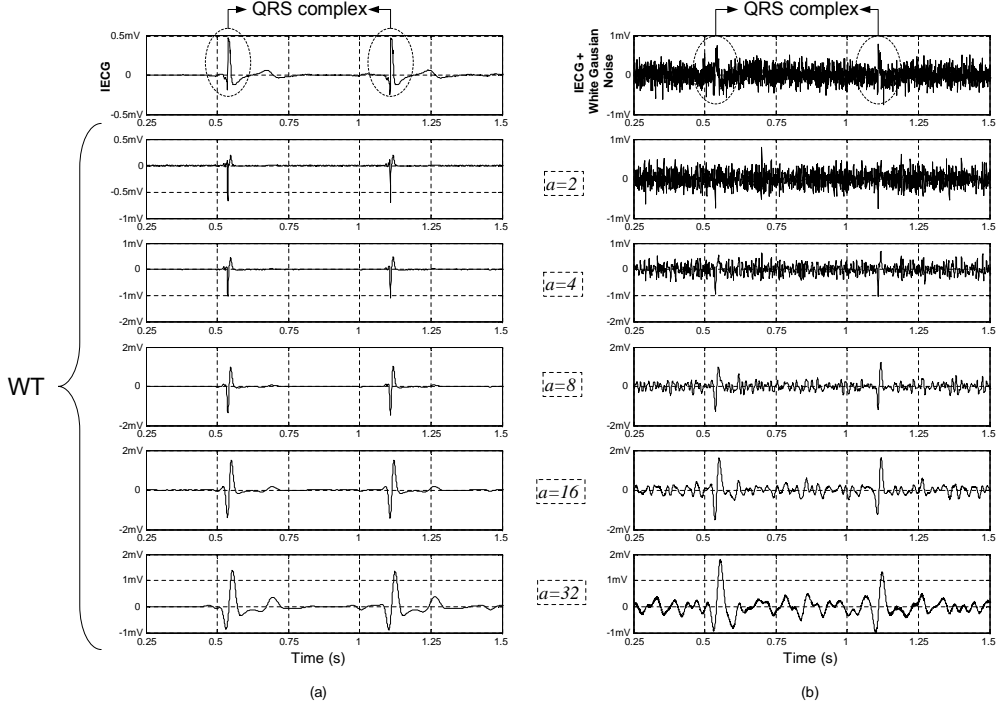


Figure 3.4: Wavelet analysis of an Intracardiac signal (a) Typical IECG (b) IECG with additive white Gaussian noise

where  $\psi(t)$  is the wavelet base (or mother wavelet) and  $*$  denotes the complex conjugation. The factor  $1/\sqrt{a}$  is used for energy normalization. Hence, the WT is based on the convolution of the signal with a dilated impulse response of a filter (defined by  $\psi(t)$ ), mapping the signal onto a two-dimensional function of time and frequency. The main idea of the WT is to look at a signal at various windows and analyze it with various resolutions. It provides an alternative to the classical Short-Time Fourier Transform (STFT) or Gabor Transform [4]. In contrast to the STFT, which uses a single analysis window, the WT uses short windows (small  $a$ ) at high frequency analysis and long windows (large  $a$ ) at low frequency analysis. The time-frequency plane of a WT is shown in Fig.3.5.a. As one can see, the time-frequency (or time-scale) representation has an intrinsic limitation: the product of the resolution in time and frequency is limited by the uncertainty principle (Heisenberg inequality)[1], [4].

$$\Delta t \Delta \omega > \frac{1}{2} \quad (3.4)$$

with

$$\Delta t = \sqrt{\frac{\int t^2 |\psi(t)|^2 dt}{\int |\psi(t)|^2 dt}} \quad (3.5)$$

$$\Delta\omega = \sqrt{\frac{\int \omega^2 |\Psi(\omega)|^2 d\omega}{\int |\Psi(\omega)|^2 d\omega}} \quad (3.6)$$

where  $\Psi(\omega)$  is the Fourier transform of the wavelet base  $\psi(t)$  and  $\Delta t$  and  $\Delta\omega$  are the time and frequency resolution, respectively. Note that the denominator of Eq.3.5 and Eq.3.6 represent the energy of the function related to Parseval's theorem. The uncertainty principle states that one can only trade time resolution for frequency resolution and vice versa. This means that the resolution in time and frequency cannot be arbitrarily small, because their product is lower bounded.

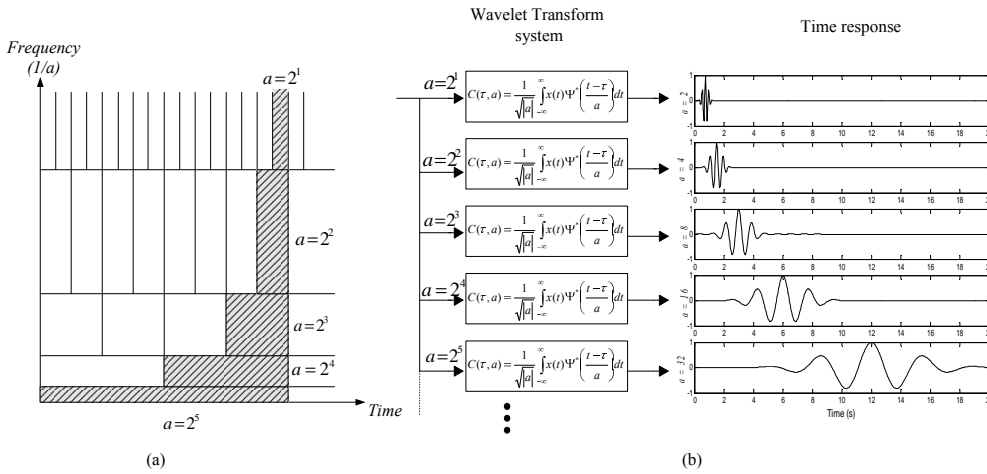


Figure 3.5: Wavelet transform system, (a) Time-frequency plane, (b) Morlet WT system with multiple scales

### 3.4.1 Continuous-time wavelet bases

The wavelet analysis is thus performed using a prototype function called the wavelet base,  $\psi(t)$  ( $\psi(t) \in L^2$ , i.e. finite energy functions). The main characteristic of the wavelet base is given by

$$\int_{-\infty}^{\infty} \psi(t) dt = 0 \quad (3.7)$$

This means that the wavelet base is oscillatory and has zero mean value. Also, this function needs to satisfy the admissibility condition so that the original signal can be reconstructed by the inverse Wavelet Transform

$$\int_{-\infty}^{\infty} \frac{|\Psi(\omega)|^2}{|\omega|} d\omega = C_\Psi < \infty \quad (3.8)$$

The admissible condition implies that the Fourier transform of the wavelet must have a zero component at zero frequency. Hence, the wavelets transforms

are inherently band-pass filters in the Fourier domain, defined as Wavelet filters. Any function that has finite energy is square integrable and satisfies the wavelet admissibility condition can be a wavelet [13].

There are several types of well-defined wavelet bases, and, depending on the application (and the properties of the wavelet function), one may be preferred over others. Three different types of wavelet bases will be presented here, being Gaussian wavelets (derivatives of a Gaussian function), Morlet and Daubechies Wavelets (dbN). A number of other wavelet bases can be found in [13], [14].

Gaussian wavelets (gaus) are symmetric with infinite support. The Gaussian wavelet family is defined from the derivatives of the Gaussian function [14] and is given by

$$\psi_n(t) = C_n \cdot \frac{d^n}{dt^n}(e^{-t^2}) \quad (3.9)$$

where  $n$  denotes the order,  $\frac{d}{dt}$  is the symbolic derivative and  $C$  is a normalizing constant, which depends on  $n$ . Gaussian functions are often used as mother wavelets since they provide the best resolution in time and in frequency (minimum time-frequency product,  $\Delta t \Delta \omega$ ). The gaus1 and gaus2 (also known as Mexican hat) are depicted in Fig.3.6.a and Fig.3.6.b, respectively.

The Morlet wavelet base is obtained from a Gaussian envelope multiplied by a cosine function [14], and described by

$$\psi(t) = \cos(5\sqrt{2}(t - \tau))e^{-(t-\tau)^2} \quad (3.10)$$

The Morlet wavelet, shown in Fig.3.6.c, can be defined as the original wavelet, where J. Morlet (a French geophysical engineer), in 1984, came up with an alternative for the short-time Fourier transform, windowing a cosine wave using a smooth window (gaussian window), which is well localized in the time-frequency domain.

A family of orthogonal wavelets was first constructed by Ingrid Daubechies in 1992 [13]. Daubechies wavelets are orthogonal functions with compact support of  $2N - 1$  and  $N$  vanishing moments, where  $N$  is the order of the wavelet. The orthogonality of the Daubechies wavelets has a very important mathematical and engineering consequence: any continuous function may be uniquely projected onto the wavelet basis functions and expressed as a linear combination of the basis functions. Daubechies wavelets are nonsymmetric and have no explicit expression except for  $N = 1$ , which is the Haar wavelet (the Haar wavelet is the simplest orthogonal function). One example of this wavelet family, Db6, is given in Fig.3.6.d.

Furthermore, in order to avoid redundancy, one can sample the scale parameter along the dyadic sequence  $(2^j)_{j \in \mathbb{Z}}$ , i.e.,  $a = 2^j$  [14]. Fig.3.5.b shows a wavelet system with multiple scales in parallel that can be used to compute the WT in real time. As an example, a Morlet WT system has been represented.

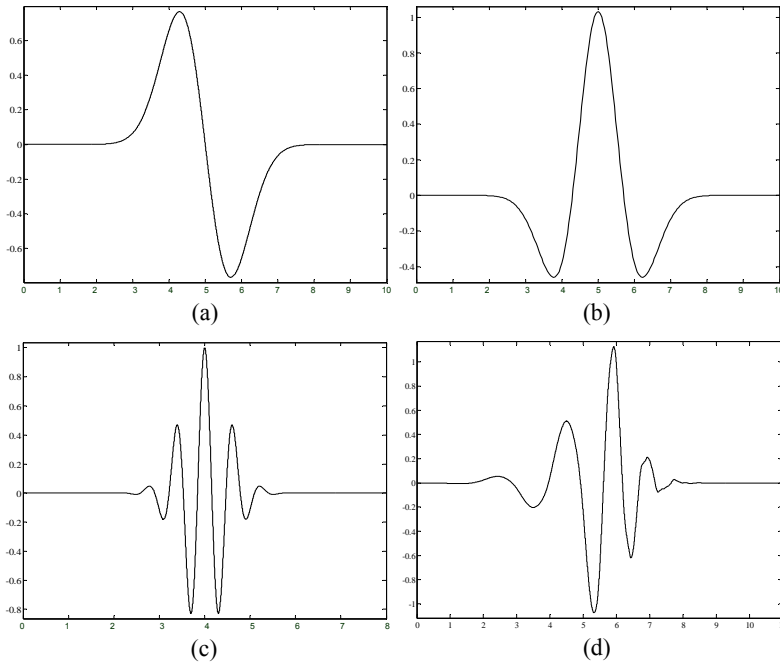


Figure 3.6: Wavelet bases; (a) First derivative of Gaussian (gaus1) (b) Second derivative of Gaussian (gaus2) (c) Morlet and (d) Daubechies (db6)

### 3.4.2 Complex continuous wavelet bases

Complex wavelets provide more detail information in transient signal detection than real-valued wavelets. Often the wavelet transform of a real signal by means of a complex wavelet is plotted in modulus-phase form, rather than using the real and imaginary representation. In the complex wavelet transform analysis, the modulus maxima and the phase crossings point out the locations of sharp signal transitions. Nevertheless, the phase information reveals isolated singularities in a signal more accurately than does the modulus [8]. Also, using the phase information, different kinds of transition points of the analyzed signal, i.e. local maxima and inflection points, can be distinguished. For instance, using the first complex Gaussian wavelet (*cgaus1*), the  $-\pi$  to  $+\pi$  phase crossings point define the inflection points, whereas  $\pm\pi$  to 0 is associated with the local maxima points (peaks), as one can see in Fig. 3.7.

One example of a complex wavelet function is the Gabor wavelet. The Gabor wavelet is obtained from a complex Gaussian function (complex exponential windowed by a Gaussian function) as basic functions [14], described by

$$\psi(t) = C \cdot e^{-j\omega t} e^{-t^2} = C \cos(\omega t) e^{-t^2} - j C \sin(\omega t) e^{-t^2} \quad (3.11)$$

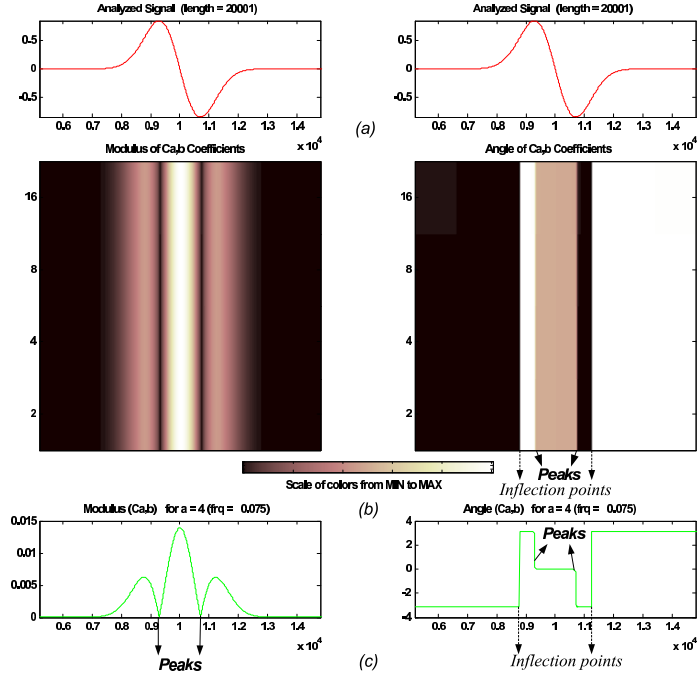


Figure 3.7: Complex wavelet transform using cgau1 (a) Input signal (b) Wavelet transform coefficients with four dyadic ( $a = 2^i$ ) scales (c) One coefficient line ( $a = 4$ )

where  $e^{-j\omega t}e^{-t^2}$  is the complex Gaussian function and  $C$  is a normalizing constant. From the Gabor wavelet one can derive some complex wavelet families, e.g. the complex Gaussian and the complex Morlet.

The modulus, the real and imaginary parts and the phase of the complex Gabor wavelet for  $\omega = 2$  are given in Fig. 3.8.

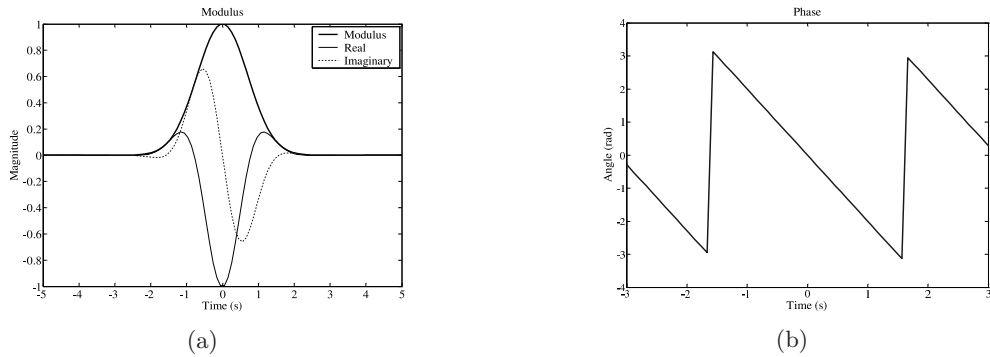


Figure 3.8: Complex Gabor Wavelet (a) Modulus (b) Phase

## 3.5 Signal Processing with Wavelet Transform

Over the last decade, wavelets have had a growing impact on signal processing theory. Wavelets are useful tools for signal processing applications such as singularity detection, denoising and data compression [8] - [17].

### 3.5.1 Singularity detection - Wavelet Zoom

Singularities (sharp signal transitions) and irregular structures often carry essential information in a signal. Singularities and edges are detected by following the wavelet transform local maxima at fine scales.

#### Modulus maxima

We use the term modulus maxima to describe any point  $(t_o, a_o)$  such that  $|W_f(t, a)|$  is locally maximum at  $t = t_o$ . This implies that

$$\frac{\partial W_f(t_o, a_o)}{\partial t} = 0 \quad (3.12)$$

$t$  and  $a$  represent the time and scale parameters of the WT, respectively. A definition of a *modulus maximum* of the wavelet transform is given as follows [14]:

“Any point  $(t_o, a_o)$  such that  $|W_f(t, a_o)| < |W_f(t_o, a_o)|$  when  $t$  belongs to either a right or a left neighborhood of  $t_o$ , and  $|W_f(t, a_o)| \leq |W_f(t_o, a_o)|$  when  $t$  belongs to the other side of the neighborhood of  $t_o$ .”

This local maximum should be a strict local maximum in either the right or the left neighborhood of  $t_o$ , to avoid having any local maxima when  $|W_f(t, a_o)|$  is constant. We call a “maxima line” any connected curve  $a(t)$  in the scale-space plane  $(t, a)$  along which all points are modulus maxima.

The singularities of a nonstationary signal are detected by finding the abscissa where the wavelet modulus maxima converge at fine scales. However, in signal processing, fractal dimensions (e.g., in the form of a Lipschitz component) are increasingly important, especially in the context of singularity processing. Signal characterizations, classifications, and recognition can benefit from information provided by the Lipschitz exponent.

#### Lipschitz exponent - Regularity

To characterize singular structures, it is necessary to precisely quantify the local regularity of a signal  $f(t)$ . Lipschitz (also known as Holder) exponents provide uniform regularity measurements over time intervals, but also at any point  $\nu$ . If  $f(t)$  has a singularity at  $\nu$ , which means that it is not differentiable at  $\nu$ , then the Lipschitz exponent at  $\nu$  characterizes this singular behavior. The wavelet theory proves that these Lipschitz exponents can be computed from the evolution across scales of the wavelet transform modulus maxima.

A function  $f$  is uniformly Lipschitz  $\alpha$  over  $[a, b]$  if for all  $\nu \in [a, b]$

$$e_\nu(t) = |f(t) - p_\nu(t)| \leq K|t - \nu|^\alpha \quad (3.13)$$

where  $p_\nu(t)$  is the Taylor polynomial,  $e_\nu(t)$  is the approximation error and  $K$  is a positive constant, which is independent of  $\nu$ . Suppose  $f$  is “ $m$ ” times differentiable, the Taylor polynomial is given by

$$p_\nu(t) = \sum_{k=0}^{m-1} \frac{f^{(k)}(\nu)}{k!} (t - \nu)^k \quad (3.14)$$

This means that the  $m^{\text{th}}$  order differentiability of  $f(t)$  in the neighborhood of  $\nu$  yields an upper bound on the error  $e_\nu(t)$  when  $t$  tends to  $\nu$ . The Lipschitz regularity refines this upper bound with non-integer exponents.

As an example, consider a signal

$$f(t) = 1 - |1 - t|^\alpha \quad (3.15)$$

shown in Fig.3.9. In the intervals,  $0 \leq t < 1$  and  $1 < t \leq 2$ , the signal is regular with Lipschitz exponent  $\alpha$ . However the regularity ends at  $t = 1$ , hence  $f(1)$  is singular with the following behavior: on the left side the singular point has a Lipschitz  $\alpha$  (increasing from the left to the right) while on the right side it has a Lipschitz  $\alpha$  (decaying from the left to the right). The exponent is also called singularity strength.

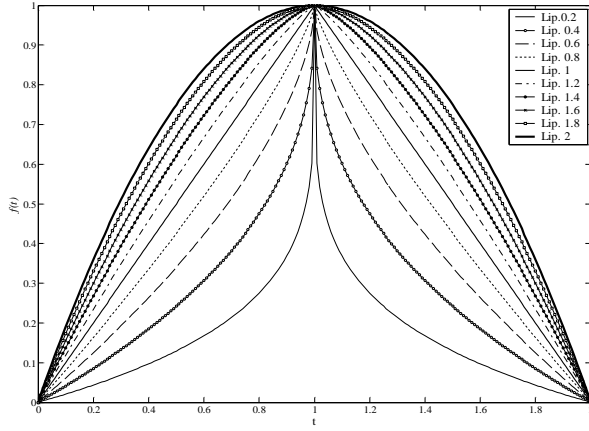


Figure 3.9: Lipschitz exponent from 0.2 to 2 for  $f(t) = 1 - |0.5 - t|^\alpha$

It is important to observe that knowing the singularity behavior at  $f(0.5)$  is sufficient to describe  $f(t)$ . Hence, singularities (i.e.,  $\alpha$  of both sides and their corresponding increasing/decaying trends) contain signal information compactly.

The Fourier transform is a powerful tool for measuring the minimum global regularity of functions. However, it is not possible to analyze the regularity

of  $f$  at a particular point  $\nu$  from the decay of  $|F(\omega)|$  at high frequencies . In contrast, since wavelets are well localized in time, the wavelet transform gives Lipschitz regularity over intervals and at points.

### Wavelet Vanishing moments

To measure the local regularity of a signal, it is not important to use a wavelet with narrow frequency support, but vanishing moments are crucial. The vanishing moment can be defined by

$$\int_{-\infty}^{+\infty} t^k \psi(t) dt = 0 \quad (3.16)$$

for  $0 \leq k < n$ . If the wavelet has  $n$  vanishing moments, then the WT can be interpreted as a multiscale differential operator of order  $n$ .

Applying the WT to a signal defined by  $f(t) = p_\nu(t) + e_\nu(t)$ , we obtain

$$Wf(t) = Wp_\nu(t) + We_\nu(t) = We_\nu(t) \quad (3.17)$$

This result shows that a wavelet estimates the exponent  $\alpha$  by ignoring the polynomial  $p_\nu$  (a phenomenon known as polynomial suppression). For this purpose, to calculate the Lipschitz  $\alpha$  from a signal, one has to use a wavelet base that presents  $n > \alpha$  vanishing moments. For instance, the first derivative of a gaussian presents one vanishing moment, where the modulus maxima are used to locate discontinuities - A function with  $\alpha = 0$  is bounded but discontinuous at  $\nu$  - and points where the function is not differentiable ( $\alpha < 1$ ). For the second derivative of a gaussian, the modulus maxima correspond to high curvatures.

### Regularity Measurements with Wavelets

The decay of the modulus maxima amplitude of the WT across scales is related to the Lipschitz regularity (uniform and pointwise) of the signal. Measuring this asymptotic decay is equivalent to zooming into signal structures with a scale that goes to zero.

The decay of  $|Wf(t, a)|$  in the neighborhood of  $\nu$  is controlled by the decay of the modulus maxima included in the *cone of influence*  $|t - \nu| \leq Ca$ .  $f$  is uniformly Lipschitz  $\alpha$  in the neighborhood of  $\nu$  if and only if there exists  $A > 0$  such that each modulus maximum in the cone satisfies

$$|Wf(t, a)| \leq Aa^{\alpha+\frac{1}{2}} \quad (3.18)$$

which is equivalent to

$$\log_2 |Wf(t, a)| \leq \log_2 A + (\alpha + \frac{1}{2}) \log_2 a \quad (3.19)$$

Eq.3.18 shows that  $|Wf(t, a)|$  decays like  $a^{\alpha+\frac{1}{2}}$  over intervals where  $f$  is uniformly Lipschitz  $\alpha$ . Mallat and Hwang [7] have proven that the local maxima of the wavelet transform modulus provide enough information for analyzing such singularities and proved that modulus maxima detect all singularities. The Lipschitz regularity at  $\nu$  is thus the maximum slope of  $\log_2|Wf(t, a)|$  as a function of  $\log_2 a$  along the maxima lines converging to  $\nu$ . Fig. 3.10 shows an example of Lipschitz exponent extraction by means of the wavelet modulus maxima across scales. The applied wavelet base is the first derivative of a Gaussian and the input signal has two singular structures,  $\alpha = 2$  and  $\alpha = 0.5$ . Note that for the case of  $\alpha = 2$ , the Lipschitz exponent is larger than the vanishing moment of the wavelet and the modulus maxima can detect the position of the inflection points, but can not characterize the singularity type. In the other hand, for  $\alpha = 0.5$ , the modulus maxima point exactly the position  $\nu$  and characterize the shape of the singularity by  $\log_2|Wf(t, a)| = 0.5$ .

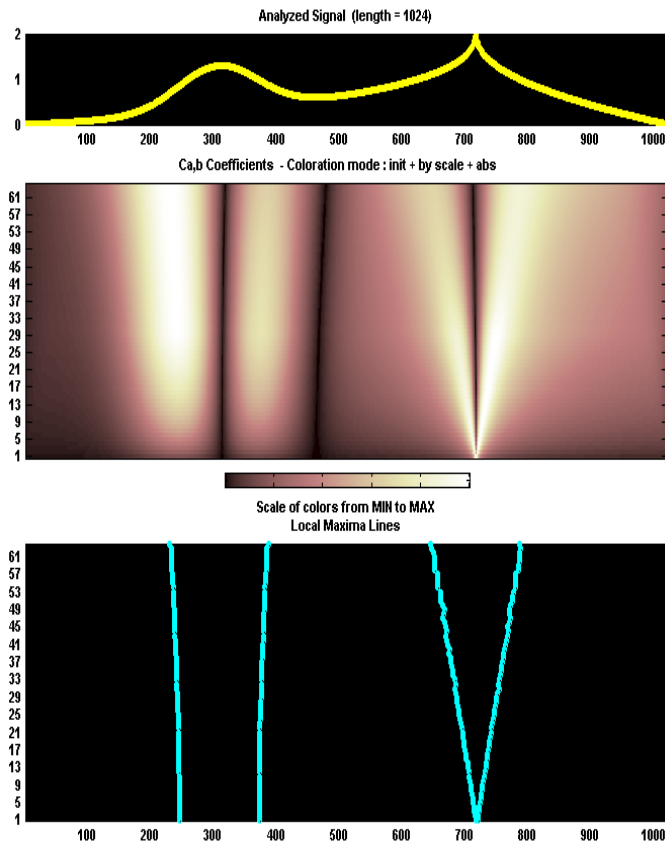


Figure 3.10: Extraction of the Lipschitz exponent equals 0.5 by means of the modulus maxima line using a gaus1 wavelet base

### 3.5.2 Denoising

Detection and classification of signals in the presence of noise and interference is a critical issue in many areas of signal and image processing and analysis. Wavelet transform has been generally applied to signal denoising due to its ability to detect transient features in signals. In essence, the WT performs a correlation analysis, so that we can expect its output to be maximum when the input signal most resembles the analysis template  $\psi(t)$ , and much smaller coefficients when there is mostly noise. This principle is the basis for the matched filter, which is the optimum detector of a deterministic signal in the presence of additive white Gaussian noise. However, the advantage of the WT compared with matched filter is that WT use several scales, and thus, decomposing the signal into several resolutions. Denoising techniques are based on the idea that the amplitude (correlation factor) rather than the location of the spectrum of the signal is different from the noise.

The denoising can be done by simply thresholding the WT coefficients based on the so-called wavelet shrinkage (nonlinear hard or soft thresholding) technique. By selecting an appropriate threshold and applying the inverse Wavelet transformation ( $WT^{-1}$ ), an asymptotically optimal denoising performance can be achieved.

### 3.5.3 Compression

Wavelet compression is a form of data compression well suited for image compression (sometimes also video compression and audio compression). Compression is possible because most real-world data are very statistically redundant and, by this, the information can be encoded (or transformed) using much less data bits than a one-by-one linear representation would use. Compression is usually achieved by setting small wavelet coefficients to zero, and this leaving out important components from the original function. A certain loss of quality is accepted (lossy compression). Using a wavelet transform, the wavelet compression methods are better at representing transients, such as percussion sounds in audio, or high-frequency components in two-dimensional images, for example an image of stars on a night sky. This means that the transient elements of a data signal can be represented by a smaller amount of information than would be the case if some other transform, such as the more widespread discrete cosine transform, had been used.

## 3.6 Low-power analog wavelet filter design

By definition, an electrical filter is a system that can be used to modify, reshape, or manipulate the frequency spectrum of an electrical signal according

to some prescribed requirements [8]. One can represent the filter by an operator  $L$ , resulting in

$$L[f(t)] = h(t) \otimes f(t) = \frac{1}{2\pi} \int_{-\infty}^{\infty} \hat{f}(\omega) \hat{h}(\omega) e^{j\omega t} d\omega \quad (3.20)$$

Thus, the operator  $L$  amplifies or attenuates the frequency components of  $f$  by  $\hat{h}(\omega)$ . Some well-known types of electrical filters can be found in literature where the corresponding frequency property ( $L$ ) is completely defined, e.g., Butterworth, Chebyshev and Elliptic filters. Those filters can be classified as Fourier filters. However, a wavelet filter is not exclusively defined by its frequency behavior and another main design aspect for an wavelet filter is the impulse response definition. In contrast to the Fourier filters, the signal is decomposed into waves of finite length in the wavelet filter. For this reason, wavelets allow different parts of the signal frequency spectrum to be filtered individually, whereas Fourier filtering affects all data points in the same manner.

Basically, the design of a low-power analog wavelet filter can be summarized by the steps shown in the block diagram of Fig.3.11, which will be investigated in the next chapters.

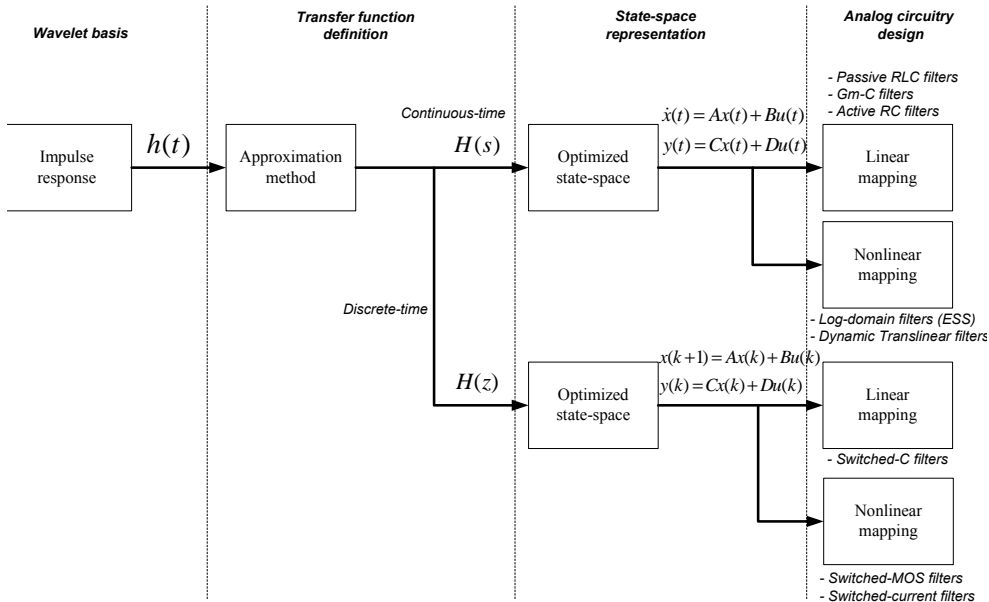


Figure 3.11: Block diagram of an analog filter design

The starting point of an analog filter design is the definition of the respective transfer function (or differential equation). However, a linear differential equation having a predefined desired impulse response does not always exist. Hence, one is obliged to use a suitable approximation method, the topic of Chapter 4. There are several mathematical techniques that are frequently

used to achieve the best approximation possible. Nonetheless, one of the most important aspects of an analog filter synthesis is that the approximating function must lead to a physically realizable network which is dynamically stable.

Next, as there are many possible state-space descriptions for a circuit that implements a certain transfer function, the designer has to find a circuit that fits his specific requirements. For low-power low-voltage applications, we optimize the state-space description of the filter for dynamic range, sensitivity and sparsity requirements (Chapter 5). We will focus on a synthesis technique that is exclusively based on integrators. Note that two general types of analog filters can be identified, namely, continuous-time and discrete-time filters. To implement a discrete-time filter, one must obtain an transfer function in the z-domain whereas a continuous-time filter is described mathematically by a rational function in the Laplace domain.

The last step will be the integrator design, which will be the main building blocks of the wavelet filter (Chapter 6). For continuous-time filters, there are basically two possible integrator implementations, based on either linear or nonlinear (e.g., log-domain) mapping. One important design aspect of the integrator that will be considered here is its ability to handle a large dynamic range in a low-voltage environment. Moreover, since in conventional ultra low-power designs resistors would become too large for on-chip integration, their superfluity is a very important advantage.

## 3.7 Conclusions

In this chapter, a comparison between frequency analysis, by means of the Fourier transform, and time-frequency representation, by means of wavelet transform, was presented. From a nonstationary example signal, the good time and frequency characteristics extraction of the wavelet was pointed out. In addition, the properties of wavelet bases functions and WT signal processing applications were described.

In the next chapter, we will describe a methodology to obtain the approximated transfer function that relates to the impulse response of the correspondent analog wavelet filter.



# Bibliography

- [1] A. D. Poularikas (Editor), *The Transforms and Applications Handbook*, CRC Press; 2 ed., 2000.
- [2] S. Mallat, *A Wavelet Tour of Signal Processing*, Academic Press, 2001.
- [3] I. Daubechies, *Ten Lectures on Wavelets*, Society for Industrial and Applied Mathematics, Philadelphia, 1992.
- [4] O. Rioul and M. Vetterli, *Wavelets and signal processing*, IEEE Signal Processing Magazine, vol. 8, no. 4, pp. 14–38, october 1991.
- [5] W. K. Chen (Editor), *The Circuits and Filters Handbook*, CRC-IEEE Press, 1995.
- [6] M. Unser and A. Aldroubi, *A review of wavelets in biomedical applications*, Proceeding of the IEEE, vol. 84, no. 4, April 1996.
- [7] S. Mallat and W. L. Hwang, *Singularity Detection and Processing with Wavelets*, IEEE Transactions on Information Theory, vol.38, no. 2, pp.617-643, March, 1992.
- [8] A. Aldroubi and M. Unser, *Wavelets in Medicine and Biology*, CRC Press, 1996.
- [9] C. K. Chui, *Wavelets: A Mathematical Tool for Signal Analysis*, SIAM, Philadelphia, 1997.
- [10] E. Hernandez and G. L. Weiss, *A First Course on Wavelets*, CRC Press, 1996.
- [11] J. J. Benedetto, *Wavelets: Mathematics and Applications*, CRC Press, 1993.
- [12] Y. Meyer, *Wavelets: algorithms and applications*, SIAM, Philadelphia, 1993.
- [13] M. Akay (Editor), *Time Frequency and Wavelets in Biomedical Signal Processing*, Wiley-IEEE Press, 1997.

- [14] I. Daubechies, *Different perspectives on wavelets; American Mathematical Society short course*, American Mathematical Society short course, San Antonio, Texas, January, 11-12, 1993.
- [15] Y. Nievergelt, *Wavelets made easy*, Birkhauser, Boston, 1999.
- [16] D. F. Walnut, *An introduction to wavelet analysis*, Birkhauser, Boston, 2002.
- [17] [www.wavelet.org](http://www.wavelet.org),

# Chapter 4

## Analog Wavelet filters: the need for approximation

*“Mathematics compares the most diverse phenomena and discovers the secret analogies that unite them.”* - Joseph Fourier

### 4.1 Introduction

The purpose of this chapter is to construct a set of wavelet filters which will perform (a part of) the wavelet transform on an ECG input signal. Each wavelet filter computes one scale, hence all filters are scaled versions of one basis filter.

As mentioned before, approximation methods should be applied to obtain the required transfer function of a wavelet impulse response. In many respects, a time-domain approximation problem invokes the general theory of mathematical approximation. Several mathematical techniques are frequently used to achieve the best approximation possible [1], which will be presented in the sections that follow.

In addition, any approximation method should be associated with some measure of error. Therefore we employ an error criterion based on the Mean Square Error (MSE) [9] which is defined as

$$\text{MSE} = \frac{1}{b-a} \int_a^b |h(t) - h'(t)|^2 dt \quad (4.1)$$

where  $h(t)$  and  $h'(t)$  are the desired impulse response and the approximated impulse response, respectively.

To obtain an approximated transfer function of a certain wavelet filter, in this chapter three main approaches will be presented. They are the CFOS-based, Padé and  $L_2$  wavelet bases approximations. Besides, to benchmark these approaches, few other time-domain approximation methods will also be described in this chapter.

## 4.2 Complex First Order filters

In this section, an analog wavelet filter design based on Complex First Order Systems (CFOS) [8], [3] will be presented. The CFOS-based approach will be mainly used to approximate Gaussian window functions, such as Gaussian, Gabor and Morlet wavelet bases and it will be shown later that in order to have an increasingly better approximation to the Gaussian function, we need to connect the CFOS stages in cascade. Thus, the starting point of the CFOS-based wavelet filter design is the definition of the number of stages which defines the appropriate Gaussian envelope to set the width of the wavelet. Before this, we will first present the properties of a Complex First Order System.

A complex filter has a transfer function with complex-valued coefficients, which is not limited to complex-conjugate pairs of poles or zeros. A single-pole complex filter with a real-axis coordinate  $\sigma$  and an imaginary-axis coordinate  $\omega$  has the transfer function given by

$$H(s) = \frac{V_{out}(s)}{V_{in}(s)} = \frac{1}{s + (\sigma - j\omega)} = \frac{s + \sigma + j\omega}{(s + \sigma)^2 + \omega^2} \quad (4.2)$$

Applying complex feedback to an integrator stage, it is possible to design an efficient complex pole realization, as one can see in Fig. 4.1

$$H(s) = \frac{\frac{1}{s}}{1 - \frac{1}{s}(-\sigma + j\omega)} \quad (4.3)$$

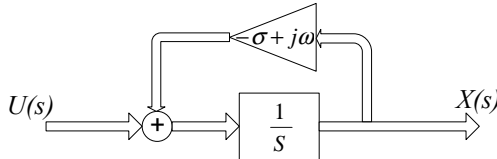


Figure 4.1: Complex feedback diagram

In Fig. 4.2 one sees the effects of this complex feedback on the pole position of the integrator in the S-plane.

A complex lossy integrator can be realized by means of two cross-coupled real integrators. This representation, denominated Complex First Order System (CFOS), is given in Fig. 4.3.

A CFOS is defined by the following set of equations [3]

$$\dot{x}(t) = (\sigma - j\omega)x(t) + (c_{re} + jc_{imag})u(t) \quad (4.4)$$

$$x(t) = x_{re}(t) + jx_{imag}(t) \quad (4.5)$$

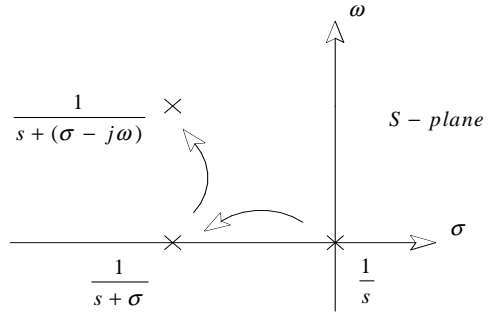


Figure 4.2: Pole positions of the integrator with the complex feedback topology

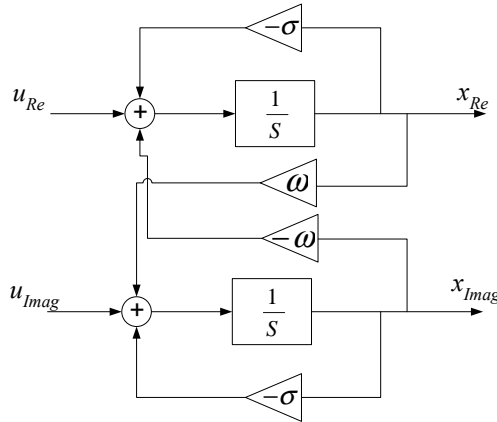


Figure 4.3: Complex First Order System block diagram

where  $u$  is an input signal assumed to be real,  $x$  is a state variable assumed to be complex,  $\sigma$ ,  $\omega$ ,  $c_{re}$  and  $c_{imag}$  are system parameters assumed also to be real. After substitution of Eq.4.5 into Eq.4.4, the real and imaginary part of  $x$ ,  $x_{re}$  and  $x_{imag}$ , can be described by

$$\dot{x}_{re} = \sigma x_{re} - \omega x_{im} + c_{re}u \quad (4.6)$$

$$\dot{x}_{imag} = \sigma x_{imag} + \omega x_{re} + c_{imag}u \quad (4.7)$$

From Eq.4.4, we can represent the envelope of the impulse response of the first order real input circuit by the following equation

$$h(t) = (c_{re} + jc_{imag})e^{\sigma t}U_{-1}(t) \quad (4.8)$$

where  $U_{-1}(t)$  denotes unit step function. Subsequently, we can connect CFOS's in cascade as shown in Fig. 4.4 in order to make a sufficient approximation to a Gaussian function.

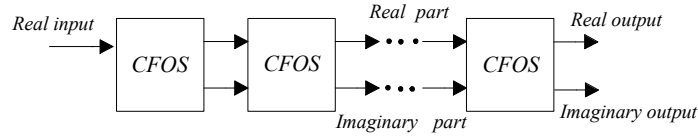


Figure 4.4: Cascade connection of CFOS

The envelope of the impulse response of these  $(n + 1)$  CFOS stages connected in cascade, with all poles at the same location, is given by

$$h(t) = (c_{re} + jc_{imag})^{n+1} \frac{t^n}{n!} e^{\sigma t} U_{-1}(t) \quad (4.9)$$

Eq.4.9 can also be defined as a Poisson function. In the theory of statistics, it is well-known that when  $n \rightarrow \infty$ , the Poisson function approaches a Gaussian function. Therefore, by increasing the number of stages, we can achieve an increasingly better approximation to the Gaussian function.

As one can see in Fig.4.5 (time-domain) and in Fig. 4.6 (frequency-domain), an improvement in the approximation to a Gaussian is obtained for a larger number of stages [4].

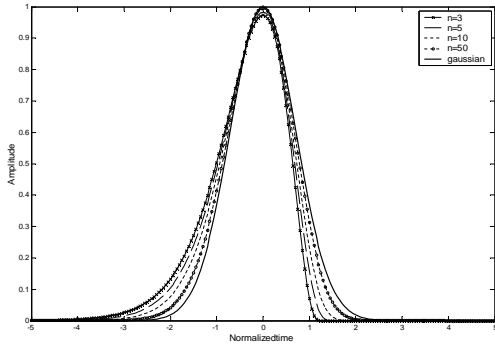


Figure 4.5: Impulse response when increasing the number of stages

This improvement is also verified in Tab.4.1, where the time resolution ( $\Delta t$ ), the frequency resolution ( $\Delta\omega$ ) and their product ( $\Delta t \Delta\omega$ ) have been given for a cascade of  $n$  stages.

Subsequently, once the Gaussian envelope has been defined, the real and the imaginary impulse responses are obtained. Applying Eq. 4.4 and Eq. 4.5, the complex impulse response of  $n + 1$  CFOS stages is given by

$$h(t) = (c_{re} + jc_{imag})^{n+1} \frac{t^n}{n!} e^{(\sigma+j\omega)t} U_{-1}(t) \quad (4.10)$$

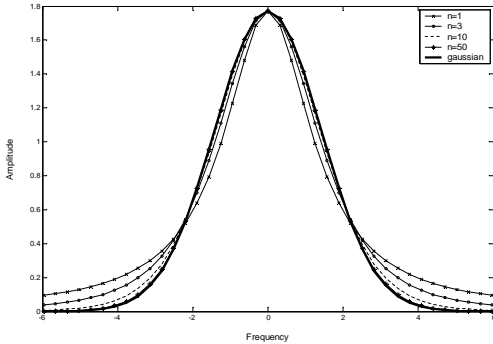


Figure 4.6: Frequency response when increasing the number of stages

| n        | $\Delta t$ | $\Delta\omega$ | $\Delta t \Delta \omega$ |
|----------|------------|----------------|--------------------------|
| 1        | 0.7068     | 1.3732         | 0.9705                   |
| 2        | 0.6124     | 1.1544         | 0.7069                   |
| 3        | 0.5773     | 1.0954         | 0.6323                   |
| 5        | 0.5477     | 1.0541         | 0.5773                   |
| 11       | 0.5222     | 1.0235         | 0.5344                   |
| 50       | 0.5050     | 1.005          | 0.5075                   |
| Gaussian | 0.5        | 1              | 0.5                      |

Table 4.1: Number of stages versus time-bandwidth product

From Eq.4.10 one easily calculates the general transfer function of the  $n + 1$  CFOS system for the real and the imaginary outputs, which are given as follows

$$H_{re}(n) = \frac{(s + \sigma) \cdot H_{re}(n - 1) - \omega \cdot H_{imag}(n - 1)}{(s + \sigma)^2 + \omega^2} \quad (4.11)$$

$$H_{imag}(n) = \frac{(s + \sigma) \cdot H_{imag}(n - 1) + \omega \cdot H_{re}(n - 1)}{(s + \sigma)^2 + \omega^2} \quad (4.12)$$

with

$$H_{re}(1) = \frac{(s + \sigma)}{(s + \sigma)^2 + \omega^2} \quad (4.13)$$

$$H_{imag}(1) = \frac{\omega}{(s + \sigma)^2 + \omega^2} \quad (4.14)$$

which correspond to the transfer function of the first order complex filter in Eq.4.2.

Choosing the right values for  $\sigma$  and  $\omega$ , we can obtain the first and the second derivatives of Gaussian for the imaginary and the real part, respectively, as one can see in Fig.4.7 for different number of stages.

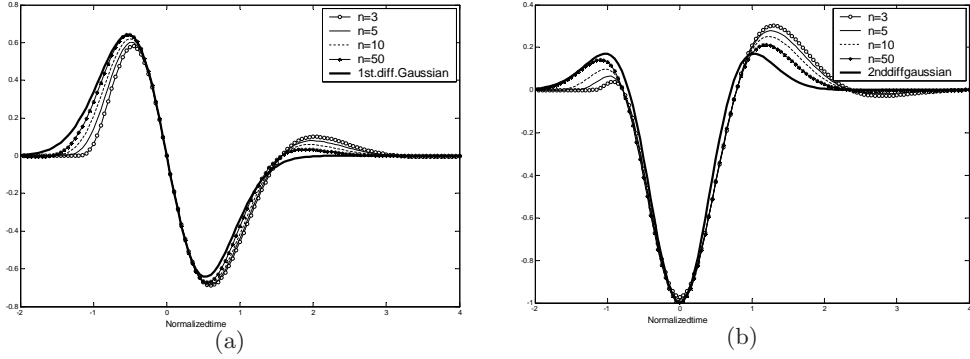


Figure 4.7: Complex Gaussian wavelet approximation using CFOS's (a) Imaginary output (First derivative of Gaussian) (b) Real output (Second derivative of Gaussian)

Finally, the Complex Morlet Wavelet can also be approximated in a similar manner. Again, we need to choose the right value for  $\omega$  in order to have the appropriate frequency component for the Morlet wavelet. In Fig.4.8 one see the impulse response of a tenth order filter.

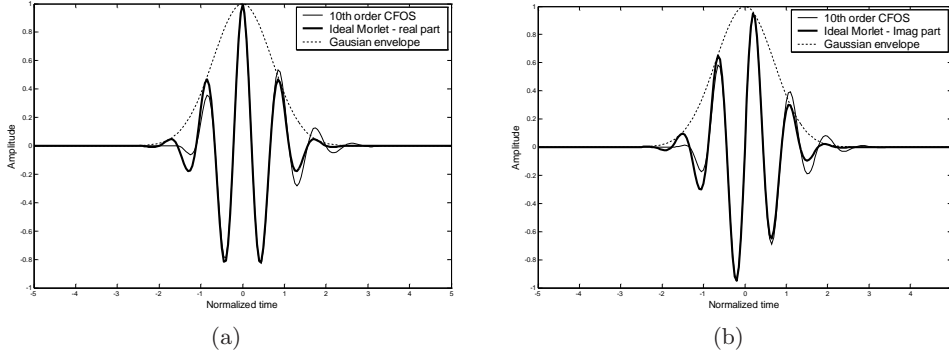


Figure 4.8: Complex Morlet wavelet approximation using CFOS's (a) Real output (b) Imaginary output

### 4.3 Padé Approximation in the Laplace domain

A method which proves to be more successful than the method presented in the previous section is provided by Padé approximation of the Laplace transform of the impulse response  $h(t)$  of the filter. Padé approximation is an approximation that concentrates around one point of the function that needs to be approximated. In the Padé approximation, the coefficients of the

approximating rational expression are computed from the Taylor coefficients of the original function [5], [6]. If the approximation rational function has a numerator of order  $m$  and a denominator of order  $n$ , the original function can be approximated up to order  $m + n$ .

The reason to apply the Padé approximation to the Laplace transform of  $h(t)$  is that it immediately yields a rational expression that is suitable for implementation. Actually, a Padé approximation of  $H(s)$  represents the transfer function of a possible filter. If we would apply the Padé approximation to  $h(t)$  in the time domain, we would have to transform this function to the Laplace domain, which would possibly yield difficult non-polynomial expressions or even a non-causal or unstable filter. Now we derive the Padé approximation of a general function  $F(s)$ . Suppose we have the truncated the Taylor series expansion of  $F(s)$  around some point, e.g.  $s = 0$

$$F(s) = c_0 + c_1 s + \dots + c_k s^k + O(s^{k+1}) \quad (4.15)$$

The constant  $c_0$  to  $c_k$  are called the Taylor coefficients of  $F(s)$ . Unfortunately,  $F(s)$  is not a suitable expression to build a filter, since it has only zeros. Henceforth, to resolve this, a Padé approximation of function  $F(s)$  is applied and is given by [11]

$$\hat{F}(s) = \frac{P(s)}{Q(s)} = \frac{p_0 + p_1 s + \dots + p_m s^m}{q_0 + q_1 s + \dots + q_n s^n} \quad (4.16)$$

where  $\hat{F}(s)$  is the truncated Taylor series given by (4.15), with  $k = m + n$ . The coefficients of  $P(s)$  can be computed as follows. When a product of two polynomials is taken, the coefficients of the product polynomial can be computed by taking the convolution of the coefficients of both factors. Thus, the coefficients of  $P(s)$  can be computed from the convolution of the Taylor coefficients of  $\hat{F}(s)$  with the finite number of coefficients of  $Q(s)$ . We can write this convolution in a matrix-vector form [5], [16]

$$[\hat{F}] \cdot [Q] = [P] \rightarrow \begin{bmatrix} c_0 & 0 & \dots & 0 \\ c_1 & c_0 & & \vdots \\ \vdots & c_1 & \ddots & 0 \\ \vdots & \vdots & \ddots & c_0 \\ \vdots & \vdots & & c_1 \\ \vdots & \vdots & & \vdots \\ c_k & c_{k-1} & \dots & c_{k-n} \end{bmatrix} \cdot \begin{bmatrix} q_0 \\ q_1 \\ \vdots \\ q_n \end{bmatrix} = \begin{bmatrix} p_0 \\ p_1 \\ \vdots \\ \vdots \\ \vdots \\ p_k \end{bmatrix} \quad (4.17)$$

As the entries of  $[\hat{F}]$  are given by the Taylor coefficients of  $F(s)$ , the entries of  $[P]$  depend only on the choice of  $[Q]$ . In other words, the choice of  $[Q]$  is determined by the restrictions on  $[P]$ . Note that the desirable value of  $[P]$  is

defined by two constraints:  $k$  should be as large as possible, since this gives the most accurate approximation;  $P(s)$  should have the desired order  $m$  ( $m \leq n$ ) for a causal filter.

From these constraints it can be concluded that the coefficients  $p_{m+1}$  to  $p_k$  should be zero. Let  $[\hat{F}]_{m+1,k}$  denote the submatrix of  $[\hat{F}]$ , containing rows  $m+1$  to  $k$  of  $[\hat{F}]$ . Then  $[Q]$  can be expressed as

$$\begin{bmatrix} p_{m+1} \\ \vdots \\ p_k \end{bmatrix} = [\hat{F}]_{m+1,k} \cdot [Q] = 0 \quad (4.18)$$

which yields

$$\underline{q} \in \text{Nullspace} \begin{bmatrix} c_{m+1} & \dots & c_0 & 0 \\ c_{m+2} & & c_1 & c_0 \\ \vdots & & & \vdots \\ c_{m+n} & \dots & & c_m \end{bmatrix} \quad (4.19)$$

with  $q_n = 1$  for normalization. Finally, the coefficients of  $[P]$  are defined by

$$\begin{bmatrix} p_0 \\ p_1 \\ \vdots \\ p_m \end{bmatrix} = \begin{bmatrix} c_0 & 0 & \dots & 0 \\ c_1 & c_0 & & \vdots \\ \vdots & c_1 & \ddots & 0 \\ \vdots & \vdots & \ddots & c_0 \\ \vdots & \vdots & & c_1 \\ c_m & c_{m-1} & \dots & c_{m-n} \end{bmatrix} \cdot \begin{bmatrix} q_0 \\ q_1 \\ \vdots \\ q_n \end{bmatrix} \quad (4.20)$$

with  $c_k = 0$  for  $k < 0$ . If the approximating rational function has a numerator of order  $m$  and a denominator of order  $n$ , the original function can be approximated up to order  $m+n$ . For instance, one can apply the Padé function to approximate the first or the second derivative of Gaussian as seen in Fig.4.9. We apply a [6/10] Padé approximation, i.e.  $m = 6$  and  $n = 10$ , which yields an approximation of order  $k = 16$  of the Taylor series expansion, resulting in an  $MSE$  of  $0.19 \cdot 10^{-4}$  and  $0.548 \cdot 10^{-3}$  for the first and the second derivative, respectively. In Table 4.2 one can see the Taylor and Padé coefficients of both functions.

In order to compare the Padé approximation with the approximation using CFOS one can verify the associated Mean-Square Error for both approximation. The results obtained varying the order of the filter are illustrated in Table 4.3, where the first and the second derivatives of a Gaussian function (Gaussian wavelet bases) have been approximated, respectively.

As seen from the Mean-Square Error comparison for  $n > 5$ , the Padé method yields a much better approximation than the method using CFOS for a filter of the same order.

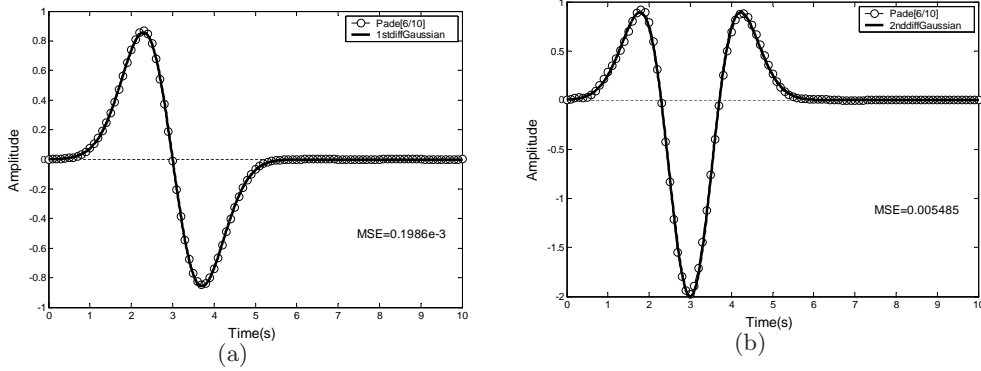


Figure 4.9: Impulse response approximation using Padé [6/10] (a) First derivative of Gaussian (b) Second derivative of Gaussian

Table 4.2: Taylor and Padé coefficients of the first and the second derivative of Gaussian

| Expression (time)                             | 1st diff. Gaussian  |   | 2nd diff. Gaussian   |   |
|---|---|---|--|---|
|   | $\psi(t) = -2(t-3)e^{-(t-3)^2}$   | $\psi(t) = (-2 + 4(t-3)^2)e^{-(t-3)^2}$   | $\hat{F}(s) = 0 + 1.77s^2 - 5.31s^3 + 8.41s^4 - 9.3s^5 + 8.03s^6 - 5.74s^7 + 3.54s^8 - 1.92s^9 + 0.94s^{10} - 0.42s^{11} + 0.17s^{12} - 0.066s^{13} + 0.023s^{14} - 0.008s^{15} - 0.007s^{16}$ | $\hat{F}(s) = 0s + 1.77s^2 - 5.31s^3 + 8.41s^4 - 9.3s^5 - 9.3s^6 + 8.03s^7 - 5.74s^8 + 3.54s^9 - 1.92s^{10} + 0.94s^{11} - 0.42s^{12} + 0.17s^{13} - 0.066s^{14} + 0.023s^{15} - 0.008s^{16} + 0.002s^{17}$ |
| Taylor expansion (Laplace domain)<br>$k = 16$ |   |   |  |   |
| [Q] coefficients<br>$n = 10$                  | $q_0 = 38.6 \cdot 10^3$<br>$q_1 = 103.6 \cdot 10^3$<br>$q_2 = 130.5 \cdot 10^3$<br>$q_3 = 102.2 \cdot 10^3$<br>$q_4 = 55.3 \cdot 10^3$<br>$q_5 = 21.7 \cdot 10^3$ | $q_6 = 6.3 \cdot 10^3$<br>$q_7 = 1.35 \cdot 10^3$<br>$q_8 = 205.6$<br>$q_9 = 20.27$<br>$q_{10} = 1$ | $q_0 = 37.8 \cdot 10^3$<br>$q_1 = 100.7 \cdot 10^3$<br>$q_2 = 126.4 \cdot 10^3$<br>$q_3 = 98.6 \cdot 10^3$<br>$q_4 = 53.3 \cdot 10^3$<br>$q_5 = 20.9 \cdot 10^3$                               | $q_6 = 6.1 \cdot 10^3$<br>$q_7 = 1.30 \cdot 10^3$<br>$q_8 = 199.7$<br>$q_9 = 19.91$<br>$q_{10} = 1$   |
| [P] coefficients<br>$n = 6$                   | $p_0 = -4.77$<br>$p_1 = 68.5 \cdot 10^3$<br>$p_2 = -22 \cdot 10^3$<br>$p_3 = 6.1 \cdot 10^3$  | $p_4 = -576.95$<br>$p_5 = 44.67$<br>$p_6 = 5.81$  | $p_0 = -4.67$<br>$p_1 = -13.21$<br>$p_2 = 11.1 \cdot 10^3$<br>$p_3 = -3.7 \cdot 10^3$  | $p_4 = 1.08 \cdot 10^3$<br>$p_5 = -131.28$<br>$p_6 = 13.54$   |

| order | CFOS        |              | Padé        |              |
|-------|-------------|--------------|-------------|--------------|
|       | First diff. | Second diff. | First diff. | Second diff. |
| n     |             |              |             |              |
| 3     | 0.0444      | 0.0513       | 0.0899      | 0.0927       |
| 4     | 0.0382      | 0.0380       | 0.0817      | 0.0468       |
| 5     | 0.0339      | 0.0302       | 0.0454      | 0.0185       |
| 6     | 0.0308      | 0.0251       | 0.0178      | 6.05e-3      |
| 7     | 0.0284      | 0.0216       | 7.75e-3     | 1.01e-3      |
| 8     | 0.0265      | 0.0190       | 2.30e-3     | 0.040e-3     |
| 9     | 0.0250      | 0.0170       | 0.74e-3     | 0.033e-3     |
| 10    | 0.0238      | 0.0154       | 0.13e-3     | 0.020e-3     |

Table 4.3: Order of the filter versus mean-square error for CFOS and Padé approximation

One of the main advantages of Padé approximation is that the linear system of equations yield a unique solution, which is generically easy to compute. Moreover, a good match is guaranteed between the given function  $\Psi(s)$  and its

approximation  $H(s)$  in a neighborhood of the selected point  $s_0$ . However, the selection of the expansion point  $s_0$  is a trade-off between stability and a good fit around zero in the time domain. Indeed, in order to obtain a good fit near  $t = 0$  by choosing  $s_0 = \infty$ , it may easily happen that the resulting approximation becomes unstable [10]. In this respect, the Padé approximation described in this section was obtained with the choice  $s_0 = 0$ , which corresponds to a good fit in the time domain for large values of  $t$  [6].

Furthermore, the selection of the orders  $m$  and  $n$  is not a straightforward task. An unlucky choice may yield an inconsistent system or an unstable approximation. Nevertheless, this is not an important issue, because one can easily solve this problem [10] by changing the value of  $m$ , for a certain  $n$ th order approximation.

In addition, the Padé approximation presents some problems of convergence when we try to approximate a function which has many oscillations, for instance, the Morlet wavelet. Due this reason we introduced the procedure described in the next section in order to obtain a stable transfer function for this kind of wavelet bases. By this, we obtain a more general procedure, which is suitable for implementation as an analog filter, to obtain various types of wavelet bases.

### Oscillated wavelet bases approximation

The proposed procedure that generates a transfer function of a wavelet base can be seen in the flow chart in Fig.4.10 [16]. The procedure is based on the Padé approximation described in the previous section. The starting point is the definition of an expression in the time domain which represents the wavelet under investigation. If the wavelet base does not have an explicit expression (e.g., Daubechies wavelets), then the splines interpolation method [9] is used. Subsequently, one determines the appropriate envelope to set the width of the wavelet. Once again, if the envelope does not have an explicit expression, the splines interpolation is applied. The Gaussian pulse has been chosen as the envelope, which is perfectly local in both the time and frequency domain. Once the envelope has been defined, the Padé approximation is executed to find a stable and rational transfer function which is suitable for implementation as an analog filter. As the main advantage of the Padé method is its computational simplicity and its general applicability [5], it can easily be applied to other envelopes as well. The Padé approximation is preceded by a two-step procedure. First, a Laplace transform is executed, and then a Taylor expansion is performed on the expression of the envelope in the Laplace domain. Finally, the wavelet is decomposed into a Fourier series to find the dominant term (the term with the largest coefficient) such that when multiplied with the envelope in the time domain, it results in the approximated wavelet base. The results obtained from the use of this method are illustrated in Fig. 4.11, where the Morlet and the Daubechies (db6) wavelet bases have been approxi-

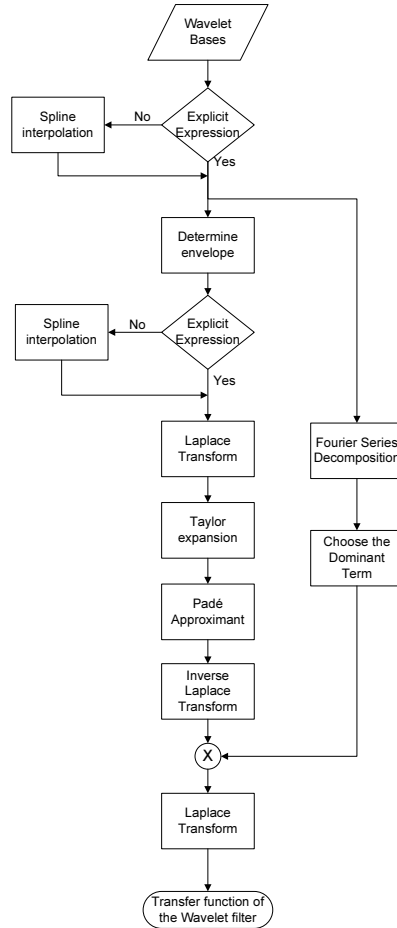


Figure 4.10: Flowchart of the wavelet filters approach

mated, respectively. Other wavelet bases can also be approximated in a similar manner.

As an example we consider a Morlet wavelet filter. The related expression of the Morlet wavelet base approach, the Padé expression of the envelope function and, the transfer function of the Morlet wavelet filter are given in Table 4.4.  $\mathcal{L}$  and  $\mathcal{L}^{-1}$  represent the Laplace transform and the inverse Laplace transform, respectively.

## 4.4 $L_2$ Approximation

Another alternative to find a suitable wavelet base approximation can be provided by the theory of  $L_2$  approximation. Approximation techniques are usually based on certain assumed criteria of measuring the error and then the error is minimized. One of the most frequently used criteria is the least-mean-

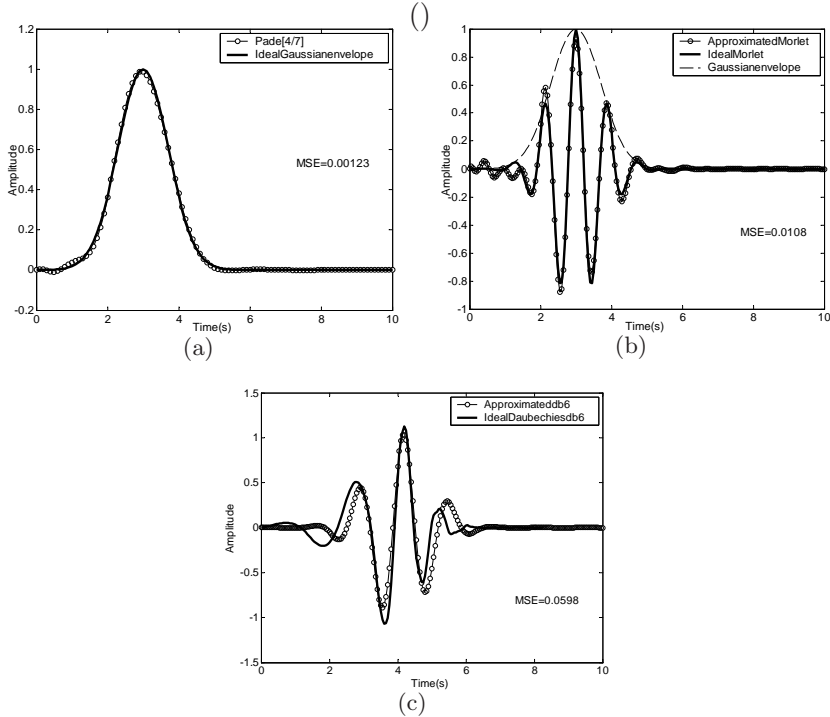


Figure 4.11: Ideal impulse (solid line) and the approximated (dashed line) response of example Wavelets filters, (a) Gaussian envelope, (b) Morlet and (c) db6 wavelet base. The mean-square errors between the ideal and the approximated impulse responses are equal 0.00123, 0.0108 and 0.0598 for the Gaussian, the Morlet and the Daubechies wavelets, respectively

square-error approximation [14]. The  $L_2$  approximation technique is based on minimizing the least-mean-square-error.

The advantage of the  $L_2$  method compared to the Padé approximation is that the  $L_2$  approximation offers a more global approximation, i.e., not concentrating on one particular point [10]; Padé is usually computed at the origin. Also, the fit is performed directly in the time domain yielding good control and easy interpretation of the optimization criteria. In addition, according to Parseval's identity [9]

$$\int_0^\infty [\psi(t) - h(t)]^2 dt = \frac{1}{2\pi} \int_{-\infty}^\infty |\Psi(j\omega) - H(j\omega)|^2 d\omega, \quad (4.21)$$

the  $L_2$  criterion can be equivalently be used in the frequency domain too. In this scheme the error integral, which is the difference between  $\psi(t)$  and its approximation  $h(t)$ , is defined by

$$\varepsilon_{L_2} = \int_0^\infty [\psi(t) - h(t)]^2 dt \quad (4.22)$$

Table 4.4: Morlet wavelet base approach parameters

|                                | Morlet wavelet base  |
|--------------------------------|--|
| Expression (time)              | $\psi(t) = \cos(5\sqrt{2}t)e^{-(t-3)^2}$   |
| Envelope                       | $\text{Gaussian} \Rightarrow e^{-(t-3)^2}$   |
| Fourier Series (Dominant term) | $\cos(5\sqrt{2}t)$   |
| Padé [3/5](Gaussian)           | $H_{gaussian}(s) = \frac{-1.31s^3 + 8.82s^2 - 25.11s + 31.74}{s^5 + 6.66s^4 + 21.14s^3 + 38.59s^2 + 39.56s + 17.91}$   |
| Morlet transfer function       | $H(s) = \mathcal{L}^{-1}\{H_{gaussian}(s)\} \times \cos(5\sqrt{2}t)$   |
|                                | $H(s) = \frac{0.9s^8 - 13s^7 + 177s^6 - 618s^5 + 345s^4 + 7 \cdot 10^4 s^3 - 4 \cdot 10^5 s^2 + 2 \cdot 10^6 s - 3 \cdot 10^6}{s^{10} + 13s^9 + 336s^8 + 3 \cdot 10^3 s^7 + 4 \cdot 10^4 s^6 + 2 \cdot 10^5 s^5 + 2 \cdot 10^6 s^4 + 8 \cdot 10^6 s^3 + 4 \cdot 10^7 s^2 + 9 \cdot 10^7 s + 3 \cdot 10^8}$ |

This means that the  $L_2$  criterion value corresponds to the energy of the difference between the wavelet and its approximation and, by this, we have an interpretation of the optimization in the time domain as well as in the frequency domain.

In this  $L_2$  approach [10], [11], [12], we first express the impulse response (in the time domain) of a general filter. After that, the error  $\varepsilon_{L_2}$  is minimized with respect to the poles and zeros of the filter. For the generic situation of stable systems with distinct poles [1],  $h(t)$  may typically have the following form

$$\begin{aligned} h(t) &= \sum_{i=1}^n A_i e^{P_i t} \\ &= \sum_{i=1}^k c_i e^{p_i t} + c_{k+1} e^{p_{k+1} t} \sin(p_{k+2} t) + c_{k+2} e^{p_{k+1} t} \cos(p_{k+2} t) \\ &\quad + \cdots + c_{n-1} e^{p_{n-1} t} \sin(p_n t) + c_n e^{p_{n-1} t} \cos(p_n t) \end{aligned} \quad (4.23)$$

where  $A_i$  and  $P_i$  can be real or complex numbers;  $c_i$  and  $p_i$  are real numbers, representing the impulse response function  $h(t)$  as a linear combination of damped exponentials and exponentially damped harmonics.  $k$  corresponds to the number of real poles and  $n$  is the order of the filter.

Given the explicit form of a wavelet base  $\psi(t)$  and the approximated impulse response  $h(t)$ , the  $L_2$ -norm of the difference  $\psi(t) - h(t)$  can now be minimized in a straightforward way using standard numerical optimization techniques and software. The most direct way to find the minimum of Eq.4.22 is by computation of all partial derivatives of  $\varepsilon_{L_2}$  with respect to  $A_i$  and  $P_i$  and setting them equal to zero, namely

$$\frac{\partial \varepsilon_{L_2}}{\partial A_i}, \frac{\partial \varepsilon_{L_2}}{\partial P_i} = 0 \quad \text{for } i = 1 \dots n \quad (4.24)$$

Note that, due to the fact that  $A_i$  and  $P_i$  can be complex numbers, we have to perform the differentiation with respect to the real parts and the imaginary parts of  $A_i$  and  $P_i$  separately.

One important aspect of the  $L_2$  approximation is that the zero-mean constraint of the wavelet bases is imposed in the computation of the error in Eq.

4.22. Thus, the resulting transfer function is such that the numerator of the transfer function does not have a constant term. In other words, the transfer function becomes zero for  $s=0$ , which implies that the integral of the wavelet approximation is zero [10].

One example of wavelet base approximation using  $L_2$  approach is given in Fig.4.12, where the Morlet wavelet base has been approximated using a 7th order transfer function.

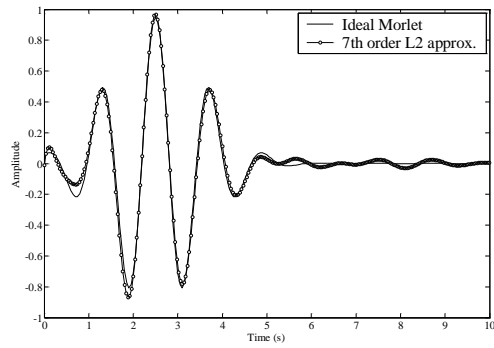


Figure 4.12: Morlet wavelet base approximation using  $L_2$  approach

Again, to compare the  $L_2$  approximation with Padé and CFOS approaches, one can check the associated Mean-Square Error for approximations, shown in Fig.4.13. The MSE has been calculated for two different wavelet bases, being the first derivative of Gaussian and the Morlet, using several filter orders. As seen from the plots, the Padé and the  $L_2$  approximations present a much better approximation than the CFOS, especially for high-order systems, whereas for low-order systems  $L_2$  presents the best performance.

As mentioned before, the  $L_2$  approach has the advantage that it allows for a description in the time domain as well as in the Laplace domain, so that both frameworks can be exploited to develop further insight. Specific points can be defined in the Laplace domain at which the approximation is required to be good, whereas in the Padé approach, the approximation is done at one specific point (usually at the origin).

One of the disadvantages of an  $L_2$ -approximation approach is that there is a risk that the numerical optimization ends in a local, non-global optimum. In general,  $L_2$  provides no global optimality guarantee. Different starting points can give different local optima and thus can be used to find better solutions [11]. Another drawback is that it is computationally more demanding than the Padé approach.

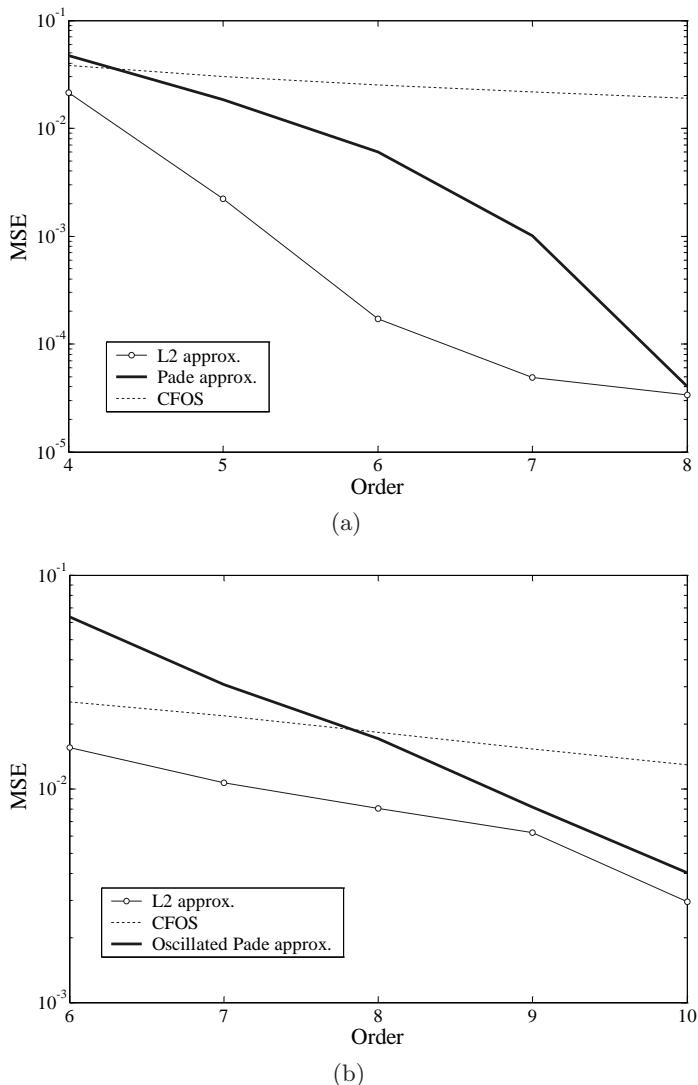


Figure 4.13: Order of the filter versus mean-square error for  $L_2$ , Padé and CFOS approximations (a) First derivative of Gaussian and (b) Morlet wavelet bases

## 4.5 Other approaches for Wavelet bases approximation

### 4.5.1 Bessel-Thomson filters - a quasi-Gaussian impulse response

The pure, theoretical, Gaussian filter is not actually physically realizable. However, there are some well-known monotonic quasi-Gaussian filters, such

as Bessel-Thomson filters, which try to approximate the ideal Gaussian in both the time domain and the frequency domain [1].

The Bessel filter is sometimes called the maximally-flat delay filter. The Bessel transfer function (also known as the Thompson function) has been optimized to obtain a linear phase, which implies a maximally flat (group) delay in the passband.

The transfer function for an ideal time delay is given by

$$T(s) = e^{-s} = \frac{1}{e^s} = \frac{1}{\sinh(s) + \cosh(s)} \quad (4.25)$$

Using the hyperbolic function identity

$$\coth(s) = \frac{\cosh(s)}{\sinh(s)} \quad (4.26)$$

and the truncated fraction expansion of the  $\coth(s)$  function

$$\coth(s) = \frac{1}{s} + \frac{1}{\frac{3}{s} + \frac{1}{\frac{5}{s} + \frac{1}{\frac{7}{s} + \dots}}} \quad (4.27)$$

the result is a quotient of polynomials where the numerator is identified with  $\cosh(s)$  and the denominator with  $\sinh(s)$ . The sum of the numerator and denominator polynomials is thus the approximation to  $e^s$ . Note that adding the numerator and denominator truncated after  $n$  terms we obtain the Bessel polynomials [1]. The general Bessel polynomial becomes

$$B_n = (2n - 1)B_{n-1} + s^2 B_{n-2} \quad (4.28)$$

where  $B_0 = 1$  and  $B_1 = s + 1$ .

Thus, the  $n$ th Bessel filter transfer function is given by

$$H_n(s) = \frac{B_0}{B_n} = \frac{1}{(2n - 1)B_{n-1} + s^2 B_{n-2}} \quad (4.29)$$

One can notice that the above transfer function represents an all-pole filter topology. The Bessel poles lie on a unit circle where the vertical spacing between the poles is equal.

Finally, the impulse response, shown in Fig.4.14, of Bessel-Thomson filters tends towards a Gaussian as the filter order is increased.

#### 4.5.2 Filanovsky's filter approach [15]

Filanovsky's method describes synthesis of pulse-forming networks with quasi-Gaussian impulse responses using passive networks. It is well known that the  $\sin^2(\pi t/\tau)$  function over one semi-period is a sufficiently good approximation to the Gaussian response. In this approach, the transfer function is obtained using the first semi-period of the  $\frac{2}{\tau} \sin^2 \frac{\pi}{\tau}(t - \frac{\pi}{2} + \frac{\tau}{2})$  function, with  $\tau \leq \pi$ , as

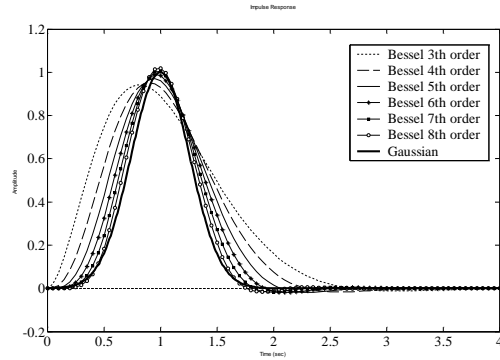


Figure 4.14: Approximated Gaussian function using Bessel filter

an initial approximation to the network impulse response. The corresponding Laplace-domain function is given by

$$F(s) = \frac{8(\pi/\tau)^2 \sinh(\tau s/2)}{\tau s[s^2 + (2\pi/\tau)^2]} e^{-\frac{\pi}{2}s} \approx e^{-\frac{\pi}{2}s} \quad (4.30)$$

where the function  $\sinh$  has been represented by the first two terms of the infinite product,  $\sinh(x) = \prod_{i=1}^{\infty} (1 + \frac{x^2}{i^2 \pi^2})$ . One can note that the above function is a non-realizable transfer function. In [15] a realizable transfer function  $\tilde{F}(s)$  was presented that approximates the previous function  $F(s)$

$$\tilde{F}(s) = \frac{A_1}{\prod_{i=0}^{n_1} [s^2 + (2i+1)^2] + A_2 s \prod_{i=1}^n [s^2 + 4i^2]} \quad (4.31)$$

where  $A_1$  and  $A_2$  are constants and should be positive and real. To find both constants  $A_1$  and  $A_2$ , one equates  $F(s)$  and  $\tilde{F}(s)$  at  $s = 0$  and  $s = j$ , respectively, which yields

$$\begin{aligned} A_1 &= \prod_{i=1}^{n_1} (2i+1)^2 \\ A_2 &= \frac{\tau[(2\pi/\tau) - 1]A_1}{8(\pi/\tau)^2 \sin(\tau/2) \prod_{i=1}^n [(2i)^2 - 1]} \end{aligned} \quad (4.32)$$

As an example, one can see the approximation of a Gaussian using the described method. The approximated impulse responses are shown in Fig.4.15a.

In addition, the first derivative of Gaussian can be described by delayed positive and delayed negative semi-periods of sine-squared functions. Applying the same procedure, one can also obtain a transfer function which describes the first derivative of a Gaussian and the impulse responses are shown in Fig.4.15b.

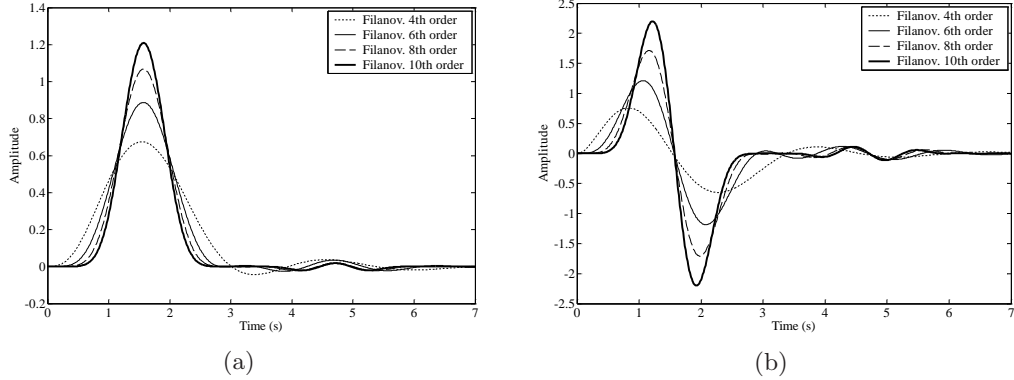


Figure 4.15: Approximated (a) Gaussian function and (b) first Gaussian wavelet base using Filanovsky's method

#### 4.5.3 Fourier-series method

The Fourier-series method is an orthogonal-function approximation in the time domain. The big advantage of this method is that the series is readily transformable into the frequency domain, as given by

$$f(t) = \sum_{k=-N}^N a_k e^{j k \omega t} \Leftrightarrow F(s) = \sum_{k=-N}^N \frac{a_k}{s - j \omega k} \quad (4.33)$$

where this Fourier series is truncated to include only terms inside the interval  $-N < k < N$ . However, the disadvantage of the Fourier-series method lies in the fact that  $f(t)$  is a periodic function. Thus, the Fourier series cannot always be used to approximate an impulse response  $h_T(t)$  limited in time (i.e.,  $h(t) = 0$  for  $t < 0$  and  $t > T$ ) directly. To overcome this limitation, the following scheme may be employed.

First, to eliminate the part of  $f(t)$  for  $t > T$ , we may use the double-step weighting function [1],  $w(t)$ , given by

$$w(t) = u_o(t) - u_o(t - T) \quad (4.34)$$

to be convolved with the function  $f(t)$ , resulting in

$$h_T(t) = w(t) \otimes f(t) \Leftrightarrow H_T(s) = (1 - e^{-sT}) \cdot F(s) \quad (4.35)$$

Thus, the effect of convolving a function with  $w(t)$  is to add to the function its own negative delayed by  $T$ . However this function is not rational and cannot be realized. To make use of this Fourier-series technique and its associated properties, some additional mathematical artifices are necessary.

Assuming that  $h_T(t)$  may be considered zero for  $t > T$ , we may create two periodic functions,  $h_{p1}(t)$  and  $h_{p2}(t)$ , such that

$$h_{p1}(t) = h_{p2}(t) = \frac{1}{2}h_T(t), \quad 0 < t < T \quad (4.36)$$

and  $h_{p1}(t)$  repeats every  $T$  with alternate sign while  $h_{p2}(t)$  repeats every  $T$  with the same sign. Due to the symmetry of these functions,  $h_{p1}(t)$  will have only odd harmonics and  $h_{p2}(t)$  will have only even harmonics. Another series  $h_{sum}$  and  $h_{sub}$ , which are related to  $h_{p1}(t)$  and  $h_{p2}(t)$  can also be defined by

$$\begin{aligned} h_{sum}(t) &= h_{p1}(t) + h_{p2}(t) \\ h_{sub}(t) &= h_{p2}(t) - h_{p1}(t) \end{aligned} \quad (4.37)$$

where  $h_{sum}$  and  $h_{sub}$  are the summation and subtraction series, respectively, of period  $2T$ . Note that the subtraction series  $h_{sub}$  represents  $h_{sum}(t)$  delayed by  $T$  seconds. Then, in the Laplace domain

$$H_{sub}(s) = H_{sum}(s)e^{-sT} \quad (4.38)$$

Substituting Eq.4.37 into Eq.4.38 and squaring both side gives

$$e^{-2sT} = \left[ \frac{H_{p2}(s) - H_{p1}(s)}{H_{p2}(s) + H_{p1}(s)} \right]^2 \quad (4.39)$$

From Eq.4.35 one can derive the approximated transfer function  $H_T(s)$ , yielding

$$H_T(s) = (1 - e^{-2sT})H_{sum}(s) = \frac{4H_{p2}(s)H_{p1}(s)}{H_{p2}(s) + H_{p1}(s)} \quad (4.40)$$

Thus a rational function has been generated that approximates the particular  $h_T(t)$ .

As an example one can find the approximated transfer function of a Gaussian function,  $e^{-0.5(t-2)^2}$ , shown in Fig.4.16a. As mentioned before, a Gaussian function can be approximated by  $\sin^2(\pi t/\tau)$ . Then, following the methodology presented before, the periodic Fourier series  $h_{p2}(t)$  and  $h_{p1}(t)$  will become

$$\begin{aligned} h_{p2}(t) &= 0.5\sin^2\left(\frac{\pi t}{4}\right) = 0.25 - 0.25\cos\left(\frac{2\pi t}{4}\right) \\ h_{p1}(t) &= 0.5\sin\left(\frac{\pi t}{4}\right) \end{aligned} \quad (4.41)$$

as shown in Fig.4.16b and Fig.4.16c, respectively.

And the corresponding transfer functions are given by

$$\begin{aligned} H_{p2}(s) &= \frac{0.25}{s} - \frac{0.25s}{s^2 + 2.467} \\ H_{p2}(s) &= \frac{0.3926}{s^2 + 0.6168} \end{aligned} \quad (4.42)$$

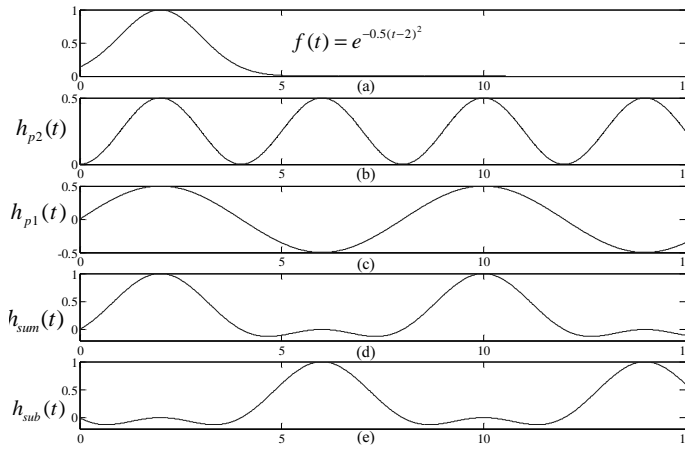


Figure 4.16: Periodic Fourier-series for the approximation method (a) Ideal Gaussian (b)  $h_{p2}(t)$  (c)  $h_{p1}(t)$  (d)  $h_{sum}(t)$  (e)  $h_{sub}(t)$

Finally, applying Eq.4.40 in order to obtain the rational transfer function for the approximated Gaussian gives

$$H_T(s) = \frac{2.467}{s^3 + 1.57s^2 + 2.467s + 0.968} \quad (4.43)$$

The approximated function in time is plotted in Fig.4.17 together with the ideal Gaussian function.

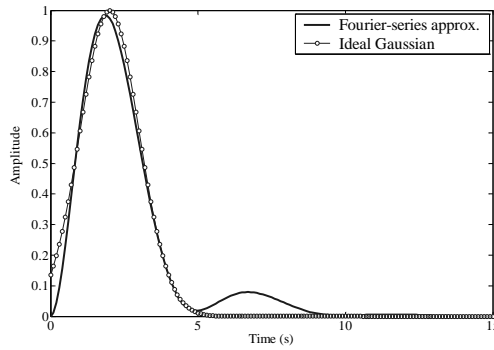


Figure 4.17: Approximated Gaussian function using Fourier-series method

From this example it is shown that the Fourier-series method is very easy to implement, especially when the Fourier series of a given function is already available. Also, the approximated function has a good matching with the desired impulse response with a very low-order system, in this case third order system for a Gaussian function approximation.

However, the drawback of this method is that the resulting transfer function is not always stable, i.e., it can have poles in the right half plane. Although the poles of both  $H_{p1}(s)$  and  $H_{p2}(s)$  are all on the  $j$ -axis, the poles of  $H_T(s)$  (from Eq.4.40) are the zeros of  $H_{p1}(s) + H_{p2}(s)$ , which could be anywhere on the  $s$  plane.

## 4.6 Discussion

In this chapter we have presented several methods to obtain good approximations in the time domain of the wavelet bases functions. One important objective of the introduced approaches is that the resulting approximated function should be rational and stable in the Laplace domain. This means that the approximating function must lead to a physically realizable network.

Nevertheless, one can notice that due to limitations in chip area, power consumption and coefficient matching, there is a trade-off between the approximation accuracy versus the order of the implemented filter. Thus, the design challenge is to obtain a low-order system while preserving a good approximation to the intended function.

We first proposed a wavelet function approximation based on Complex First Order Systems (CFOS). The Gaussian approximation using CFOS is improved by the Poisson distribution,  $\frac{t^n}{n!}$ , where  $n$  represents the number of CFOS stages. Therefore, we can achieve an increasingly better approximation to the Gaussian function by increasing  $n$ . As a consequence, from the CFOS-based approach one can obtain wavelet bases related to the Gaussian function, such as Gaussian, Gabor and Morlet wavelet bases.

To obtain a more general procedure, the Padé approximation was introduced, which can theoretically implement any function that is represented by a Taylor series. The Padé approximation is used to approximate the Laplace transform of the desired wavelet transfer function by a suitable rational function around a selected point  $s_o$  (in the example we used  $s_o = 0$ ).

Another approach that can approximate all kinds of wavelet functions was given by the  $L_2$  method. The advantage of this method compared to the Padé is that the  $L_2$  offers a more global approximation, i.e., not concentrating on one particular point. Also the  $L_2$  method can be applied in the time domain as well as in the Laplace domain. However, the computation complexity of this method is much higher than the CFOS-based and the Padé approximation, and, depending on the starting point, there is a risk for non-global optimum numerical approximation for certain  $n$ th order system.

From a Mean-Square Error (*MSE*) comparison, we have analyzed the performance of the given approximation methods. For low-order systems,  $L_2$  approximation yields better wavelet matching than the CFOS-based and Padé approaches. However, increasing the order of the filter the approximation accuracy becomes very similar for both  $L_2$  and Padé.

In addition, three other approaches for time-domain approximation were presented. First, a Bessel-Thomson filter was presented. The transfer function of this filter, an all-pole transfer function, is based on the Bessel polynomial. The approximation of a Gaussian function using the Bessel-Thomson filter results in a high-order system, mainly because the transfer function is found indirectly from the requirements in the frequency domain. Another limitation of this method is that it is restricted to just Gaussian function approximation.

The approach defined here as the Filanovsky's method obtains the approximated transfer function using the first semi-period of the sine squared function as an initial approximation to the network impulse response. From the obtained Gaussian and first derivative of Gaussian approximations, one can conclude that the approximation accuracy of this method is not so good compared to the Padé and the  $L_2$  approaches.

Finally, a very simply method based on Fourier-series has been presented. The Fourier-series method leads to the same order of accuracy as the Fourier-series approximation of  $h(t)$  in the time interval  $0 < t < T$ .

Hence Bessel, Filanovsky and Fourier-series approximations are most suitable for those impulse responses that do not have any discontinuity or in situations where a large number of poles is acceptable.

## 4.7 Conclusions

Due to their general applicability, and the excellent accuracy results, in this thesis, the Padé and the  $L_2$  approximations have been chosen, which generate reasonable low-order and good fit transfer functions.

Thus, the Padé and the  $L_2$  transfer functions describing the wavelet filter will be implemented in a suitable filter topology in the next chapter. We will map these transfer functions onto certain state space descriptions that are suitable for low-power implementation.

# Bibliography

- [1] K. L. Su, *Time Domain Synthesis of Linear Networks*, Prentice-Hall, Englewood Cliffs, NJ, 1971.
- [2] H. Kamada and N. Aoshima, *Analog Gabor Transform Filter with Complex First Order System*, in Proc. SICE, pp.925-930, 1997.
- [3] N. Aoshima, *Analog realization of Complex First Order System and its application to vowel recognition*, in Proc. SICE, pp.1239-1244, 1995.
- [4] S. A. P. Haddad, R. P. M. Houben and W. A. Serdijn, *Analog Wavelet Transform Employing Dynamic Translinear Circuits for Cardiac Signal Characterization*, in proc. ISCAS, Bangkok, Thailand, May 25-28, 2003.
- [5] G. A. Baker Jr., *Essentials of Padé Approximants*, Academic Press, New York, 1975.
- [6] A. Bultheel and M. Van Barel, *Padé techniques for model reduction in linear system theory: a survey*, Journal of Computation and Applied Mathematics, vol.14, pp.401-438, 1986.
- [7] S. A. P. Haddad, S. Bagga and W. A. Serdijn, *Log-domain wavelet bases*, IEEE Transactions on Circuits and Systems - I: Regular Papers, vol. 52, no. 10, pp. 2023-2032, Oct. 2005.
- [8] S. A. P. Haddad, N. Verwaal, R. Houben and W. A. Serdijn, *Optimized dynamic translinear implementation of the gaussian wavelet transform*, in Proc. IEEE Int. Symp. Circuits and Systems, vol.1, pp.145-148, Vancouver, Canada, May 23-26, 2004.
- [9] D. Zwillinger, *Standard Mathematical Tables and Formulae*, CRC Press, 30 edition, 1996.
- [10] J. M. H. Karel, R. L. M. Peeters, R. L. Westra, S. A. P. Haddad, W. A. Serdijn, *Wavelet approximation for implementation in dynamic translinear circuits*, proc. IFAC World Congress 2005, Prague, July 4-8, 2005.

- 
- [11] J. M. H. Karel, R. L. M. Peeters, R. L. Westra, S. A. P. Haddad, W. A. Serdijn, *An L2-based approach for wavelet approximation*, proc. CDC-ECC 2005, Seville, Spain, December 12-15, 2005.
  - [12] J. M. H. Karel, R. L. M. Peeters, R. L. Westra, S. A. P. Haddad, W. A. Serdijn, *Optimal discrete wavelet design for cardiac signal processing*, proc. EMBC 2005, Shanghai, China, September 1-4, 2005.
  - [13] T. Kailath, *Linear Systems*, Prentice Hall Inc., 1980.
  - [14] J. Leblond and M. Olivi, *Weighted H2-approximation of tranfer functions*, Mathematics of COntrol, Signals and Systems, vol.11, pp. 28-39, 1998.
  - [15] I. M. Filanovsky and P. N. Matkhanov, *Synthesis of Time Delay Networks Approximating the Pulse Response Described by an Integer Power of a Sinusoid Over Its Semi-Period*, Analog Integrated Circuits and Signal Processing, Vol.28, no.1, pp.83-90, July 2001.
  - [16] R. Schaumann and M. V. Valkenburg, *Design of Analog Filters*, Oxford University Press, ISBN: 0-19-511877-4.

# Chapter 5

# Optimal State Space Descriptions

*“What we know is not much.*

*What we do not know is immense.” - Pierre-Simon Laplace*

This chapter describes the next step towards the implementation of the wavelet filter. Departing from the transfer functions defined in Chapter 4, we derive a state space description of the filter. Since state space descriptions are not unique representation of a dynamical system, they allow the designer to find an implementation that fits the best to the requirements, e.g. easy coefficients, a prescribed circuit topology, or maximum dynamic range. The description is transformed into the desired form by state space transforms or similarity transforms. In the context of low-power, low-voltage analogue integrated circuits, the most important requirements are the dynamic range, the sensitivity, and the sparsity, all of which will be treated in the sections that follow.

## 5.1 State space description

In the state space method, the  $n$ th-order differential equation (DE) describing a dynamic system is organized as a set of first-order DE's. The common form of a state space description is given by

$$\begin{aligned}\frac{dx(t)}{dt} &= Ax(t) + Bu(t) \\ y(t) &= Cx(t) + Du(t)\end{aligned}\tag{5.1}$$

The input and output signals of the system are  $u(t)$  and  $y(t)$ , respectively. The vector variable  $x(t)$  represents the state of the system. The minimum number of state variables required to represent a given system is usually equal to the order  $n$  of the system's defining differential equation.  $A$ ,  $B$  and  $C$  are the

state, input, and output matrices of the state-space description, respectively, as illustrated by the block diagram in Fig.5.1. The entries of  $A$ ,  $B$ ,  $C$  and  $D$  are derived directly from the coefficients of the transfer function [1], [2], [3], [4].

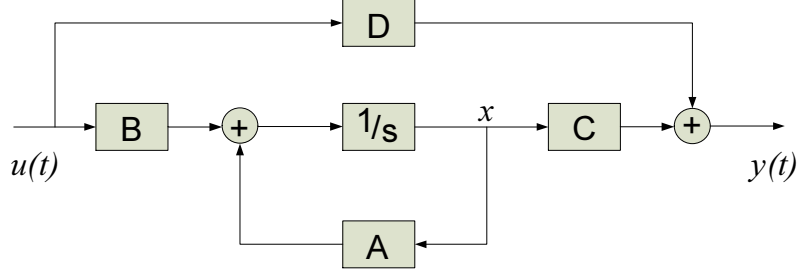


Figure 5.1: Block diagram of the state space description

The state of a dynamic system directly describes the distribution of internal energy in the system [1]. State variables must be linearly independent. So, we can relate the state to the system inputs and outputs and thus connect the internal variables to the external inputs and outputs, whereas the transfer function relates only the input to the output and does not show the internal behavior [2].

The general expression of the transfer function corresponding to a state space description can be easily derived from Eq.5.1 and is given by

$$H(s) = C \cdot (sI - A)^{-1} \cdot B + D \quad (5.2)$$

The entries of the matrices  $A$ ,  $B$ ,  $C$  and  $D$  are derived directly from the coefficients of the transfer function. The poles of the transfer function are the eigenvalues of  $A$ . In other words, the denominator of the transfer function is given by the determinant of  $sI - A$ , where  $I$  is the identity matrix. The zeros of the filter are constituted from the contents of all four system matrices, and is given by  $C \cdot adj(sI - A) \cdot B + D$ , where  $adj$  computes the adjoint of the respective matrix [2].

One can also derive from Eq.5.1 two intermediate transfer functions,  $F(s)$  and  $G(s)$ , which are the signal and noise transfer functions, respectively [5].  $F(s)$  represents the transfer function from the filter input  $u(s)$  to the integrator outputs  $x(s)$

$$F(s) = \frac{x(s)}{u(s)} = (sI - A)^{-1} \cdot B \quad (5.3)$$

and  $G(s)$  contains the transfer function from integrator inputs to the filter output  $y(s)$

$$G(s) = \frac{y(s)}{\epsilon(s)} = C \cdot (sI - A)^{-1} \quad (5.4)$$

where  $\epsilon(s)$  models the noise generated at the input of the integrator.

The internal state variables are the smallest possible subset of system variables that can represent the entire state of the system at any given time. Hence, the output of a system at any instant is determined completely from a knowledge of the system state and the input at that instant. Nevertheless, a given transfer function can be converted into a state equation in several ways. This is due to the fact that the initial conditions of a system can be specified in many different ways, and consequently, the system state can be specified in many forms. This means that state variables (and as a consequence, the state space equations) are not unique.

## 5.2 Dynamic Range

A system's dynamic range is essentially determined by the maximum processable signal magnitude and the internally generated noise. It is well known that the system's controllability and observability gramians play a key role in the determination and optimization of the dynamic range [10], [5].

The controllability and observability gramians are derived from the state space description. The definition of the controllability gramian, related to the system matrices  $A$  and  $B$  equals:

$$K = \int_0^\infty e^{At} B B^T e^{A^T t} dt = \frac{1}{2\pi} \int_{-\infty}^{+\infty} F(j\omega) F^*(j\omega) d\omega \quad (5.5)$$

The observability gramian, related to the system matrices  $A$  and  $C$  equals:

$$W = \int_0^\infty e^{A^T t} C^T C e^{At} dt = \frac{1}{2\pi} \int_{-\infty}^{+\infty} G^*(j\omega) G(j\omega) d\omega \quad (5.6)$$

If  $A$  is stable, the controllability ( $K$ ) and observability ( $W$ ) gramians are the unique, symmetric solutions of the following two Lyapunov equations

$$AK + KA^T + 2\pi BB^T = 0 \quad (5.7)$$

$$A^T W + WA + 2\pi C^T C = 0 \quad (5.8)$$

where  $A$ ,  $B$  and  $C$  are the state, input, and output matrices of the state-space description, respectively.

In [6] it is shown that, in order to maximize the dynamic range of the system, one should minimize the objective functional, which represents the relative improvement of the dynamic range and contains all parameters which are subject to manipulation by the designer. The objective functional is given by

$$F_{DR} = \frac{\max_i k_{ii}}{(2\pi)^2} \sum_i \frac{\alpha_i}{C_i} w_{ii} \quad (5.9)$$

where  $k_{ii}$  and  $w_{ii}$  are the main diagonal elements of  $K$  and  $W$ , respectively,  $\alpha_i = \sum_j |A_{ij}|$  is the absolute sum of the elements on the  $i$ -th row of  $A$ , and  $C_i$  is the capacitance in integrator  $i$ .

### 5.2.1 Dynamic Range Optimization

Departing from the transfer function derived in Chapter 4, one can generate a state space description of the filter, which is optimized with respect to the Dynamic Range [7], [6]. In [6] a method to optimize the state space description of a dynamical system is presented, based on the observability and controllability gramians. The resulting system has, under certain conditions, the maximum dynamic range achievable, given the total amount of capacitance.

The optimization is based on space transforms, also known as similarity transforms. A similarity (coordinate) transform, indicated by an invertible matrix  $T$ , defines a new state vector

$$x' = T^{-1}x \quad (5.10)$$

assuming  $\det(T) \neq 0$ .

And consequently, the transformation results in new system matrices, given by

$$\begin{aligned} A' &= T^{-1}AT \\ B' &= T^{-1}B \\ C' &= CT \\ D' &= D \end{aligned} \quad (5.11)$$

By the state space transformation the controllability and observability gramians become optimal

$$\begin{aligned} K' &= T^{-1}KT^{-T} \\ W' &= T^TW \end{aligned} \quad (5.12)$$

where  $T^{-T} = (T^{-1})^T$ .

As the dynamic range of a circuit is defined as the ratio of the maximum and the minimum signal level that it can process, optimization of the dynamic range is equivalent to the simultaneous maximization of the (distortionless) output swing and the minimization of the overall noise contribution [7].

From the state space representation, geometry concepts can be useful in visualizing the solution of a system. In [6], Rocha gives a geometric interpretation of the optimization of the dynamic range. A visualization of the optimization procedure can be seen in Fig.5.2, for a system with tree state variables. The output swing is related via the controllability gramian to the

space of 'occurring' state-space vectors. Under the assumption of a random input signal, the shape of this space is generally a multidimensional ellipsoid. The constraint that each integrator has a maximum representation capacity ( $M$ ) defines a multidimensional cuboid, which, for a distortionless transfer, should contain the former mentioned ellipsoid completely. As the mean square radius of the ellipsoid is equivalent to the maximum output swing, the output swing is maximal when the mean square radius is. This can occur if and only if the ellipsoid becomes a spheroid. In that case the controllability gramian is a diagonal matrix with equal diagonal entries, which means that all axes of the ellipsoid have equal length. Thus, the first optimization step boils down to a similarity transform, such that the controllability gramian of the new system becomes a diagonal matrix with equal diagonal entries. This transform is given by

$$T_K = P_K D_K^{1/2} \quad (5.13)$$

where  $P_K$  is the eigenvector matrix of  $K$  and  $D_K$  is a diagonal matrix whose diagonal entries are the eigenvalues of  $K$ . In the second step of the optimization procedure, the system is optimized with respect to its noise contribution. Rocha defines another ellipsoid, which describes the noise that is added to the state vector in each direction. While preserving the result of the first optimization step, it is possible to rotate the state space, such that the observability gramian becomes a diagonal matrix as well. In that case, the axes of the noise ellipsoid are aligned with the 'system axes'. The transformation of  $W$  is defined as

$$T_W = P_W \quad (5.14)$$

where  $P_W$  is the eigenvector matrix of  $W$ .

Finally, profiting from the well-known fact that the relative noise contribution of an integrator decreases when the capacitance and bias current increase, we match the optimal capacitance distribution to the noise contributions of each individual integrator (noise scaling), i.e., the diagonal entries of  $W$ , combined with the coefficients in matrix  $A$ , which is defined by [6]

$$C_i = \frac{\sqrt{\alpha_i w_{ii} k_{ii}}}{\sum_j \sqrt{\alpha_j w_{jj} k_{jj}}} \quad (5.15)$$

### 5.3 Sparsity

The drawback of a dynamic-range optimal system is that its state-space matrices are generally fully dense, i.e., all the entries of the A, B, C matrices are filled with nonzero elements. These coefficients will have to be mapped onto circuit components, and will result in a complex circuit with a large number of

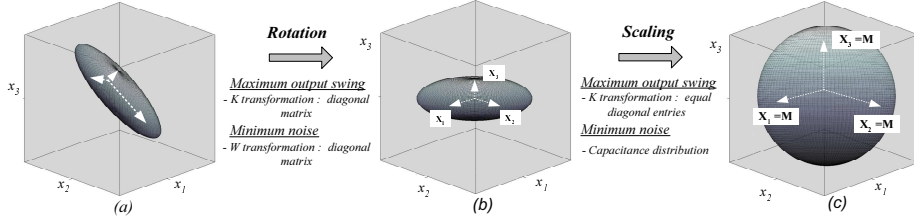


Figure 5.2: Dynamic Range optimization based on the similarity transformation of K and W and capacitance distribution. The coordinate axes represent the state variables and the cuboid represents the maximum signal amplitude (M) that the integrators are able to handle (a) The initial state space representation (ellipsoid) is usually not well adapted to the integrator's representations capacity bounds (cuboid) (b) The (rotated) ellipsoid's principal axes are now aligned to the coordinate axes, as a result of the diagonalization procedure to the matrices K and W (c) Finally, the optimized state representation is obtained by scaling the states variables. Note that the sphere represents the maximum possible mean square radius which can be fitted into the integrator's capacity cuboid.

interconnections. For high-order filters it is therefore necessary to investigate how a realization of the desired transfer function having sparser state-space matrices would compare to the one having maximal dynamic range.

By definition, a sparse matrix is a matrix populated primarily with zeros. For a less complex circuit, it is possible, for instance, to transform the state space matrix  $A$  in a similar decomposition and by this reducing the number of non-zero coefficients in  $A$ . One important characteristic of a similarity transformation matrix  $T$  is that, considering a system of order  $n$ ,  $T$  has  $n^2$  degrees of freedom. Thus, the system can be transformed in several ways, achieving the desired sparsity requirements.

However, these transformations lead to an increase in the system noise and consequently to an increase in the objective functional, (5.9). Considering the fact that for a given system the choice of state is not unique, in the next subsections we will review some well-known state forms and analyze the state space matrices with respect to dynamic range and sparsity.

### 5.3.1 Orthogonal transformations

The orthogonal (unitary) transformation-based forms are called condensed forms. Some examples of these condensed forms are the Hessenberg and the Schur decomposition, which will be described below.

Any orthogonal transformation, described by  $T^T T = I$ , has  $n(n - 1)/2$  degrees of freedom and, consequently, it is possible to create  $n(n - 1)/2$  zeros.

In other words, these transformations are extremely useful in zeroing specified elements in a matrix.

### Hessenberg decomposition

A Hessenberg decomposition is a matrix decomposition of a matrix  $A$  into a unitary matrix  $U$  and a Hessenberg matrix  $A_{Hess}$  such that

$$A = UA_{Hess}U^T \quad (5.16)$$

For real matrices, a unitary matrix is a matrix  $U$  for which  $U^{-1} = U^T$ .  $A_{Hess}$  is similar to  $A$  and has the same eigenvalues as  $A$ . The Hessenberg decomposition transforms a matrix in an upper diagonal matrix where only the elements of the main sub-diagonal are different from zero

$$A_{Hess} = \begin{bmatrix} a_{11} & a_{12} & a_{13} & \dots & a_{1,n-1} & a_{1,n} \\ a_{21} & a_{22} & a_{23} & \dots & a_{2,n-1} & a_{2,n} \\ 0 & a_{32} & a_{33} & \dots & a_{3,n-1} & a_{3,n} \\ 0 & 0 & a_{43} & \dots & a_{4,n-1} & a_{4,n} \\ \vdots & \vdots & \vdots & \ddots & \vdots & \vdots \\ 0 & 0 & 0 & \dots & a_{n,n-1} & a_{n,n} \end{bmatrix} \quad (5.17)$$

where the matrix  $B$  and  $C$  have no specific structure, being defined by  $B_{Hess} = U^{-1}B$  and  $C_{Hess} = CU$ . Then, as one can see in Eq.5.17, an upper Hessenberg matrix has zero everywhere below the diagonal except for the first subdiagonal row. However, if the matrix  $A$  is symmetric, the Hessenberg form becomes a tridiagonal representation.

### Schur decomposition

The Schur decomposition of a square matrix  $A$  is a matrix decomposition of the form

$$A_{Schur} = Q^T A Q = D + N \quad (5.18)$$

where  $Q$  is a orthogonal (unitary) matrix and  $A_{Schur}$  is an upper triangular matrix which is the sum of a  $D = diag(\lambda_1, \lambda_2, \dots, \lambda_n)$  (i.e., a diagonal matrix consisting of eigenvalues  $\lambda$  of  $A$ ) and a strictly upper triangular matrix  $N$ . Thus, the eigenvalues of  $A$  appear on the main diagonal of  $A_{Schur}$ .

The Schur decomposition of a square matrix  $A$  involves finding a unitary matrix  $Q$  that can be used for a similarity transformation of  $A$  to form a block upper triangular matrix  $A_{Schur}$ , defined by

$$A_{Schur} = \begin{bmatrix} a_{11} & a_{12} & a_{13} & \dots & a_{1,n-1} & a_{1,n} \\ 0 & a_{22} & a_{23} & \dots & a_{2,n-1} & a_{2,n} \\ 0 & 0 & a_{33} & \dots & a_{3,n-1} & a_{3,n} \\ 0 & 0 & 0 & \dots & a_{4,n-1} & a_{4,n} \\ \vdots & \vdots & \vdots & \ddots & \vdots & \vdots \\ 0 & 0 & 0 & \dots & 0 & a_{n,n} \end{bmatrix} \quad (5.19)$$

The Schur decomposition always exists and so the similarity transformation of  $A$  to upper triangular always exists. This contrasts with the eigensystem similarity transformation, used to diagonalize a matrix, which does not always exist.

For complex values, Schur decomposition produces a quasi-triangular matrix. Under real (orthogonal) transformations one can not triangularize a matrix if it has complex conjugate eigenvalues. Instead one can always obtain a quasi-triangular form with  $1 \times 1$  or  $2 \times 2$  blocks on the diagonal corresponding to the real and complex conjugate eigenvalues, respectively.

With respect to sparsity, the preference is for the Schur decomposition rather than for the Hessenberg decomposition, because it returns a matrix with a larger number of zeros.

### 5.3.2 Canonical form representations

From control theory, it is known that a general transfer function, described in Eq.5.20, can be written directly into (controllable or observable) canonical form [1], [4].

$$H(s) = \frac{p_{n-1}s^{n-1} + p_{n-2}s^{n-2} + \dots + p_1s + p_0}{s^n + q_{n-1}s^{n-1} + \dots + q_1s + q_0} \quad (5.20)$$

The entries of  $A$ ,  $B$ ,  $C$  and  $D$  of a canonical form are derived from coefficients inspection of the transfer function, as given below.

A state-space system in controllable canonical form has the following structure

$$A_c = \begin{bmatrix} 0 & 1 & 0 & \dots & 0 \\ 0 & 0 & 1 & \dots & 0 \\ \vdots & \vdots & \vdots & \ddots & \vdots \\ 0 & 0 & 0 & \dots & 1 \\ -q_0 & -q_1 & -q_2 & \dots & -q_{n-1} \end{bmatrix} \quad B_c = \begin{bmatrix} 0 \\ 0 \\ \vdots \\ 0 \\ 1 \end{bmatrix} \quad (5.21)$$

$$C_c = [p_0 \ p_1 \ \dots \ p_{n-2} \ p_{n-1}] \quad D = [0]$$

This state-space realization is called controllable canonical form because the resulting model is guaranteed to be controllable. The coefficients of the numerator appear in the  $C_c$  matrix and the coefficients of the denominator appear (with opposite sign) as the last row of the  $A_c$  matrix. The central feature of the controllable form is that each state variable is connected by the feedback to the control input, as shown in Fig.5.3.

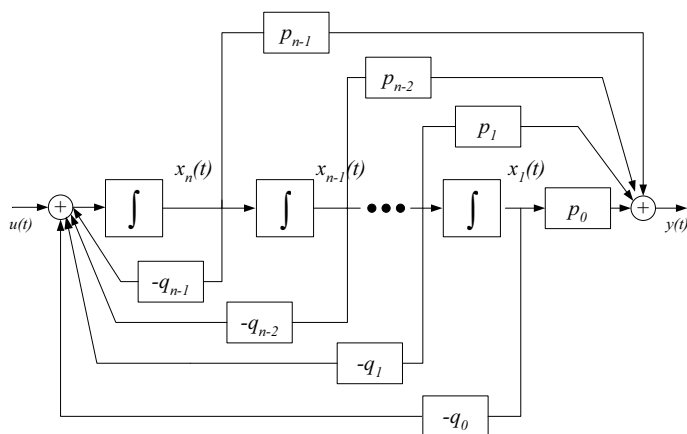


Figure 5.3: Controllable canonical form realization

The transfer function coefficients can also be used to construct another type of canonical form, the observable canonical form defined by

$$A_o = \begin{bmatrix} 0 & 0 & \dots & 0 & -q_0 \\ 1 & 0 & \dots & 0 & -q_1 \\ \vdots & \vdots & \vdots & \vdots & \vdots \\ 0 & 0 & \dots & 0 & -q_{n-2} \\ 0 & 0 & \dots & 1 & -q_{n-1} \end{bmatrix} \quad B_o = \begin{bmatrix} p_0 \\ p_1 \\ \vdots \\ p_{n-2} \\ p_{n-1} \end{bmatrix} \quad (5.22)$$

$$C_o = [0 \ 0 \ \dots \ 0 \ 1] \quad D = [0]$$

This state-space realization is called observable canonical form because the resulting model is guaranteed to be observable. The coefficients of the numerator appear in the  $B_o$  matrix and the coefficients of the denominator appear (with opposite sign) as the last column of the  $A_o$  matrix. Fig.5.4 shows the implementation of these matrices in a block diagram.

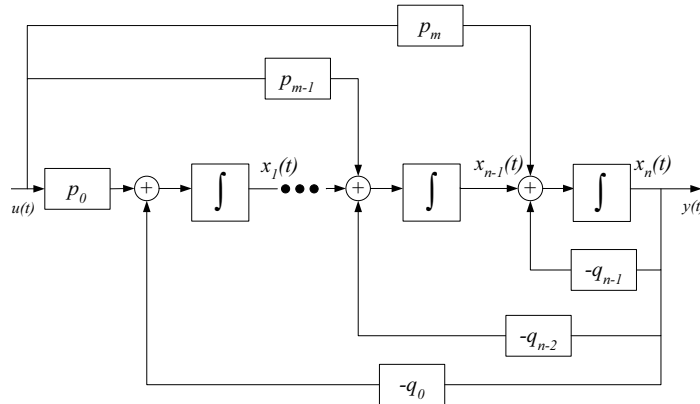


Figure 5.4: Observable canonical form realization

One can note the relationship between the controllable and observable canonical forms. The  $A$  matrices in these two cases are the transpose of one another, and the  $B$  of one is the transpose of  $C$  in the other, and vice versa. This is defined as a duality relation.

Controllability and observability are qualitative properties of a system. These properties depend on the elements of the  $A$ ,  $B$  and  $C$  matrices. Controllability refers to the ability of the input to control (or affect) each of the system modes, whereas the observability occurs when each of the modes can be detected at the output. A basic result in control theory is that a system in state-space form is controllable if and only if the matrix  $[B, AB, A^2B, \dots, A^{n-1}B]$  has a full rank  $n$  (i.e., is invertible). The rank of an arbitrary rectangular

matrix  $A$  is the dimension of the largest square submatrix that has nonzero determinant, i.e., defines the number of linearly independent rows or columns in a matrix. Similarly, a state-space system is observable if and only if  $[CCA \dots CA^{n-1}]^T$  is nonsingular with rank equals  $n$ .

The advantage, with respect to sparsity, of a canonical decomposition is that the canonical forms have  $n^2$  elements assigned either to 0 or to 1, which corresponds to a extremely sparse matrix.

### 5.3.3 Biquad Structure

A high-order transfer function  $H(s)$  can be factored into the product of the first and second order transfer functions. Hence, as shown in Fig. 5.5, a filter can be implemented as a cascade of second-order biquadratic blocks, also called biquad stages (and a first-order block, if necessary) [8].

$$H(s) = H_1(s).H_2(s).H_3(s)\dots H_N(s)$$

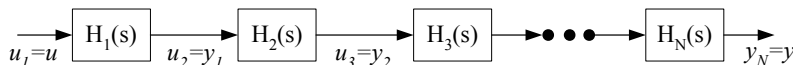


Figure 5.5: Biquad cascade realization of an nth-order transfer function

The signal flow graph of a biquad stage is shown in Fig.5.6.

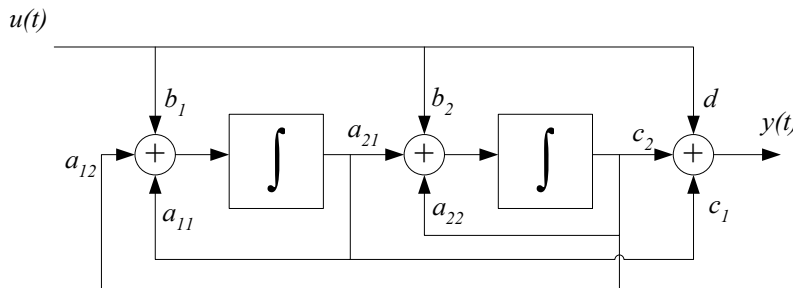


Figure 5.6: Block diagram of the second-order biquad

The corresponding second-order transfer function of a biquad,  $H_i(s)$ , is expressed in terms of  $A$ ,  $B$ ,  $C$  and  $D$ .

$$H_i(s) = \frac{(c_1 b_1 + c_2 b_2)s + c_1 a_{12} b_2 + c_2 a_{21} b_1 - c_1 a_{22} b_1 - c_2 a_{11} b_2}{s^2 + (-a_{11} - a_{22})s + a_{11} a_{22} - a_{12} a_{21}} + d \quad (5.23)$$

Cascading of n stages means that we connect the output of  $H_{n-1}(s)$  to the input of  $H_n(s)$ , such that the product of the individual transfer functions  $H_i(s)$  implements the prescribed function  $H(s)$ . Note that the numerators and denominators of  $H_i(s)$  can be combined in different ways in order to obtain the

final transfer function  $H(s)$ . One way to decrease the coefficients sensitivity, is by grouping the zeros with the nearest pole pair. Finally, one can derive the combined state space description of the cascade connected system which is given by

$$\begin{aligned} A &= \begin{bmatrix} A_1 & 0 & 0 & \dots & 0 \\ B_2 C_1 & A_2 & 0 & \dots & 0 \\ B_3 D_2 C_1 & B_3 C_2 & A_3 & \dots & 0 \\ B_4 D_3 D_2 C_1 & B_4 D_3 C_2 & B_4 C_3 & \dots & 0 \\ \vdots & \vdots & \vdots & \vdots & \vdots \\ B_N D_{N-1} \dots D_2 C_1 & B_N D_{N-1} \dots D_3 C_2 & B_N D_{N-1} \dots D_4 C_3 & \dots & A_N \end{bmatrix} \\ B &= \begin{bmatrix} B_1 \\ B_2 D_1 \\ B_3 D_2 D_1 \\ B_4 D_3 D_2 D_1 \\ \vdots \\ B_N D_{N-1} \dots D_1 \end{bmatrix} \quad C^T = \begin{bmatrix} D_N \dots D_2 C_1 \\ D_N \dots D_3 C_2 \\ D_N \dots D_4 C_3 \\ \vdots \\ D_N C_{N-1} \\ C_N \end{bmatrix} \end{aligned} \tag{5.24}$$

The main advantage of cascade filters is their generality, i.e., any arbitrary stable transfer function can be realized as a cascade circuit, and very easy tuning because each biquad is responsible for the realization of only one pole-zero pair. By this, the realizations of the individual critical frequencies of the filter are decoupled from each other. The disadvantage of this decoupling is that for high-order filters, cascade designs are often found to be too sensitive to component variations.

### 5.3.4 Diagonal controllability gramian - an Orthonormal Ladder Structure

When designing high-order filters, it is very desirable to concentrate on circuits that are less sensitive to component variations. It is known that an optimal dynamic range system will also have optimal sensitivity [7]. Nevertheless, in order to improve the state-space matrices' sparsity, an orthonormal ladder structure can be implemented, which still presents a good behavior with respect to sensitivity. Fig.5.7 shows a block diagram of a general orthonormal ladder filter [9]. As shown in the block diagram, the filter output is obtained from a linear combination of the outputs of all integrators.

Another useful property of orthonormal ladder filters is the ability to realize any stable transfer function. Arbitrary poles are realized using the ladder feedback structure while transmission zeros are realized using an output summing stage. Additionally, since for a given transfer function the orthonormal ladder realization is unique, the design procedure is more easily automated

than the process of finding an optimal biquad cascade design where pole-zero pairing and cascade ordering are important.

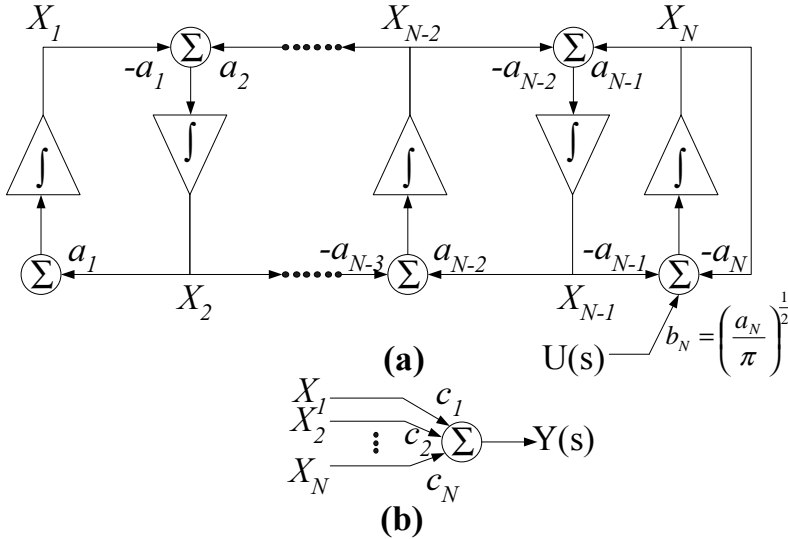


Figure 5.7: Block diagram of an orthonormal ladder filter, (a) Leapfrog structure; (b) Output summing stage

The  $A$ ,  $B$  and  $C$  matrices of this structure are given by

$$A = \begin{bmatrix} 0 & \alpha_1 & & \dots & 0 \\ -\alpha_1 & 0 & \alpha_2 & \dots & 0 \\ & -\alpha_2 & 0 & \alpha_3 & \dots \\ \vdots & \ddots & \ddots & \ddots & \vdots \\ 0 & \dots & -\alpha_{n-2} & 0 & \alpha_{n-1} \\ 0 & \dots & & -\alpha_{n-1} & \alpha_n \end{bmatrix} \quad B = \begin{bmatrix} 0 \\ 0 \\ 0 \\ \vdots \\ 0 \\ \sqrt{\frac{\alpha_n}{\pi}} \end{bmatrix} \quad C^T = \begin{bmatrix} c_1 \\ c_2 \\ c_3 \\ \vdots \\ c_{n-1} \\ c_n \end{bmatrix} \quad (5.25)$$

The  $A$  matrix is tridiagonal and is very nearly skew-symmetric except for a single nonzero diagonal element. One important property of orthonormal ladder filters is the fact that the resulting circuits are inherently state scaled, i.e., the controllability gramian is already a identity matrix [9]. From the Lyapunov equation in Eq. 5.7 and assuming  $K = I$ ,  $B$  results in an all zeros matrix except for the  $N$ th element with  $b_n$  given by  $\sqrt{\frac{\alpha_n}{\pi}}$ . The drawback of this structure is that the system is not optimized with respect to its noise contribution, i.e. the observability gramian  $W$  is not transformed.

The coefficients  $\alpha$  are defined as

$$\begin{aligned}\alpha_i &= \sqrt{\frac{1}{x_i x_{i+1}}} \quad 1 \leq i < n; \\ \alpha_n &= \frac{1}{x_n} \quad i = n.\end{aligned}\tag{5.26}$$

where  $x_i$  are the reactive components of a singly terminated LC ladder structure. In order to calculate the values of the reactive elements  $x_i$  one needs to apply a continued fraction expansion on the denominator of the transfer function  $H(s) = \frac{N(s)}{D(s)}$ . The denominator can be converted into a simple continued fraction by the following procedure. First, the polynomial  $D(s)$  of degree  $n$  is represented by

$$D(s) = D_{even}(s) + D_{odd}(s)\tag{5.27}$$

where  $D_{even}(s)$  and  $D_{odd}(s)$  are the even and the odd parts of  $D(s)$ , respectively. Then, applying the ratio between both parts such as

$$\begin{aligned}D_{cf}(s) &= \frac{D_{even}(s)}{D_{odd}(s)} \quad \text{if } n \text{ is even} \\ D_{cf}(s) &= \frac{D_{odd}(s)}{D_{even}(s)} \quad \text{if } n \text{ is odd}\end{aligned}\tag{5.28}$$

we end up with the continued fraction expansion of  $D(s)$  in the following manner

$$D_{cf}(s) = \frac{P}{Q} = x_0 + \frac{r_0}{Q} = x_0 + \frac{1}{x_1 + \frac{r_1}{r_0}} = \dots = x_0 + \frac{1}{x_1 + \frac{1}{x_2 + \frac{1}{\dots + \frac{1}{x_n}}}}\tag{5.29}$$

where the  $r_i$  are the remainders and the  $x_i$  the integral parts of the intermediate fractions which defines the reactive components values.

Finally, in order to implement the numerator  $N(s)$  of the transfer function  $H(s)$ , the proper C vector must be obtained. Using the intermediate functions  $F_i$ , the coefficients  $c_i$  can be written as

$$N(s) = c_1 \cdot F_1 + c_2 \cdot F_2 + \dots + c_n \cdot F_n\tag{5.30}$$

where

$$\begin{aligned}F_1 &= \sqrt{\frac{x_1}{\pi}} \cdot N(0) \\ F_2 &= \frac{s}{\alpha_1} F_1 \\ F_i &= \frac{1}{\alpha_{i-1}} (s F_{i-1} + \alpha_{i-2} F_{i-2}), \quad 3 \leq i \leq n\end{aligned}\tag{5.31}$$

The result is the state-space structure given in Eq. 7.36 with the coefficients calculated from Eq. 5.26 and Eq. 5.30.

### 5.3.5 Sparsity versus Dynamic Range comparison

A comparative analysis of the Dynamic Range and the Sparsity properties of several state space representations will be performed in this section. First, Fig. 5.8 shows the obtained objective functionals (FDRs) for a specific transfer function, in this case the Padé [8/10] Morlet wavelet filter transfer function given in Table 4.4. As one can see, the FDR of the orthonormal ladder structure ( $FDR_{orth} = 21.6$  dB) is very close to the optimal representation ( $FDR_{opt} = 19.8$  dB), only 1.8 dB larger than the optimum one, whereas the canonical forms present the largest FDRs ( $FDR_{cont,can} = 149$  dB and  $FDR_{obs,can} = 167$  dB).

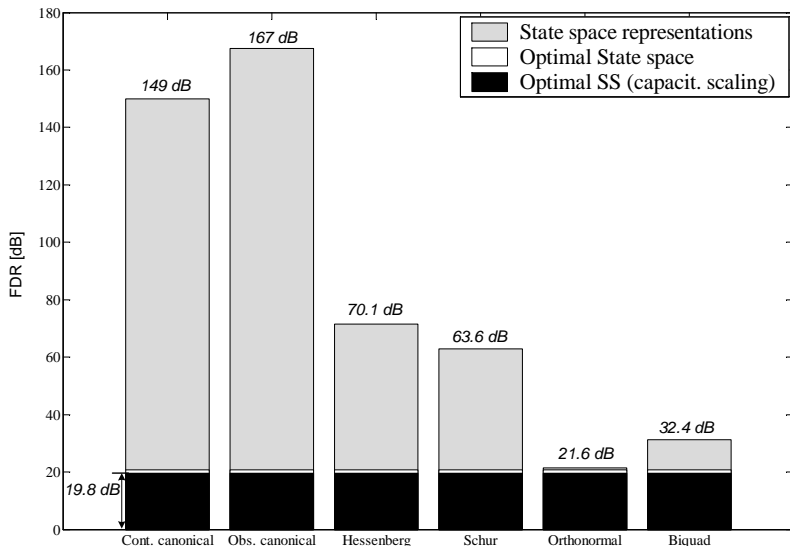


Figure 5.8: FDR comparison of different state space descriptions for the Padé [8/10] Morlet wavelet filter transfer function in Table 4.4

Furthermore, in order to compare the Dynamic Range versus the order of the system, Fig. 5.9 illustrates the FDR of different state space descriptions applied to a Gaussian wavelet filter transfer function. The transfer function of the filter was obtained by a Padé approximation with order varying from 2 to 10. Note that for lower order, all the state space representations present a similar performance, with FDR values close to each other, whereas for higher order, the FDRs of some representations deviate too much from the optimal case. In this case, the Dynamic Range optimization becomes a very important requirement in high-order analog filters design. Again, one can see that the orthonormal state space is very close to the optimal representation even for high-order systems.

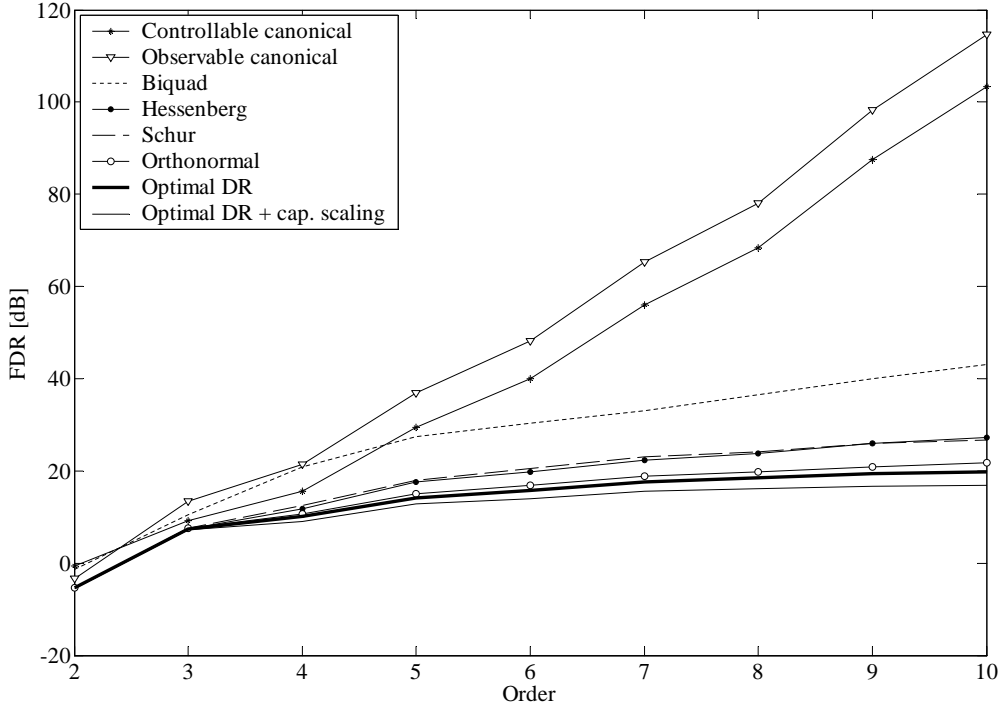


Figure 5.9: FDR versus order of the filter for different state space representations

### 5.3.6 New Sparsity Figure-of-Merit (SFOM)

In order to define the sparsity property versus dynamic range for a specific state space description, we derive a new figure-of-merit. The static power consumption of an analog active filter is basically determined by the bias currents inside the filter. From a state space representation one can define the total bias current by  $N_c I_o$  where  $N_c$  represents the number of nonzero coefficients presented in the state matrix  $A$ ,  $B$  and  $C$  and  $I_o$  is the current necessary to implement each coefficient. As a result, the static power consumption of a filter can be written as

$$P_{static} = N_c I_o V_{cc} \quad (5.32)$$

On the other hand, in [6], the dynamic power dissipation of a n-th order filter has been expressed in terms of the dynamic range, and yields

$$P_{dynamic} = 8n f k T \xi f DR = 4nf \left( \frac{M}{\delta(p)} \right)^2 \text{Tr}(KQ) \frac{1}{FDR} \quad (5.33)$$

where  $n$  is the order of the filter,  $f$  is the operating frequency,  $M$  is the maximum output amplitude,  $\delta(p)$  is a nonlinear monotonically increasing function of the fraction of time  $p$  that the integrators are allowed to clip, and is rep-

resented by  $\delta(p) = -2 \ln(1 - p)$ .  $Tr$  represents the trace of a matrix and  $Q = C^T C$  is the state weighting matrix.  $Tr(KQ)$  is invariant under a similarity transformation and is thus beyond the designer's control.

Dividing  $P_{static}$  by  $P_{dynamic}$  we end up with

$$\frac{P_{static}}{P_{dynamic}} = \frac{N_c I_o V_{cc}}{4n \left(\frac{M}{\delta(p)}\right)^2 \text{Tr}(KQ) \frac{1}{\text{FDR}}} = \frac{I_o V_{cc}}{4 \left(\frac{M}{\delta(p)}\right)^2 \text{Tr}(KQ)} \frac{N_c \text{FDR}}{n} \quad (5.34)$$

where  $\frac{I_o V_{cc}}{4 \left(\frac{M}{\delta(p)}\right)^2 \text{Tr}(KQ)}$  is defined by the circuit implementation, while  $\frac{N_c \text{FDR}}{n}$  can be controlled at system level. So, in order to design an optimal state space description with respect to Dynamic Range and Sparsity, we present a new figure-of-merit, giving by

$$SFOM = \frac{N_c \times \text{FDR}}{n} \quad (5.35)$$

From Eq. 5.35 one can see that the optimal case is the one with  $SFOM$  minimum, i.e., the system which presents a good sparsity (large number of zeros) while preserving a low FDR (i.e., a large Dynamic range).

The number of nonzero coefficients  $N_c$  for different state space representations is given in Table 5.1.

Table 5.1: Number of nonzero coefficients  $N_c$  in  $A$ ,  $B$  and  $C$

|             |                             |
|-------------|-----------------------------|
| Optimal     | $n^2 + 2n$                  |
| Hessenberg  | $\frac{n(n+1)}{2} + 3n - 1$ |
| Schur       | $\frac{n(n+1)}{2} + 2n$     |
| Canonical   | $3n$                        |
| Biquad      | $5n$                        |
| Orthonormal | $3n$                        |

Finally, several SFOMs versus the order of the system are plotted in Fig. 5.10. As expected, the orthonormal presents the best performance (lower SFOM) mainly due to its excellent sparsity behavior and its near-optimum FDR property.

## 5.4 Sensitivity

To accurately realize a transfer function using analog integrated filters, the circuit components of the filter must match closely, and the sensitivity of the transfer function to the values of the filter's components must be low. This sensitivity depends on the filter network, and thus depends on the state-space

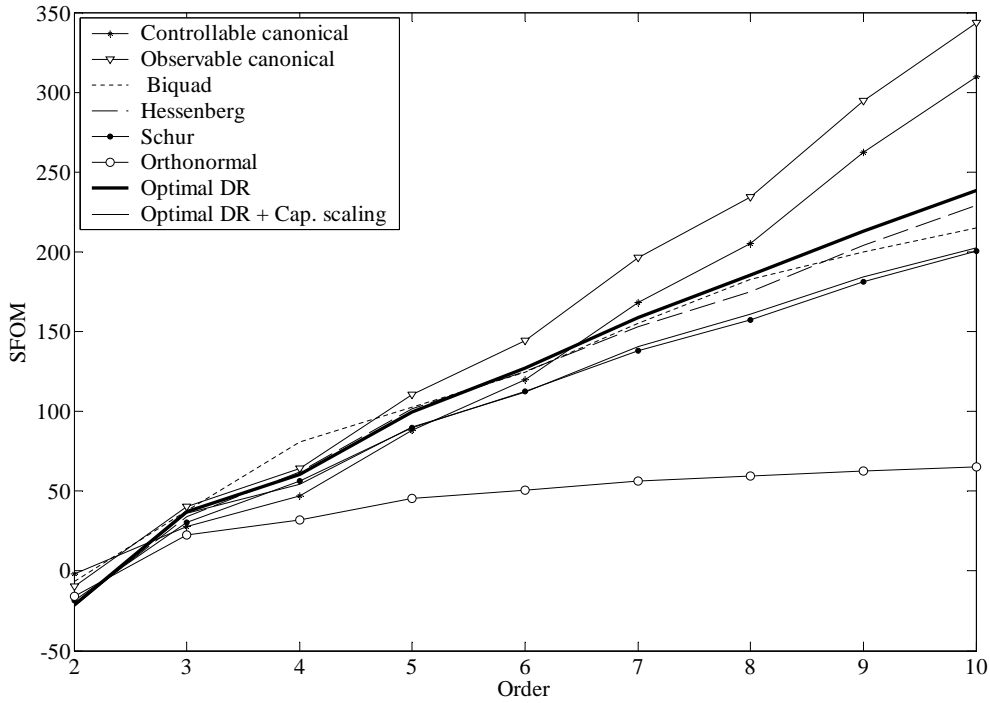


Figure 5.10: SFOM versus order of the filter for different state space description

representation. Hence, the sensitivity of the transfer function of a particular state-space representation is an important criterion for the comparison of different network realizations.

The sensitivity of the transfer function  $H(s)$  to the component values of a state-space realization depends on the sensitivity to the entries of the state matrices  $A$ ,  $B$  and  $C$  ( $D$  is usually zero). Here we will consider an absolute sensitivity measurement, which can be used to establish the relationship between the absolute changes  $\Delta a_{ij}$ ,  $\Delta b_i$  and  $\Delta c_j$  [8].

The absolute sensitivities of  $H(s)$  with respect to variations of the coefficients can be given by [10].

$$\begin{aligned}
 S_{a_{ij}}(s) &= \frac{\partial H(s)}{\partial a_{ij}} = c(sI - A)^{-1}e_i e_j (sI - A)^{-1}b = G_i(s)F_j(s) \\
 S_{b_i}(s) &= \frac{\partial H(s)}{\partial b_i} = c(sI - A)^{-1}e_i = G_i(s) \\
 S_{c_i}(s) &= \frac{\partial H(s)}{\partial c_i} = e_i(sI - A)^{-1}b = F_i(s)
 \end{aligned} \tag{5.36}$$

where  $e_i$  is the unit vector with  $i$ th element unity. In the case of a statistical derivation analysis, the frequency dependent variances of the transfer function are defined as

$$\begin{aligned}
\Sigma_{\Delta H, A}^2(s) &= E\left\{\left|\sum_{i=1}^n \sum_{j=1}^n S_{a_{ij}} \Delta a_{ij}\right|^2\right\} \\
&= \sum_{i=1}^n \sum_{j=1}^n |S_{a_{ij}}|^2 = G(s)G^*(s)F^*(s)F(s) \\
\Sigma_{\Delta H, B}^2(s) &= E\left\{\left|\sum_{i=1}^n S_{b_i} \Delta b_i\right|^2\right\} = \sum_{i=1}^n |S_{b_i}|^2 = G(s)G^*(s) \\
\Sigma_{\Delta H, C}^2(s) &= E\left\{\left|\sum_{j=1}^n S_{c_j} \Delta c_j\right|^2\right\} = \sum_{j=1}^n |S_{c_j}|^2 = F^*(s)F(s) \quad (5.37)
\end{aligned}$$

where the variations of the coefficients have been considered statistically independent. Integrating the transfer function variances over the whole frequency range, new sensitivity measures related to the observability and controllability gramians have been defined in [10], and are given by

$$\begin{aligned}
m_A &\leq \text{tr}(K)\text{tr}(W) \\
m_B &= \text{tr}(W) \\
m_C &= \text{tr}(K) \quad (5.38)
\end{aligned}$$

where  $m_A$ ,  $m_B$  and  $m_C$ , represent, respectively, the sensitivity of the matrices  $A$ ,  $B$  and  $C$  to their coefficients. Finally, the total sensitivity measure,  $m_T$ , of a transfer function with respect to the state space representation matrices can be obtained as

$$m_T = m_A + m_B + m_C \leq \text{tr}(K)\text{tr}(W) + \text{tr}(K) + \text{tr}(W) \quad (5.39)$$

The maximum sensitivity measure (worst-case sensitivity), considering  $m_T = \text{tr}(K)\text{tr}(W) + \text{tr}(K) + \text{tr}(W)$ , can be seen in Fig. 5.11 as function of the order  $n$  of a specific transfer function, for different state space representations. One can note that the optimal DR state space representation will also be optimal with respect to sensitivity. The Schur and Hessenberg decomposed from an optimal system also present an optimal sensitivity because the orthogonal transformation does not affect the sensitivity. The orthonormal structure has a reasonable low sensitivity to coefficient mismatch, close to the optimal case. Both controllable and observable canonical forms have the worst sensitivity measures for high order filters, as expected.

### 5.4.1 New Dynamic Range-Sparsity-Sensitivity Figure-of-Merit (DRSS)

To conclude the analysis of the state space descriptions we will present a new figure of merit that expresses the correlation of Dynamic Range, Sparsity and

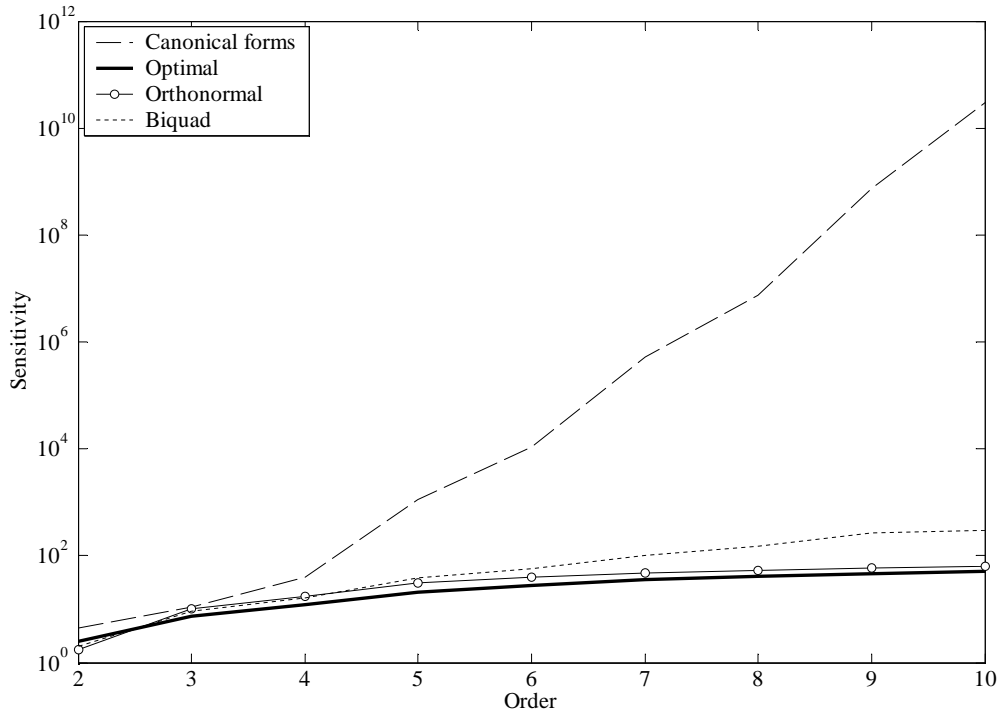


Figure 5.11: Sensitivity versus order of the filter for different state space description

Sensitivity parameters. In order to relate these three aspects, we introduce the Dynamic range-Sparsity-Sensitivity figure-of-merit (DRSS), given by

$$DRSS = \frac{N_c \times FDR \times m_T}{n} \quad (5.40)$$

As one can see from Eq. 5.40, the objective functional,  $FDR$ , gives the relative improvement of the dynamic range,  $\frac{N_c}{n}$  is related to the sparsity of the system and  $m_T$  defines the sensitivity of the matrices  $A$ ,  $B$  and  $C$  with respect to their coefficients. Fig. 5.12 shows the DRSS figure-of-merit versus the order of the system. Again, the orthonormal ladder structure presents the best performance (minimum DRSS) compared to the other state space descriptions presented in this chapter. Thus, we can state that the orthonormal structure is the optimal state space description for a system design where the most important requirements are the dynamic range, sparsity and sensitivity. Although the state space description obtained from the optimization procedure in Section 5.2.1 gives us the optimal representation with respect to dynamic range and sensitivity, its matrices are fully dense, and consequently, its SFOM and DRSS performances are relatively poor.

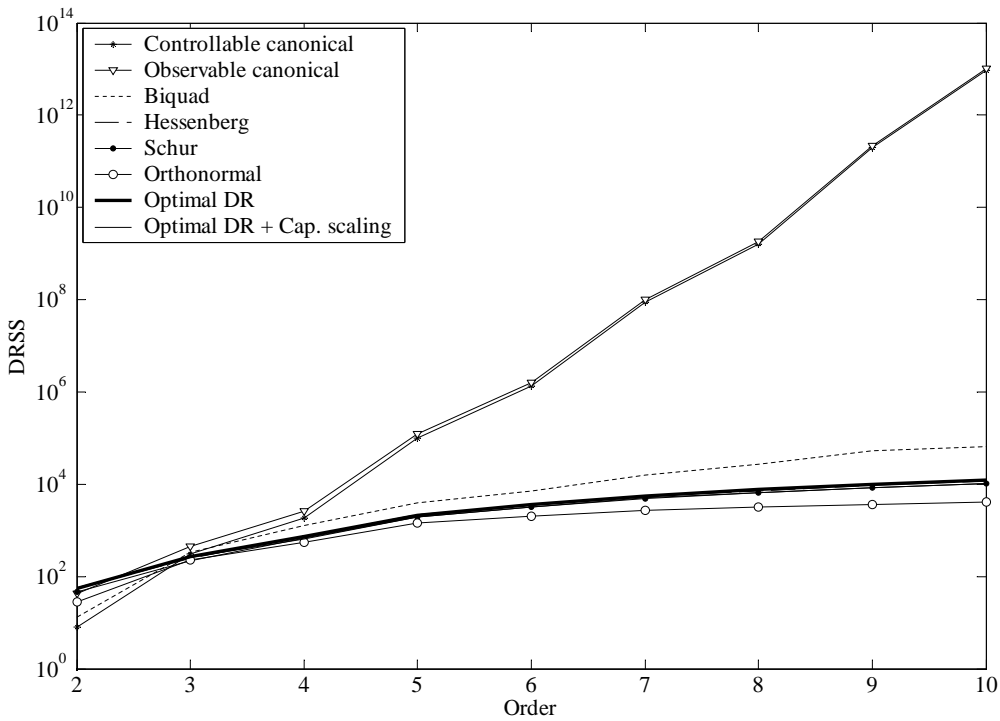


Figure 5.12: DRSS figure-of-merit versus order of the system

## 5.5 Conclusion

In this chapter we presented the description and a comparison of several state space representations. The analysis was based on dynamic range, sparsity and sensitivity properties, which are the most relevant aspects for an ultra low-power analog dynamic system. From the two new figure-of merits described above, viz., the SFOM and DRSS, we concluded that the orthonormal ladder structure is the optimal state space representation, and therefore, it will be used for the design of wavelet filters and biomedical systems in Chapter 7.



# Bibliography

- [1] T. Kailath, *Linear Systems*, Englewood Cliffs, Prentice Hall Inc., 1980.
- [2] B.P. Lathi, *Linear systems and signals*, Oxford University Press, New York, 2002.
- [3] P.M. DeRusso, R.J. Roy, C.M. Close and A.A. Desrochers, *State Variables for Engineers*, Wiley, New York, 2nd Ed., 1998.
- [4] J.D. Aplevich, *The essentials of linear state-space systems*, Wiley, New York, 2000.
- [5] W. M. Snelgrove and A. S. Sedra, “Synthesis and analysis of state-space active filters using intermediate transfer function,” *IEEE Transactions on Circuits and Systems*, , no. 3, pp. 287–301, march 1986.
- [6] D. P. W. M. Rocha, *Optimal Design of Analogue Low-power Systems, A strongly directional hearing-aid adapter*, Phd thesis, Delft University of Technology, April 2003.
- [7] G. Groenewold, “Optimal dynamic range integrators,” *IEEE Transactions on Circuits and Systems-I*, vol. 39, no. 8, pp. 614–627, august 1992.
- [8] W.k<sub>i</sub> Chen (Editor-in-Chief), *The Circuits and Filters Handbook*, CRC press, IEEE press, 1995.
- [9] D. A. Johns, W. M. Snelgrove, and A. S. Sedra, “Orthonormal ladder filters,” *IEEE Transactions on Circuits and Systems*, vol. 36, no. 3, pp. 337–343, march 1989.
- [10] L. Thiele, “On the sensitivity of linear state-space systems,” *IEEE Transactions on Circuits and Systems*, , no. 5, pp. 502–510, may 1986.



## Chapter 6

# Ultra Low-power Integrator Designs

*“Exploiting the transistor’s potential caused many headaches. A colleague called it a ‘persistor’, because persistence was what it took to make it.”* - William Shockley

The trends towards lower power consumption, lower supply voltage and higher frequency operation have increased the interest in new design techniques for analogue integrated filters. In this chapter, we will focus only on ultra low-power integrated continuous-time filter designs. The current state-of-the-art design approaches for such filters are transconductance amplifier-capacitor ( $gm\text{-}C$ ) and translinear (log-domain) methods, which will be described in the following sections.

As mentioned in previous chapters, one can implement an  $n$ -th order linear differential equation, which describes a filter of the same order, by means of  $n$  intercoupling integrators. An on-chip integrator is an electronic circuit that realizes the transfer function  $\frac{G}{sC}$ , where  $G$  is implemented by a (trans)conductor stage (which converts voltage-to-current), and the integrating component  $\frac{1}{sC}$  is usually realized by a capacitor (integrating a current into a voltage). Therefore, integrators can be seen as the main building blocks of a filter topology and, consequently, in this chapter we will concentrate on the design of ultra low-power integrators.

### 6.1 $G_m\text{-}C$ filters

One of the most popular technique for realizing analog integrated filters is the transconductance amplifier-capacitor, or simply  $G_m\text{-}C$  technique [1]. The main circuit building block of a  $G_m\text{-}C$  integrator, as shown in Fig.6.1, is a linear transconductance cell, which converters the input voltage into an output

current. The output current of the  $G_m$  block and, consequently, the capacitance current, is linearly related to the differential input voltage signal by

$$I_{cap} = G_m V_{in} \quad (6.1)$$

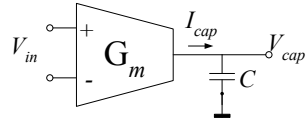


Figure 6.1: A single-ended  $G_m$ -C integrator

This output current is applied to the integrating capacitor,  $C$ , resulting in a voltage across  $C$ , given by

$$V_{cap} = \frac{I_{cap}}{sC} = \frac{G_m V_{in}}{sC} \quad (6.2)$$

which defines the integrator time constant to be  $\tau = C/G_m$ . Besides the linearity, an additional requirement for this transconductance amplifier, in order to be applied in a filter, is that it should have a well-known transconductance value which is not the case, for instance, for an operational-amplifier (Opamp).

As one will see in the next chapter, in the field of medical electronics, active filters with large time constants are often required to design low cutoff-frequency filters (in the Hz and sub-Hz range), necessitating the use of large capacitors or very low transconductances. To limit capacitors to practical values, a transconductor with an extremely small transconductance  $G_m$  (typically a few  $nA/V$ ) is needed. Two very low-frequency transconductor designs, that rely on CMOS transistors operating in the triode region, will be presented here.

### 6.1.1 nA/V CMOS Triode-Transconductor

The transconductor proposed in [2] is based on the use of CMOS transistors operating in the strong-inversion triode region(SI-TR). As shown in [2], transistors kept in the triode region benefit from a lower  $G_m/I_D$  ratio than the ones operating in saturation (active) or weak-inversion regions. This means that, for a certain biased current  $I_D$ , the triode transconductor presents the lowest  $G_m$  value. In addition, triode-based transconductors have better linearity performance than transconductors with transistors operating in saturation.

The triode-transconductor is shown in Fig. 6.2. It should be stated here that in this circuit, not all transistors are in the triode region. Only  $M_{1A}$  and  $M_{1B}$  are biased in the strong-inversion triode region, whereas the other transistors are operating in the weak inversion region.

Input transistors  $M_{1A}-M_{1B}$  have their drain voltages regulated by an auxiliary amplifier that comprises the current conveyer  $M_{2A}-M_{2B}$ ,  $M_{3A}-M_{3B}$  and

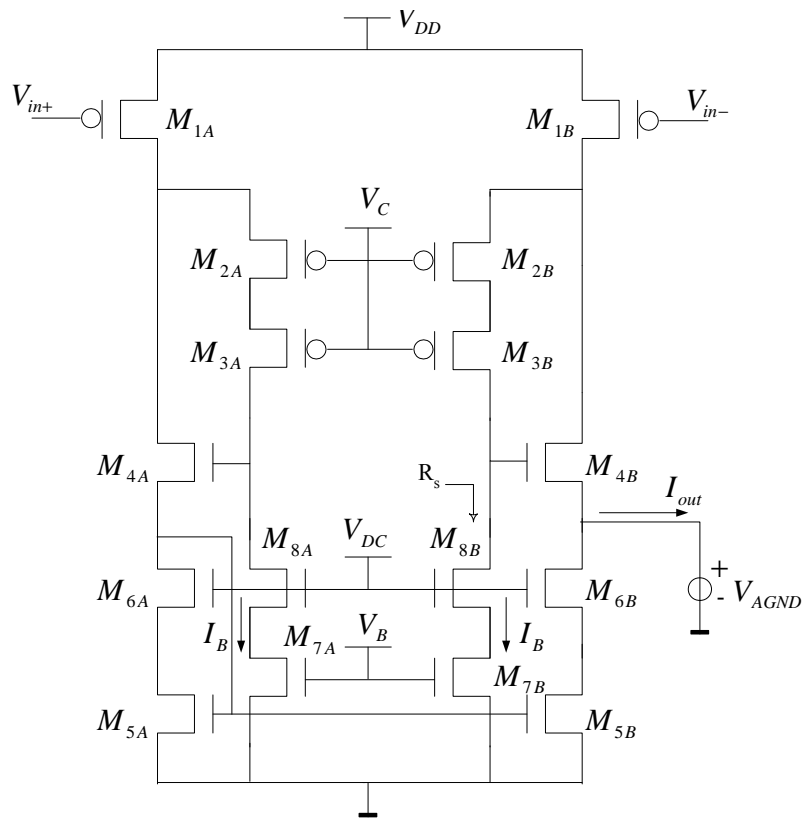
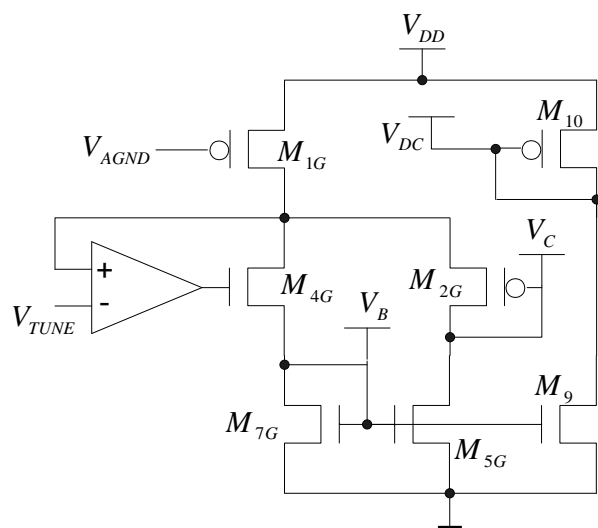
Figure 6.2: Schematic of the  $nA/V$  CMOS triode-transconductor [2]

Figure 6.3: Circuit diagram of the bias generator [2]

$M_{4A}$ - $M_{4B}$ , and bias current sources  $M_{7A}$ - $M_{7B}$  and  $M_{8A}$ - $M_{8B}$ . Internal voltages  $V_B$ ,  $V_C$  and  $V_{DC}$  are derived from the bias circuit shown in Fig.6.3 [Jader]. The bias generator is structurally alike the transconductor so that the external voltage  $V_{TUNE}$  is reflected to the drain of  $M_{1A}$ - $M_{1B}$ . A low voltage cascade current mirror comprising  $M_{5A}$ - $M_{5B}$  and  $M_{6A}$ - $M_{6B}$  provides a single-ended output. Referring  $V_{TUNE}$  to  $V_{DD}$ , one can define the  $G_m$  of the transconductor as

$$G_m = \beta \cdot V_{TUNE} \quad (6.3)$$

with  $\beta = \frac{W}{L} \mu C_{ox}$ . In order to obtain a  $G_m$ -C filter realization using the proposed integrator, we must be able to map the corresponding filter coefficients on the respective  $G_m$  values. From the transconductance definition in Eq.6.3, one can notice that we may vary the value of  $G_m$  by changing the drain-source voltage ( $V_{TUNE}$ ) or, alternatively,  $\beta$  (the aspect ratio  $W/L$ ) of transistor  $M_1$ . In Fig. 6.4 one can see the acquired  $G_m$  values varying from 1nA/V to 5nA/V with  $V_{TUNE}$  changing from 10mV to 50mV, respectively, for a fixed aspect ratio ( $\frac{W}{L} = \frac{0.6\mu m}{240\mu m}$ ) (solid line).

However, due to the additional bias stages required to obtain different filter coefficients, realization of the various  $V_{TUNE}$  bias generators would increase the power consumption by a factor of  $(n - 1) \cdot P_{Bias}$ , where  $n$  is the number of implemented coefficients and  $P_{Bias}$  represents the power consumption of the biasing stage. Hence, from a power consumption perspective, the best choice to obtain the  $G_m$  values is by tuning  $\beta$ . Various values of  $G_m$ , ranging from 1nA/V to 5nA/V are also shown in Fig. 6.4 for  $W_{M1A,M1B}$  linearly varying from  $0.6\mu m$  to  $3\mu m$ , respectively, with  $V_{TUNE}$  equals to 10mV (dashed line).

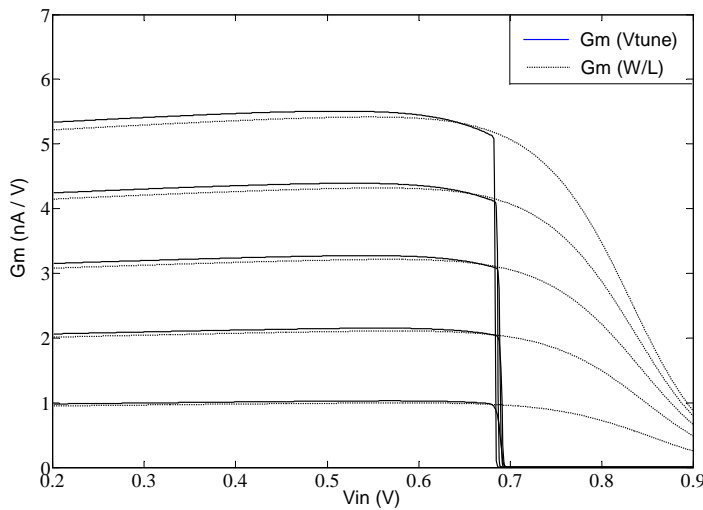


Figure 6.4: Different  $G_m$  values obtained by varying  $V_{TUNE}$  (solid line) or  $W_{M1A,M1B}$  (dashed line)

### 6.1.2 New pA/V Delta-Gm ( $\Delta - G_m$ ) Transconductor

In order to decrease the values of  $G_m$  even further, a new CMOS triode-transconductor design is presented here. The schematic of the pA/V Delta-Gm Transconductor is given in Fig. 6.5.

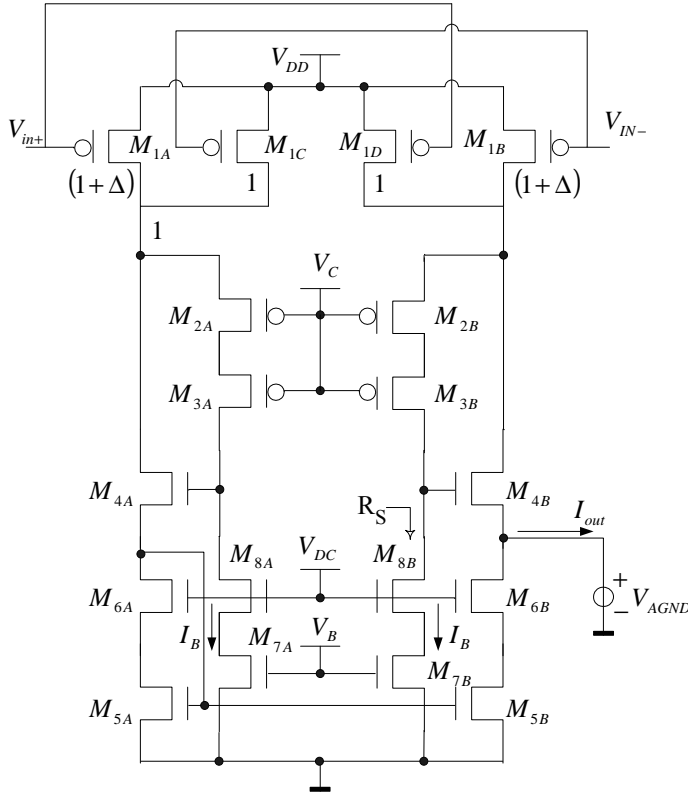


Figure 6.5: Schematic of the  $pA/V$  Delta-Gm Transconductor

The description of the proposed integrator is given as follows. The  $G_{mT}$  of the transconductor is given by

$$G_{mT} = \frac{I_{out}}{V_{in}} \quad (6.4)$$

The current  $I_{out}$  can be defined in terms of the currents flowing through transistors  $M_{1A}$ - $M_{1B}$ - $M_{1C}$ - $M_{1D}$ , resulting in

$$I_{out} = -I_{M1A} - I_{M1C} + I_{M1D} + I_{M1B} \quad (6.5)$$

which can be expressed as

$$I_{out} = G_{m_{M1A}} V_{in+} + G_{m_{M1C}} V_{in-} - G_{m_{M1D}} V_{in+} - G_{m_{M1B}} V_{in-} \quad (6.6)$$

Employing Eq. 6.3 for a transistor operating in strong-inversion triode region and assuming that the aspect ratios of  $M_{1A}$  and  $M_{1B}$  are  $(1 + \Delta)$  times larger than the ones of  $M_{1C}$  and  $M_{1D}$ , we end up with

$$\begin{aligned} I_{out} &= \frac{W(1 + \Delta)}{L} \mu C_{ox} V_{TUNE} V_{in+} + \frac{W}{L} \mu C_{ox} V_{TUNE} V_{in-} \\ &- \frac{W}{L} \mu C_{ox} V_{TUNE} V_{in+} - \frac{W(1 + \Delta)}{L} \mu C_{ox} V_{TUNE} V_{in-} \end{aligned} \quad (6.7)$$

$$= \Delta \frac{W}{L} \mu C_{ox} V_{TUNE} (V_{in+} - V_{in-}) \quad (6.8)$$

Assuming  $V_{in} = V_{in+} - V_{in-}$  and  $\beta = \frac{W}{L} \mu C_{ox}$ , the transconductance of the circuit in Fig. 6.5 is given by

$$G_{m_T} = \Delta \beta V_{TUNE} = \Delta G_m \quad (6.9)$$

where  $G_m$  is the transconductance of the triode-transconductor shown in Fig. 6.2.

In order to verify the circuit principle, we have simulated the new pA/V Delta-Gm transconductor using a standard 0.35μm CMOS technology. The  $G_{m_T}$  values can be seen in Fig. 6.6 with  $\Delta$  varying from 1 to 0.1. As one can see, extremely small values of  $G_{m_T}$  can now be obtained, ranging from 1nA/V up to 100pA/V for a triode-transconductance  $G_m$  equal to 1nA/V.

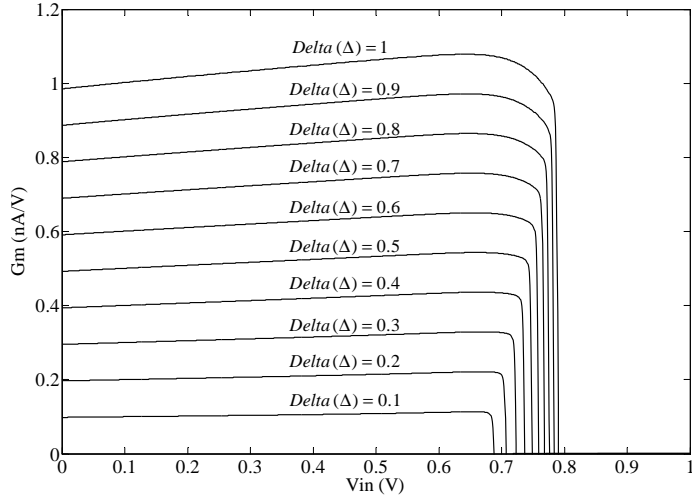


Figure 6.6:  $G_m$  values obtained by varying  $\Delta$  from 0.1 to 1

## 6.2 Translinear (Log-domain) filters

The supply voltage severely restricts the maximum Dynamic Range (DR) achievable using conventional filter implementation techniques, such as opamp-

MOSFET-C, gm-C and switched-capacitor. In addition, since transistors are inherently non-linear transconductors, these techniques require the development of linearization or compensation schemes, usually at the expense of power consumption or bandwidth. The class of translinear (TL) filters has emerged in recent years [3], [4] as a promising approach to face the analog filters' challenges, i.e., lower power consumption, lower supply voltage and higher frequency operation.

The translinear approach is a current-mode technique [5], which is inherently non-linear and performs a compression and an expansion on the processed signal. This property is called the companding (compressing and expanding) principle [4]. The benefit of a companding system is that a signal with certain DR can be processed in a system block with a smaller DR than the signal, and by this, offer low-voltage and low-power operation.

Translinear circuits [6], [7], also known as Log-domain [8], Externally Linear Internally Nonlinear systems (ELIN) [9] or Exponential-State Space (ESS) [10] circuits, exploit the exponential large-signal transfer function of the semiconductor devices to implement a desired linear or nonlinear differential equation, which will be explained below.

### 6.2.1 Static and Dynamic Translinear principle

Translinear circuits are based on the exponential relation between voltage and current, a characteristic for any device whose operation is dominated by minority carries, such as diodes, bipolar transistors and MOS transistors operating in the weak inversion region. They can be divided into Static and Dynamic Translinear circuits.

Static Translinear (STL) circuits are implemented to realize any static transfer function. Their principle applies to loops of semiconductor junctions [5]. A TL loop is characterized by an even number of junctions. The number of devices with a clockwise orientation equals the number of counterclockwise oriented devices. An example of a four-PN junction TL loop is shown in Fig. 6.7. The STL principle states that this circuit can be best described in terms of the collector currents  $I_1$  through  $I_4$ . The translinear loop is thus described by a simple equation in terms of products of currents, being

$$I_1 I_3 = I_2 I_4 \quad (6.10)$$

Linear or nonlinear dynamic, i.e., frequency-dependent, functions (differential equations) can be implemented by Dynamic Translinear (DTL) circuits. The DTL principle is shown in the sub-circuit in Fig.6.8 [11].

This circuit is described in terms of the output current  $I_{out}$  of the exponential device and the capacitance  $I_{cap}$  flowing through the capacitance C.

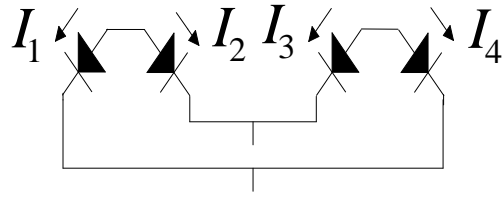


Figure 6.7: A four-PN junction translinear loop

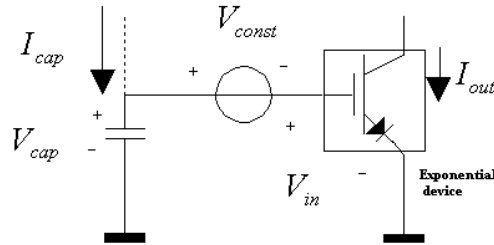


Figure 6.8: Principle of dynamic translinear circuits

Note that the dc voltage source  $V_{const}$  does not affect  $I_{cap}$ .  $I_{out}$  is based on the exponential law and can thus be described by:

$$I_c = I_s e^{\frac{V_{cap}}{V_T}} \quad (6.11)$$

$V_{cap}$ ,  $I_s$ ,  $V_T$  being the capacitance voltage, a specific current and a specific voltage respectively. An expression for  $I_{cap}$  can be derived from the time derivative of the output current:

$$CV_T \dot{I}_{out} = I_{cap} I_{out} \quad (6.12)$$

where the dot represents differentiation with respect to time. This expression defines the principle of dynamic translinear circuits: “A time derivative of a current can be mapped onto a product of currents.” For the realization of this product of currents the conventional static translinear principle can be used. Using dynamic translinear circuits, several classes of filters have been proposed [5, 6]. The characteristics of these classes can be derived from their output structures. Strictly speaking, the class of log-domain filters is based on a single-transistor output structure in line with Fig.6.8. Nevertheless, other output stages can be used to implement non-linear differential equations, e.g., the ones that belong to oscillators [12] and RMS-DC converters [4].

### 6.2.2 Log-domain integrator

Electronics circuits map mathematical operations onto silicon. In order to accomplish this, the mathematical equations (in case of filters, differential

equations) should be transformed into a set of electrical equations, which represent voltage or current relations. In log-domain circuits the mathematical input and output variables are related linearly to currents (current mode operation), whereas the relation between the state variables and the capacitance voltages has a logarithmic character. However, by proper use of the correspondence relation, the linearity of the overall transfer function of the system can be maintained.

A typical log-domain integrator can be characterized by the diode-capacitance circuit in Fig.6.9a and the corresponding block diagram is given by Fig.6.9b [17].

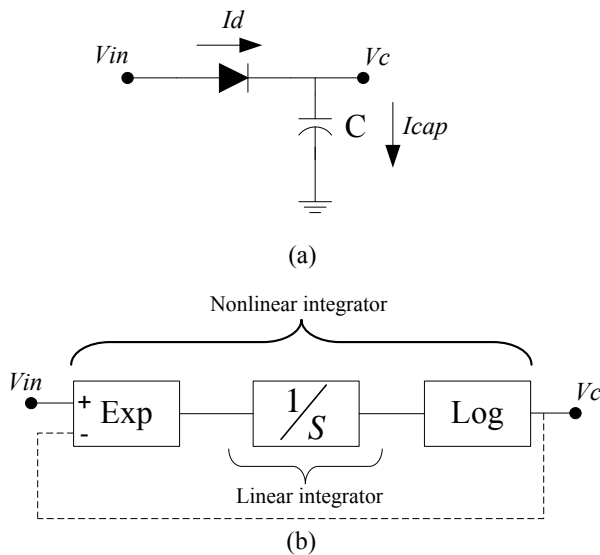


Figure 6.9: (a) Typical representation of the log-domain integrator (b) Corresponding block diagram

The capacitance current  $I_{cap}$  can be expressed in terms of the voltages  $V_{in}$  and  $V_C$ , which obeys the exponential law of the device (in this case, the diode)

$$I_{cap} = I_d = CV_C = I_s e^{\frac{V_{in}-V_C}{V_T}} \quad (6.13)$$

where  $I_s$  is the reverse saturation current and assuming that the capacitor is not loaded and  $I_{cap} = I_d$ . From the basic log-domain equation presented above, one can notice that such an integrator is inherently nonlinear. Then, in order to maintain the overall linearity of the log domain system, an input current signal is converted into a voltage by a logarithmic converter (typically, a bipolar transistor), and is then processed internally by the nonlinear integrator before it is converted into an output current signal by an exponential converter (another bipolar transistor). The block diagram of a linear log-domain filter is illustrated in Fig.6.10.

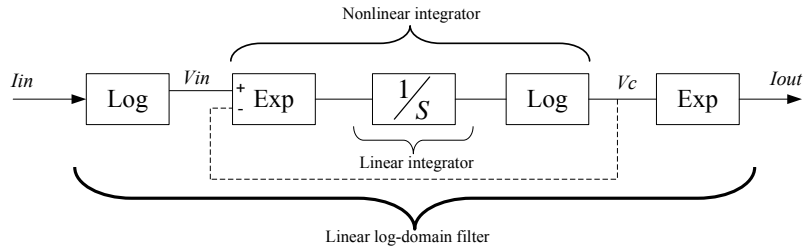


Figure 6.10: Linear Log-domain filter block diagram

One can see the linearity of the expression of the log-domain filter applying  $V_{in} = V_T \ln\left(\frac{I_{in}}{I_s}\right)$  and  $V_C = V_T \ln\left(\frac{I_{out}}{I_s}\right)$  into Eq.6.13

$$CV_T \frac{d}{dt} \left[ \ln \left( \frac{I_{out}}{I_s} \right) \right] = I_s \frac{e^{\ln(\frac{I_{in}}{I_s})}}{e^{\ln(\frac{I_{out}}{I_s})}} \Rightarrow CV_T \dot{I}_{out} = I_{in} \quad (6.14)$$

which represents a first-order linear differential equation in current domain.

From a circuit design perspective, the most simple implementation of a first-order log-domain filter is given by the combination of the static and the dynamic translinear loops, shown in Fig.6.7 and Fig.6.8, respectively. A bipolar filter implementation is given in Fig.6.11. According to the STL principle, the products of the currents of forward biased junctions in the clockwise and counter-clockwise oriented devices are equal. Hence

$$I_1 I_3 = I_2 I_4 \Rightarrow I_{in} I_o = (I_o + I_{cap}) I_{out}. \quad (6.15)$$

The DTL loop equation, defined by the capacitor and transistor  $Q_4$ , is given by

$$I_{cap} I_{out} = CV_T \dot{I}_{out}. \quad (6.16)$$

Using Eq.6.15 and Eq.6.16, this yields

$$CV_T \dot{I}_{out} + I_o I_{out} = I_o I_{in} \quad (6.17)$$

which is a linear differential equation, describing a low-pass filter with cutoff frequency  $\omega_c$  according to

$$\omega_c = \frac{I_o}{CV_T}. \quad (6.18)$$

In the next sections, we will present some log-domain integrator designs, which are suitable for high frequency and/or low-power low voltage applications.

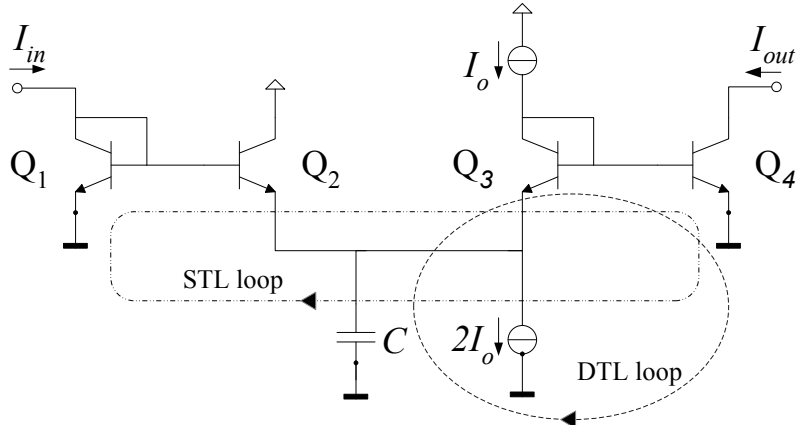


Figure 6.11: First-order low-pass log-domain filter

### 6.3 Class-A log-domain filter design examples

Under class-A operation, the collector currents of the transistors in the log-domain filter have to be strictly positive for the transistor to work in the active exponential region. Consequently, the ac signal has to be superimposed on a dc bias current  $I_o$ . That is, for a correct operation of the input and output filter stages without clipping distortion, the relation  $I_{in}, I_{out} > -I_o$  has to be satisfied at all times.

A few class-A log-domain integrator design examples will be presented here.

#### 6.3.1 Bipolar multiple-input log-domain integrator

One example of an low-power log-domain integrator is given in Fig.?? [15], which represents a bipolar multiple-input log-domain integrator.

A pair of log-domain cells with opposite polarities and an integrating capacitor form the core of the integrator.  $V_{ip}$  and  $V_{in}$  are the noninverting and inverting input voltages, respectively, and the input currents are  $I_{ip}$  and  $I_{in}$ , which are superimposed on the dc bias currents. The output voltage  $V_o$  is given by the voltage across the capacitor. The circuit is composed of two identical log-domains cells, a voltage buffer, and a current mirror. The log-domain cells  $Q_1-Q_2$  and  $Q_3-Q_4$  generate the log-domain currents  $I_{c2}$  and  $I_{c4}$ , respectively. A voltage buffer realized by  $Q_5-Q_6$  is inserted between them. Therefore, the output log-domain voltage  $V_o$  at the emitter of  $Q_2$  also appears at the emitter of  $Q_4$ . Finally, to obtain a log-domain integrator equation, a current mirror  $Q_7-Q_8$  is used to realize the difference between the two log-domain currents on the capacitor node. The connection from the bases of transistors  $Q_7$  and  $Q_8$  to the collector of  $Q_6$  closes the feedback loop around  $Q_6$  and  $Q_7$ . This connection is convenient because it ensures that the overall voltage headroom

is minimized. The equation that relates the input and output voltages to the current flowing in the integrating capacitor becomes

$$C_i \frac{dV_o}{dt} = (I_o + I_{ip}) e^{\frac{V_{ip}-V_o}{V_T}} - (I_o + I_{in}) e^{\frac{V_{in}-V_o}{V_T}} \quad (6.19)$$

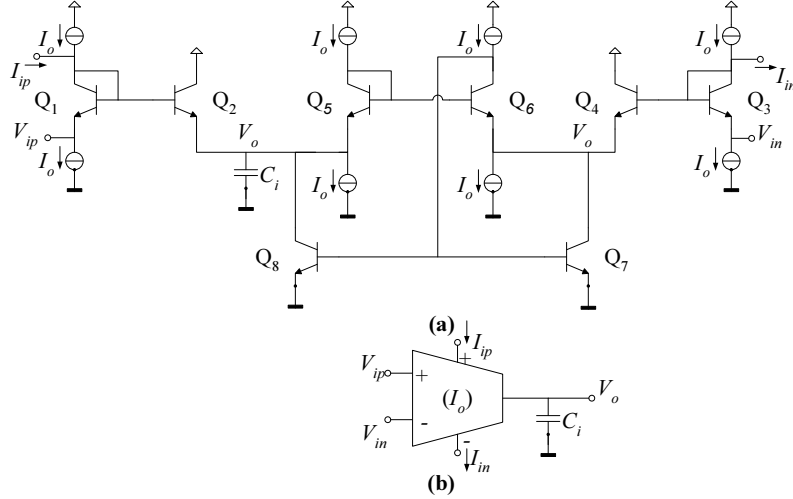


Figure 6.12: (a) The multiple-input low power log-domain integrator, and (b) its symbol [15]

Notice that the input and output voltages of the integrator are at the same dc level. Therefore log-domain filter synthesis can easily be achieved by direct coupling of these integrators.

### 6.3.2 CMOS multiple-input log-domain integrator

Log-domain filters can also be implemented using MOS transistors biased in weak inversion (WI) in order to preserve the exponential I-V characteristic required by the log-domain companding principle. MOS transistors do not suffer from the base current drawback of bipolar transistors. On the other hand, maintaining the transistors biased in weak inversion usually requires large devices and results in frequency limitations. The CMOS integrator proposed in [16] is given in Fig.6.13.

Note that the relation between the input and output voltages and the capacitance current is also given by Eq.6.19. In the previous implementation shown in Fig.6.12, the integration capacitor is connected to the emitter (or source for MOS in WI) of a transistor. In this way, the capacitor is charged/discharged by a current which is exponentially dependent on the capacitor voltage, representing an inherent feedback. In the implementation in Fig.6.13, the same feedback is accomplished by connecting the capacitor to the drain of the exponential transconductors,  $M_2$  and  $M_3$ , while the capacitance

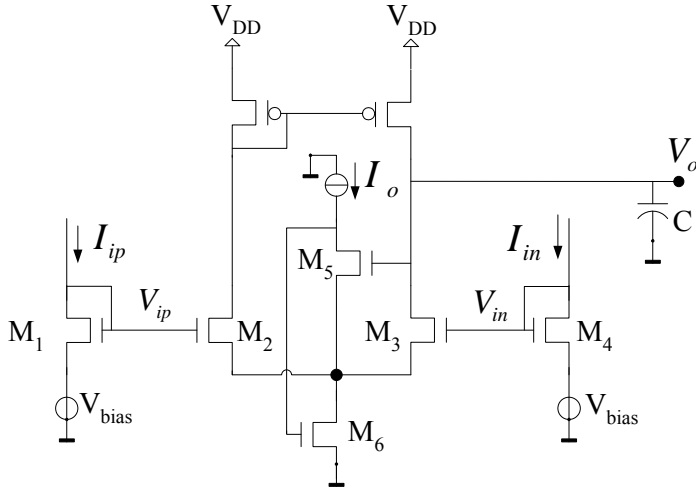


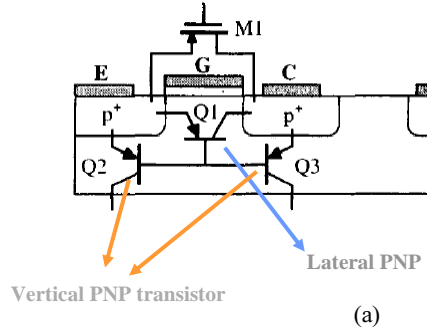
Figure 6.13: Inverting and noninverting Class-A CMOS log-domain integrator [16]

voltage is sensed at their source through the adjustable level shifter made of current source  $I_o$  and transistors  $M_3$  and  $M_5$ . The capacitor is now discharged by the drain current of transistor  $M_3$  and charged by the drain current of  $M_2$  through the current mirror  $M_7$ - $M_8$ .

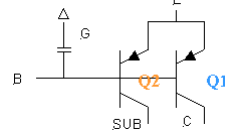
### 6.3.3 New high-frequency log-domain integrator in CMOS technology

Usually, only active devices are used to implement translinear circuits, being bipolar transistors [17], MOS transistors in the weak inversion region [18] or lateral bipolar transistors in standard CMOS technology [19].

Due to low-cost fabrication process, efforts have been taken to extend the log-domain approach from bipolar to CMOS technology. In addition to the economic reasons, MOS transistors do not suffer from the base current drawback of bipolar transistors. The exponential dependence of the drain current upon the gate-source voltage in subthreshold operation may suggest the use of MOS devices in DTL circuits. However, since such conditions are met by only a large device width or low current density, the speed of subthreshold circuits is severely limited. The same high frequency limitation holds for lateral bipolar transistors in standard CMOS technology [19]. An alternative topology to implement DTL and Log-domain circuits, which improves the high-frequency performance, is proposed here [20]. It is based on the exponential relation between voltage and current of passive PN-diodes (diode connection of lateral PNP transistor in CMOS technology), shown in Fig.6.14, and uses the CMOS transistor only to provide gain, in accordance with the original idea proposed by Adams [3].



(a)



(b)

Figure 6.14: (a) CMOS process cross section [Duerden et al., ISCAS 2001] (b) Schematic representation of PNP transistors

The earliest log-domain filter as proposed by Adams, 1979, lends itself to be implemented in any CMOS IC technology and does not require exponential behavior of the CMOS transistors. See Fig. 6.15. The circuit is a first-order low-pass filter. The analysis of this circuit is given below.

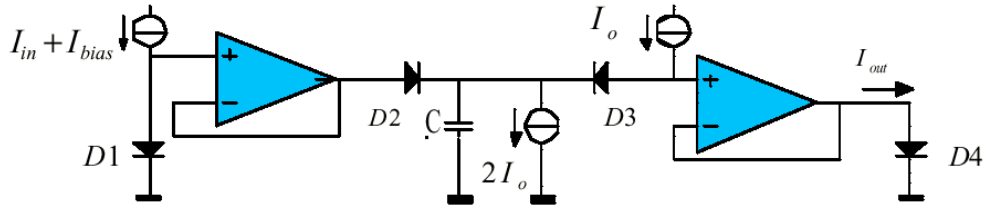


Figure 6.15: Adams' low-pass log-domain filter

The four (exponential) diodes,  $D_1-D_4$ , constitute a TL loop. The combination of the capacitor C, the right voltage follower (an opamp in unity-gain configuration) and diode D4 is similar to the output sub-circuit shown in Fig. 1. Diode D3 is biased by a dc current  $I_o$  and therefore complies with a constant voltage source. The output current flows through diode D4. The current through D2 equals  $(I_o + I_{cap})$  and the input current, together with biasing current  $I_{bias}$ , flows through diode D1. According to the TL principle,

the products of the currents of forward biased junctions in the clockwise and counter-clockwise oriented devices are equal. Hence:

$$(I_{bias} + I_{in})I_o = (I_o + I_{cap})(I_{dc} + I_{out}) \quad (6.20)$$

Using 6.16 and 6.20, this yields:

$$CV_T \dot{I}_{out} + I_o I_{out} = I_o I_{in} \quad (6.21)$$

which represents the linear differential equation of a low-pass filter.

### Voltage follower

The main requirements of the voltage followers that are employed in the circuit of Fig.6.15 are high-frequency response, low gain error, high linearity and a sufficiently low output resistance. The proposed voltage follower, to be implemented in CMOS technology, is based on a symmetrical structure of a two-stage topology [21]. Compared to single-stage topologies, two-stage topologies increase the loop gain and therefore decrease the output impedance of the circuit. The characteristics of this particular circuit are a nominally zero systematic offset and highly reduced harmonic distortion and transfer gain error.

The two-stage topology adopts the Miller compensation technique to achieve stability in closed-loop conditions. However, such compensation also results in a right half-plane zero in the open-loop gain, due to the forward path through the compensation capacitor to the output. The right half-plane zero reduces the maximum achievable gain-bandwidth product, since it makes a negative phase contribution to the open-loop gain at a relatively high frequency. An optimized compensation strategy is based on the use of a voltage follower [22]. It efficiently uses the finite output conductance of a voltage buffer to provide pole-zero compensation, thus allowing a great increase in the loopgainpoles [23] product to be achieved. The voltage buffer is implemented with the common-drain configuration shown in Fig. 6.16.

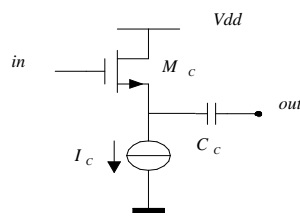


Figure 6.16: Voltage buffer for frequency compensation

The circuit diagram of the voltage follower is depicted in Fig.6.17. M1 and M2 form the source-coupled pair of the differential stage. M3 and M4 are both diode-connected to improve the symmetry of the topology. Transistors M5

and M6 enhance the overall loop gain while maintaining identical source-drain voltage drops across transistors M7 and M8. Transistors M7-M14 implement the bias circuit. M13 is employed to obtain a good matching between p-channel and n-channel current sources. Finally, transistor M15 is used for the frequency compensation as described above. M1-M4 and M5-M9 have the same aspect ratios respectively.

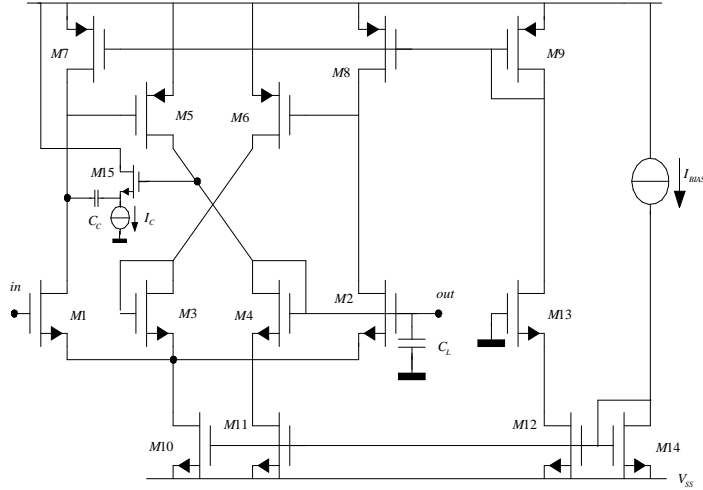


Figure 6.17: Circuit diagram of the voltage follower

### Simulation results

The circuit was simulated using PSPICE transistor and diode models of the  $0.35\text{ }\mu\text{m}$  CMOS Si-gate AMS IC process. The filter has been designed to operate from a 3.3-V supply. Bias current  $I_o$  ranges from 50nA to 0.5mA.

Fig.6.18 depicts the cut-off frequency as a function of current  $I_o$  for four different capacitance (C) values: 100 fF, 1 pF, 10 pF and 100 pF.

From this plot, it can be deduced that this filter can be controlled over a wide frequency range. Also indicated is that the filter exhibits less than 1% THD for a capacitance equal to 10 pF for a 316 kHz input signal and 2.4% THD for a capacitance equal to 100 fF at 100 MHz. The cut-off frequency for  $I_o = 50\mu\text{A}$  and  $C = 100\text{ fF}$  equals 222 MHz. Note that this circuit exhibits a better high-frequency performance than the circuit presented in [3] which yields a cut-off frequency below 30 MHz.

The AC response of the low-pass filter with  $I_o$  equal to 5 nA, 50 nA,  $0.5\mu\text{A}$ ,  $5\mu\text{A}$  and  $50\mu\text{A}$ , respectively, and C equal to 10pF is shown in Fig.6.19. The cut-off frequencies of these filter responses are 3.13 kHz, 31.6 kHz, 316.2 kHz, 3.10 MHz and 31.62 MHz, respectively.

Note that either lossless or inverting lossy integrators can be realized by adding appropriate unity-gain positive feedback or applying current mirrors respectively.

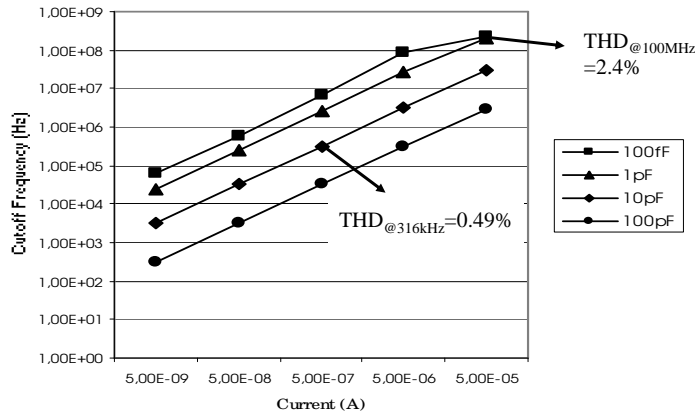


Figure 6.18: Simulated cut-off frequency as a function of current  $I_o$  for five different capacitor values.

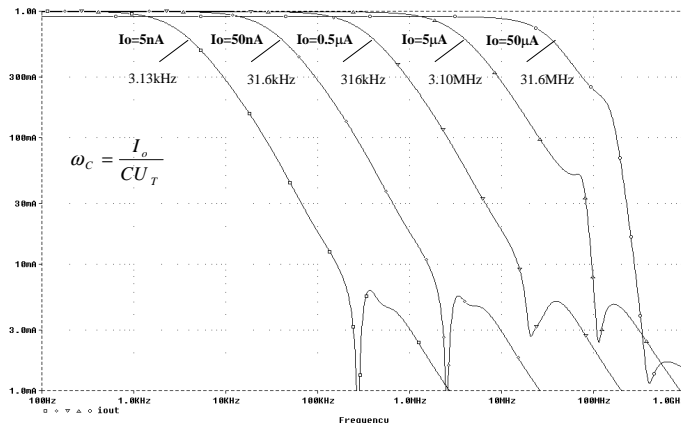


Figure 6.19: Simulated log domain filter response with  $C = 10\text{pF}$ .

As was mentioned before, using the companding principle one can design analog integrated circuits with higher Dynamic Range compared to conventional circuit design techniques. Moreover, the Dynamic Range of low-voltage companding analog circuits can further be extended using Class-AB current-mode based circuit topologies, which will be discussed in the next section.

## 6.4 Low-power Class-AB *Sinh* Integrators

Class AB circuit design is an efficient approach to matching the requirements of good linearity, low noise contribution and low power consumption. In a Class-AB topology the quiescent bias levels in the active devices are set at relatively low levels, usually much lower than the expected signal swings. Consequently, for small signals the circuit operates in Class-A and for large signal swings

operates with the efficiency of a Class-B design. This results in a higher Dynamic Range (DR) compared to conventional Class-A operation together with an improvement in power efficiency.

In log-domain filters operating in class A, the currents are limited by  $I_{in}, I_{out} > -I_o$ . This means that the restriction in current-mode circuits is only single-sided. Hence, the combination of the companding circuit technique and Class-AB operation enables us to obtain more power-efficient analog signal processing where the DR can be extended without increasing the maximum SNR or the quiescent power consumption.

The hyperbolic-sine (*Sinh*) function is at the base of most of the Class-AB translinear filters. Instead of a single transistor in common-emitter configuration as for class A integrators, the class-AB sinh filter is characterized by hyperbolic-sine transconductors, as described in the following sections.

#### 6.4.1 A State-Space formulation for Class-AB Log-domain integrator

In [24], a general state-space description for a *sinh* filter has been proposed. The formulation consists of the hyperbolic sine mapping on the state variable. As an example, consider a first-order lowpass state-space description

$$\begin{aligned}\dot{x} &= -\omega_0 x + \omega_0 u \\ y &= x\end{aligned}\tag{6.22}$$

Applying the state variable mapping, the state-space variables can now be expressed as

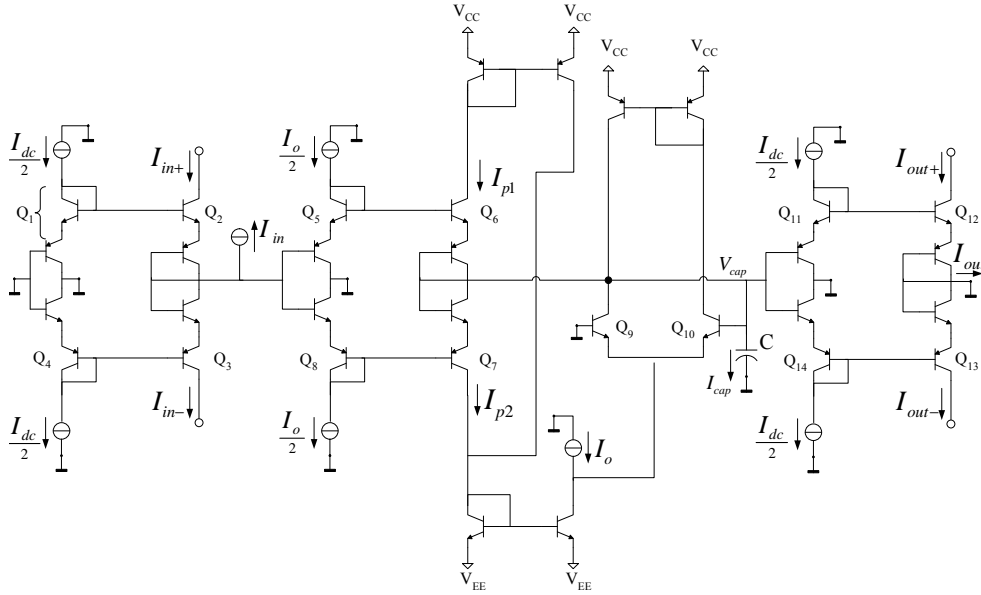
$$\begin{aligned}x &= 2CV_T \sinh(V_{cap}/2V_T) \\ u &= 2CV_T \sinh(V_{in}/2V_T)\end{aligned}\tag{6.23}$$

resulting in the externally linear internally nonlinear system defined by

$$\begin{aligned}C\dot{V}_{cap} &= 2CV_T \omega_0 \{\cosh(V_{in} - V_{cap})/2V_T] - 1\} \tanh(V_{cap}/2V_T) \\ &\quad + 2CV_T \omega_0 \sinh[(V_{in} - V_{cap})/2V_T] \\ I_{out} &= 2CV_T \sinh(V_{cap}/2V_T)\end{aligned}\tag{6.24}$$

The circuit which realizes this state-space representation is shown in Fig. 6.20. The corresponding mapping contains compound transistors in order to implement the *tanh* function.

The analysis of this first-order low-pass filter consists of 5 static and 1 dynamic fundamental translinear loops, given by

Figure 6.20: Class-AB *Sinh* low-pass filter [24]

STL:

$$I_{Q2}I_{Q3} = I_{Q1}I_{Q4} \Rightarrow I_{in+}I_{in-} = I_{dc}/4 \quad (6.25)$$

$$I_{Q6}I_{Q7} = I_{Q5}I_{Q8} \Rightarrow I_{p1}I_{p2} = I_o^2/4 \quad (6.26)$$

$$I_{Q12}I_{Q13} = I_{Q11}I_{Q14} \Rightarrow I_{out+}I_{out-} = I_{dc}/4 \quad (6.27)$$

$$I_{Q2}I_{Q6}I_{Q12} = I_{Q1}I_{Q5}I_{Q11} \Rightarrow 8I_{in+}I_{p1}I_{out+} = I_oI_{dc}^2/4 \quad (6.28)$$

$$I_{Q9}I_{Q12}I_{Q12} = I_{Q10}I_{Q11}I_{Q11} \Rightarrow 4I_9I_{out+}^2 = I_{10}I_{dc}^2 \quad (6.29)$$

DTL:

$$I_{cap} = 2CV_T \frac{\dot{I}_{out+}}{I_{out+}} \quad (6.30)$$

where the dot represents differentiation with respect to time. It is interesting to notice that the corresponding loops in 6.25, 6.26 and 6.27 are geometric mean TL loop equations and the loop defined by 6.29 contains both compound transistors,  $Q_{11}$  and  $Q_{12}$ , and single bipolar transistors,  $Q_9$  and  $Q_{10}$ .

Thus, for the differential pairs, the currents  $I_{Q11}$  and  $I_{Q12}$  can be defined and is given by

$$I_9 = \frac{1}{2}(2I_{p1} - I_o - I_{cap}) \quad (6.31)$$

$$I_{10} = \frac{1}{2}(2I_{p2} - I_o + I_{cap}) \quad (6.32)$$

And from relations 6.25-6.28 we can define  $I_{p1}$  and  $I_{p2}$  in terms of  $I_{in+}$ ,  $I_{in-}$ ,  $I_{out+}$  and  $I_{out-}$ , which yields

$$I_{p1} = \frac{I_o I_{dc}^2}{8I_{in+} I_{out+}} \quad (6.33)$$

$$I_{p2} = \frac{I_o I_{dc}^2}{8I_{in-} I_{out-}} \quad (6.34)$$

Then, applying these equations into 6.31-6.32 we can also represent  $I_9$  and  $I_{10}$  in terms of the input and output currents, and replacing these values in 6.29, we finally end up with the linear differential equation representing the low-pass filter

$$I_{in} = I_{out} + \frac{2CV_T}{I_o} \dot{I}_{out} \quad (6.35)$$

#### 6.4.2 New Class-AB *Sinh* integrator based on State-Space formulation using single transistors

The circuit shown in Fig.6.20 contains compound and single transistors. In order to have the TL loops with only single transistors, a new structure for the Class-AB *Sinh* lossy integrator is presented here. The schematic is shown in Fig.6.21.

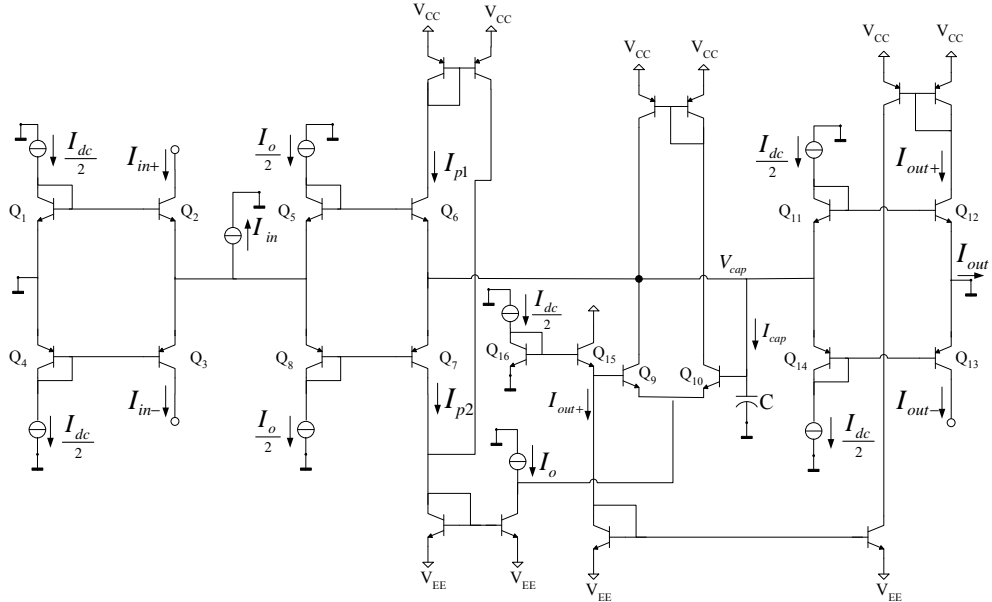


Figure 6.21: New Class-AB *Sinh* low-pass filter

The proposed integrator consists of three hyperbolic-sine transconductors,  $Q_1 - Q_4$ ,  $Q_5 - Q_8$  and  $Q_{11} - Q_{14}$ , two static TL loops comprising transistors  $Q_{16} - Q_{15} - Q_9 - Q_{10} - Q_{11} - Q_{12}$  and  $Q_1 - Q_2 - Q_5 - Q_6 - Q_{11} - Q_{12}$  and one

dynamic TL loop  $C - Q_{11} - Q_{12}$ . The translinear analysis of the new integrator is the same as the one presented in Section 6.4.1. As one can see, in order to implement Eq.6.29, the transistors  $Q_{15}$  and  $Q_{16}$  have been introduced.

To validate the correct mapping of the equations, we have implemented the lossy integrator using quasi-ideal exponential devices, i.e. bipolar transistors with very large current gain ( $\beta = 10^6$ ). The transient responses of the input currents ( $I_{in+}$  and  $I_{in-}$ ) and the output current ( $I_{out}$ ); the capacitance current  $I_{cap}$  and the intermediate currents  $I_{p1} - I_9$  and  $I_{p2} - I_{10}$  are given in Fig.6.22a and Fig.6.22b, respectively, showing the correct mapping of the equations presented in previous section. Note that from Eq.6.31 and Eq.6.32, we have

$$I_{p1} - I_9 = \frac{1}{2}(I_o + I_{cap}) \quad (6.36)$$

$$I_{p2} - I_{10} = \frac{1}{2}(I_o - I_{cap}) \quad (6.37)$$

which corresponds to the waveforms shown in Fig.6.22b.

As one can see, the generic state-space formulation for *sinh* integrators is quite abstract and does not provide much insight into the operation of these filters. Due to this fact, we will present in the next sections other approaches for *sinh* filter design which are much easier to apply to both the synthesis and analysis of Class-AB filters.

### 6.4.3 Companding *Sinh* Integrator

The design proposed in [25]] is based on the general block diagram of a companding integrator, defined by Seevinck [4].

The block diagram of a companding *sinh* integrator is given in Fig.6.23. It consists of a divider, a linear time integrator, a hyperbolic-sine expander block that generates the output current  $I_{out}$  from the internal capacitance voltage  $V_{cap}$ ,  $I_{out} = \sinh(V_{cap})$ , and a hyperbolic-cosine block that generates the derivative of the output signal  $I_{out}$  with respect to  $V_{cap}$ ,  $I_{cosh} = \frac{d\sinh(V_{cap})}{dV_{cap}} = \cosh(V_{cap})$ .

From the block diagram given in Fig.6.23, one can see that the capacitance current can be defined as

$$I_{cap} = \frac{I_{in}}{I_{cosh}} \quad (6.38)$$

The V-I transfer function of the *sinh* output structure, is described by

$$I_{out} = 2I_o \sinh\left(\frac{V_{cap}}{V_T}\right) = I_o e^{\frac{V_{cap}}{V_T}} - I_o e^{-\frac{V_{cap}}{V_T}}. \quad (6.39)$$

Despite the nonlinear relations of the output current to the capacitance voltage and the capacitance current to the input current, the integrator can be

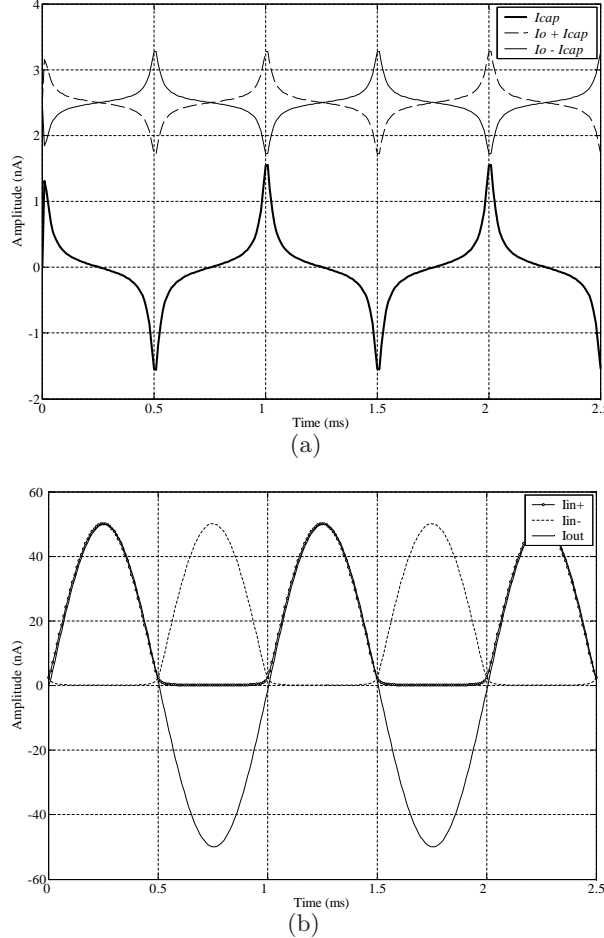


Figure 6.22: Transient response of the New Class-AB *Sinh* integrator based on State-Space formulation ,(a) ( $I_{in+}$ ,  $I_{in-}$ ) and ( $I_{out}$ ), (b)  $I_{cap}$ ,  $I_{p1} - I_9$  and  $I_{p2} - I_{10}$

considered to be an implementation of a first-order linear differential equation  $I_{in} = dI_{out}/dt$  by applying the chain rule

$$I_{in} = I_{cap} \cdot I_{cosh} = C \cdot \frac{dV_{cap}}{dt} \cdot \frac{dsinh(V_{cap})}{dV_{cap}} \Rightarrow I_{in} = C \cdot \frac{dI_{out}}{dt}. \quad (6.40)$$

### Circuit design

To implement the companding integrator presented in Fig.6.23, a class-AB sinh integrator has been proposed in [25]. The basic schematic is shown in Fig. 6.24.

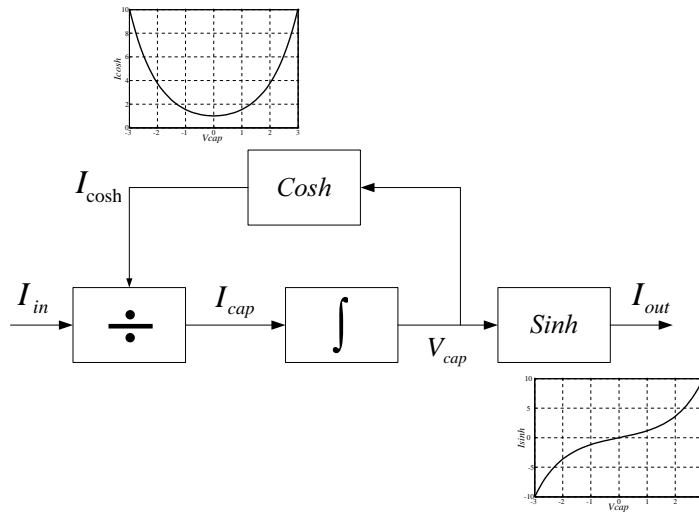


Figure 6.23: Block diagram of the companding sinh integrator

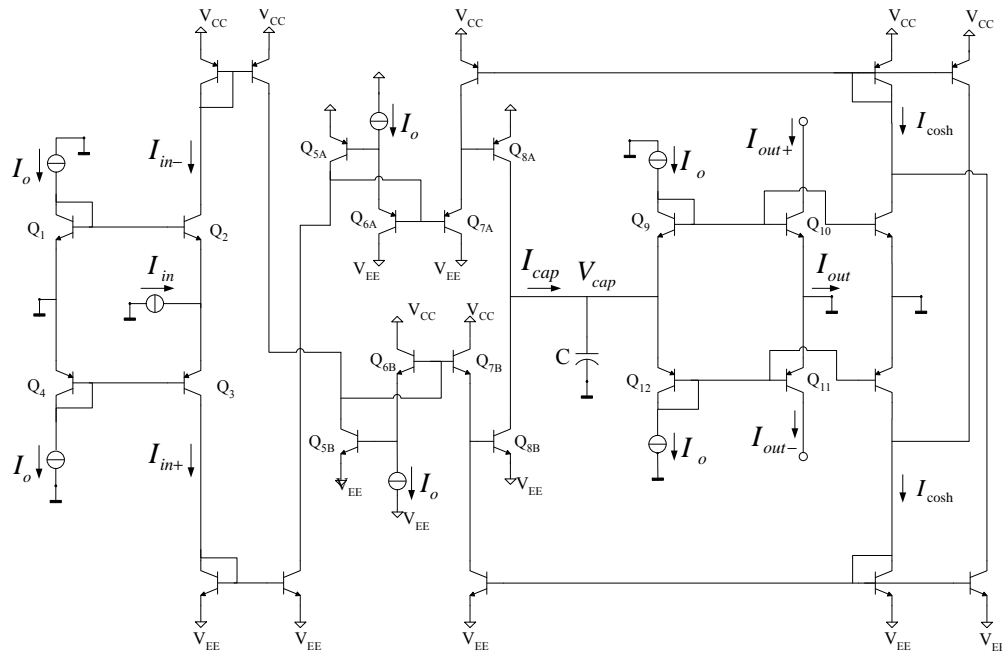


Figure 6.24: Schematic of the lossless sinh integrator [25]

The translinear analysis of this circuit is quite simple. First, a current splitter is required to split the input current  $I_{in}$  into two parts,  $I_{in+}$  and  $I_{in-}$ , both strictly positive, such that

$$I_{in} = I_{in+} - I_{in-} \quad (6.41)$$

The current splitter comprising transistors  $Q_1$  through  $Q_4$  is a geometric-mean current splitter, and implements the function

$$I_{Q2}I_{Q3} = I_{Q1}I_{Q4} \Rightarrow I_{in+}I_{in-} = I_{dc}^2 \quad (6.42)$$

The dividers for both positive and negative inputs are given by the translinear loops  $Q_{5A} - Q_{6A} - Q_{7A} - Q_{8A}$  and  $Q_{5B} - Q_{6B} - Q_{7B} - Q_{8B}$  respectively, which yields

$$I_{5A}I_{6A} = I_{7A}I_{8A} \Rightarrow (I_{in+})I_o = (I_{out+} + I_{out-})I_{8A} \quad (6.43)$$

$$I_{5B}I_{6B} = I_{7B}I_{8B} \Rightarrow (I_{in-})I_o = (I_{out+} + I_{out-})I_{8B} \quad (6.44)$$

The current flowing through the capacitor is given by

$$I_{cap} = I_{8A} - I_{8B} \quad (6.45)$$

In addition, from the DTL loops, the capacitance current can be related to the output currents by

$$I_{cap} = CV_T \frac{\dot{I}_{out+}}{I_{out+}} = -CV_T \frac{\dot{I}_{out-}}{I_{out-}} \quad (6.46)$$

Finally, applying 6.41, 6.43, 6.44 and 6.46 into 6.45 and considering a *Sinh* output stage which implements  $I_{out} = I_{out+} - I_{out-}$ , we end up with

$$I_o I_{in} = CV_T \dot{I}_{out} \quad (6.47)$$

which represents a linear lossless integrator. Note that applying a unity-feedback path from the output to the input, one can obtain a lossy integrator configuration.

#### 6.4.4 New Ultra Low-power Class-AB *Sinh* Integrator

To implement the companding integrator presented in Fig.6.23, we propose a new ultra low-power Class-AB *sinh* integrator. The schematic of the completed integrator is given in Fig.6.25.

Instead of a single transistor in common-emitter configuration in class A integrators, the class-AB *sinh* filter is characterized by hyperbolic-sine transconductors.

One can analyze the new *sinh* integrator in terms of Translinear Loops (TL). As seen from Fig. 6.25, the integrator consists mainly of 3 *sinh* transconductors, defined from the translinear loops  $Q_{1A} - Q_{2A} - Q_{2B} - Q_{1B}$ ,  $Q_{3A} - Q_{4A} - Q_{4B} - Q_{3B}$  and  $Q_{5A} - Q_{6A} - Q_{6B} - Q_{5B}$ , which implement the current splitter, the divider-Cosh block and the Sinh output stage, respectively.

At the output, the relation between  $I_{out}$ ,  $I_{out+}$  and  $I_{out-}$ , defined from the Sinh output stage  $Q_{5A} - Q_{6A} - Q_{6B} - Q_{5B}$ , is described by

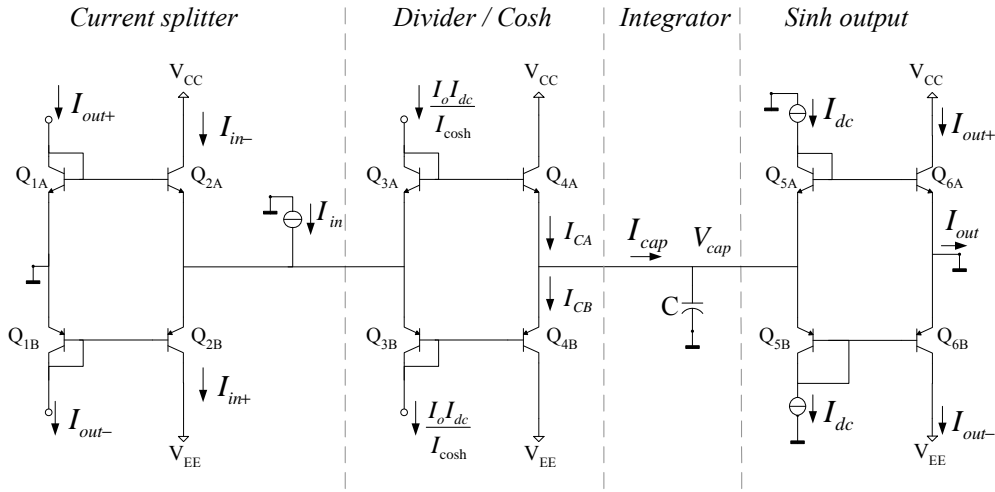


Figure 6.25: Circuit diagram of the proposed class-AB sinh integrator

$$I_{out} = I_{out+} - I_{out-} \quad (6.48)$$

$$I_{out+} \cdot I_{out-} = I_{dc}^2. \quad (6.49)$$

The current splitter comprising transistors  $Q_{1A}$  through  $Q_{1B}$ , which is a geometric-mean current splitter, implements

$$I_{in} = I_{in+} - I_{in-} \quad (6.50)$$

$$I_{in+} \cdot I_{in-} = I_{out+} \cdot I_{out-} = I_{dc}^2. \quad (6.51)$$

In addition, the third *sinh* transconductor  $Q_{3A} - Q_{4A} - Q_{4B} - Q_{3B}$  realizes the divider-Cosh block, thus defining the correct non-linear current through the capacitor to obtain a global linearization, i.e., an externally linear transfer function. The currents  $I_{CA}$ ,  $I_{CB}$  and  $I_{cap}$  are given by

$$I_{cap} = I_{CA} - I_{CB} \quad (6.52)$$

$$I_{CA} \cdot I_{CB} = \frac{I_{dc} I_o}{I_{cosh}} \cdot \frac{I_{dc} I_o}{I_{cosh}} \quad (6.53)$$

assuming  $I_{cosh} = I_{out+} + I_{out-}$ . Hence, considering also the static translinear loop  $Q_{1A} - Q_{2A} - Q_{3A} - Q_{4A} - Q_{5A} - Q_{6A}$ , we have

$$I_{Q_{1A}} I_{Q_{3A}} I_{Q_{5A}} = I_{Q_{2A}} I_{Q_{4A}} I_{Q_{6A}} \Rightarrow I_{out+} \cdot \frac{I_{dc} I_o}{I_{cosh}} \cdot I_{dc} = I_{in-} \cdot I_{CA} \cdot I_{out+}. \quad (6.54)$$

Thus, substituting Eq.6.51 into Eq.6.54, we end up with

$$I_{CA} = \frac{I_{in} + I_o}{I_{cosh}} \quad (6.55)$$

and having Eq.6.55, Eq.6.53 and Eq.6.51, the current  $I_{CB}$  can be written as

$$I_{CB} = \frac{I_{in} - I_o}{I_{cosh}}. \quad (6.56)$$

Subtracting Eq.6.56 from Eq.6.55 results in

$$I_{CA} - I_{CB} = \frac{I_{in} + I_o}{I_{cosh}} - \frac{I_{in} - I_o}{I_{cosh}} \Rightarrow I_{cap} = \frac{I_{in} I_o}{I_{cosh}}. \quad (6.57)$$

From Eq.6.57, we can verify that the proposed integrator indeed implements a companding  $\sinh$  integrator as shown in Fig.6.23. Next, from the dynamic translinear loops, consisting of  $C - Q_{5A} - Q_{6A}$  and  $C - Q_{5B} - Q_{6B}$ , we obtain

$$I_{cap} I_{out+} = CV_T \dot{I}_{out+} \quad (6.58)$$

and

$$I_{cap} I_{out-} = -CV_T \dot{I}_{out-} \quad (6.59)$$

where the dot represents differentiation with respect to time. Finally, substituting Eq.6.58 and Eq.6.59 in Eq.6.57, we can obtain the input-output relation

$$I_{in} = \frac{CV_T}{I_o} \dot{I}_{out} \quad (6.60)$$

which is a linear differential equation, describing an inherent lossless companding integrator with time constant  $\tau = \frac{CV_T}{I_o}$ . In order to obtain a lossy integrator we can easily introduce a negative feedback path from the output to the input of the integrator, resulting in

$$I_{in} = I_{out} + \frac{CV_T}{I_o} \dot{I}_{out} \quad (6.61)$$

describing a first-order low-pass filter with cutoff frequency  $\omega_C$  according to

$$\omega_C = \frac{I_o}{CV_T}. \quad (6.62)$$

Simulating first the proposed integrator using quasi-ideal exponential devices, i.e. bipolar transistors with very large current gain ( $\beta = 10^6$ ), one can see in Fig.6.26 the magnitude of the frequency response of the  $\sinh$  lossy integrator, with the cutoff frequency varying from 318 Hz to 636 kHz, showing the large frequency tuning range typical to translinear filters.

The externally linear internally nonlinear (ELIN) behavior of the integrator can be seen from the output current and the capacitance current, respectively, in Fig.6.27 for an input signal swing much larger than the bias current  $I_o$ .

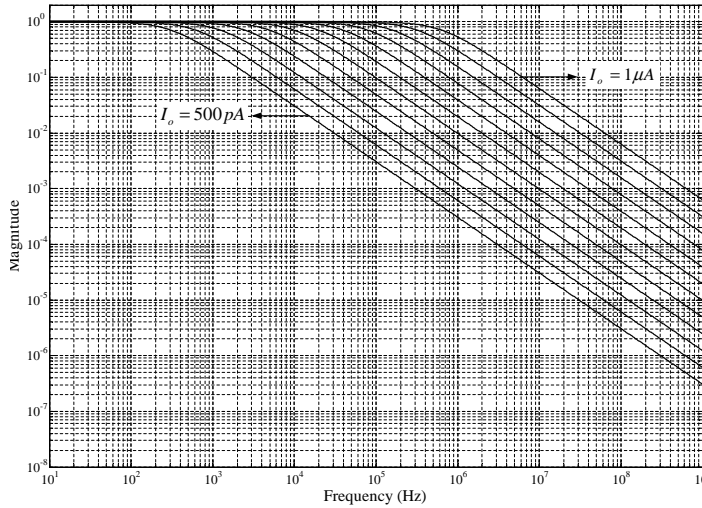


Figure 6.26: Frequency response changing  $I_o$  from 500pA to 1uA using quasi-ideal exponential devices

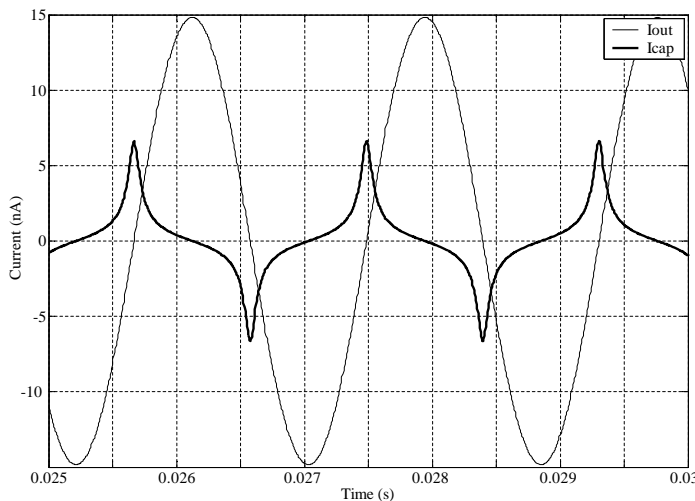


Figure 6.27: Output current and capacitance current for large input signal swing using quasi-ideal exponential devices

### CMOS Integrator Implementation

To validate the circuit principle, we have implemented and simulated the proposed integrator using models of AMS's 0.35  $\mu$ m CMOS IC technology. The circuit has been designed to operate from a 1.5-V ( $\pm 0.75V$ ) supply voltage. The schematic of the completed integrator is given in Fig.6.28. The bipolar transistors have been replaced by equivalent CMOS transistors operating in weak inversion. The transistors have an aspect ratio of  $100\mu/1\mu$ , in order to extend the weak inversion operation up to  $2\mu A$ . In addition, to realize the

expression  $\frac{I_o I_{dc}}{I_{cosh}}$ , we added in the loops transistors  $M_7$  and  $M_8$ . The current  $I_{cosh}$  can be obtained easily by adding the positive and the negative output currents.

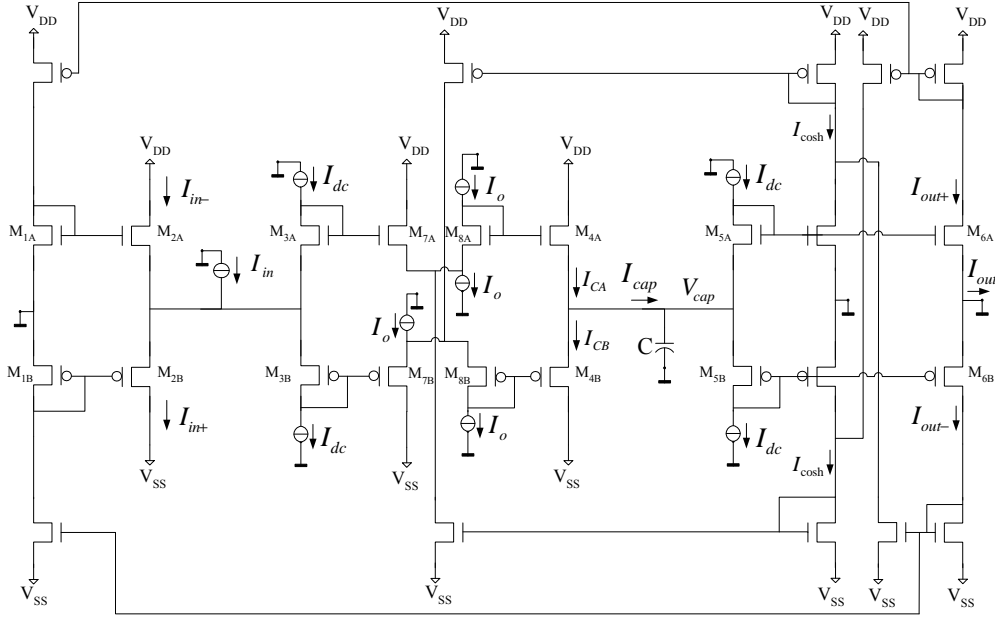


Figure 6.28: Schematic of the CMOS class-AB sinh integrator

In class-AB operation, a static non-linear current splitter is used at the input to divide the bipolar input current  $I_{in}$  into two currents  $I_{in+}$  and  $I_{in-}$ , which are both strictly positive. The current splitter presented here is a geometric-mean splitter, comprising transistors  $M_{1A} - M_{2A} - M_{2B} - M_{1B}$ , where the corresponding equations are given by

$$I_{in+}, I_{in-} = \frac{\pm I_{in} + \sqrt{I_{in}^2 + 4I_o^2}}{2}. \quad (6.63)$$

The output splitter currents are shown in fig.6.29, for a sinusoidal input signal with an amplitude of 10nA and a bias current  $I_o$  of 1nA.

As shown in Fig. 6.23, and in Eq.6.48 and Eq.6.57, the companding integrator can be characterized by a hyperbolic-sine transconductor at the output and a combined *cosh*-divider block at the input, which relates the currents  $I_{out}$  and  $I_{cosh} = \frac{I_{in} \cdot I_o}{I_{cap}}$  to the capacitance voltage  $V_{cap}$ , respectively. The simulated transfer functions of those blocks are shown in Fig. 6.30. The simulated output current with respect to the capacitance voltage is shown in Fig. 6.30a whereas the ratio between the input and capacitance currents versus  $V_{cap}$  is illustrated in Fig. 6.30b.

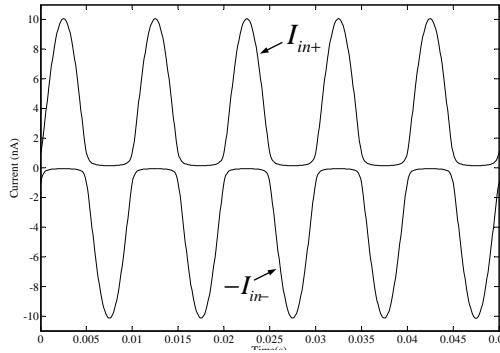
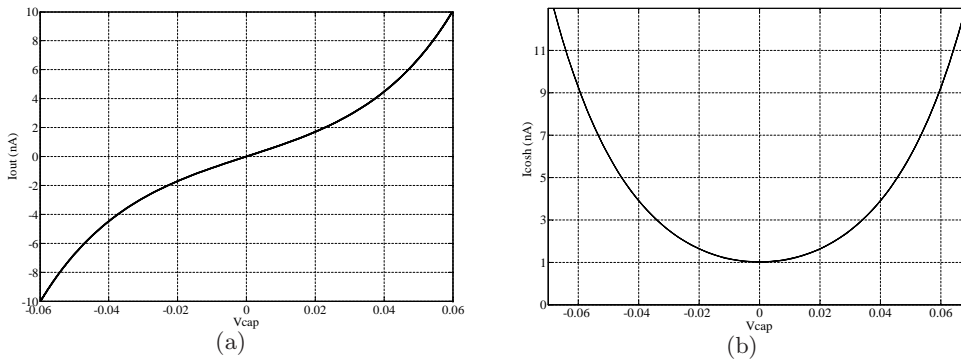


Figure 6.29: Simulated current splitter output currents

Figure 6.30: Simulated currents with respect to the capacitance voltage  $V_{cap}$   
(a) output current  $I_{out}$  and (b)  $I_{cosh}$ 

The hyperbolic-sinusoidal transconductance of the output stage results in an inherently nonlinear dynamic relation between  $I_{cap}$  and  $I_{out}$ , which can be described by [7]

$$I_{cap} = CV_T \frac{\dot{I}_{out}}{\sqrt{I_{out}^2 + 4I_o^2}}. \quad (6.64)$$

As shown in Fig.6.31,  $I_{cap}$  is nearly sinusoidal for low values of  $m$ , where  $m$  represents the modulation index ( $m = I_{in}/I_o$ ). This linear behavior can be explained through the denominator of Eq.6.64, which does not vary that much for low output currents. Thus, the  $I_{cap}$  is more or less proportional to the derivative of  $I_{out}$ . The capacitance current becomes more nonlinear when  $m$  increases, i.e. for large output swings, as seen in Fig.6.31.

However, despite the nonlinear nature of the capacitance currents in *sinh* integrators, an exactly linear transfer function can be realized, as one can see in Fig.6.32, where the output is still defined by a sine function for  $m$  varying from 1 to 20.

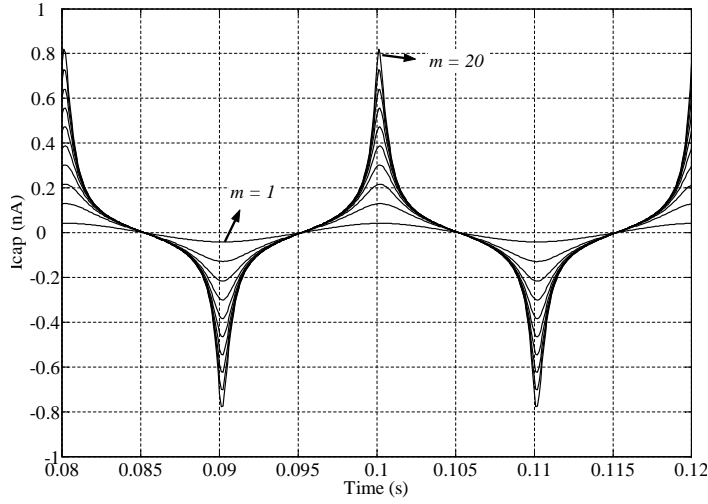


Figure 6.31: Simulated capacitance current  $I_{cap}$  with  $I_o$  equals 1nA and input amplitude changing from 1nA to 20nA

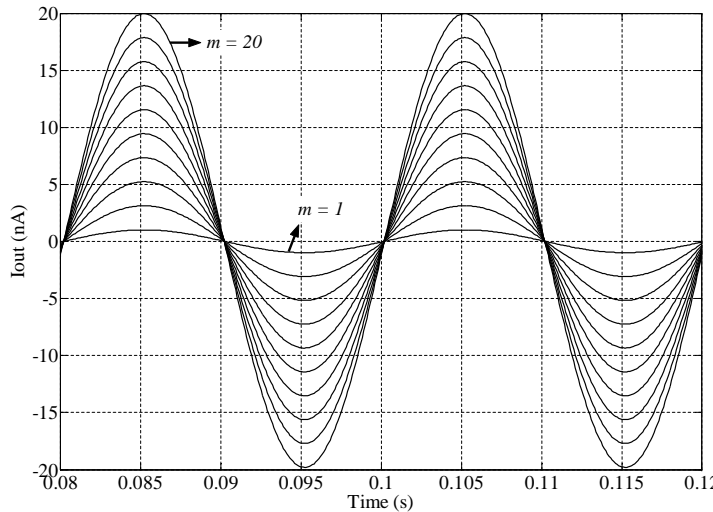


Figure 6.32: Simulated output current  $I_{out}$  with  $I_o$  equals 1nA and input amplitude changing from 1nA to 20nA

In addition, one can see the linear tunability of the filter, described in Eq.6.61, from the simulated frequency response, given in Fig.6.33. With reference to Eq.6.62, the cutoff frequency is directly proportional to bias current  $I_o$ , changing from 318 Hz to 1.2 MHz with  $I_o$  equal to 500 pA and 2  $\mu$ A, respectively, and C equal to 10 pF. Thus, it can be deduced that the cutoff frequency of the filter can be linearly controlled over a wide frequency range.

The Dynamic Range (DR), defined as the ratio between the maximum signal amplitude for a given distortion (in this case, 1-dB compression point)

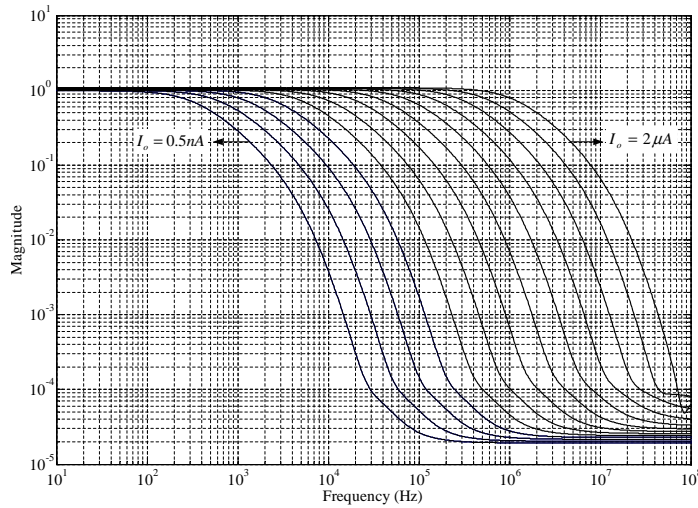


Figure 6.33: Frequency response changing  $I_o$  from 500pA to 2uA

and the noise floor, is shown in Fig.6.34. The output RMS current noise is 4.2pA, resulting in a DR at the 1-dB compression point of approximately 75 dB.

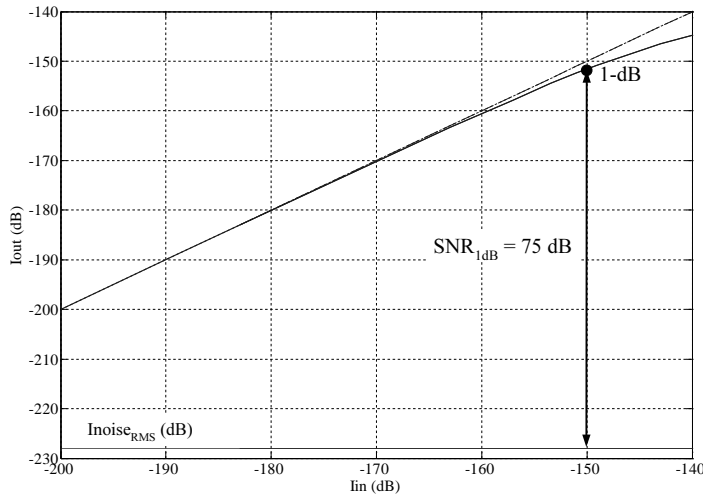


Figure 6.34: Signal-to-noise ratio at 1dB compression point for  $I_o = 1nA$

Fig.6.35 shows the total harmonic distortion (THD) at the output as a function of the modulation index  $m$  and input signal frequency. At a frequency much lower than the cutoff frequency ( $f_c$ ), i.e.  $f_c/10$ , the THD is kept below 1%, with a modulation index as high as 20. As expected, the THD increases for an input signal frequency close to  $f_c$ . In this case,  $f_c$  equals 636 Hz and

results in a THD at the cutoff frequency of 0.3% for  $m = 1$  and 3.2% for  $m = 20$ . The performance of the filter is summarized in Table 6.1.

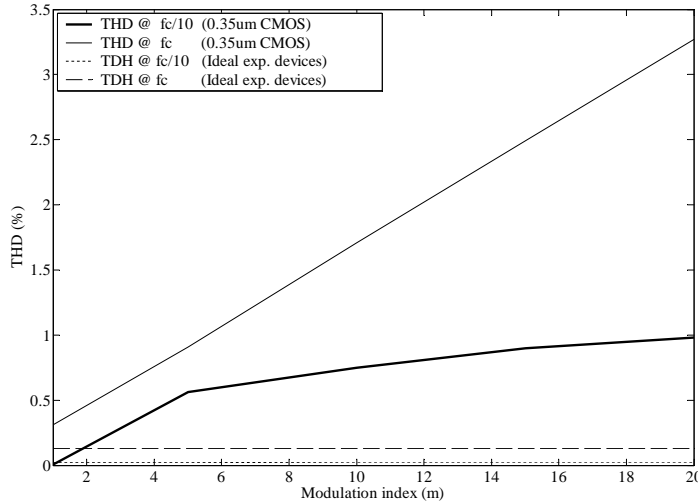


Figure 6.35: Total Harmonic Distortion versus  $m$  for frequencies  $@fc$  and  $@fc/10$

Table 6.1: Performance of the proposed integrator for two different cutoff frequencies

| Technology                             | 0.35 $\mu$ m CMOS  |                      |
|--|--------------------|----------------------|
| Bias current                           | $I_o = 1\text{nA}$ | $I_o = 2\mu\text{A}$ |
| Capacitance                            | 10pF               | 10pF                 |
| Supply voltage                         | 1.5V               | 1.5V                 |
| Center frequency ( $f_c$ )             | 636Hz              | 1.27MHz              |
| Total bias $I_o$ (Lossless integrator) | 11nA               | 22 $\mu$ A           |
| Total bias $I_o$ (Lossy integrator)    | 14nA               | 28 $\mu$ A           |
| Power dissipation                      | 22.5 nW            | 45 $\mu$ W           |
| Dynamic Range (1-dB)                   | 75 dB              | 75 dB                |
| Noise current (rms)                    | 4.2pA              | 6.9nA                |
| Supply voltage range                   | 1V - 3V            | 1.5V - 3V            |
| Power diss. per pole & $f_c$           | 35.37pJ            | 35.37pJ              |

Table 6.2 makes a comparison with other log-domain Class-AB designs. The first advantage of this design is that it uses only one capacitor to implement a Class-AB integrator, which saves considerable chip area. This is particularly important for low-frequency designs where we inevitably need to use large capacitance values. Furthermore, the proposed circuit presents an excellent performance with respect to power efficiency. The power efficiency of a continuous-time filter is a figure of merit used in comparing various filter

topologies and can be estimated by means of the power dissipation per pole  $P_{diss}$  & cut-off frequency  $f_c$ , defined as  $\frac{P_{diss}}{f_c}$  [30].

Table 6.2: Performance comparison of the proposed class-AB integrator with other implementation

|  | Serdijn et al. [25] | Punzenberger et al. [26] | El-Gamal et al. [27] | Python et al. [28] | Redondo et al. [29] | This work          |
|--|---------------------|--------------------------|----------------------|--------------------|---------------------|--------------------|
| Technology                                   | Bipolar             | BiCMOS                   | Bipolar              | CMOS               | CMOS                | CMOS               |
| Capacitance                                  | $1 \cdot C$         | $2 \cdot C$              | $2 \cdot C$          | $2 \cdot C$        | $2 \cdot C$         | $1 \cdot C$        |
| Bias current (without splitter)              | $13 \cdot I_o$      | $11 \cdot I_o$           | $12 \cdot I_o$       | $12 \cdot I_o$     | $13 \cdot I_o$      | $9 \cdot I_o$      |
| Supply voltage                               | 3.3V                | 1.2V                     | 1.2V                 | 1.5V               | 1V                  | 1.5V               |
| Cut-off freq. ( $\omega_c$ )                 | $\frac{I_o}{CV_T}$  | $\frac{I_o}{CV_T}$       | $\frac{I_o}{CV_T}$   | $\frac{I_o}{CV_T}$ | $\frac{I_o}{CV_T}$  | $\frac{I_o}{CV_T}$ |
| $P_{diss}$ per pole & $\omega_c$ (quiescent) | $42 \cdot CV_T$     | $13 \cdot CV_T$          | $14 \cdot CV_T$      | $18 \cdot CV_T$    | $13 \cdot CV_T$     | $13 \cdot CV_T$    |

## Conclusions

A new ultra low-power Class-AB *Sinh* integrator based on hyperbolic-sine transconductors is presented. The proposed integrator uses only one grounded capacitor and shows excellent power efficiency, compared with existing log-domain Class-AB implementations. The lossy integrator is simulated using CMOS transistors in weak-inversion, operating from a 1.5-V ( $\pm 0.75$ V) supply voltage. The total current consumption of the first-order low-pass filter is 14nA and the DR at the 1-dB compression point is 75 dB. The filter can handle signals much larger than the bias current, while keeping THD below 1%.

## 6.5 Discussion

In the linear transconductors presented here, the input transistors are kept in the triode-region to benefit from the lowest  $G_m/I_D$  ratio. The main advantage of this technique is the ability to obtain extremely small transconductances, which enable us to design very low-frequency filters. Translinear circuits become difficult to integrate when it's necessary to design low cutoff-frequency filters for use in the Hz and sub-Hz range. For example, for  $G_m = 1nA/V$ , the proposed transconductor need to be biased with a quiescent current  $I_o = 315pA$ . To achieve the same time constant and considering the same bias current, the translinear circuits needs an increase of 12.6 times in the capacitor value. Or, to maintain the same capacitor, it is necessary to decrease the current to 25pA, which is difficult to obtain precisely.

Contrary to the Translinear approach, the time constant of the filter (and, of course, the corresponding cut-off frequency) is controlled by a voltage rather

than by a current, which is limited by the supply voltage; whereas the frequency tunability of the translinear circuits can be controlled over a wide range, usually several decades. Moreover, in linear  $G_m$ -C filters, due to the inherently non-linear behavior of the transistors, the transconductors have to be linearized, in order to implement the desire transfer function. This unavoidably degrades the available transconductance, resulting in a poor current efficiency.

The main advantages of translinear circuits with respect to other low-power techniques are, first of all, the property of handle a large dynamic range in a low-voltage environment. In contrast to  $G_m$ -C filters, the capacitor current is no longer a linear function of the input voltage, but an exponential one. This means, that the voltages in translinear filters are logarithmically related to the currents, and, as a result, the voltage excursions are small, typically only a few tens of millivolts. Thus, the maximum signal swing in a current-mode circuit is not limited by the supply voltage anymore.

Second of all, the static and dynamic translinear principles can be applied to the implementation of a wide variety of nonlinear functions, static nonlinear polynomial transfer functions and nonlinear differential equations, respectively. Also, only transistors and capacitors are required to realize a filter function. Since in conventional ultra low-power designs resistors would become too large for on-chip integration, their superfluity is a very important advantage. Other advantages are that they present a high functional density and are theoretically process and temperature independent.

## 6.6 Conclusions

Several ultra low-power integrator designs were presented in this chapter. The integrators were based on two different techniques, being the  $G_m$ -C approach and the translinear (log-domain) method. The advantages and the limitations of these techniques were also highlighted. To summarize, both techniques can be directly used in low-power analog filters and ultra low-power biomedical systems designs, as can be seen in the next chapter.

# Bibliography

- [1] R. Schaumann and M.E. van Valkenburg, “Design of Analog Filters,” *Oxford University Press*, 2<sup>nd</sup> Ed., USA, 2001.
- [2] J.A. de Lima and W.A. Serdijn, “A Compact nA/V CMOS Triode Transconductor and its Application to Very-Low Frequency Filters,” *proc. ISCAS*, Kobe, Japan, May 23-26, 2005.
- [3] R.W. Adams, “Filtering in the log domain,” preprint 1470, presented at the 63rd AES Conference, New York, May 1979.
- [4] E. Sevinck, “Companding current-mode integrator: a new circuit principle for continuous-time monolithic filters,” *Electronics Letters*, 26(24), pp.2046-2047, 1990.
- [5] B. Gilbert, “Translinear circuits: a proposed classification,” *Electronics Letters*, 11(1), pp.14-16, 1975.
- [6] J. Mulder, W.A. Serdijn, A.C. van der Woerd and A.H.M. van Roermund, *Dynamic Translinear and Log-Domain Circuits: Analysis and Synthesis*, Boston, MA: Kluwer, 1999.
- [7] Jan Mulder, “Static and Dynamic Translinear Circuits”, *Phd thesis, Delft University of Technology*, Oct. 1998.
- [8] D.R. Frey, “Log Domain filtering: An approach to current mode filtering,” *Proc. Elect. Eng.*, pt. G, vol.140, pp. 406-416, Dec. 1993.
- [9] Y. Tsividis, “Externally linear, time-invariant systems and their application to companding signal processors,” *IEEE Transactions on Circuits and Systems-II*, vol.44, pp. 65-85, Feb. 1997.
- [10] D.R. Frey, “Exponential state space filters: A generc current mode design strategy,” *IEEE Transactions on Circuits and Systems-I*, vol.43, pp. 34-42, Jan. 1996.
- [11] J. Mulder, W.A. Serdijn, A.C. van der Woerd and A.H.M. van Roermund, “Dynamic Translinear Circuits - An overview,” *Analog Integrated Circuits and Signal Processing J.*, vol.22, no. 2-3, pp. 111-126, Mar. 2000.

- [12] W.A. Serdijn, J. Mulder, A.C. van der Woerd and A.H.M. van Roermund, "The design of wide-tunable translinear second-order oscillators," *proc. IEEE ISCAS*, Hong Kong, vol.2, pp. 829-832, May. 1997.
- [13] J. Mulder, A.C. van der Woerd, W.A. Serdijn and A.H.M. van Roermund, "An RMS-DC converter based on the dynamic translinear principle," *IEEE Journal of Solid-State Circuits*, vol.32, no. 7, 1997.
- [14] G. W. Roberts and V. W. Leung, *Design and Analysis of Integrator-Based Log-Domain Filter Circuits*, Kluwer Academic Publishers, The Netherlands, 2000.
- [15] M. N. El-Gamal and G. W. Roberts, "A 1.2v npn-only integrator for log-domain filtering," *IEEE Transactions on Circuits and Systems - II*, vol. 49, no. 4, pp. 257-265, April 2002.
- [16] D. Python and C. Enz, "A Micropower Class-AB CMOS Log-Domain Filter for DETC Applications," *IEEE Journal of Solid-State Circuits*, vol.36, no. 7, pp. 1067-1075, Jul. 2001.
- [17] W.A. Serdijn, M. Broest, J. Mulder, A.C. van der Woerd and A.H.M. van Roermund, "A Low-Voltage Ultra Low-power Translinear Integrator for Audio Filter Applications", *IEEE Journal of Solid-State Circuits*, vol.32, no. 4, pp. 577-582, Apr. 1997.
- [18] C. Toumazou, J. Ngarmnil and T.S. Lande, "Micropower log-domain filter for electronic cochlea", *IEE Electronics Letters*, vol.30, no.22, pp. 1839-1841, Oct. 1994.
- [19] G.D. Duerden, G.W. Roberts and M.J. Deen, "The development of bipolar log domain filters in a standard CMOS process", in *Proc. IEEE Int. Symp. Circuits and Systems*, vol.1, pp. 1470-1476, May 2001.
- [20] S.A.P. Haddad and W.A. Serdijn, "High-Frequency Dynamic Translinear and Log-domain Circuits in CMOS Technology", in *Proc. IEEE Int. Symp. Circuits and Systems*, vol.3, pp. 313-316, May 2002.
- [21] G. Palumbo and S. Pennisi, "A High-Performance CMOS Voltage Follower", in *Proc. IEEE Int. Conf. Electronics, Circuits and Systems*, vol.2, pp. 21-24, 1998.
- [22] G. Palmisano and G. Palumbo, "An Optimized Compensation Strategy for Two-Stage CMOS OPAMPS", *IEEE Transactions on Circuits and Systems - I*, vol. 42, no. 3, pp. 178-182, Mar. 1995.
- [23] C.J.M. Verhoeven, A. van Staveren, G.L.E. Monna, M.H.L. Kouwenhoven and E. Yildiz, "Structured Electronic Design - Negative-Feedback Amplifiers", *Kluwer Academic Publishers*, 2003.

- [24] D.R. Frey and A.T. Tola, "A State-Space Formulation for Externally Linear Class AB Dynamical Circuits," *IEEE Transactions on Circuits and Systems-II*, vol.46, no. 3, pp. 306-314, Mar. 1999.
- [25] W.A. Serdijn, M.H.L. Kouwenhoven, J. Mulder and A.H.M. van Roermund "Design of High Dynamic Range Fully Integratable Translinear Filters," *Analog Integrated Circuits and Signal Processing*, Kluwer, 19, pp. 223-239, 1999.
- [26] M. Punzenberger and C. Enz, "A 1.2-V Low-Power BiCMOS Class AB Log-Domain Filter," *IEEE Journal of Solid-State Circuits*, vol. 32, no. 12, pp. 1968-1978, Dec. 1997.
- [27] M.N. El-Gamal, R.A. Baki and A. Bar-Dor, "30-100-MHz NPN-Only Variable-Gain Class-AB Instantaneous Companding Filters for 1.2-V Applications," *IEEE Journal of Solid-State Circuits*, vol. 35, no. 12, pp. 1853-1864, Dec. 2000.
- [28] D. Python and C. Enz, "A Micropower Class-AB CMOS Log-Domain Filter for DECT Applications," *IEEE Journal of Solid-State Circuits*, vol. 36, no. 7, pp. 1067-1075, Jul. 2001.
- [29] X. Redondo and F. Serra-Graells, "1V Compact Class-AB CMOS Log Filters" in *Proceedings IEEE International Symposium Circuits and Systems*, pp. 2000-2003, May 2005.
- [30] C. Toumazou, G. Moschytz, and B. Gilbert, "Trade-Offs in Analog Circuit Design", *Kluwer Academic Publishers*, The Netherlands, 2002.



## Chapter 7

# Ultra Low-power Biomedical System Designs

*"There's nothing you can do that cannot be done." - Lennon/McCartney*

The methodology presented in previous chapters will now be employed in the design of several ultra low-power biomedical systems and analog wavelet filters.

In the first part of this chapter, a benchmark cardiac sense amplifier, i.e. the front end of a pacemaker, based on the Dynamic Translinear (DTL) circuit technique is presented. The system consists of a voltage-to-current converter, a bandpass filter, absolute value and RMS-DC converter circuits and an event detection circuit. From simulations, it is demonstrated that the DTL technique is a good alternative to conventional sense amplifiers for intra cardiac applications since they handle the required dynamic range and perform non-linear operations at low supply voltages.

Another approach for ultra low-power analog QRS complex detection circuit, for pacemaker applications, is presented in this chapter. The system is based on the Wavelet Transform (WT) and detects the wavelet modulus maxima of the QRS complex. It consists of a wavelet transform filter based on CFOS approach, an absolute value circuit, a peak detector and a comparator. Simulations indicate a good performance of the Wavelet Transform and the QRS complex detection.

To validate both systems principles and to check the circuits performances, the sub-circuits as well as the whole systems have been implemented in our in-house bipolar semi-custom DIMES IC process, SIC3A. Typical transistor parameters are  $f_{T,npn,max} = 15\text{GHz}$  and  $\beta_{F,npn} = 150$  (smallest emitter size) [1].

Moreover, a few wavelet filter designs will also be presented. Two convenient methods to provide the transfer function of the wavelet filter are given by the Padé and  $L_2$  approximations and, thus, two designs based on these

approaches, for Gaussian wavelet base, will be designed using the  $G_m$ -C and the DTL circuit techniques, respectively. In addition, a complex wavelet filter design, based on the combination of the real and the imaginary state-space descriptions is described.

Finally, the implementation of a Morlet wavelet filter using the procedure in Chapter 4 is presented. First, the approximation based on the Padé method is used to calculate the transfer function of the filter, whose impulse response is the Morlet wavelet base. Next, to meet low-power low-voltage requirements, we optimize the state-space description of the filter with respect to dynamic range, sensitivity and sparsity, as presented in Chapter 5. The filter design that follows is based on an orthonormal ladder structure and employs log-domain integrators as main building blocks. We have implemented the log-domain state-space wavelet filter in IBM's  $0.18\mu m$  BiCMOS IC process.

## 7.1 Dynamic Translinear Cardiac Sense Amplifier for Pacemakers

Conventional pacemaker topologies usually are divided into an analog part (comprising a sense amplifier and a heart stimulator) and a digital part (comprising a micro controller). The sense amplifier plays a fundamental role in providing information about the current state of the heart. It is designed to detect and monitor intracardiac signal events (e.g., R-waves in the ventricle). After signal sensing, the signal is fed to the digital microprocessor that decides upon the appropriate pacing therapy to be delivered by the stimulator. However, the algorithm in the microprocessor requires from the sense amplifier the accurate measurement of the heart activity even in the presence of noise and interference. The diverse features of the intracardiac signals, therefore, require a large dynamic range, i.e., a large signal-to-noise-plus-interference level, for the sense amplifier.

This design presents the applicability of DTL circuits to the design of cardiac sense amplifiers to be implemented in pacemakers. In Fig.7.1 a suitable block diagram of a sense amplifier for cardiac signal detection is given [2]. The system consists of a V-I (voltage-to-current) converter, a bandpass filter, absolute value [3] and RMS-DC converter circuits [4], and a comparator circuit ???. The chip microphotograph of the sense amplifier implemented in SIC3A semi-custom IC process is given in Fig. 7.2. Additionally, an EMI filter is implemented off-chip for electromagnetic interference cancellation (not shown). It is a 2nd order bandpass filter to suppress dc and signals beyond 1kHz. The V-I converter is required as the input and output quantities of the EMI filter are voltages and translinear circuits are inherently current-mode as will be treated in Section 3. The bandpass filter is used to specifically select intra-cardiac signals, in our case being the QRS complex or R-wave, and to minimize the effect of the overlapping myocardial interference signals and low

## 7.1 Dynamic Translinear Cardiac Sense Amplifier for Pacemakers

---

frequency breathing artifacts. The center frequency of the bandpass filter is located at 25 Hz. The reason to use an absolute value circuit is to be independent from the electrode position in the heart. Accommodation to changes in the average input signal level is realized using the RMS-DC converter. This circuit implements two functions, a squarer-divider and a lowpass filter. At the end of the block schematic, the detection signal (a binary value) is generated depending upon a threshold level, which is given by:

$$I_{Thr} = I_{ABS} - \left( \frac{3}{4} I_{RMS} + I_{CTh} \right) \quad (7.1)$$

where  $I_{Thr}$  is the adaptive threshold level, the  $I_{ABS}$  variable is the output signal of the absolute value circuit.  $I_{RMS}$  is the output of the RMS-DC converter.  $I_{CTh}$  is a constant value that can be derived from typical values of the input signal.

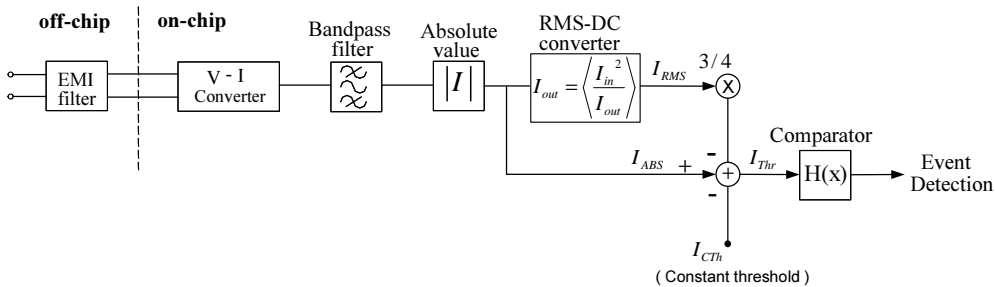


Figure 7.1: Block diagram of the sense amplifier

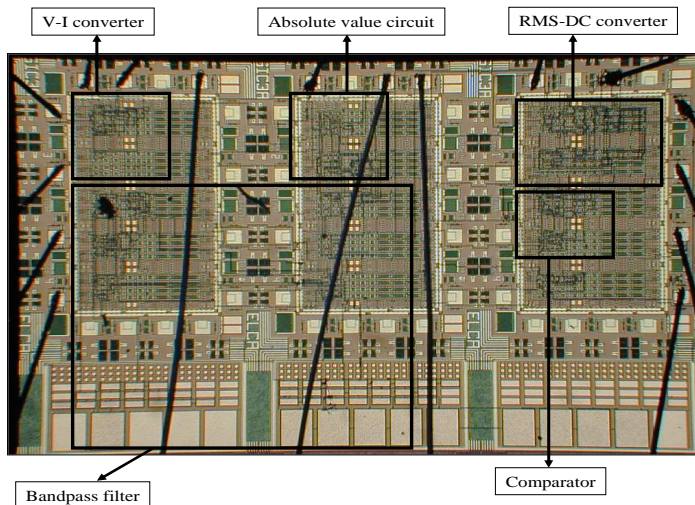


Figure 7.2: Sense amplifier chip microphotograph

### 7.1.1 Differential voltage to single-ended current converter

The output signal of the EMI filter is a differential voltage, in the order of a few millivolts, and the input signal of the bandpass filter is a single-ended current. The required transformation of the differential input voltage into a single-ended current can be simply performed by a differential pair loaded by two current mirrors as shown in Fig.7.3. Note that the transconductance factor is determined by the value of the current  $I_o$  and equals  $I_o/4V_T$ . Since the output nodes of the EMI filter are floating, the differential input nodes of the V-I converter need to be biased at a voltage in between the power supplies. This CM (common-mode) input voltage is set by the CM loop comprising Q3-Q7 and approximates  $V_{cc} - 3V_{be}$ .

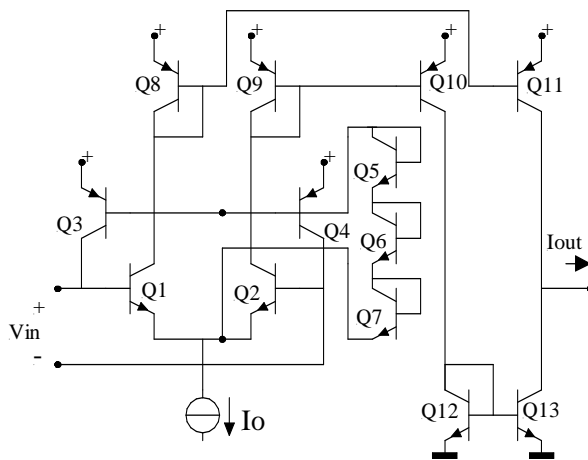


Figure 7.3: Differential input voltage to single-ended current converter

The dc transfer of the V-I converter circuit is given in Fig. 7.4. The value of current  $I_o$  is 10.4nA resulting in a transconductance factor of  $0.18 \mu\text{A}/\text{V}$  to accommodate the desired input signal range.

### 7.1.2 Bandpass filter

To achieve sufficient selectivity around 25 Hz the filter is implemented by a cascade of two biquadratic bandpass filter sections. These biquads, in turn, are realized by two lossy integrators according to the block diagram given in Fig. 7.5a. The integrators comprise four transistors and one capacitor in a loop and implement

$$CV_T \dot{I}_{out} + I_o I_{out} = I_o I_{in} \quad (7.2)$$

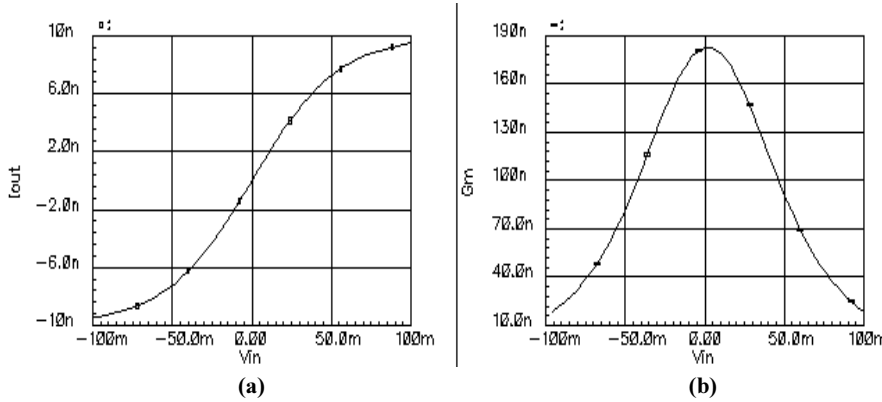


Figure 7.4: DC transfer of the V-I converter (a) V-I characteristic (b) Transconductance factor.

where  $I_o$  is a dc bias current and  $I_{out}$  is the low-pass filtered version of  $I_{in}$ . The expression above is a linear differential equation, describing a low-pass filter with cutoff frequency  $\omega_C$  according to

$$\omega_C = \frac{I_o}{CV_T} \quad (7.3)$$

In Fig. 7.5b the circuit diagram of one biquad for realizing a part of the bandpass filter is given. The integrator loops are defined by transistors Q1-Q4 and capacitor C1 and Q5-Q8 and C2, respectively. A positive feedback network using current mirror Q11-Q12 turns the lossy integrator into a lossless integrator.

For a system with the poles in Butterworth position the values of the capacitances are given by

Lossy integrator:

$$C_1 = \frac{I_o}{V_T(p_1 + p_2)} \quad (7.4)$$

Lossless integrator:

$$C_2 = \frac{I_o}{V_T\sqrt{p_1 p_2}} \quad (7.5)$$

where  $p_1$  and  $p_2$  are the poles of the Butterworth polynomial implemented by the biquad. The magnitude and phase response of the bandpass filter is shown in Fig.10a and Fig.10.b, respectively. Note that the center frequency of the bandpass is indeed located around 25 Hz. The first biquad has  $I_o$  and  $C_1$  and  $C_2$  equal to 2nA, 80pF and 170pF respectively. For the second biquad these values are 0.4nA, 94pF and 131pF, respectively.

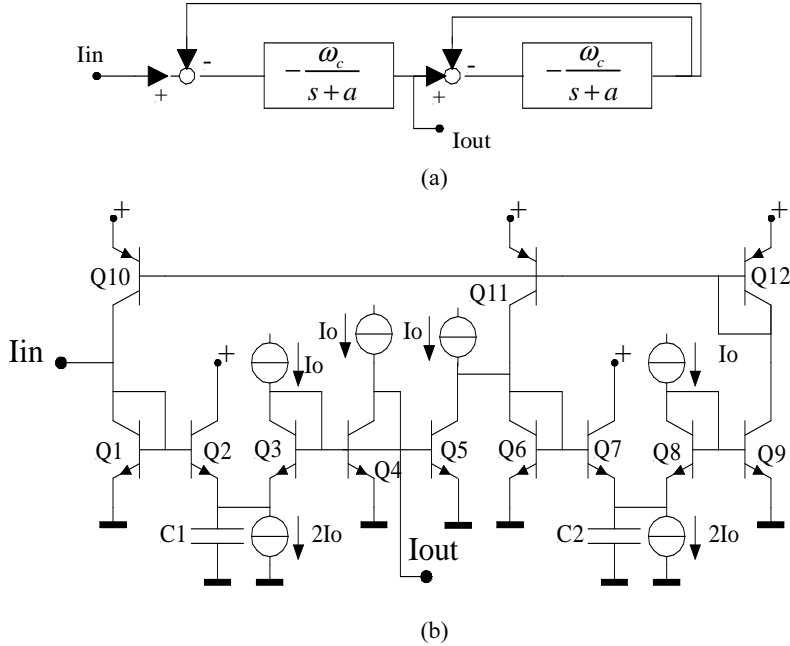


Figure 7.5: (a) Block diagram of the bandpass biquad filter (b) Circuit schematic

### 7.1.3 Absolute value and RMS-DC converter circuits

Since the polarity of the input signal is not known, its absolute value is generated. The required function  $I_{out} = |I_{in}|$  is realized with the circuit in Fig.7.7 [3]. The translinear loop in the circuit consists of transistors Q2, Q1, Q5 and Q7, implementing

$$(I_o + I_{out})(I_o - I_{out}) = (I_o + I_{in})(I_o - I_{in}) \quad (7.6)$$

The dc transfer of the absolute value circuit is given in Fig.7.8. The circuit provides correct operation up to  $I_o$ .

The RMS transfer is implemented by a squarer/divider circuit [4] and a low-pass filter and produces

$$I_{out} = \int \frac{I_{in}^2}{I_{out}} dt \quad (7.7)$$

Its translinear differential equation describing a first-order RMS-DC conversion then follows as

$$CV_T \dot{I}_{out} I_{out} + I_o I_{out}^2 = I_o I_{in}^2 \quad (7.8)$$

Note that this is a nonlinear differential equation. A possible implementation is shown in Fig.7.9 [4]. Q1 through Q6 form the static translinear loop

## 7.1 Dynamic Translinear Cardiac Sense Amplifier for Pacemakers

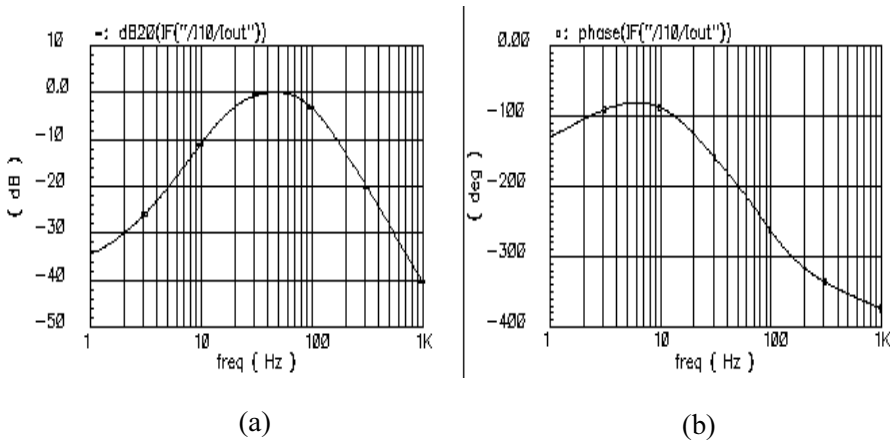


Figure 7.6: Frequency response of the biquad (a) Magnitude (b) Phase

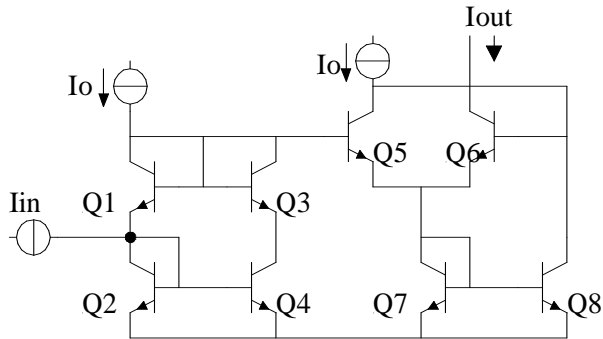


Figure 7.7: Absolute value circuit

implementing  $(I_{cap} + I_o)I_{out}^2 = I_{in}^2$  and C, Q4-Q6 the dynamic translinear loop, implementing  $2CV_T I_{out} = I_{cap} I_{out}$ . The quadratic factors  $I_{in2}$  and  $I_{out2}$  are implemented by Q1-Q2 and Q5 - Q6 respectively. Q7 and Q8 are buffers to avoid the base current error in Q2 and Q4.

The output current of the RMS-DC converter is a time average of the input signal as seen from Eq.7.8. The cut-off frequency is given by Eq.7.3. To achieve a cut-off frequency of 1.5Hz, the values of  $I_o$  and C in Fig.7.9 are 0.125nA and 1nF respectively. A transient analysis of the RMS-DC converter connected to the absolute value circuit is given in Fig.7.10. With a sinusoid applied at the input to validate the operation of the circuit, having a frequency of 10Hz and amplitude of 1.5nA, the RMS-DC circuit produces an output (drawn line) amplitude around 1nA, which is close to the ideal response (dotted line).

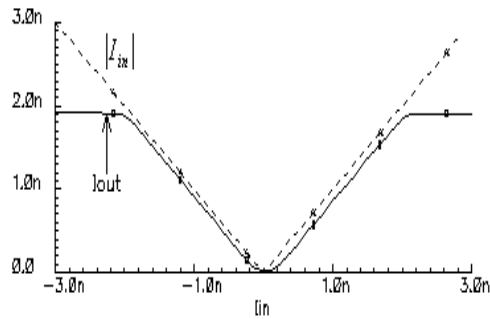


Figure 7.8: DC transfer of the absolute value circuit

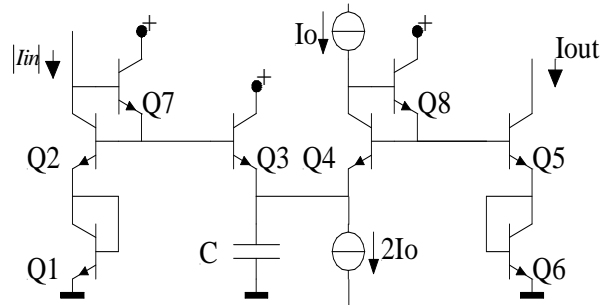


Figure 7.9: RMS-DC converter circuit

#### 7.1.4 Detection (Sign function) circuit

Since TL circuits can implement polynomial functions only, we first need to approximate the Sign function by a polynomial function. A static translinear loop equation to achieve a good approximation to the Sign function is described by [3]

$$(I_o + I_{in})(I_o - I_{out})(I_o + I_{out}) = (I_o - I_{in})(I_o + I_{in})(I_o + I_{out}) \quad (7.9)$$

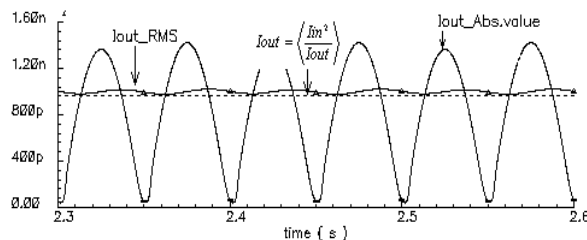


Figure 7.10: RMS-DC converter circuit

yielding

$$\begin{cases} I_{out} = 0 & \text{if } I_{in} < 0 \\ I_{out} = I_o & \text{if } I_{in} > 0 \end{cases} \quad (7.10)$$

Its corresponding TL circuit is given in Fig. 7.11 [3].

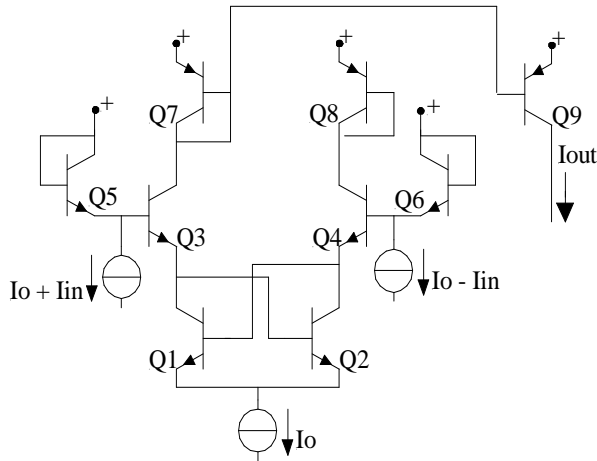


Figure 7.11: Comparator circuit

In Fig. 7.12, the DC transfer of the comparator circuit, with  $I_o$  equal to 1nA, is shown.

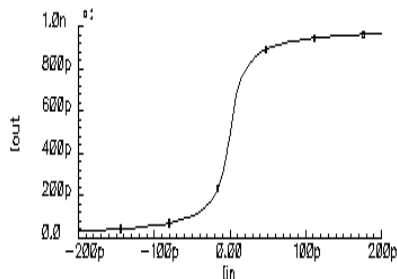


Figure 7.12: DC response of the comparator circuit

Finally, a test signal is applied to the system to verify the performance and efficiency of the complete sense amplifier according to Fig.7.1. A typical intra-cardiac signal measured in the ventricle, shown in Fig.7.13a, is applied to the input of the system. The transient responses of the blocks are shown in Fig.7.13b. The system is clearly able to detect the R-wave, which represents the cardiac event that the circuit was supposed to detect.

The characteristics of the sense amplifier are summarized in Tab. 7.1.

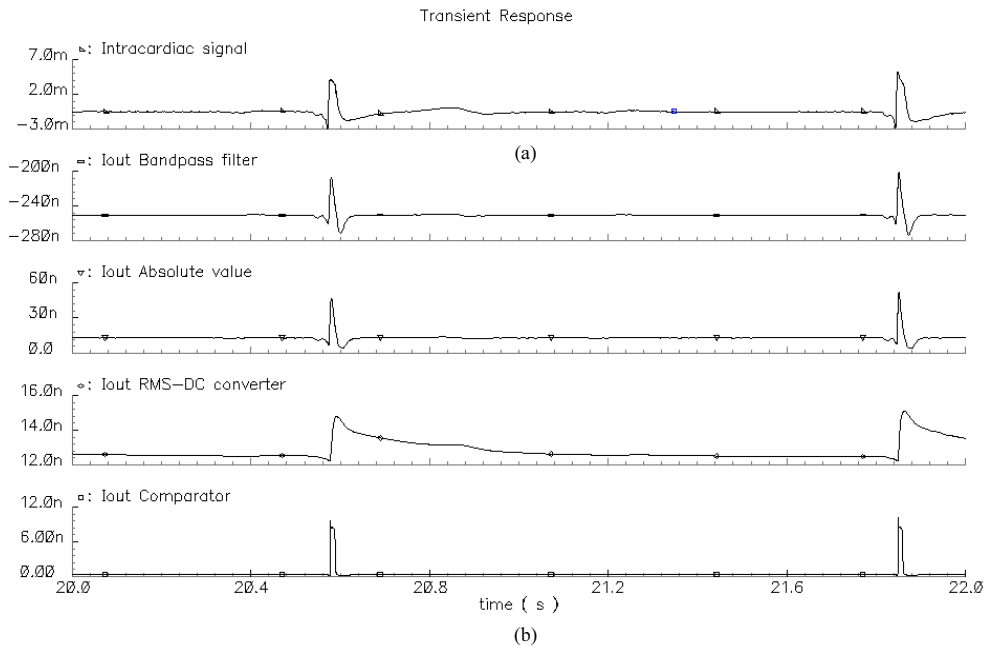


Figure 7.13: (a) Intra-cardiac signal (b) transient response of the complete sense amplifier

Table 7.1: Simulated sense amplifier characteristics

|  |        |
|--|--------|
| Power supply   | 2.0V   |
| Total bias current                                       | 120 nA |
| Power consumption  | 240 nW |
| Eq. rms noise voltage @ V-I converter input              | 0.1 mV |
| Eq. rms noise current @ Abs. value circuit output        | 3.6 pA |
| SNR @ Abs. value circuit output (10Hz - 1kHz)            | 39 dB  |
| Eq. rms noise current @ comparator input while switching | 6.5 pA |

## 7.2 QRS-complex wavelet detection using CFOS

QRS complex detection is important for cardiac signal characterization. Many systems have been designed in order to perform this task. In [5] it was shown that, in spite of the existence of different types, a basic structure is common for many algorithms. This common structure is given in Fig. 7.14a. It is divided into a filtering stage (comprising linear and/or nonlinear filtering) and a decision stage (comprising peak detection and decision logic).

The algorithm detection of the QRS complex presented here is based on modulus maxima of the wavelet transform. The two maximas with opposite signs of the WT correspond to the complex QRS and are illustrated in Fig. 7.14b.

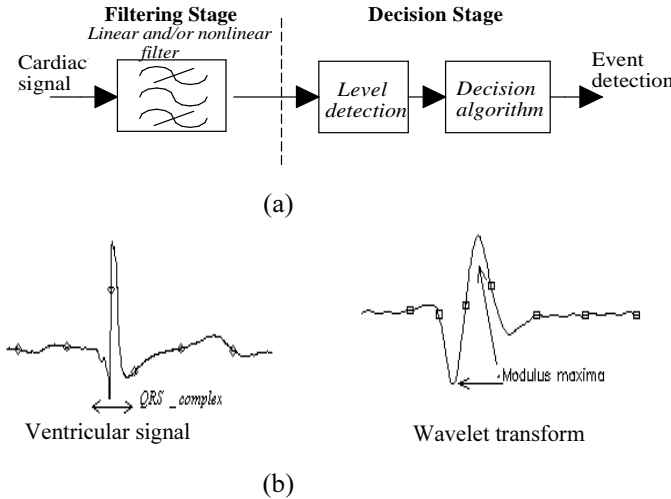


Figure 7.14: (a) Block diagram of the basic structure of the QRS detectors [5]  
(b) Cardiac signal and the modulus maxima of the WT

The block diagram is given in Fig.7.15 and contains the required circuits to design the QRS detection system [6].

At the input, a wavelet filter is situated which implements an approximation to the first derivative Gaussian WT. The complete filter comprises multiple scales in parallel in order to compute the WT in real time. Subsequently, the signal is fed through an absolute value circuit, followed by a peak detector, to generate an adjustable threshold level according to

$$T_{hj} = \text{Abs} - \frac{3}{4} \text{Peak} \quad (7.11)$$

with

$$\begin{cases} \text{Peak} = \text{Abs} & \text{for } \text{Abs} \geq \text{Peak} \\ \frac{d\text{Peak}}{dt} = -\tau \text{Peak} & \text{for } \text{Abs} \leq \text{Peak} \end{cases} \quad (7.12)$$

where  $T_{hj}$  is the threshold value for scale  $a=2^j$ ,  $\text{Abs}$  is the absolute value and  $\text{Peak}$  is the output value of the peak detector circuit.  $\tau$  is the time constant of the peak detector and the  $\frac{d}{dt}$  represents differentiation with respect to time.

The final signal processing block is a comparator in order to detect the modulus maxima position of the QRS complex. The time localization of the modulus maxima and the classification of characteristic points of the cardiac signal is processed by the digital logic circuit, and will not be described here.

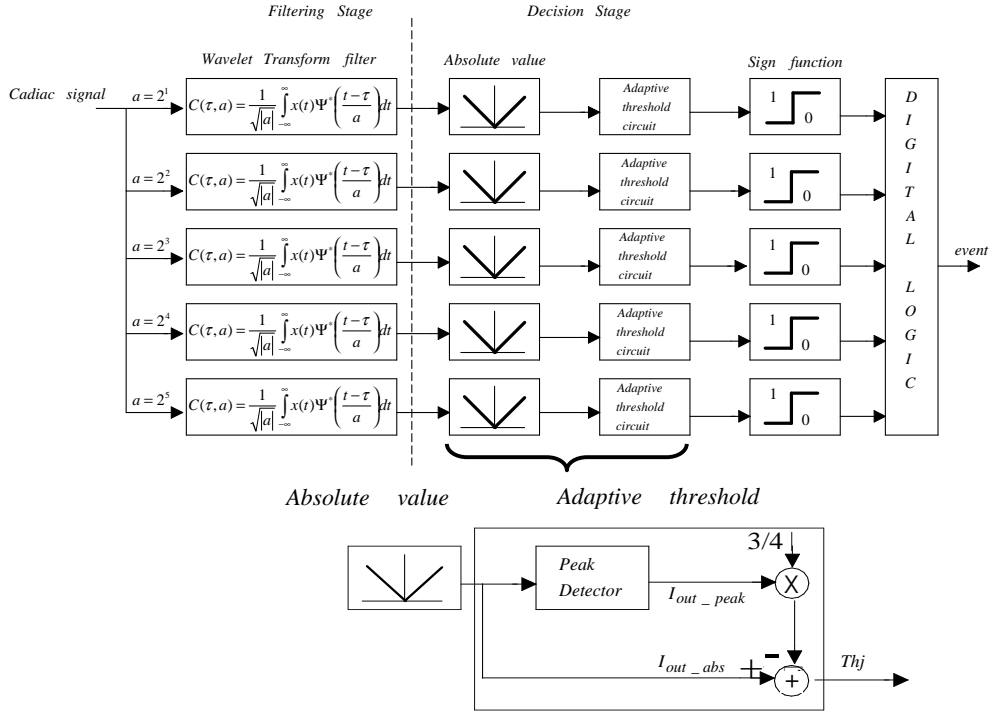


Figure 7.15: Block diagram of the wavelet system

### 7.2.1 Filtering stage - CFOS wavelet filter

We first propose an analog bandpass filter, of which the impulse response is an approximated first-derivative gaussian window function. In order to achieve this, we adapted the Wavelet Transform filter introduced in [7]. This filter has been implemented with a cascade of Complex First Order Systems (CFOS) [8].

We apply the DTL circuit technique to the design of the analog implementation of the WT. In Fig.3, the equivalent dynamic translinear circuit for realization of a CFOS is depicted. The related expressions are given by

$$\dot{I}_{x(re)} = \frac{I_o}{CV_T} I_{x(re)} - n \frac{I_o}{CV_T} I_{x(im)} + \frac{I_o}{CV_T} I_{u(re)} \quad (7.13)$$

$$\dot{I}_{x(im)} = \frac{I_o}{CV_T} I_{x(im)} + n \frac{I_o}{CV_T} I_{x(re)} + \frac{I_o}{CV_T} I_{u(im)} \quad (7.14)$$

where  $I_{u(re)}$  is the real input signal,  $I_{u(im)}$  is the imaginary input signal;  $I_{x(re)}$  and  $I_{x(im)}$  represent the real and imaginary part of the output signal, respectively.  $n$  is defined by  $n = \frac{\omega}{\sigma}$ , where  $\omega$  and  $\sigma$  are the corresponding parameters of the complex first order system equation in Chapter 4. In order to implement a Wavelet Transform, we need to be able to scale and shift this Gaussian function in time. By changing the values of the capacitance  $C$

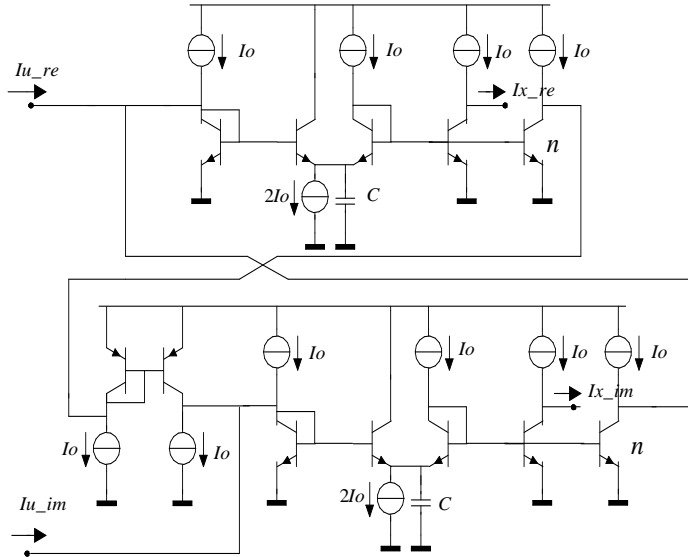


Figure 7.16: Equivalent DTL circuit for complex input for the analog CFOS stages

accordingly we implement short windows at high frequencies and long windows at low frequencies.

Fig. 7.17a shows the ideal impulse response of the wavelet filter with 3 CFOS stages, whereas in Fig.7.17b the simulated impulse response is presented. The number of stages has been chosen by trading time-frequency resolution (Chapter 4) for power consumption and noise contribution. For cardiac signal characterization, we are interested in the approximation to a first derivative Gaussian function, which is present in the imaginary output.

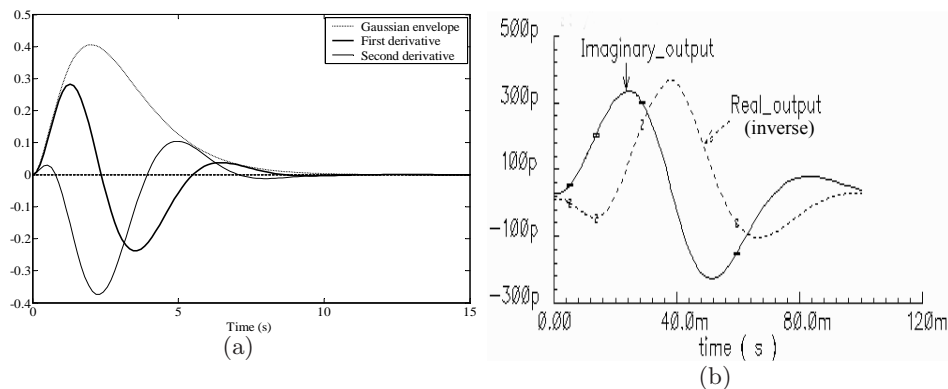


Figure 7.17: Impulse response of the wavelet filter with 3 CFOS stages (a) Ideal, (b) Simulated response

### 7.2.2 Decision stage - Absolute value and peak detector circuits

Fig. 7.18a. shows a simple circuit [9] to implement an absolute value function. Its operation is given as follows: when  $I_{in}$  is positive, it is handled by current-mirror Q1-Q2; when negative, it is conveyed to the summation node S by cascode transistor Q3. The bias voltage at the base of Q3 is obtained by the two diode-connected transistors Q4 and Q5. The basic design of the employed peak detector is shown in Fig. 7.18b. Its operation is as follows: When  $I_{in} > I_c, Q1$  (collector current of Q1), capacitor C is rapidly charged by Q4 until  $I_{in} = I_c, Q1$ . For  $I_{in} < I_c, Q1$ , C is discharged by the rather small base current of Q3. The comparator circuit described in Section 7.1 will also be used here.

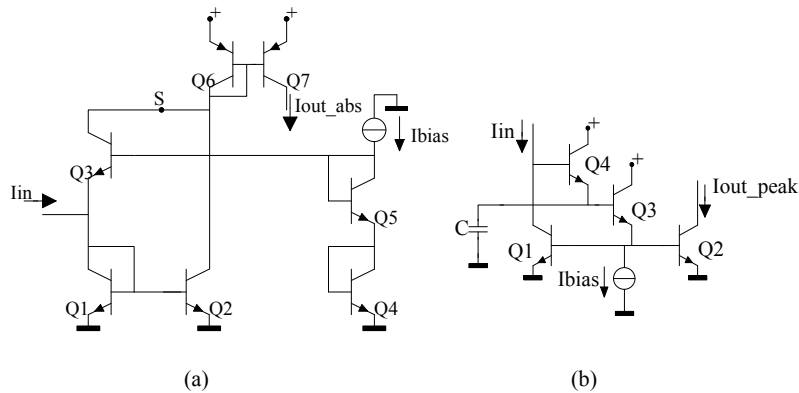


Figure 7.18: (a) Absolute value circuit (b) Peak detector circuit

The DC response of the absolute value circuit is given in Fig. 7.19a.  $|I_{in}|$  is also shown, for reference purposes. The transient responses of the absolute value and the peak detector circuits are provided in Fig. 7.19b, respectively, for a ventricular signal at the absolute circuit input.

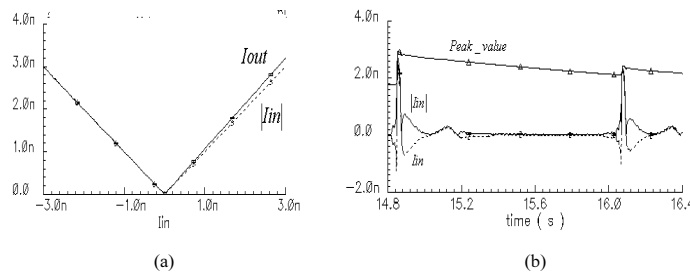


Figure 7.19: (a) DC Response of the absolute value circuit (b) Transient response of the absolute value and peak detector circuits with a ventricular signal at the input.

Finally, in order to verify the performance and efficiency of the whole system, a set of cardiac signals was applied to the input of the system. Fig.7.20a shows the ideal wavelet transform for 5 scales with a ventricular signal at the input. In Fig.7.20b gives the simulation result of 3 CFOS stages; one can see the similarity between the ideal WT and the WT from the CFOS filter.

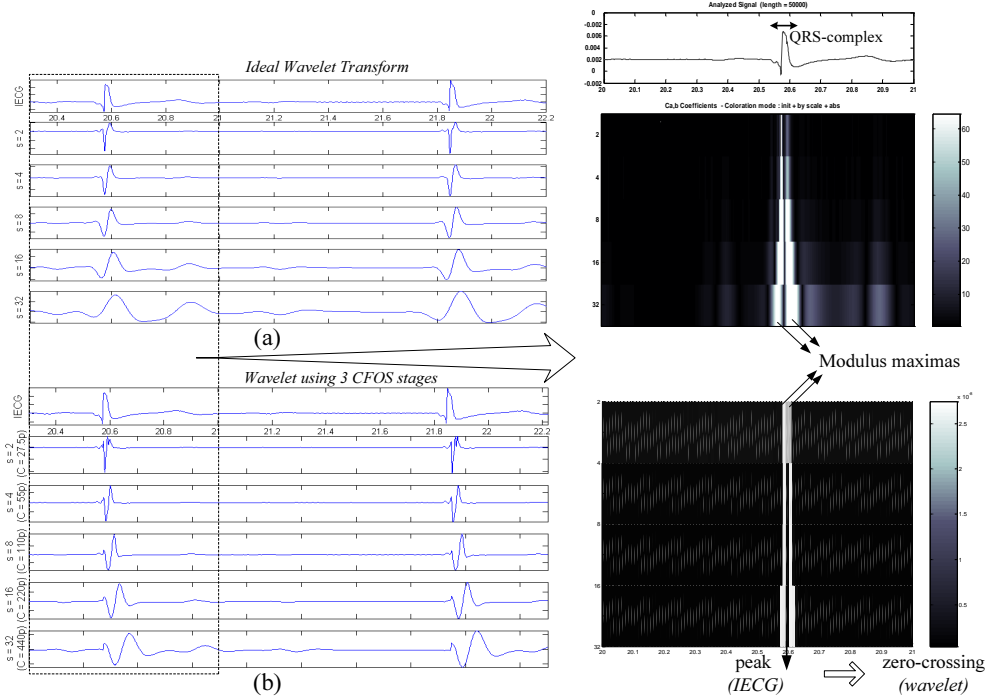


Figure 7.20: (a)Ideal wavelet transform (b)Wavelet using 3 CFOS stages

Then, to show the denoising property of the wavelet, we apply a noisy signal into the QRS detection system. Fig.7.21b shows a typical ventricular signal with 50Hz interference (input signal) and in Fig.7.21c gives the wavelet transform at various scales. We can see in Fig.7.21d that the modulus maxima of the QRS complex for a specific scale ( $a = 2^4$ ) of the WT indeed have been detected. The total power consumption is 55nW per scale.

### 7.2.3 Measurement results

A microphotograph of the circuit implemented in DIMES SIC3A IC process is shown in Fig.7.22. In this design, we have chosen to have off-chip capacitors. Hence, different wavelet scales can be obtained by simply using different capacitance values. From the characteristics of cardiac signals we have chosen to use the scales as defined in Table 7.2.

To check the performance of the wavelet filter, we will first measure its impulse response. Ideally, an impulse is defined as a pulse with infinite am-

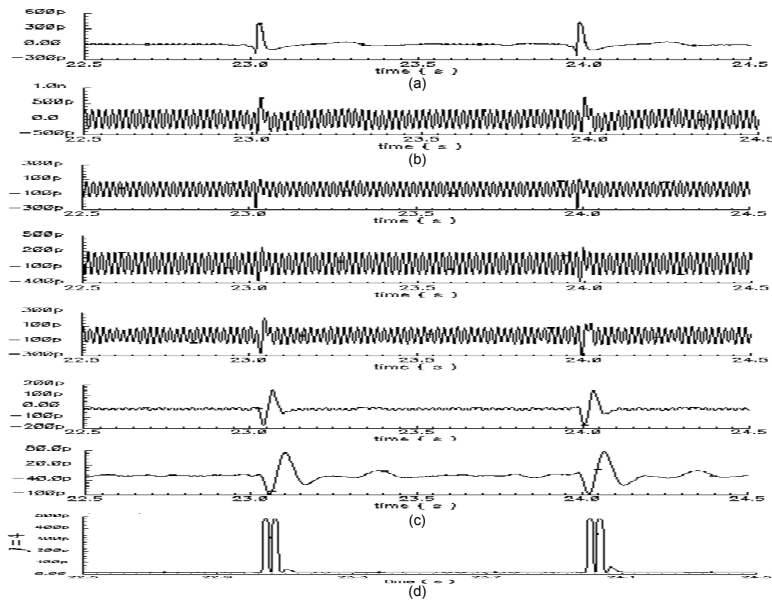


Figure 7.21: (a) Ventricular signal (b) Ventricular signal with 50Hz interference (c) the wavelet transform at five subsequent scales (d) QRS complex modulus maxima detection for  $j=4$ .

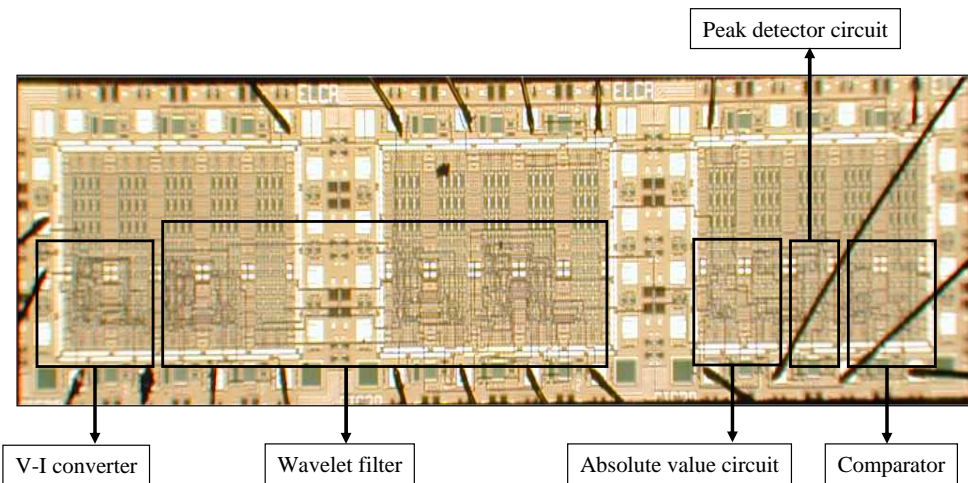


Figure 7.22: Chip microphotograph of the QRS-complex wavelet detection

plitude and zero width. Nevertheless, since the input signal is limited by the bias current of the filter, we can not apply an impulse of infinite height. Also, in order to deliver some energy to the circuit, we should give the pulse a finite length. Strictly speaking, the response to a finite length pulse is not the same as the mathematical impulse response. However, if the pulse length is short compared to the length of the dynamics in the impulse response, the difference

Table 7.2: Frequency response and capacitance value of the wavelet system  
at dyadic scales

| Scale $a$ | Capac. C(F) | Center Freq. (Hz) height |
|-----------|-------------|--------------------------|
| $2^1$     | 27.5p       | 174                      |
| $2^2$     | 55p         | 87                       |
| $2^3$     | 110p        | 43.5                     |
| $2^4$     | 220p        | 21.7                     |
| $2^5$     | 440p        | 11                       |

is negligible. Then, to measure properly the impulse response of the filter, we applied at the input an pulse signal of length 0.5ms. The imaginary and the real output response of the filter with a 165pF ( $3 \times 55\text{pF}$ ) total capacitance and a bias current  $I_o$  equals 1nA is given in Fig. 7.23.



Figure 7.23: Measured imaginary and real impulse responses

Fig.7.24 compares the measured impulse response from the imaginary output of the wavelet filter with the simulated and the ideal responses using 3 CFOS stages. As one can see, the responses are very similar which confirms the excellent performance of the filter.

As described above, the wavelet transform can be obtained by just scaling the impulse response of the filter in time. This is done by simply controlling the capacitance value C. Fig. 7.25a shows a 3-scales wavelet system by scaling the off-chip capacitors values from 27.5pF to 110pF with a factor of 2 (dyadic scales). The resulting center frequencies giving in Fig. 7.25b range from 174Hz to 43Hz. The value of current  $I_o$  equals 1nA.

The output transient response of the whole system, i.e., the filter, the absolute value and the comparator circuits, for a pulse input signal is given

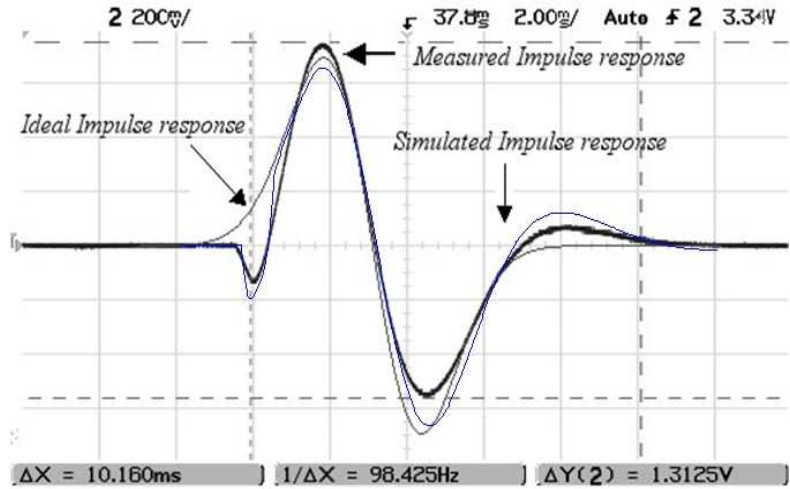


Figure 7.24: Comparison of the measured imaginary impulse response with the simulated and the ideal impulse responses using 3 CFOS stages

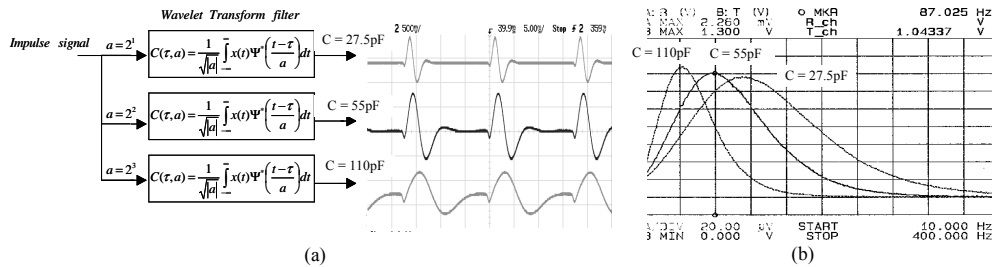


Figure 7.25: Measured (a) Impulse and (b) frequency response for 3 scales

in Fig. 7.26. The circuit operates from a 2-V supply voltage and dissipates in total 110nW per scale.

As stated before, wavelets allow analysis of the ECG signal focusing on the signal at various levels of detail. Analyzing the structure of the electrogram over multiple scales allows discrimination of electrogram features pertaining over all scales from those only seen at fine or coarse scales. As one can see in Fig. 7.26, at very fine scales (smaller values of scale  $a$ ), details of the electrogram, i.e. the QRS-complex, are revealed. At coarse scale (larger values of the scale factor  $a$ ), the overall structure of the electrogram can be studied while overlooking the details. Note that by this global view, the P-wave, the QRS-complex and the T-wave can be detected.

One important application of wavelet transforms is for in-band noise removal or denoising. The out of band noise can be removed by applying a linear time-invariant filtering approach (Fourier analysis). However, it cannot



Figure 7.26: Measured output transient of the filter, the absolute and the comparator circuits

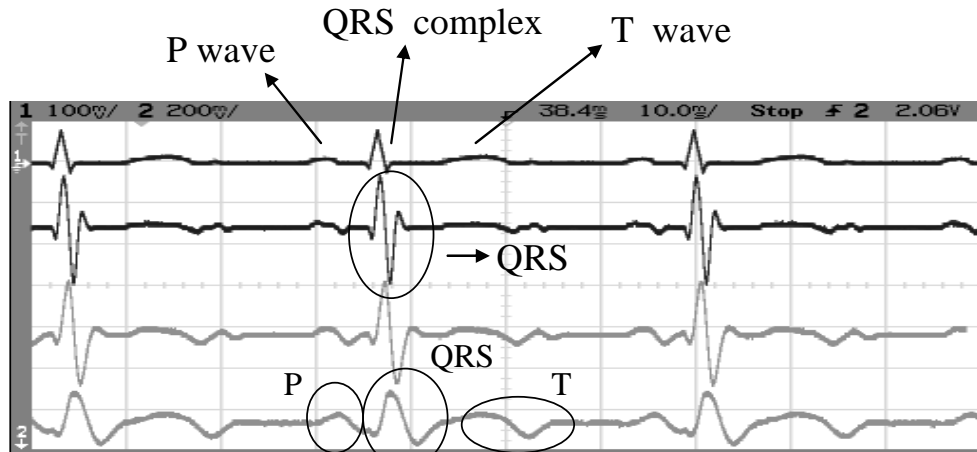


Figure 7.27: Measured output transient of the filter with an ECG input signal

be removed when it overlaps the signal spectrum. Being a multiscale analysis technique, the wavelet transform offers the possibility of selective noise filtering and reliable parameter estimation. Denoising is based on correlation factor (amplitude) discrimination. This feature can be used to distinguish cardiac signal points from noise and interferences, regardless of the frequency content of the noise. Fig. 7.28 shows a typical ventricular signal with additive white gaussian noise (a random signal with a flat power spectral density). One can see in Fig. 7.28 that the wavelet can effectively remove the in-band and out of band noise present in the signal and the modulus maxima of the QRS-complex is identified.

The measured performance of the QRS complex detection wavelet system are summarized in Tab. 7.3.

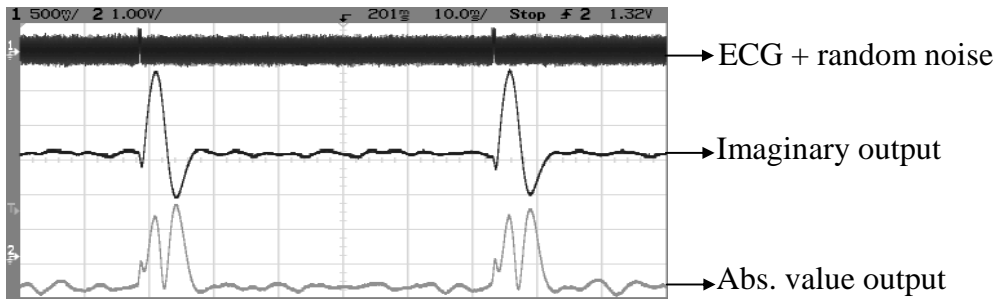


Figure 7.28: Measured output transient of the filter for an ECG input signal with additive random noise

Table 7.3: Measured performance of the QRS complex detection complex wavelet system

| Technology                                | Bipolar DIMES SIC3A |
|---|---------------------|
| Supply voltage                            | 2.0V                |
| Total bias current<br>(per scale)         | 55 nA               |
| CFOS bias current<br>(per scale)          | 35 nA               |
| Power consumption                         | 110 nW              |
| Eq. rms noise voltage @ input             | 130 $\mu$ V         |
| Dynamic range<br>(1-dB compression point) | 41 dB               |

## 7.3 Wavelet filter designs

### 7.3.1 Gaussian filters

In many biomedical research applications, the first order derivative of the Gaussian function, is a favorite mother wavelet [10], which is given by

$$\Psi(t) = -2 \cdot t \cdot e^{-t^2} \quad (7.15)$$

There are two reasons for the use of the Gaussian wavelet. The main reason is that the product of its time resolution and its frequency resolution takes the theoretical minimum value of 1/2. Consequently, a wavelet transform with the gaussian wavelet gives the most accurate estimation of frequency components localized in time. The second reason can be seen from detection theory. A certain waveform in a signal with additive gaussian white noise will be detected optimally if the impulse response of the filter is the time-reverse of that waveform. Applying this to the case of ECG analysis, we denote some

similarity between the contents of the ECG, particularly the QRS complex, and the gaussian wavelet. Therefore the first order derivative of the gaussian function is a good approximation to the 'matched' filter.

### Optimized Padé implementation using DTL circuits [11]

The first step of this implementation is the approximation of the ideal gaussian wavelet by using the Padé approach. On the basis of the mean-square error shown in Fig. 4.13.a, one can see that the [3/5] Padé approximation is a suitable candidate for implementation. It is almost symmetrical, it has almost no overshoot and its time-frequency resolution product is only 5% above the Heisenberg limit of 1/2, while its order 5, is reasonable. The corresponding transfer function is given by

$$H_{[3/5]}(s) = \frac{5.75s^3 - 18.3s^2 + 92.4s}{s^5 + 8.33s^4 + 33s^3 + 74.8s^2 + 94.5s + 52.3} \quad (7.16)$$

Second, the filter's state space description is optimized with respect to dynamic range, using the method presented in Section 5.2.1. The fully optimized state space description for the filter described by Eq. 7.16 is defined as

$$\begin{aligned} A &= \begin{bmatrix} -0.176 & 1.36 & 0.309 & 0.192 & 0.0792 \\ -1.80 & -0.283 & -0.194 & -0.547 & -0.122 \\ -0.734 & -0.346 & -0.257 & -1.34 & -0.201 \\ 0.912 & 1.95 & 2.67 & -1.73 & -1.38 \\ -2.11 & -2.46 & -2.26 & 7.77 & -5.88 \end{bmatrix} \\ B &= \begin{bmatrix} 0.593 \\ 0.753 \\ 0.717 \\ -1.86 \\ 3.43 \end{bmatrix} \quad C^T = \begin{bmatrix} 0.121 \\ -0.115 \\ -0.0615 \\ -0.08 \\ -0.026 \end{bmatrix} \end{aligned} \quad (7.17)$$

And the normalized capacitance distribution becomes

$$\text{Cap} = C (0.342 \ 0.304 \ 0.168 \ 0.146 \ 0.039) \quad (7.18)$$

where  $C$  represents the unit-less value of the total capacitance. Compared to a straightforward implementation, i.e. canonical form, the dynamic range of the optimized state space description has increased by approximately 20 dB.

Next, we will design the circuit implementing our wavelet filter, based on the multiple-input log-domain integrator. The multiple-input log-domain integrator is shown in Fig. 7.29. The operation of the circuit is as follows. A positive voltage across the base-emitter junction of Q1 causes a collector current, which discharges the capacitance through the collector-base connection. A positive voltage across the base-emitter junction of Q2 causes a collector current, which charges the capacitance via the current mirror on top. The net current flowing into the capacitance is the difference of collector currents from

the positive and negative input side.  $V_{ip}$  and  $V_{in}$  are the positive and negative input currents, respectively. In addition, we implement the state space coefficients ( $a_{ij}$  or  $b_i$ ), by placing constant voltage sources,  $V_{mp}$  and  $V_{mn}$ , in series with each base-emitter junction. Finally, we propose to subtract a constant number  $\alpha$  of each  $\exp()$  term in order to perform the integration operation for both positive and negative input variables. This is implemented by the transistors Q3 and Q4 and the constant voltages sources  $V_{bp}$  and  $V_{bn}$ , respectively. An alternative view on subtracting a constant number is defining the operating point. This is basically the same as biasing. However, in contrast to the regular design of linear circuits, we cannot separate the design of the signal processing function and the design of the bias function. Since the circuit is nonlinear and intended to be used in the large signal range, the superposition principle is not valid. Therefore, the biasing function is an integrated part of the signal processing design. Thus, the current flowing into the capacitance is defined as

$$\begin{aligned} I_{cap} = C\dot{V}_{cap} &= I_s e^{\left(\frac{V_{cap} + V_{mp} - V_{ip}}{V_T}\right)} - I_s e^{\left(\frac{V_{cap} + V_{mn} - V_{in}}{V_T}\right)} \\ &+ I_s e^{\left(\frac{V_{cap} + V_{bp}}{V_T}\right)} - I_s e^{\left(\frac{V_{cap} + V_{bn}}{V_T}\right)} \end{aligned} \quad (7.19)$$

with

$$V_{mp,mn} = V_T \ln \left( \frac{(a_{ij}, b_i) \cdot C_i V_T}{I_s} \right) \quad (7.20)$$

$$V_{bp,bn} = \alpha V_{mp,mn} \quad (7.21)$$

where  $a_{ij}$ ,  $b_i$  are the multiplication coefficients of the matrix A or matrix B in the state space description.  $V_{mp,mn}$  are the positive and negative multiplication voltages respectively.  $V_{bp,bn}$  are the positive and negative voltages which implement the biasing function.  $I_s$  is the saturation current.

In order to maintain the overall linearity of a log-domain system, a LOG stage must be added to the input, while an EXP stage is required at the output. The LOG and EXP stages are shown in Fig. 7.30. By adding a summation stage at the output, we can obtain the expression for output current. The nullors can be implemented by a cascade of a common-collector and a common-emitter stage, or, in case of a BiCMOS process, a single common-source stage.

A block schematic of the total filter is drawn in Fig. 7.31. The A-matrix, B-matrix and C-matrix each have five connections to the capacitances.

The state space representation for a fifth order system can be written as

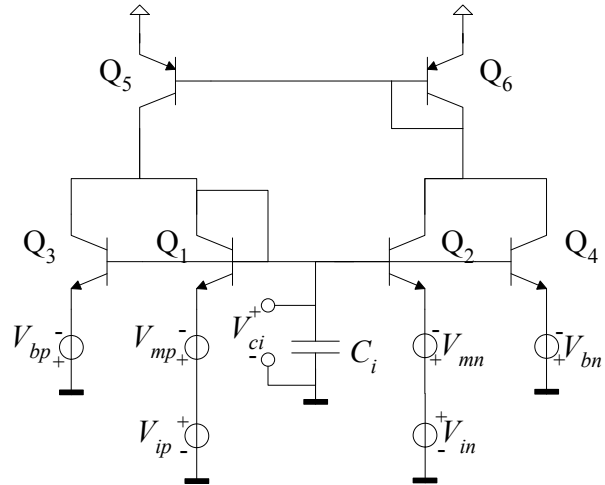


Figure 7.29: Log-domain integrator

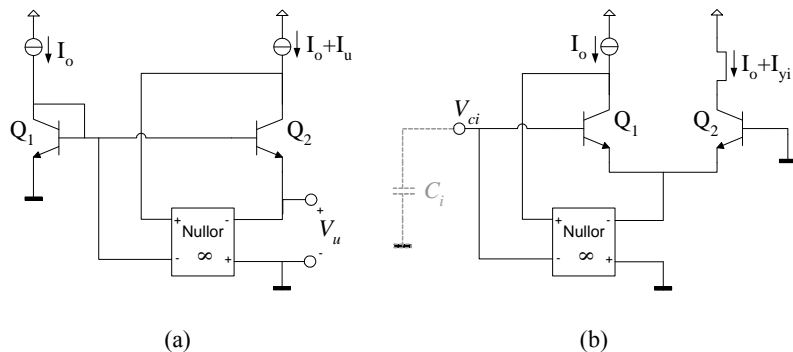


Figure 7.30: (a) LOG stage (b) EXP stage

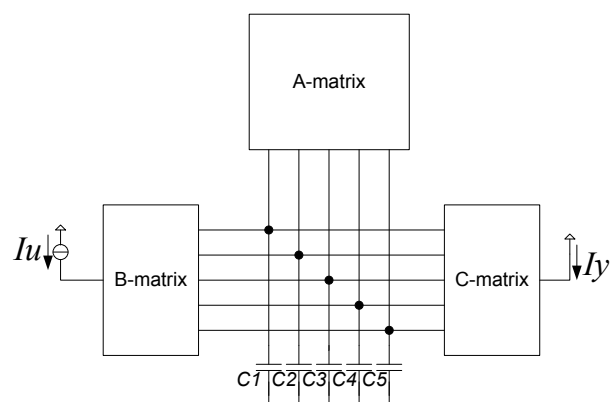


Figure 7.31: (Block diagram of the complete system

$$\begin{aligned}\dot{x}_i &= \sum_{j=1}^5 \tau^{-1} a_{ij} x_j + b_i u \\ y &= \sum_{i=1}^5 c_i x_i\end{aligned}\quad (7.22)$$

where  $\tau = \frac{C V_T}{I_o}$  represents the time constant of the filter. We define the five states  $x_1$  to  $x_5$  with an exponential relation to the capacitance voltages  $V_{c1}$  to  $V_{c5}$ . The input signal  $u$  and output signal  $y$  are linearly related to the currents  $I_u$  and  $I_y$ . So the correspondence relation is defined as

$$\begin{aligned}I_{Ci} &= - \sum_{j:a_{ij}>0} |a_{ij}| \tau^{-1} C_i V_T e^{\left(\frac{V_{Ci}-V_{Cj}}{V_T}\right)} + \sum_{j:a_{ij}<0} |a_{ij}| \tau^{-1} C_i V_T e^{\left(\frac{V_{Ci}-V_{Cj}}{V_T}\right)} \\ &+ \sum_j a_{ij} \tau^{-1} C_i V_T e^{\left(\frac{V_{Ci}}{V_T}\right)} - b_i I_o I_u e^{\left(\frac{V_{Ci}}{V_T}\right)} \\ &= - \sum_{j:a_{ij}>0} |a_{ij}| I_o e^{\left(\frac{V_{Ci}-V_{Cj}}{V_T}\right)} + \sum_{j:a_{ij}<0} |a_{ij}| I_o e^{\left(\frac{V_{Ci}-V_{Cj}}{V_T}\right)} \\ &+ \sum_j a_{ij} I_o e^{\left(\frac{V_{Ci}}{V_T}\right)} - b_i I_o I_u e^{\left(\frac{V_{Ci}}{V_T}\right)}\end{aligned}\quad (7.23)$$

and

$$I_y = \sum_{i=1}^5 c_i \left( I_o e^{\left(\frac{V_{Ci}}{V_T}\right)} - I_o \right) \quad (7.24)$$

We see that the terms of the capacitance current have the same form as in Eq.7.19 and thus the state space matrices can be implemented by interconnecting multiple-input log-domain integrator stages.

To check the circuit performance, the system has been simulated using models of our in-house bipolar semi-custom IC process, SIC3A. The circuit has been designed to operate from a 2-V supply voltage. First, we have set  $\tau = 1\text{ms}$ , which gives  $I_o = 1\text{nA}$  and  $C = 40\text{pF}$ . The impulse response of the circuit was simulated by applying an input pulse waveform of length  $0.1\mu\text{s}$  and of height  $1\text{nA}$ . The acquired output signal is plotted in Fig. 7.32. The output current presents an offset of approximately  $80\text{pA}$ . For illustration we have added the plots of the mathematical impulse response of the original state space filter and the delayed first derivative of the Gaussian.

As we can see in Fig. 7.32, the simulated impulse response differs only slightly from the approximated response, which was acquired directly from the, Padé approximation. We conclude that the coefficients have been implemented successfully.

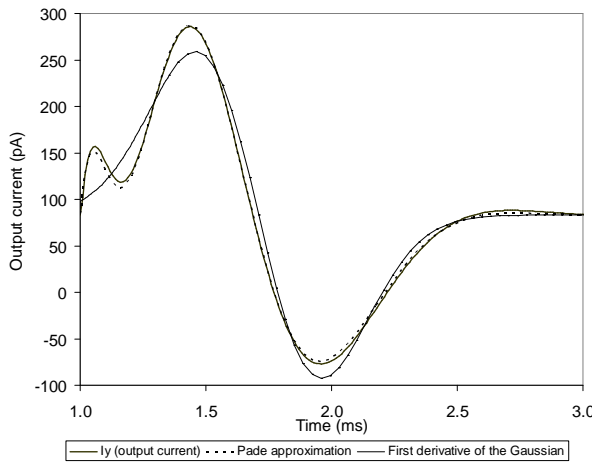


Figure 7.32: Simulated Impulse response of the filter

### $L_2$ approximation employing CMOS triode-transconductors

The filter design that follows is based on an orthonormal ladder structure and employs the  $nA/V$  and the  $pA/V\Delta - G_m$  transconductors described in Sections 6.1.1 and 6.1.2, respectively.

The wavelet base approximation using the proposed  $L_2$  approach is given in Fig. 7.33, where the first derivative of a Gaussian wavelet base (gaus1) has been approximated using the corresponding 6th-order transfer function

$$H_{[4/6]}(s) = \frac{-0.16s^4 + 8.32s^3 - 6.64s^2 + 139s}{s^6 + 5.9s^5 + 30.5s^4 + 83.1s^3 + 163s^2 + 176s + 93.3} \quad (7.25)$$

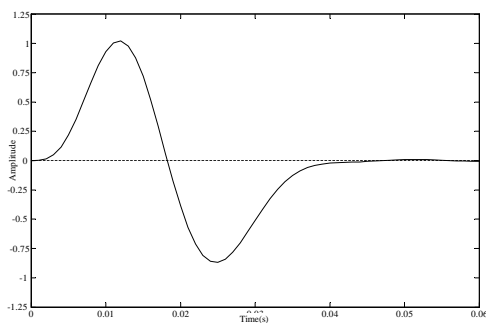


Figure 7.33: 6th-order  $L_2$  approximation of the gaus1

The block diagram of the wavelet filter is given in Fig. 7.34, where two different transconductors have been employed as the basic building block, being the  $nA/V$  and the  $pA/V\Delta - G_m$  (with  $\Delta = 0.4$ ) transconductors. The values of  $G_m$  and the total capacitance, required to implement the transfer function

in Eq.7.25, are also shown in Fig. 7.34. Note that, maintaining the same time constant for both transconductors and using the  $\Delta - G_m$  block with  $\Delta = 0.4$ , we are able to reduce the corresponding  $G_m$  values, and, consequently reduce the total capacitance by a factor of 0.4.

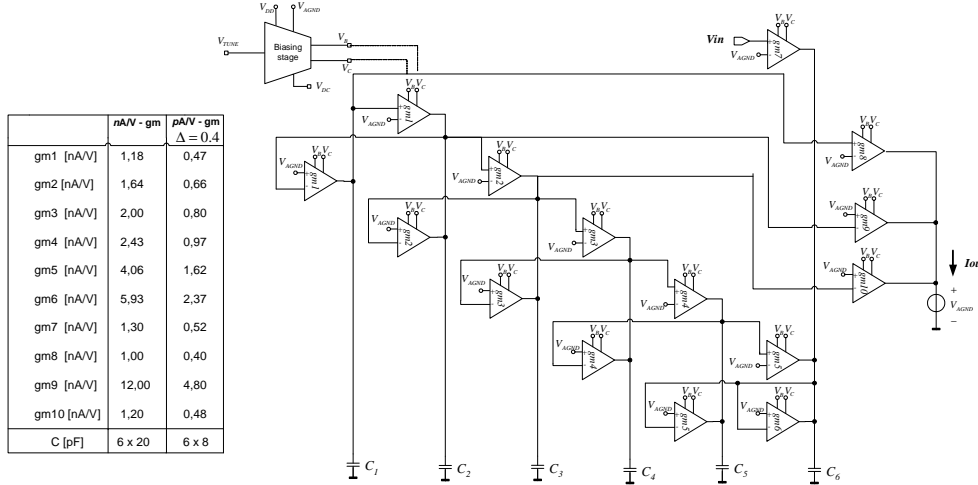


Figure 7.34: Block diagram of the wavelet filter

The wavelet  $G_m$ -C filters have been simulated using AMS's 0.35/ $\mu$ m CMOS transistors model. In order to implement the different coefficients of the state-space representation we can vary the width of transistors  $M_{1A}$  and  $M_{1B}$ , as mentioned before. Fig. 7.35 shows the simulated impulse response of the wavelet filter for  $V_{TUNE} = 20$ mV . The excellent approximation of the first Gaussian wavelet (gaus1) can be compared with the obtained L2-approximated function to confirm the performance of the Gm-C filter. The total filter's current consumptions, using the  $nA/V$  and the  $pA/V\Delta - G_m$  transconductors, are 56nA and 114nA, respectively, operating from a 1.5-V supply voltage. The performance of the filters is summarized in Table 7.4.

Finally, to implement a Wavelet Transform, we need to be able to scale and shift in time (and, consequently in frequency) the gaus1 function. By changing the values of the  $V_{TUNE}$  accordingly we implement different scales, while preserving the impulse response waveform, as one can see in Fig. 7.36a. Fig. 7.36b illustrates 4 dyadic scales with center frequencies ranging from 14Hz to 120Hz for  $V_{TUNE}$  varying from 10mV to 80mV, respectively.

### 7.3.2 Complex Wavelet filter implementation

In this design we present an analog implementation of the complex Gabor wavelet transform using the Padé approximation. The complex wavelet filter design is based on the combination of the real and the imaginary state-space descriptions that implement the respective transfer functions. In other words,

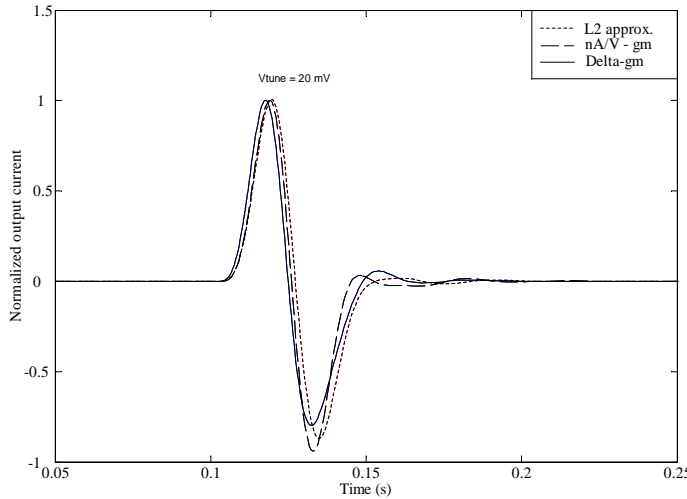
Figure 7.35: Simulated and  $L_2$ -approximated impulse response

Table 7.4: Performance of the wavelet filters

|                                      | $n\mathbf{A}/\mathbf{V} - \mathbf{G}_m$ | $p\mathbf{A}/\mathbf{V} - \mathbf{G}_m (\Delta = 0.4)$ |
|--------------------------------------|---|--|
| Technology                           | $0.35\mu\text{m}$ CMOS                  |  |
| Minimum $G_m$ [nA/V]                 | 1                                       | 0.4  |
| $G_m$ variation [%]<br>(Monte Carlo) | 2.7                                     | 2.9  |
| Total capacitance [pF]               | 120                                     | 48   |
| $V_{TUNE}$ [mV]                      | 20                                      | 20   |
| Filter power [nW]                    | 51                                      | 114  |
| Supply voltage                       | 1.5V                                    | 1.5V   |
| Input RMS noise [ $\mu\text{V}$ ]    | 119                                     | 460  |
| THD [dB]                             | -53                                     | -51  |

a complex filter is implemented by an ordinary state-space structure for the real part and an extra  $C$  matrix for the imaginary part [12].

The Gabor wavelet is obtained from a complex Gaussian function (complex exponential windowed by a Gaussian function) as basic functions, as described by

$$\psi(t) = C \cdot e^{-j\omega t} e^{-t^2} = C \cos(\omega t) e^{-t^2} - j C \sin(\omega t) e^{-t^2} \quad (7.26)$$

where  $e^{-j\omega t} e^{-t^2}$  is the complex Gaussian function and  $C$  is a normalizing constant. From the Gabor wavelet one can derive some complex wavelet families, e.g. the complex Gaussian and the complex Morlet. The complex Morlet wavelet is obtained by simply applying  $\omega = \pi \sqrt{\frac{2}{\ln 2}} \simeq 5.3364$  [13] in Eq.7.26.

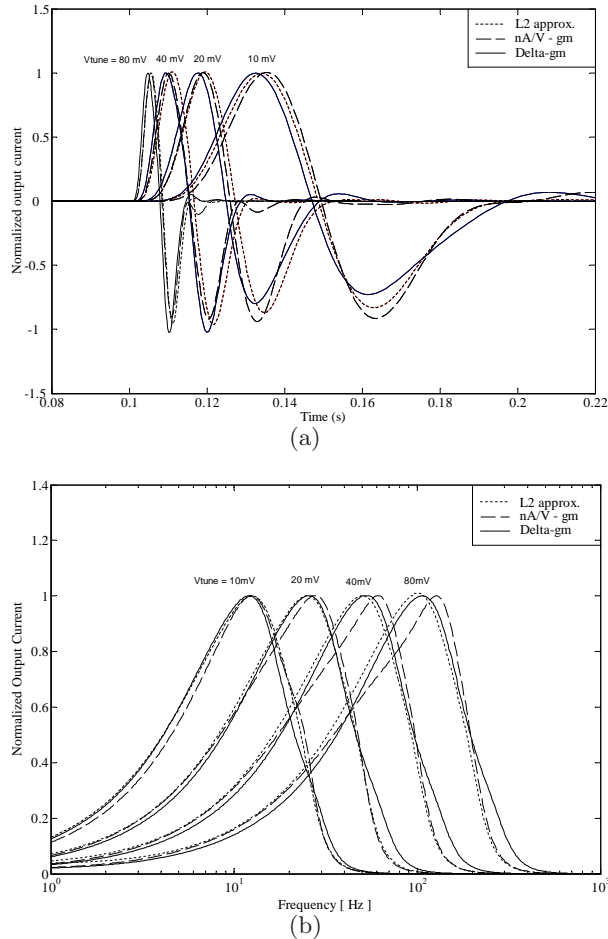


Figure 7.36: Wavelet filter scaling by changing  $V_{TUNE}$  (a) Impulse response, (b) Frequency response

The complex Gaussian wavelet family is defined from the derivatives of the Gabor wavelet [14] and is given by

$$\psi_n(t) = C_n \cdot \frac{d^n}{dt^n} (e^{-j\omega t} e^{-t^2}) \quad (7.27)$$

where  $n$  denotes the order,  $\frac{d}{dt}$  is the symbolic derivative and  $C$  is a normalizing constant, which depends of  $n$ .

In order to implement the complex Gabor wavelet filter, we first apply a [2/5] Padé approximation (i.e.  $m = 2$  and  $n = 5$ , which yields an approximation of order  $k = 7$  of the Taylor series expansion) to obtain the Gaussian envelope. The transfer function resulting from this approximation is given by

$$H_{gaus}(s) = \frac{5.7s^2 - 18.2s + 92.416}{s^5 + 8.3s^4 + 33s^3 + 74.8s^2 + 94.5s + 52.3} \quad (7.28)$$

To obtain the transfer function of the real and the imaginary parts of the Gabor function in Eq.7.26 one can easily apply

$$H_{Gabor}(s) = \frac{s}{s^2 + \omega^2} * H_{gaus}(s) - j \frac{\omega}{s^2 + \omega^2} * H_{gaus}(s) \quad (7.29)$$

where the asterisk  $*$  is the symbol for convolution and  $\frac{s}{s^2 + \omega^2}$  and  $\frac{\omega}{s^2 + \omega^2}$  are the Laplace transforms of  $\cos(\omega t)$  and  $\sin(\omega t)$ , respectively. Notice that both transfer functions are related by

$$H_{Real}(s) = -\frac{s}{\omega} * H_{Imag}(s) \quad (7.30)$$

From Eq.7.30, one can verify that the poles of the real and the imaginary transfer function are the same, only differing in the zeros. Therefore, we can implement both transfer functions by changing only the C-matrix of the state-space representation, as shown in Fig.7.37.

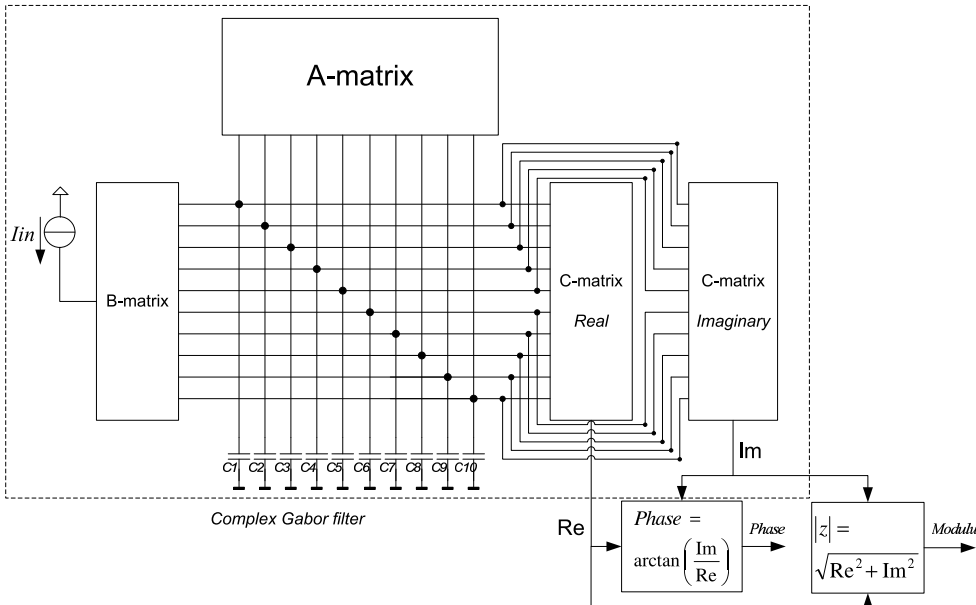


Figure 7.37: Block diagram of the Complex Wavelet system

Using the procedure described in Eq.7.29, yields tenth order transfer functions with 7 zeros. Its corresponding impulse responses are given in Fig.7.38.

### Circuit design

The filter design that follows is also based on an orthonormal ladder structure and the bipolar multiple-input low-power log-domain integrator presented in Section 6.3.1 will be used as the basic building block for the implementation of the tenth order state space equations of the Gabor wavelet filter.

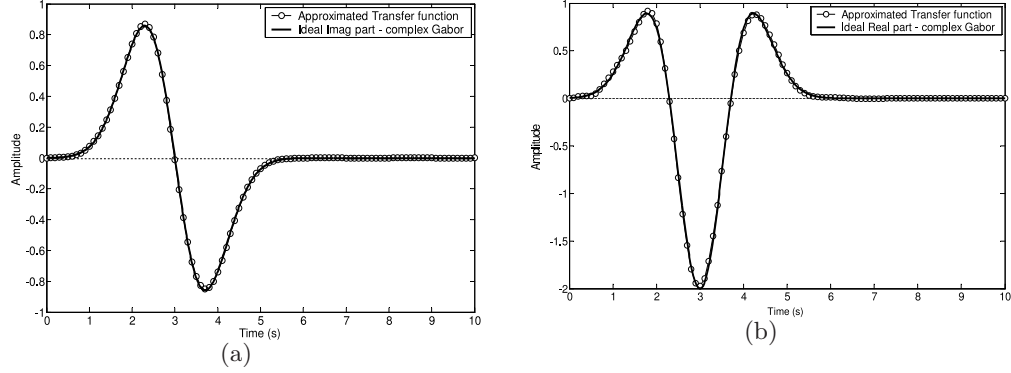


Figure 7.38: Complex Gabor Impulse response approximation (a) Imaginary output (b) Real output

The static translinear principle can be applied to the implementation of the required nonlinear transfer functions of the modulus and arctangent stages. First, the required modulus function  $|z| = \sqrt{Re^2 + Im^2}$  is realized with the circuit in Fig.7.39(a) [3]. The translinear loops in the circuit consist of transistors  $Q_1, Q_7, Q_8$  and  $Q_4$  and  $Q_6, Q_{11}, Q_{10}$  and  $Q_4$ , implementing

$$\begin{aligned} 2(I_o - Re)(I_o + Re) &= (\sqrt{2}I_o - z)(\sqrt{2}I_o + z + p) \\ 2(I_o - Im)(I_o + Im) &= (\sqrt{2}I_o - z)(\sqrt{2}I_o + z - p) \end{aligned} \quad (7.31)$$

where  $I_o$  is the bias current and  $p$  is a coupling parameter equal to  $\frac{2Re^2 - z^2}{z - \sqrt{2}I_o}$ . Notice that both variables,  $Re$  and  $Im$ , are bipolar quantities.

From the complex waveforms shown in Fig.7.38, we can now obtain the phase information by simply applying the arctangent to the ratio between the imaginary and the real outputs. This operation can be approximated using the translinear principle as [4]

$$Phase = \frac{Im}{0.63Re + \sqrt{0.88Re^2 + Im^2}} \simeq \frac{2}{\pi} \arctan\left(\frac{Im}{Re}\right) \quad (7.32)$$

where the square root term is provided by the modulus circuit in previous section. The division operation can easily be implemented using the factorization  $z = \frac{x}{y} \Rightarrow \frac{I_o+z}{I_o-z} = \frac{y+x}{y-x}$  [3] and the schematic is given in Fig.7.39(b) [15]. We have simulated the filter, the modulus stage and the phase stage using models of IBM's  $0.18\mu m$  BiCMOS IC technology. The filter has been designed to operate from a  $1.2V$  supply and a  $100pF$  total capacitance. Fig.7.40 shows the impulse response of the real and imaginary outputs of the wavelet filter. The excellent approximation of the complex Gabor wavelet can be compared with the ideal Gabor function to confirm the performance of the filter. Finally,

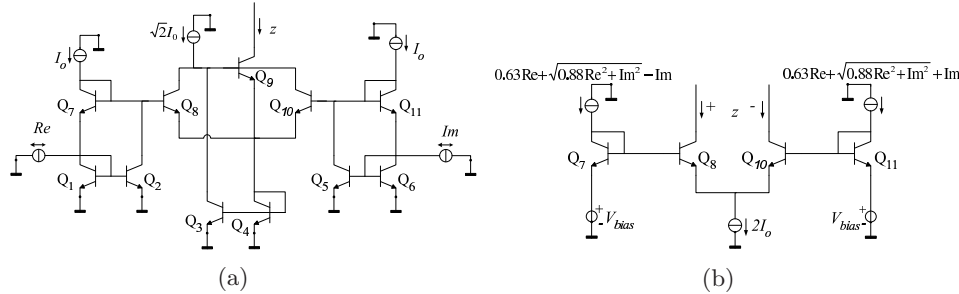


Figure 7.39: (a) Modulus (Vector magnitude) circuit [3] (b) Divider circuit for the Arctangent stage [15]

Fig.7.41 shows the modulus stage and phase stage outputs, which are close to the ideal cases for the complex Gabor wavelet in Fig.3.8.

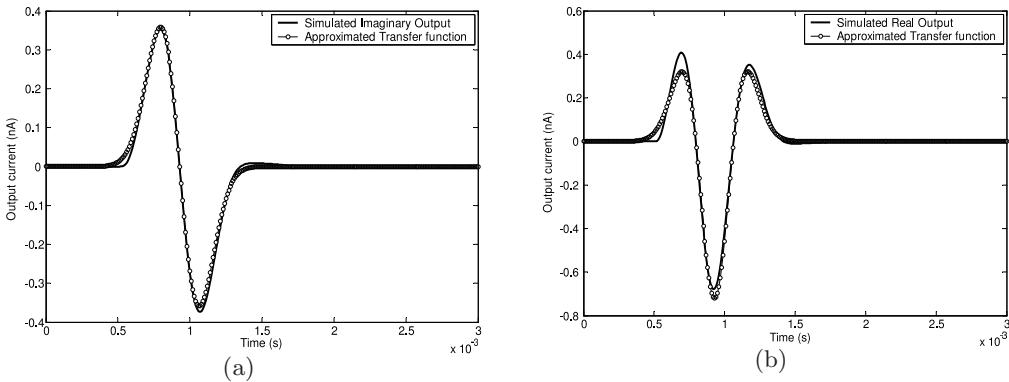


Figure 7.40: Simulated impulse responses of the complex Gabor wavelet filter  
 (a) Imaginary output (b) Real output

## 7.4 Morlet Wavelet Filter

The discussion in this section shall be related to the design and implementation of a Morlet wavelet filter [16].

The Morlet wavelet base is obtained from a Gaussian envelope multiplied by a cosine function (cosine windowed by a Gaussian function) [14], and is described by

$$\psi(t) = \cos(5\sqrt{2}(t-3))e^{-(t-3)^2} \quad (7.33)$$

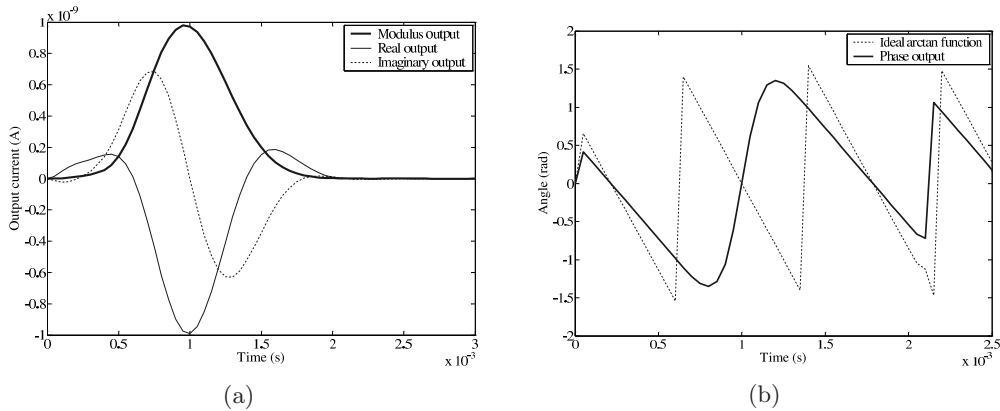


Figure 7.41: Simulated complex Gabor wavelet filter (a) Modulus and (b) Phase responses

In order to control the frequency range of the wavelet system and the respective scales, one can add a time constant term  $\tau$  into Eq.7.33, resulting in

$$f(t) = \cos\left(\frac{5\sqrt{2}}{\tau}(t - 3 \cdot \tau)\right) e^{-\left(\frac{t-3 \cdot \tau}{\tau}\right)^2} \quad (7.34)$$

and the corresponding Fourier transform is giving by

$$F(\omega) = \frac{\sqrt{\pi}}{2} \left( e^{-\frac{1}{4}\left(\frac{\omega-5\sqrt{2}\cdot\tau^{-1}}{\tau^{-1}}\right)^2} + e^{-\frac{1}{4}\left(\frac{\omega+5\sqrt{2}\cdot\tau^{-1}}{\tau^{-1}}\right)^2} \right) \quad (7.35)$$

The time and frequency response of the Morlet wavelet base are given in Fig.7.42. Note that by changing  $\tau$  the Q-factor of the filter remains constant and in this case is equal to 2,55.

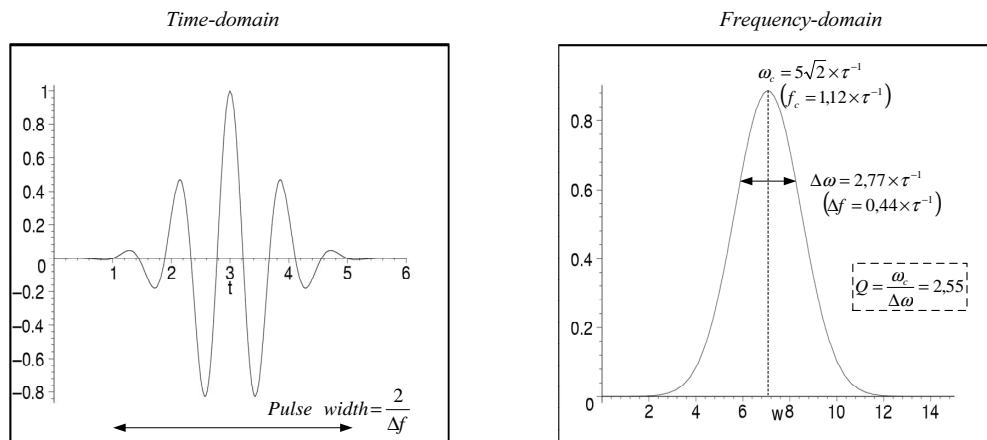


Figure 7.42: Ideal Morlet function. Time and frequency response

As described before, the Padé approximation has some convergence problems when one tries to approximate a function with many oscillations, such as the Morlet wavelet. Thus, in Section 7.4 we presented a generalized procedure for implementing analog filters of various types of wavelet bases. The results obtained from the use of this method for have been illustrated in Fig.4.11 and in Table 4.4.

The flow chart in Fig. 7.43. summarizes the implementation of this procedure to obtain the tenth-order Morlet wavelet filter transfer function.

From the discussion in Chapter 5, we opt again for an orthonormal state space representation. The  $A$ ,  $B$  and  $C$  matrices of this structure for the defined transfer function are given by

$$A = \begin{bmatrix} 0 & 6.54 & 0 & 0 & 0 & 0 & 0 & 0 & 0 & 0 \\ -6.54 & 0 & 1.83 & 0 & 0 & 0 & 0 & 0 & 0 & 0 \\ 0 & -1.83 & 0 & 6.59 & 0 & 0 & 0 & 0 & 0 & 0 \\ 0 & 0 & -6.59 & 0 & 2.72 & 0 & 0 & 0 & 0 & 0 \\ 0 & 0 & 0 & -2.72 & 0 & 6.37 & 0 & 0 & 0 & 0 \\ 0 & 0 & 0 & 0 & -6.37 & 0 & 3.89 & 0 & 0 & 0 \\ 0 & 0 & 0 & 0 & 0 & -3.89 & 0 & 6.27 & 0 & 0 \\ 0 & 0 & 0 & 0 & 0 & 0 & -6.27 & 0 & 5.88 & 0 \\ 0 & 0 & 0 & 0 & 0 & 0 & 0 & -5.88 & 0 & 10.47 \\ 0 & 0 & 0 & 0 & 0 & 0 & 0 & 0 & -10.47 & -13.31 \end{bmatrix} \quad (7.36)$$

$$B = \begin{bmatrix} 0 \\ 0 \\ 0 \\ 0 \\ 0 \\ 0 \\ 0 \\ 0 \\ 0 \\ 2.05 \end{bmatrix}$$

$$C = [ 0.75 \ -1.34 \ 0.75 \ 0.68 \ -0.57 \ 0.44 \ -0.002 \ -0.10 \ 0.04 \ 0 ]$$

In this case, the objective functional becomes  $F_{DR} = 147.90$ , which is not so far from the optimum case ( $F_{DR} = 96.98$ ), which is the absolute minimum value of the objective functional associated with this transfer function. The Dynamic Range has decreased by only 1.83dB. Finally, the normalized capacitance distribution is given by  $(C_1, \dots, C_{10}) = C'(0.142, 0.162, 0.110, 0.117, 0.086, 0.091, 0.073, 0.080, 0.073, 0.061)$ , where  $C'$  represents the unit-less value of the total capacitance when expressed in F.

#### 7.4.1 Circuit design

By applying a simple mapping to the linear state-space equations (7.36), we can obtain the corresponding log-domain circuit realization which employs the log-domain integrator cell. Note that the implemented filter is a tenth order filter.

The block diagram of the log-domain implementation of (7.36) is illustrated in Fig.7.44, using the log-domain integrator cell described in Section 6.3.1 [17]. Note that each column of the filter structure corresponds to a row in the state-space formulation. The parameter  $A_{ij}$  is implemented by the corresponding

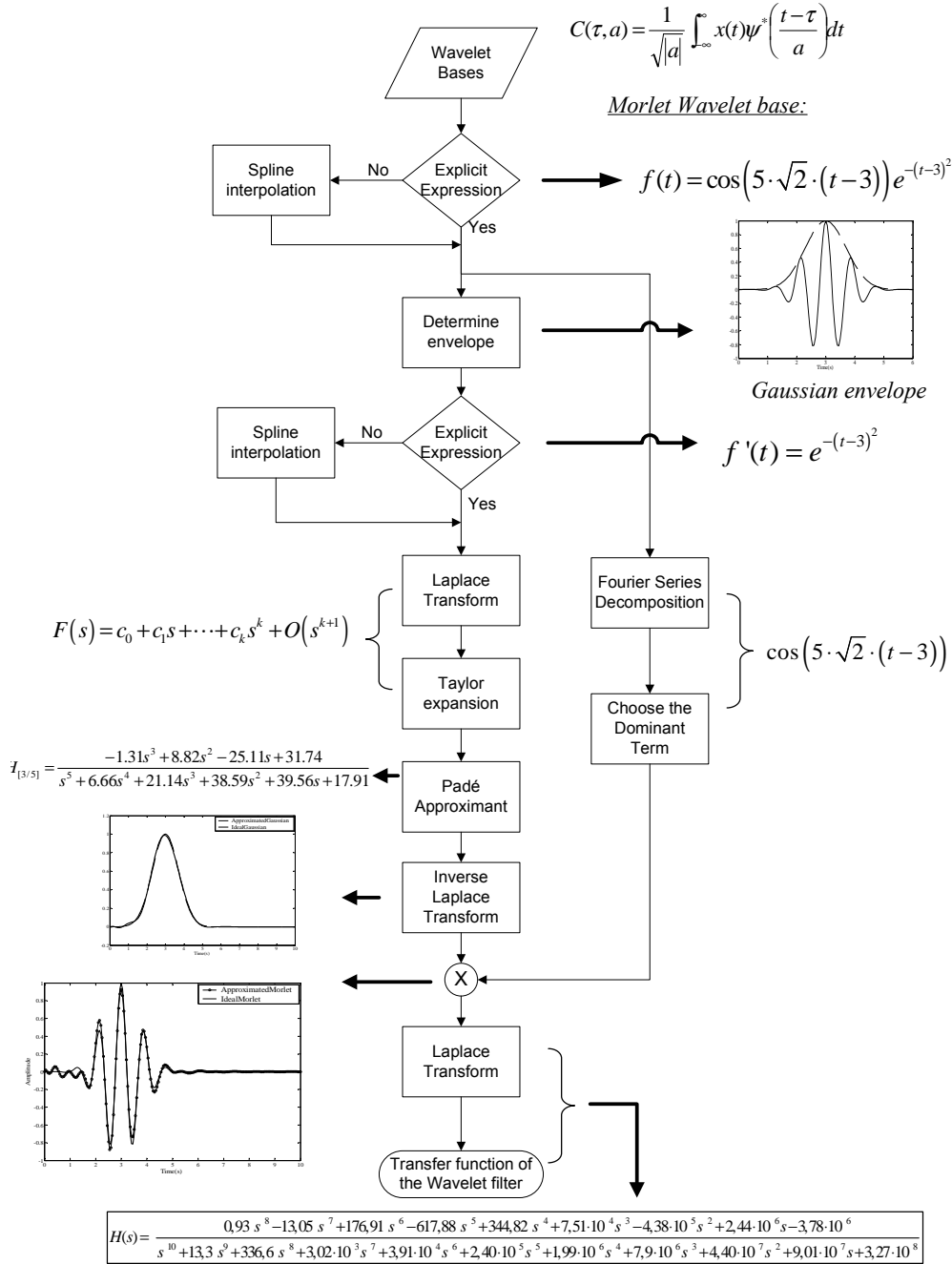


Figure 7.43: Flowchart of the wavelet base approximation

log-domain integrator with bias current  $I_{A_{ij}}$ , defined by

$$I_{A_{ij}} = A_{ij} \cdot \frac{2\pi\tau^{-1}}{2Q} C_i V_T \quad (7.37)$$

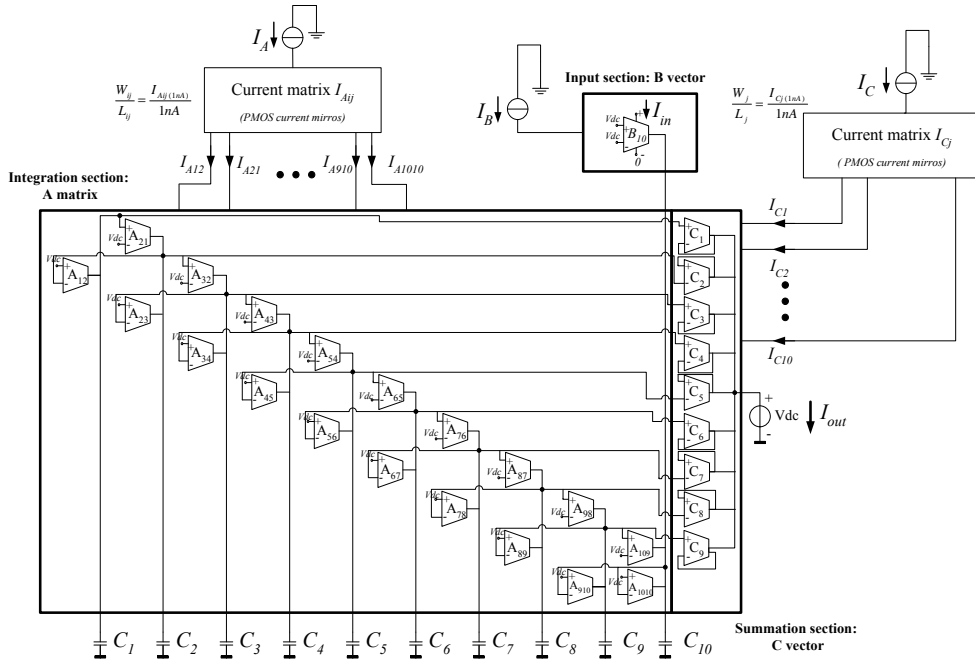


Figure 7.44: Complete State-space filter structure

where  $\tau^{-1}$  and  $Q$  are, respectively, the inverse of the time constant and the quality factor mentioned in Section 3.6 and  $C_i$  represents the  $i$ -th capacitance of the filter. The input section, as governed by the state-space vector  $B$ , can be defined as the input  $LOG$  operator and is realized by the first row from the top of Fig.7.44. The current  $I_{Bi}$  is related to the parameter  $B_i$  by

$$I_{Bi} = B_i \cdot \frac{2\pi\tau^{-1}}{2Q} C_i V_T \quad (7.38)$$

In the orthonormal case, only one non-zero parameter of the  $B$  vector is present ( $B_{10}$ ). Consequently,  $I_{Bi} = I_B$ . Finally, in order to restore the overall system linearity one should realize the weighted summation state with the corresponding  $EXP$  operators. Then the bias current vector  $I_{Cj}$ , which is controlled by the vector  $C$ , is defined as

$$I_{Cj} = C_j \cdot I_B \quad (7.39)$$

Then, the normalizing current  $I_A$  in Fig.7.44, which will control the overall time constant of the filter, is implemented by

$$I_A = \frac{I_{Aij}}{\frac{W_{Aij}}{L_{Aij}}} \quad (7.40)$$

with

$$\frac{W_{Aij}}{L_{Aij}} = \frac{I_{Aij}(1nA)}{1nA} \quad (7.41)$$

where  $\frac{W_{Aij}}{L_{Aij}}$  are the aspect ratios of the PMOS current mirrors and were defined for  $I_A$  equals to 1nA. The current  $I_C$  is obtained in a similar way, giving by

$$I_C = \frac{I_{Cj}}{\frac{W_{Cj}}{L_{Cj}}} \quad (7.42)$$

for  $\frac{W_{Cj}}{L_{Cj}}$  being the aspect ratios of the transistors in current matrix  $I_{Cj}$  and defined by

$$\frac{W_{Cj}}{L_{Cj}} = \frac{I_{Cj}(1nA)}{1nA} \quad (7.43)$$

Fig.7.45 shows the impulse response of the wavelet filter for  $I_A = I_C = 1nA$  and  $I_B = 2nA$ , which corresponds to  $\tau^{-1} = 5,178 \cdot 10^3$ . The excellent approximation of the Morlet wavelet can be compared with the ideal Morlet function to confirm the performance of the log-domain filter. Fig.7.46 shows the Monte Carlo analysis for process and mismatch variation of the technology in use. As evident from the Monte Carlo simulation (i.e. after 100 runs), the system characteristics show insensitivity towards both absolute and relative variations in the process parameters. Even though the impulse response may be slightly affected, the wavelet analysis is not completely distorted.

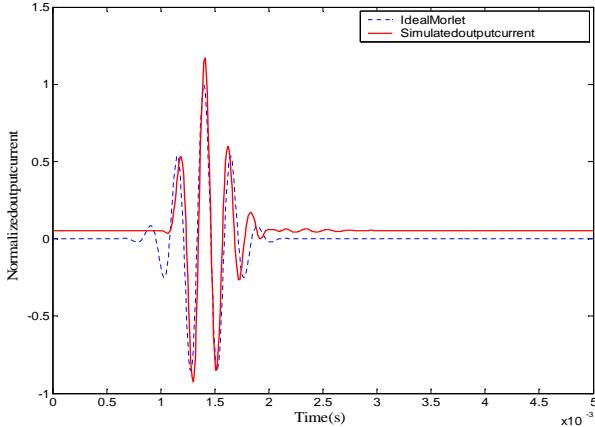


Figure 7.45: Simulated impulse response

In addition, in order to verify the performance of the whole wavelet system, one needs to scale and shift the wavelet base function. By changing the values of the bias currents accordingly, one can obtain a dyadic scale system, as illustrated in Fig.7.47. Alternatively, one also may change the capacitance values,  $C_i$ . To implement a wavelet system, which usually consists of 5 dyadic scales, one needs to implement a filter bank (a parallel structure) with a total capacitance of 193.75pF (capacitance value scaled by a factor of two, i.e., 100pF for the first scale, 50pF for the second, 25pF for the third, 12.5pF for the fourth and 6.25pF for the last scale), preserving the same bias current. This result indicates that the system shown in Fig.7.15 is feasible.

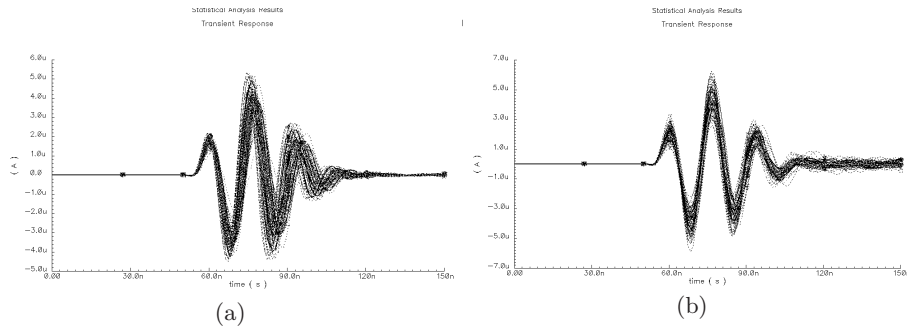


Figure 7.46: Monte Carlo analysis (a) process variation, (b) mismatch variation

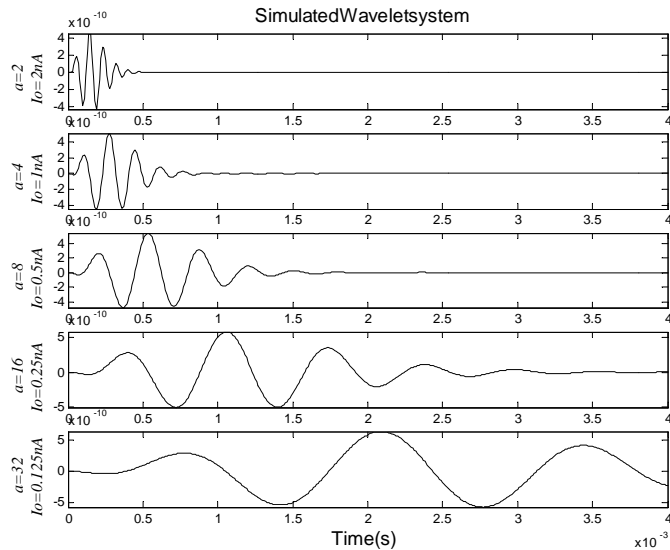


Figure 7.47: Simulated impulse responses of a wavelet system with 5 scales. The scales are obtained by varying the current (from 0.125nA to 2nA) or the capacitance (from 100pF to 6.25pF).

#### 7.4.2 Measurement results of the Morlet wavelet filter [18]

To validate the circuit principle, we have implemented the log-domain state-space wavelet filter in IBM's 0.18 $\mu$ m BiCMOS IC process. A microphotograph of the circuit is shown in Fig.7.48.

The measurement setup is presented in Fig.7.49. Log-domain filters process signals in the current domain. Accurate current measurements require linear transconductance and transimpedance stages at the input and at the output, respectively. These are implemented by a large resistor at the input and by a Keithley 428 nanoamp transimpedance amplifier at the output. However the

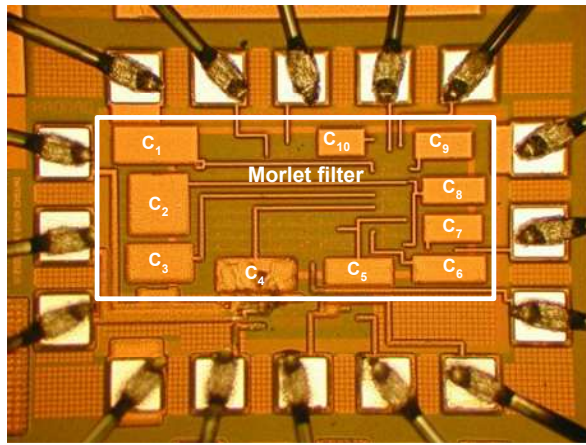


Figure 7.48: Chip microphotograph. The die area is  $0.89\text{mm}^2$  ( $0.78\text{mm} \times 1.14\text{mm}$ ) and the filter active area is  $0.28\text{mm}^2$  ( $0.35\text{mm} \times 0.79\text{mm}$ )

transimpedance amplifier has a cutoff frequency up to 175kHz, depending on the gain factor. To be able to measure beyond 100 kHz, a transimpedance stage implemented by a low noise op amp (LF 356) and a  $1\text{k}\Omega$  shunt feedback resistor is used. The cutoff frequency of this stage is 10MHz.

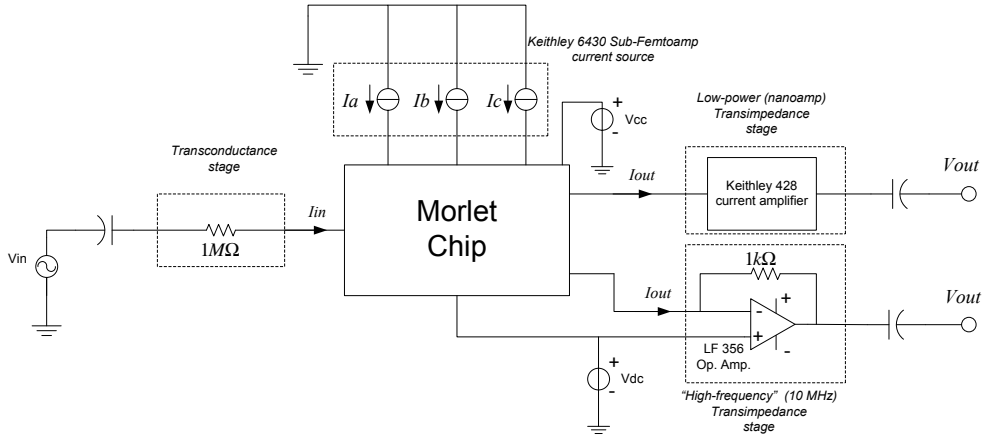


Figure 7.49: Measurement setup

The circuit has been designed to operate from a 1.5V supply. Fig.7.50 shows the measured impulse response of the wavelet filter and the respective frequency response for  $I_A = I_C = 4.3\text{nA}$  and  $I_B = 8.5\text{nA}$ , which corresponds to  $\tau^{-1} = 22 \cdot 10^3$ . The transient response of the Morlet wavelet filter can be compared with the simulated filter response to confirm the performance of the log-domain filter.

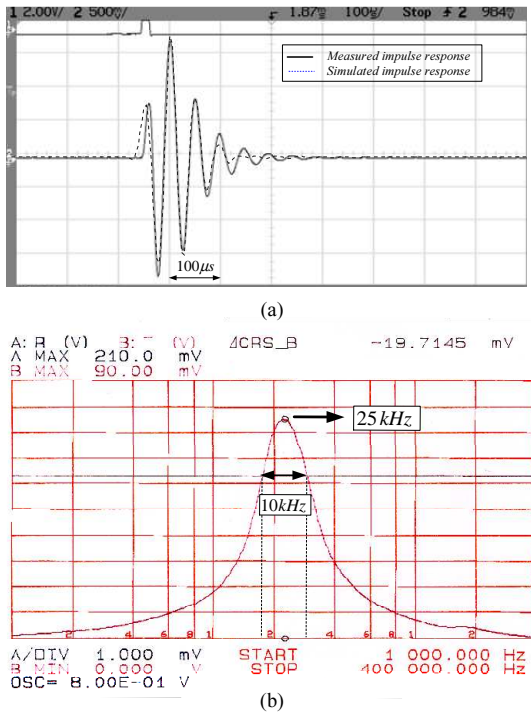


Figure 7.50: Measurement results (a) Measured and simulated impulse response (b) Measured frequency response

The total filter's current consumption is  $4.5\mu\text{A}$  with a  $100\text{pF}$  total capacitance. The rms output current noise is  $66.97\text{pA}$ , resulting in a DR at the 1-dB compression point of approximately 30dB. The power efficiency of any band-pass continuous-time filter is a figure of merit to be able to compare various filter topologies and can be estimated by means of the power dissipation per pole, center frequency ( $f_c$ ), and quality factor ( $Q$ ) defined as [30]

$$\text{Power per pole \& bandwidth} = \frac{P_{diss}}{n \cdot f_c \cdot Q} \quad (7.44)$$

where  $P_{diss}$  is the total power dissipation and  $n$  is the order of the filter. The power efficiency of this filter is equal to  $10.58\text{pJ}$ .

By changing the values of the bias currents accordingly, one can obtain a dyadic scale system, as illustrated in Fig.7.51. The current  $I_A$  has been scaled from  $2\text{nA}$  to  $8\text{nA}$ , resulting in a 3-scales wavelet system.

Finally, in order to show that the same procedure can be applied for medium frequency applications, we tuned the frequency response of the filter by varying the bias current over about three decades with center frequencies ranging from  $14\text{kHz}$  to  $8.1\text{MHz}$ , while preserving the impulse response waveform. Again, one can obtain the wavelet scales around this frequency (i.e.  $8.1\text{MHz}$ ) by scaling the current, accordingly.

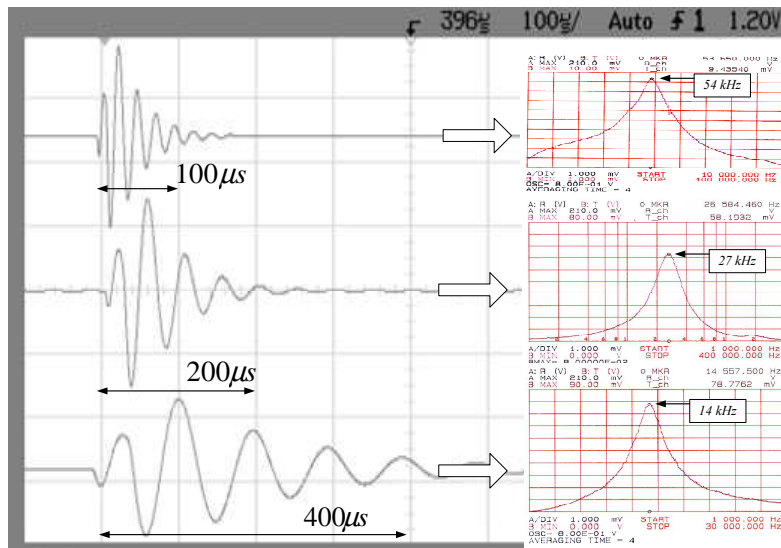


Figure 7.51: Measured Impulse and frequency response for 3 scales

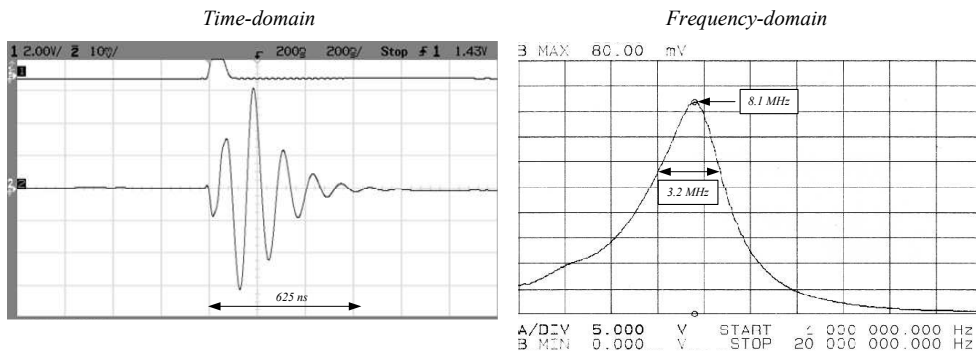


Figure 7.52: Time and frequency response of the Morlet filter varying the bias current  $I_a$  to  $1.4\mu A$  for high frequency operation

The performance of the filter is summarized in Table 7.4.2.

## 7.5 Conclusions

Several ultra low-power biomedical system and wavelet filter designs were presented in this chapter. First, a cardiac sense amplifier based on the Dynamic Translinear circuit technique has been proposed. It comprises a V-I converter, a bandpass filter and absolute value, RMS-DC converter and comparator circuits. The obtained results in the sense amplifier demonstrate the desired performance of the sub-circuits and efficient detection of the R-wave for a typical intracardiac signal in an ultra low-power environment.

Table 7.5: Performance per scale for two different operating frequencies

| Technology                                | 0.18 $\mu$ m BiCMOS  |                        |
|---|----------------------|------------------------|
| Die area                                  | 0.89mm <sup>2</sup>  |                        |
| Active area                               | 0.28mm <sup>2</sup>  |                        |
| Bias current                              | $I_o = 4.3\text{nA}$ | $I_o = 1.4\mu\text{A}$ |
| Total capacitance                         | 100pF                | 100pF                  |
| Supply voltage                            | 1.5V                 | 1.6V                   |
| Center frequency ( $f_c$ )                | 25kHz                | 8.1MHz                 |
| Power dissipation                         | 6.75 $\mu\text{W}$   | 2.3mW                  |
| Dynamic Range (1-dB)                      | 30 dB                | 30 dB                  |
| Noise current (rms)                       | 66.97pA              | 481.3nA                |
| Supply voltage range                      | 1.2V - 1.8V          | 1.5V - 2.1V            |
| Power dissipation per pole<br>$f_c$ and Q | 10.58pJ              | 11.13pJ                |

Secondly, a new QRS-complex detection circuit for pacemaker applications has been proposed. The circuit is based on the wavelet transform. Applying the DTL principle, an analog system consisting of a wavelet filer, an absolute value circuit, a peak detector and a comparator has been designed. The simulated and measured results for a typical cardiac signal demonstrate a good performance in generating the desired Wavelet Transform and achieving correct QRS-complex detection.

Next, two analog implementations of the Gaussian wavelet transform in an ultra low power environment, using the  $G_m$ -C and the DTL circuit techniques have been presented. Simulations from different continuous-time integrator designs demonstrated excellent approximations to the ideal wavelets using both Padé and  $L_2$  approaches.

Furthermore, an analog implementation of the complex wavelet transform was presented. The complex wavelet filter design was derived from the combination of the real and the imaginary state-space descriptions. By this, we were able to implement a complex filter, i.e. both real and imaginary transfer functions, with just an extra  $C$  matrix into an ordinary state-space structure and several complex wavelets can be obtained.

Finally, a Morlet wavelet filter using the procedure in Chapter 4 has been presented. Measurements demonstrated an excellent approximation of the Morlet wavelet base. The filter was optimized with respect to dynamic range. Moreover, sensitivity and sparsity were also taken into account in the design of the filter. Hence, the filter was able to meet the requirements imposed by a low-power environment. From the results obtained, we deduced that this procedure could very well be used to approximate other wavelet bases as well and to implement them on chip in an analog fashion using little power.



# Bibliography

- [1] W. Straver, “Design Manual - SIC3A,” *Internal Report, Delft University of Technology*, Jan. 1999.
- [2] S.A.P. Haddad, S. Gieljes, R.P.M. Houben and W.A. Serdijn, “An Ultra Low-Power Dynamic Translinear Sense Amplifier for Pacemakers,” *proc. ISCAS*, Bangkok, Thailand, vol. 5, pp. 37-40, May 25-28, 2003.
- [3] E. Sevinck, *Analysis and synthesis of translinear integrated circuits*, Elsevier, Amsterdam, 1988.
- [4] J. Mulder, A.C. van der Woerd, W.A. Serdijn and A.H.M. van Roermund, “An RMS-DC converter based on the dynamic translinear principle,” *IEEE Journal of Solid-State Circuits*, vol.32, no. 7,1997.
- [5] B. U. Kohler, C. Hennig and R. Orglmeister, *The principles of software QRS detection*, IEEE Engineering in Medicine and Biology, pp.42-57, February, 2002.
- [6] S.A.P. Haddad, R.P.M. Houben and W.A. Serdijn, “Analog Wavelet Transform Employing Dynamic Translinear Circuits for Cardiac Signal Characterization,” *proc. ISCAS*, Bangkok, Thailand, vol. 1, pp. 121-124, May 25-28, 2003.
- [7] S.A.P. Haddad and W.A. Serdijn, “Mapping the Wavelet Transform onto silicon: the Dynamic Translinear approach,” *proc. ISCAS*, Phoenix, U.S.A., vol. 5, pp. 621-624, May 26-29, 2003.
- [8] H. Kamada and N. Aoshima, “Analog Gabor Transform Filter with Complex First Order System”, in *Proc. SICE*, pp.925-930, 1997.
- [9] B. Gilbert, “Current-mode circuits from a translinear viewpoint: a tutorial,” Chapter 2 in C. Toumazou, F. J. Lidgey and D. G. Haigh (editors), *Analogue IC design: the current-mode approach*, IEE circuits and systems series 2, Peter Peregrinus, 1990.
- [10] J. S. Sahambi and S. N. Tandon and R. K. P. Bhatt, “Using Wavelet Transform for ECG Characterization”, *IEEE Engineering in Medicine and Biology*, pp.77-83, February, 1997.

- [11] S. A. P. Haddad, N. Verwaal, R. Houben and W. A. Serdijn, “Optimized dynamic translinear implementation of the gaussian wavelet transform”, *in Proc. ISCAS*, vol.1, pp.145-148, Vancouver, Canada, May 23-26, 2004.
- [12] S.A.P. Haddad, J.M.H. karel, R.L.M. Peeters, R.L. Westra and W.A. Serdijn, “Analog Complex Wavelet Filters”, *in Proc. ISCAS*, pp.3287-3290, Kobe, Japan, May 23-26, 2005.
- [13] I. Daubechies, *Ten Lectures on Wavelets*, Society for Industrial and Applied Mathematics, Philadelphia, 1992.
- [14] S.Mallat, *A Wavelet Tour of Signal Processing*, Academic Press, 2001.
- [15] C. Toumazou, F. J. Lidgey and D. G. Haigh, *Analogue IC design: the current-mode approach*, IEE circuits and systems series 2, United Kingdom, 1990.
- [16] S. A. P. Haddad, S. Bagga and W. A. Serdijn, “Log-domain wavelet bases”, *IEEE Transactions on Circuits and Systems - I: Regular Papers*, vol. 52, no. 10, pp. 2023-2032, Oct. 2005.
- [17] G. W. Roberts and V. W. Leung, *Design and Analysis of Integrator-Based Log-Domain Filter Circuits*, Kluwer Academic Publishers, The Netherlands, 2000.
- [18] S.A.P. Haddad, J.M.H. karel, R.L.M. Peeters, R.L. Westra and W.A. Serdijn, “Ultra Low-power Analog Morlet Wavelet filter in  $0.18\mu\text{m}$  BiC-MOS Technology”, *in Proc. ESSDERC-ESSCIRC*, pp. 323-326, Grenoble, France, Sep. 12-16, 2005..

## Chapter 8

# Conclusions and Future Research

*“What you've got they can't deny it  
can't sell it, or buy it. Walk on ...” - Bono Vox*

Since the first artificial pacemaker was introduced, much has changed and will continue to change in the future. The complexity and reliability in modern pacemakers has increased significantly, mainly due to developments in integrated circuit design, providing, for instance, diagnostic analysis, adaptive rate response and programmability. Nevertheless, the future trends for pacemakers indicate that much more advanced signal processing methods will be required than nowadays. Signal analysis methods improving discrimination of signals from noise and interference are of great importance. Also, due to various pathological states of the heart recently reported, morphological aspects of the cardiac signal needs to be taken into account.

The Wavelet Transform (WT) has been shown to be a very efficient tool for analysis of non-stationary signals, like cardiac signals. Being a multiscale analysis technique, it offers the possibility of selective noise filtering and reliable parameter estimation, and therefore, can contribute efficiently to the morphological analysis. WT has been extensively used in biomedical signal processing, mainly due to the versatility of the wavelet tools. Signal analysis methods derived from wavelet analysis carry large potential to support a wide range of biomedical signal processing applications including noise reduction, feature recognition and signal compression.

In implantable medical devices, such as pacemakers, the power consumption is a critical issue, due to the limited power density and the longevity of currently available portable batteries. This implies that the design of such devices has to be optimized for very low power dissipation. Due to the relatively huge amount of power required for the analog-to-digital conversion and its improvement in power efficiency over the years, we now predict that

the implementation of a fully digital wavelet signal processor in implantable pacemakers will not be feasible for many decades to come.

For this reason, we proposed a method for implementing the novel biomedical signal processing based on Wavelet Transform using continuous-time analog circuitry. The methodology is based on the development of ultra low-power analog integrated circuits that implement the required signal processing, taking into account the limitations imposed by an implantable device.

First, a brief overview of the history and development of circuit designs applied in pacemakers was presented in Chapter 2. Also, based on future trends for pacemakers, some features and improvements for modern cardiac sensing systems were described and we pointed out the need for a morphological wavelet analysis of the cardiac signal.

Next, in Chapter 3, a comparison between frequency analysis, by means of the Fourier transform, and time-frequency representation, by means of the wavelet transform, was depicted. From a example of a nonstationary signal, the good extraction of the time and frequency characteristics of the wavelet was revealed. In addition, the properties of wavelet bases functions and WT signal processing applications were described.

From the wavelet definition, we stated that the implementation of a wavelet filter is based on a bandpass filter design that presents an impulse response equal to a wavelet base. In order to obtain the transfer function of certain wavelet filter, mathematical approximation techniques are required. In Chapter 4, we indicated several methods to obtain good approximations in the time domain of the wavelet bases functions. One important objective of the introduced approaches is that the resulting approximated function should be rational and stable in the Laplace domain. This means that the approximating function must lead to a physically realizable network. Nevertheless, we can notice that due to limitations in chip area, power consumption and coefficient matching, there is a trade-off between the approximation accuracy versus the order of the implemented filter. Thus, the design challenge is to obtain a low-order system while preserving a good approximation to the intended function. Due to their general applicability, and the excellent accuracy, the Padé and the  $L_2$  approximations were chosen, which generate reasonable low-order and good-fit transfer functions.

Subsequently, in Chapter 5 we presented the description and a comparison of several state space representations. There are many possible state space descriptions for a circuit that implements a certain transfer function. The same holds for practical realizations. This allows the designer to find a circuit that fits his specific requirements. From the two new figure-of merits defined in this chapter, we concluded that the orthonormal ladder structure is the optimal state space representation with respect to dynamic range, sparsity and sensitivity, which represent the most important design aspects in low-power low-voltage analog filters.

The trend towards lower power consumption, lower supply voltage and higher frequency operation has increased the interest in new design techniques for analogue integrated filters. A few ultra low-power integrator designs were presented in Chapter 6, being, a new pA/V Delta-Gm CMOS triode-transconductor, two Class-A log-domain integrators and a new ultra low-power Class-AB *sinh* integrator. The integrators were based on two different techniques, being the  $G_m$ -C approach and the translinear (log-domain) method, which can be directly used in low-power analog filters and ultra low-power biomedical system designs. The advantages and the limitations of these techniques were also highlighted.

Finally, the methodology presented in previous chapters was employed in the design of several ultra low-power biomedical systems and analog wavelet filters. Two ultra low-power biomedical systems and four wavelet filter designs were presented in Chapter 7. First, a cardiac sense amplifier based on the Dynamic Translinear circuit technique was proposed. The obtained results in the sense amplifier demonstrate the desired performance of the sub-circuits and efficient detection of the R-wave for a typical intracardiac signal in an ultra low-power environment. Moreover, a new QRS-complex detection circuit, based on the wavelet transform, for pacemaker applications has been proposed. The simulated and measured results for a typical cardiac signal demonstrate a good performance in generating the desired Wavelet Transform and achieving correct QRS-complex detection. At last, a few wavelet filter designs were also presented. Two convenient methods to provide the transfer function of the wavelet filter are given by the Padé and  $L_2$  approximations and, thus, some designs based on these approaches, for Gaussian, complex Gabor and Morlet wavelet bases, were designed using the  $G_m$ -C and the DTL circuit techniques. Simulations and measurements demonstrated an excellent approximation of the desired wavelet base.

From the results obtained, we deduced that this procedure can very well be used to approximate several wavelet bases and other time-domain waveforms as well as to implement them on chip in an analog fashion using little power.

## 8.1 Future Research

In this thesis, the transient detection capability of the WT has been exploited for detection of the QRS complex. However, other important aspects in the cardiac signal, such as T wave or QT interval can also be detected using wavelets.

Further analysis techniques of cardiac signals using wavelets are being developed by the Electronics Research Laboratory of Delft University of Technology, together with the University of Maastricht and Medtronic Bakken Research Center. Research on concepts such as the mathematical modelling of cardiac signals and pathologies, and the design of WT-based algorithms for intelligent sensing and feature extraction are under progress. In addition, a

fully integrated implementation of the analog WT circuit to be used in pacemakers is currently being investigated.

It remains to be demonstrated in clinical practice that these novel signal analysis methods will contribute to the further development and application of dynamical electrocardiography in implantable devices.

### **Biomedical Applications of Wavelets**

In this thesis we presented the application of the WT in cardiac signal (ECG) analysis. Nevertheless, Wavelet Transform has become a powerful method in many other medical ultra low-power applications due to their suitability for analyzing nonstationary signals.

The Wavelet Transform is extremely versatile for the analysis of various electrophysiological signals (EXG), i.e., Electroencephalogram (EEG), Electromyogram (EMG), and Electrocardiogram (ECG). As an example, neurological EEG signals represent rhythmic potential fluctuations on the head surface created by the synchronous discharge of nerve cells and has been used to diagnose epilepsy. One of the early signs of a seizure is the presence of characteristics transient waveforms in the EEG (spikes and sharp waves). The sharp and size of these waveforms can vary from one patient to the other substantially. WT is used as the detection tool due to the very mixed nature of these phenomena and the wavelet analysis have been shown to be useful in identifying the features localized within the EEG signal. Then, one could apply the proposed low-power wavelet filter design methodology for an EEG characterization in neurostimulator implantable devices.

Finally, one can consider the applications of 2-D wavelets to biomedical imaging in an ultra low-power environment, for instance artificial retinae. Human beings have the capacity to recognize objects in natural visual scenes with high efficiency despite the complexity of such scenes, which usually contain multiple objects. Each object in our environment can cause considerably different patterns of excitation in our retinae depending on the observed viewpoint of the object. One possible mechanism for dealing with this situation is selective attention. The scene is first analyzed at a coarse resolution level, and the focus of attention enhances iteratively the resolution at the location of an object until the object is identified, similar to the principle of multiresolution wavelet analysis. Thus, the 2-D wavelet transform can be very well used for image processing tasks like detection, extraction, or classification of the various features in the images. In addition, the amount of information is usually very large and compression methods are highly needed in order to reduce the required processing time and/or archiving space. High level of compression should be achieved without loss of information. Because wavelet transform coefficients are localized in both frequency and space, they are theoretically better suited to image compression than other common transform methods. Wavelets have recently been applied to medical image compression and were

found to be very effective. However, power consumption is an important issue in a battery-operated artificial retinae design. Image computation usually requires large arrays of pixels. Thus, due to the massive parallel process necessary for artificial implantable vision systems, digital processing, where a huge amount of A/D converters would be required (one A/D converter per pixel), turns out to be impracticable. This makes the analog implementation much more efficient than digital one with respect to power consumption and chip area, and again the approach described in this thesis can be used for a complex biomedical image processing design in an ultra low-power environment.

### **Ultra Wideband Applications**

Impulse radio, or Ultra Wideband (UWB) radio, is a promising new technology for wireless communications. Rather than modulating the information on a carrier, the data is transmitted using a coded series of very narrow pulses, carrying information in the time and the frequency domain. From the properties of the WT described before, one can say that the Wavelet bases are good candidates for these pulses. In the AIRLINK research project, a collaboration of TNO-FEL and various groups within Delft University of Technology, impulse radio is being investigated. The real-time synthesis of UWB pulses by means of low-power analog integrated circuits is one of the core research issues in this project and as shown in Appendix D, the same methodology procedure described in this thesis can be very well used into the design of UWB pulse generators and time-domain delays.



## Appendix A

# High-Performance Analog Delays

A delay is a fundamental block in signal-processing systems. Pure delays should ideally not change the magnitude or shape of the input signal. Considering a fixed delay of  $\tau$ , its frequency-domain transfer function is defined by the exponential  $H(s) = e^{-\tau s}$ , which cannot be realized with a finite number of lumped elements [1]. The best solution is an approximation with a rational quotient of polynomials:  $G(s) = N(s)/D(s)$ . One common approach to approximate a delay transfer function is through the use of Bessel polynomials leading to an all-pole filter approximation called Bessel-Thomson realization. Another approximation yielding a rational expression suitable for implementation through the use of a Taylor expansion of the frequency-domain non-rational transfer function around one point is called the Padé approximation. By narrowing of a Gaussian impulse-response function with the use of smaller pulse width  $s$ , the delta time-domain impulse response of a delay is approximated as a third method in this work. The new delay-approximation method is completed through the application of a Padé approximation on the Laplace transform of the Gaussian function. The performance of these different approximations of a delay filter has been systematically compared, in regard to achievable cut-off frequency and time-domain characteristics. It was revealed that our Gaussian approximation of the time domain transfer function decreased overshoot in the step response, while keeping the other characteristics fixed.

### A.1 Bessel-Thomson approximation

Bessel Thomson is the most widely used approximation method of delay filters. This method leads to a family of low-pass all-pole transfer functions  $T(s)$ ,

which would give approximately constant time delay over as large frequency range as possible. The resultant transfer functions are of the form [1]:

$$T_n(s) = \frac{B_0(s)}{B_n(s)} = \frac{1}{(2n - 1) \cdot B_{n-1}(s) + s^2 \cdot B_{n-2}(s)} \quad (\text{A.1})$$

where  $B_n(s)$  is the general Bessel polynomial of order  $n$  with  $B_0(s) = 1$  and  $B_1(s) = s + 1$ . In this approximation, the only degree of freedom available is the filter order, determined by the number of poles. A frequency-domain analysis of these filters illustrates a low-frequency behavior in which the roll-off frequencies are increased by filter-order increase. Fig. A.1 illustrates the correspondent amplitude and delay responses of Bessel-Thomson filters of order 1 to 12.

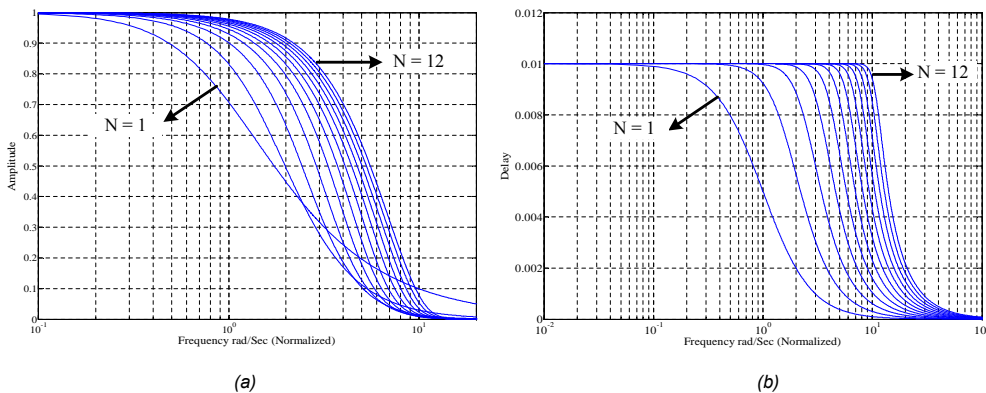


Figure A.1: (a) Bessel-Thomson filter amplitude responses for orders 1 to 12  
(b) Phase responses of the same filters

Fig. A.2 illustrates the step responses of different orders of Bessel-Thomson delay filters. The most important characteristic of the Bessel-Thomson filter, which is an overshoot-free step response, in addition to the resultant decrease of rise time due to filter-order increase can also be viewed here.

## A.2 Padé approximation

Fig. A.3 illustrates that in a Padé-approximated delay filter, for an increase of denominator order, the 3-dB cut off frequency of amplitude response increases, while peaking occurs for increase of order difference between numerator and denominator.

A delay-response simulation of Padé-approximated delay filters for different order differences between numerator and denominator order ( $n-m$ ), while increasing the denominator order ( $n$ ) from 5 to 12 is illustrated in Fig. A.4. This figure illustrates that for higher denominator order, higher delay roll-off frequency is achieved, while the peaking effect near the roll-off frequency

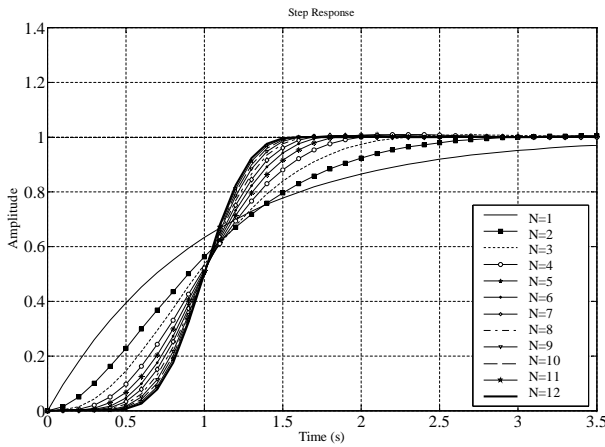


Figure A.2: Step response of different order Bessel-Thomson filters

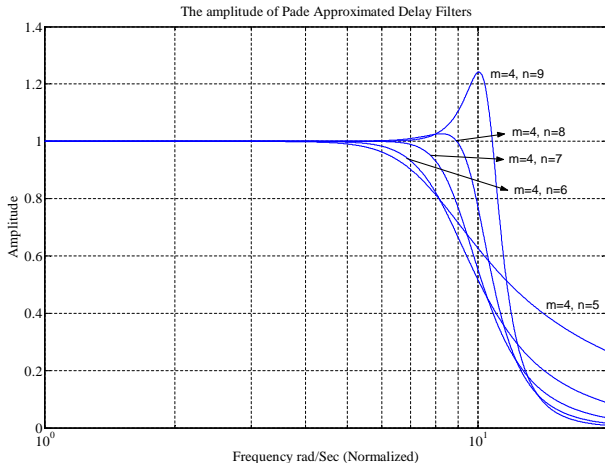


Figure A.3: Amplitude response of Padé-approximated delay filters with  $m=4$  and  $n=5 \dots 9$

increases for higher numerator and denominator order differences. More accurate delay response is achieved for smaller order difference and higher denominator order.

A series of time-domain simulations on the step response of Padé-approximated delay filters illustrates that the rise time decreases with the increase of the denominator order (Fig. A.5), while zero-time oscillations are generated when the order difference between the denominator and numerator decreases. These zero-time oscillations are not favorable and might cause instability in some applications.

Fig. A.6 illustrates that the filter order increase results in a faster step response while filters with larger numerator and denominator order difference provide smaller rise times.

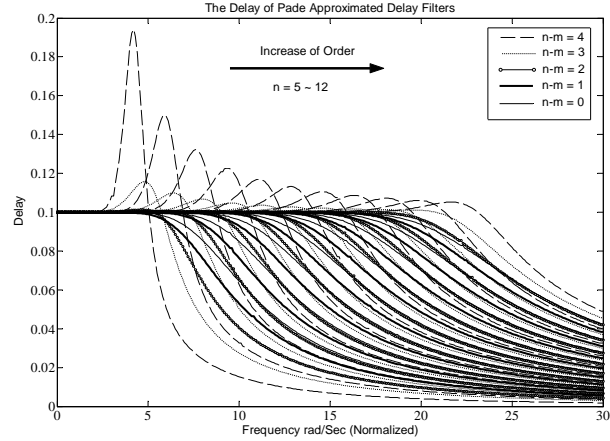


Figure A.4: Delay response of Padé-approximated delay for different order difference and different denominator order

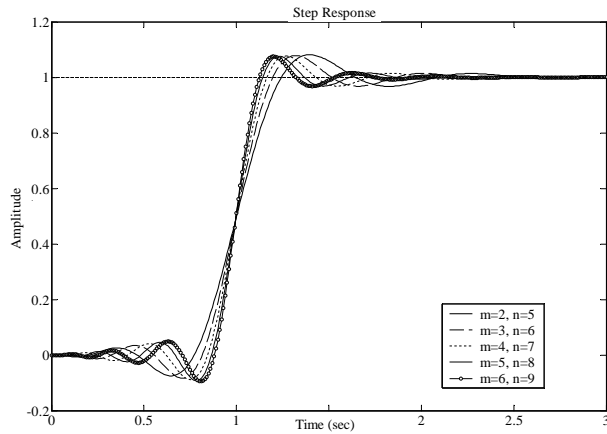


Figure A.5: Rise-time decrease with filter order increase

### A.3 Comparison of Bessel-Thomson and Padé approximation delay filters

In this section a comparison of the frequency-domain and time-domain performance metrics of Bessel-Thomson and Padé-approximated delay filters are illustrated. According to amplitude and delay responses sketched for different order combinations of Bessel-Thomson and Padé delay filters, in Fig. A.7 and Fig. A.8 respectively, the lower orders of Padé approximation can always achieve higher frequencies than the highest reasonable Bessel-Thomson approximations.

A comparison of step responses of both approximations (Fig. A.9.a) illustrates that Padé-approximated delay filters always introduce more overshoot

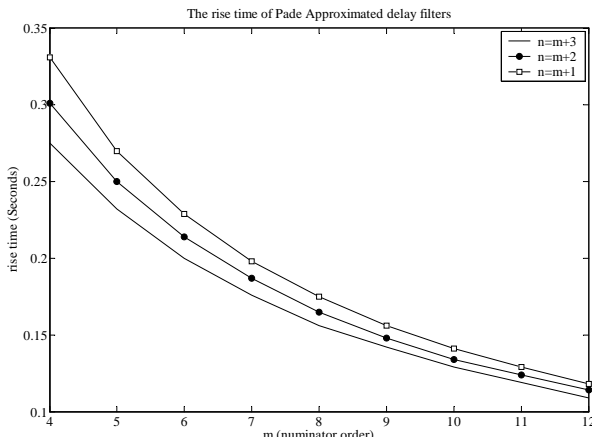


Figure A.6: Rise-time comparison for different combination of numerator and denominator orders

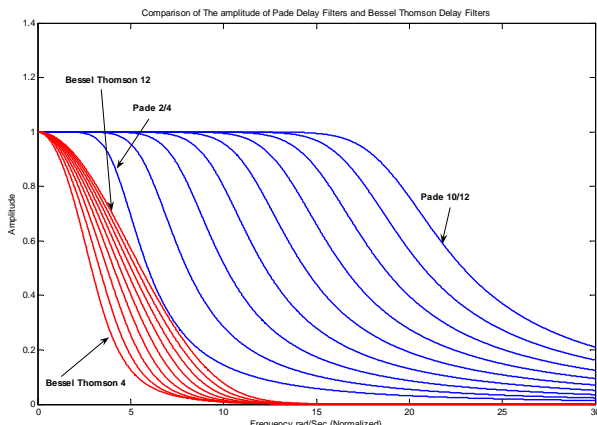


Figure A.7: Amplitude comparison of Bessel-Thomson delay filters of orders 4 to 12 vs. Padé approximated delay filters of order 2/4 to 10/12.

and oscillations in comparison to Bessel-Thomson counterparts, while the former has smaller rise times (Fig. A.9.b).

In order to have the higher frequency and faster time-domain response of Padé approximation, together with less overshoots as the Bessel-Thomson approximation achieves, a new approximation method is introduced in the following section.

## A.4 Gaussian Time-domain impulse-response method

The time-domain impulse response of a delay function is a delta function. A delta function can be approximated by narrowing of a Gaussian time-domain

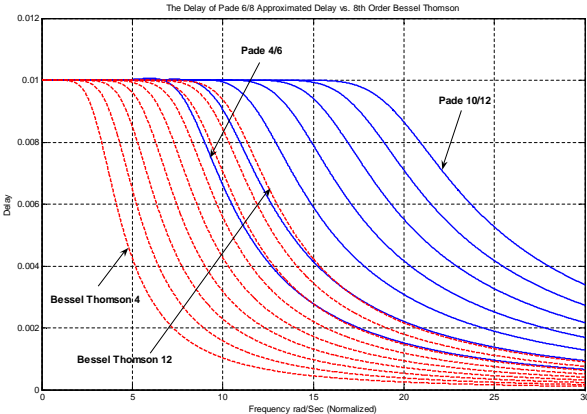


Figure A.8: Delay comparison of Bessel-Thomson delay filters of orders 4 to 12 vs. Padé approximated delay filters of order 2/4 to 10/12.

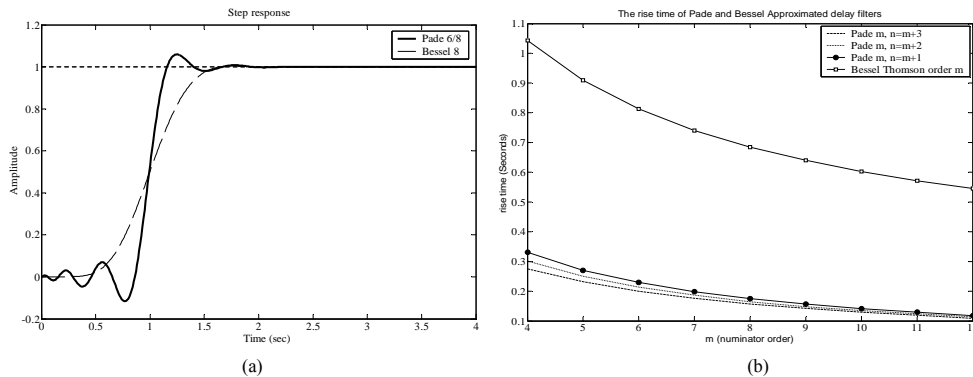


Figure A.9: Comparison of (a) step response and (b) rise-time in both approximations

transfer function with the use of smaller pulse width  $s$ , as illustrated by Eq. A.2 and Fig. A.10.

$$h(t) = \frac{1}{\sigma\sqrt{2\pi}} e^{-\frac{(t-\mu)^2}{2\sigma^2}} \quad (\text{A.2})$$

In this method a Padé approximation is applied to the Laplace transform of a Gaussian impulse response [3]. Figure A.11 illustrates that the amplitude response of the Gaussian impulse-response delay filter becomes closer to the response when using a Bessel-Thomson approximation for larger values of  $s$ , decreasing the roll-off frequency, while Fig. A.12 illustrates that the effect on the delay response is minimum.

An investigation of the Gaussian impulse-response delay filter's step response proves that the increase of  $s$ , making the impulse response wider, leads to a decrease of the zero-time oscillations and overshoots, while it hardly in-

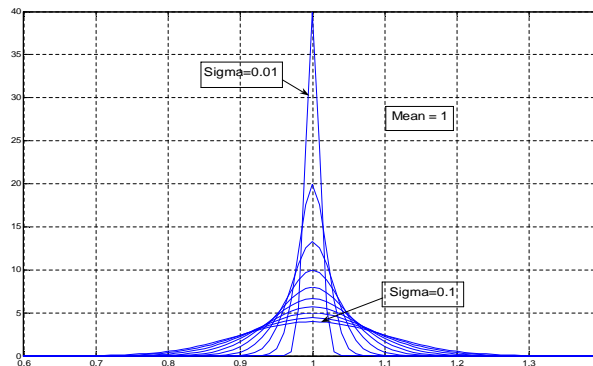


Figure A.10: A Gaussian function's response vs. the change of  $\sigma$

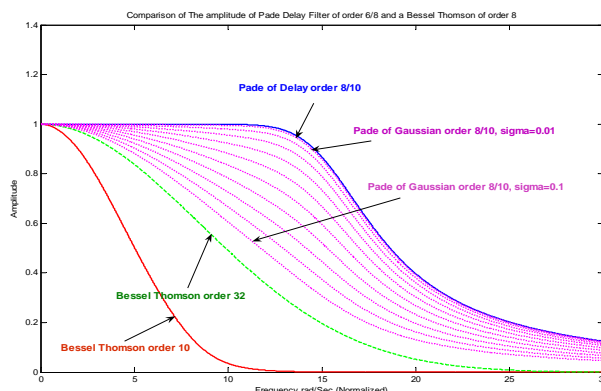


Figure A.11: The amplitude response of the Gaussian impulse-response delay vs.  $s$  in comparison to normal Padé-approximated delay and Bessel-Thomson responses

creases the rise time. It is revealed that using a time-domain Gaussian impulse response gives the possibility of decreasing the overshoots and zero-time ringings in a Padé approximation of delay by increasing  $s$ , while the price paid is an increase of insertion loss in the amplitude response and a slightly slower rise time in the system step response. Fig. A.13 compares the step response of a 6/8 Padé-approximated delay filter with the same order Gaussian impulse response delay filter with  $s$  value equal to 0.05. As illustrated by this graph, for the same nominator and denominator order, the Gaussian impulse response delay has less overshoot.

We can conclude that while Bessel Thomson is the most widely used method of delay-filter approximation, higher frequency and faster delay responses can be achieved through the use of Padé approximation at the expense of more overshoot. The here introduced method of Gaussian time-domain impulse response produces a rational transfer function that is ready

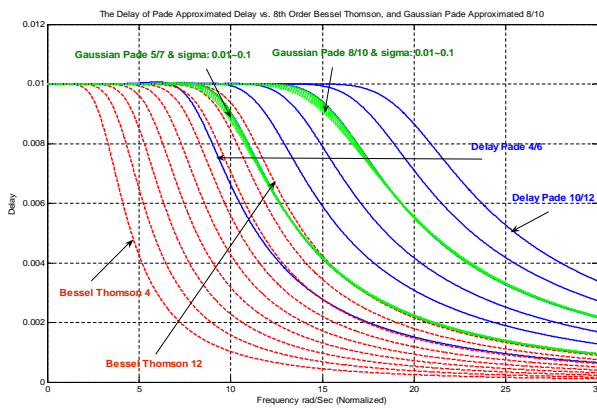


Figure A.12: The delay response of the Gaussian impulse response delay for various values of  $s$  in comparison to normal Padé-approximated delay and Bessel-Thomson responses

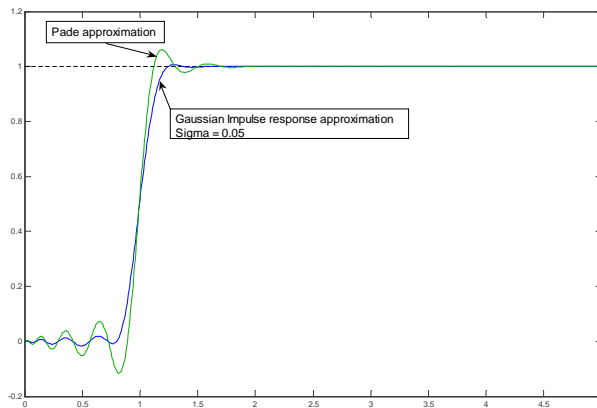


Figure A.13: The step response of a Gaussian impulse-response delay for a value of  $\sigma = 0.05$  vs. a Padé-approximated delay filter of the same (6/8) filter order

for implementation in an analog fashion and realizes a delay with both a large bandwidth and little overshoot.

## Appendix B

# Model reduction - the Balanced Truncation method

A wavelet filter design trade-off involves the approximation accuracy versus the complexity (model order) of the implemented filter. On the other hand, for analog active filters, the power consumption is directly proportional to the order of the filter. Thus, the design challenge is to obtain a low-order system while preserving a good approximation matching.

To overcome these difficulties one can employ model order reduction that consists in an approximation of the dynamical system by a reduced order system. It is required that the approximate system preserve properties of the original system. Clearly, it is also desirable that the approximation error is small.

There exist various model reduction approaches for standard state space systems such as balanced truncation and moment matching approximations. Balanced truncation method, which will be described here, usually presents better approximation results compared to moment matching method. Also, this method is strongly related to the controllability and observability gramians, which is suitable for the dynamic range optimization procedure presented in Sec.5.2.1. The balanced truncation method (BT) consists in transforming the state space system into a balanced form whose controllability and observability gramians become diagonal and equal.

Then, the model reduction problem is one of finding a state-space system of order  $k < n$ , such that the error  $E$  with respect to the  $L_\infty$  norm is minimized over all state-space systems of order  $k$

$$E = \|H(s) - H_k(s)\|_{L_\infty} \quad (\text{B.1})$$

where  $H(s)$  is the original transfer function and  $H_k(s)$  is the transfer function of the reduced-order model. The balanced truncation method produces a guaranteed stable reduced model with globally accurate frequency response approximation ( $L_\infty$ -error bound). In the continuous-time case, a reduced-

order model computed by BT approximates the original one well at high frequencies, with a perfect match at  $\omega = \infty$ , which is suitable for time-domain approximation around  $t = 0$ .

The starting point of the  $k$ -th order (square-root) balanced truncation reduction is the calculation of the Cholesky factors  $Z^B$  and  $Z^C$  of the gramians  $K$  and  $W$ , respectively. Any square matrix can be written as the product of a lower triangular matrix  $Z$  and an upper triangular matrix  $Z^T$ ; this is called the Cholesky decomposition and is given with respect to the gramians by

$$\begin{aligned} K &= Z^B(Z^B)^T \\ W &= Z^C(Z^C)^T \end{aligned} \quad (\text{B.2})$$

A merit of the BT method is that it relies on the Cholesky factors  $Z^B$  and  $Z^C$  of the gramians  $K$  and  $W$  rather than the gramians themselves, which has advantages in terms of numerical stability.

The next step of the reduction method is the calculation of the Singular Value Decomposition (SVD) of the product  $(Z^C)^T Z^B$

$$(Z^C)^T Z^B = U^L \Sigma (U^R)^T \quad (\text{B.3})$$

with

$$U^R = [u_1^R \dots u_n^R], \quad U^L = [u_1^L \dots u_n^L], \quad \Sigma = \begin{bmatrix} \sigma_1 & \dots & 0 \\ \vdots & \ddots & \vdots \\ 0 & \dots & \sigma_n \end{bmatrix} \quad (\text{B.4})$$

where  $U^L$  and  $U^R$  are orthogonal matrices, and  $\Sigma$  is a diagonal matrix containing the singular values of  $(Z^C)^T Z^B$ . The singular values  $\sigma_1, \dots, \sigma_n$  are known as the Hankel singular values of the system.

If the system is normalized properly, i.e. internally balanced, the diagonal  $\text{diag}(\sigma_1, \sigma_2, \dots, \sigma_n)$  of the joint gramian can be used to reduce the model order. Because this diagonal reflects the combined controllability and observability of individual states of the balanced model, you can delete those states with a small  $\sigma_i$  while retaining the most important input-output characteristics of the original system.

Finally, most model reduction methods for dynamic systems are proceeded by projection, which is usually implemented using orthogonal projection matrices. BT is a projection method with left projection matrix  $S^C$  and right projection matrix  $S^B$ , such that  $(S^C)^T S^B = I_{k \times k}$ , given by

$$S^B = Z^B [u_1^R \dots u_k^R] \begin{bmatrix} 1/\sqrt{\sigma_1} & \dots & 0 \\ \vdots & \ddots & \vdots \\ 0 & \dots & 1/\sqrt{\sigma_k} \end{bmatrix} \quad (\text{B.5})$$

and

$$S^C = Z^C [u_1^L \dots u_k^L] \begin{bmatrix} 1/\sqrt{\sigma_1} & \dots & 0 \\ \vdots & \ddots & \vdots \\ 0 & \dots & 1/\sqrt{\sigma_k} \end{bmatrix} \quad (\text{B.6})$$

Then, the new  $k$ -th order BT realization is given by

$$A'_k = (S^C)^T A S^B, \quad B'_k = (S^C)^T B, \quad C'_k = C S^B \quad (\text{B.7})$$

To conclude, from Eq.B.5 and Eq.B.6, one can see that every state space system can be transformed to balanced form by means of a state change  $x' = Tx$ , where the balancing transformation is given by  $T = \Sigma^{\frac{1}{2}} U^L (Z^B)^{-1} = \Sigma^{-\frac{1}{2}} U^R (Z^C)^T$ . And the controllability and observability gramians of the balanced  $k$ -th order reduced system are diagonal and equal, defined by

$$K'_k = W'_k = \Sigma = \text{diag}(\sigma_1, \sigma_2, \dots, \sigma_k) \quad (\text{B.8})$$

To illustrate the model reduction method for wavelet filters design, we applied the BT approach into state space systems obtained from the Padé and  $L_2$  approximations, shown in Fig.B.1.a and Fig.B.1.b, respectively. One can note that we could reduce the 10th order (first derivative of Gaussian) state space obtained by the Padé method to a 7th order system and the 7th order  $L_2$  Morlet approximation into a 6th order.

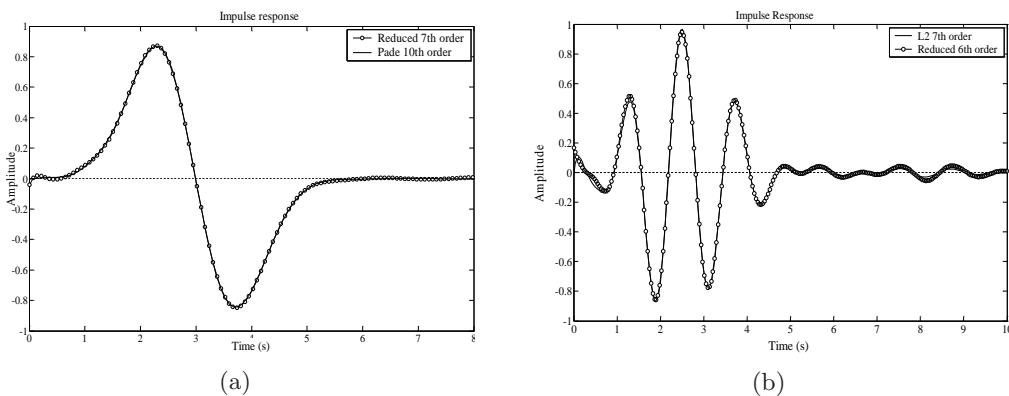


Figure B.1: Model reduction for (a) First derivative of Gaussian Padé and (b) Morlet wavelet  $L_2$  approximations

### Reduced model and optimal dynamic transformations comparison

In order to obtain the optimal dynamic range for the reduced model, we compare the similarity transformations for the Balanced realization with the one presented in Sec.5.2.1.

One can see that the first step for both transformations is similar, where makes the controllability Gramian equal to the identity. Since  $K$  is symmetric, its singular value decomposition has the form  $K = P_K D_K P_K^T$ , defining the first transformation as  $T_{K1} = P_K D_K^{1/2}$ . In these first transformed coordinates,  $K_1 = I$  and  $W_1 = T_{K1}^T W T_{K1}$ .

In the second step of the balanced realization, we perform an SVD on  $W_1$  to get  $W_1 = P_{W1} D_{W1} P_{W1}^T$ . The second transformation is defined as  $T_{W2,bal} = P_{W1} D_{W1}^{-1/4}$ . In the new coordinates, both Gramians are equal and diagonal:  $K_{2,bal} = W_{2,bal} = D_{W1}^{1/2}$ . Whereas, for dynamic range optimization, we do not apply the scaling  $D_{W1}^{-1/4}$ , and the transformation is just the rotation  $T_{W2,opt} = P_{W1}$ .

Thus, considering the fact that the composite transformation  $(T_1 T_2)$  for the balanced and optimized realization are given by  $T_{bal} = D_K^{1/2} P_K P_{W1} D_{W1}^{-1/4}$  and  $T_{opt} = D_K^{1/2} P_K P_{W1}$ , respectively, to optimize the reduced model with respect to the dynamic range, we need to apply just a scaling transformation  $T_{scal} = W_2^{1/2}$

## Appendix C

# Switched-Capacitor Wavelet Filters

In this appendix we will present two discrete-time wavelet base implementations, being the first derivative of a Gaussian *gaus1* and the Morlet, by means of switched-capacitor filter technique.

As a filtering technique, switched-capacitors (SC) filters have become extremely popular due to their accurate frequency response as well as good linearity and dynamic range. Accurate discrete-time frequencies are obtained since filters coefficients are determined by capacitance ratios which can be set quite precisely in an integrated circuit. Once the coefficients of a SC discrete time filter are accurately determined, its overall frequency response remains a function of the clock (or sampling) frequency and the capacitors ratio [2].

Then, to design the wavelet switched-capacitor filters will first obtain the equivalent transfer functions. However, in order to obtain the approximation of the desired wavelet base, we will apply first the Padé and the  $L_2$  approximations in continuous-time domain to have the laplace-domain transfer function and after that use a z-transformation (impulse invariant) to obtain the proper transfer function in z-domain.

The Padé and  $L_2$  approximated transfer functions for the Gaussian and the Morlet wavelet bases, respectively, and the corresponding approximated waveforms (Fig. C.1) are given below.

Padé [3/7] approximation of the *gaus1* wavelet base:

$$H_{gaus1}(s) = \frac{8.06s^3 - 50.67s^2 + 151.65s}{s^7 + 8.35s^6 + 37.07s^5 + 107.56s^4 + 213.23s^3 + 282.58s^2 + 228.17s + 85.58} \quad (\text{C.1})$$

$L_2$  [6/8] approximation of the Morlet wavelet base:

$$H_{mor}(s) = \frac{0.88s^6 + 1.61s^5 + 45.48s^4 + 128.4s^3 - 451.3s^2 + 1576s}{s^8 + 5.34s^7 + 117.9s^6 + 440.9s^5 + 4610s^4 + 11020s^3 + 69880s^2 + 82960s + 337900} \quad (\text{C.2})$$

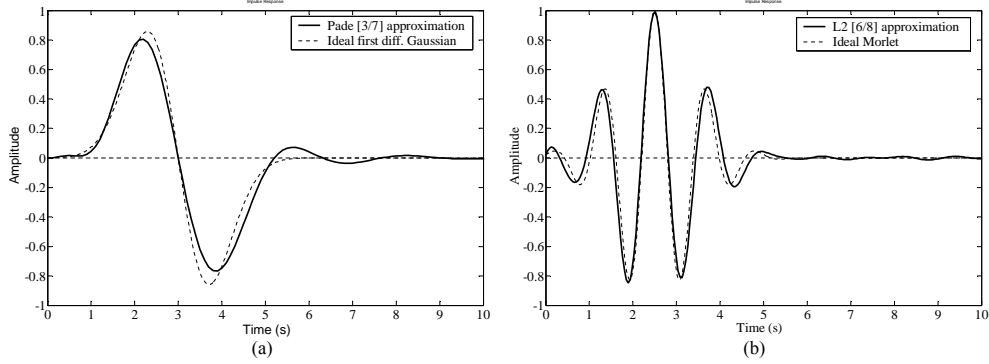


Figure C.1: Continuous-time approximated impulse response for (a) Padé [3/7] approximation of the *gaus1* and (b)  $L_2$  [6/8] approximation of the Morlet wavelet base

In order to implement the filter in the discrete-time in z-domain, the impulse invariance technique has been chosen to preserve the impulse response of the continuous-time analysis by defining the relationship

$$h_d[k] = T_s h_c(kT_s) \quad (\text{C.3})$$

where  $T_s$  is the sample frequency,  $h_d[k]$  and  $h_c(kT_s)$  are the discrete and continuous time impulse response, respectively. This means that, the discrete and continuous time impulse responses match, up to a scale factor  $T_s$ , at the sample instance. Then, the corresponding discrete-time z-domain transfer functions applying impulse invariant z-transformation yields

$$H_{\text{gaus1}}(z) = \frac{0.0039z^7 - 0.011z^6 + 0.026z^5 + 0.014z^4 - 0.03z^3 - 0.003z^2}{z^8 - 4.2z^7 + 7.7z^6 - 8.3z^5 + 5.7z^4 - 2.4z^3 + 0.58z^2 - 0.06z} \quad (\text{C.4})$$

and

$$H_{\text{mor}}(z) = \frac{0.0021z^8 - 0.0067z^7 + 0.0015z^6 + 0.024z^5 - 0.05z^4 + 0.047z^3 - 0.022z^2 + 0.004z}{z^8 - 6.5z^7 + 19.4z^6 - 34.3z^5 + 39.4z^4 - 30z^3 + 14.8z^2 - 4.3z + 0.58} \quad (\text{C.5})$$

Fig. C.2 shows both discrete-time impulse response for the Gaussian and the Morlet wavelets.

Next, to design the SC wavelet filter we will obtain the spate space representation in z-domain, applying the same procedure described in Chapter 5. In this case, we have chosen to obtain first the optimal DR state space and then apply the Schur transformation. Nevertheless, we must take into account that switched-capacitor integrators implement  $H(z) = \frac{1}{z-1}$  instead of  $H(s) = \frac{1}{s}$ . So, the state space description of a SC filter is given by

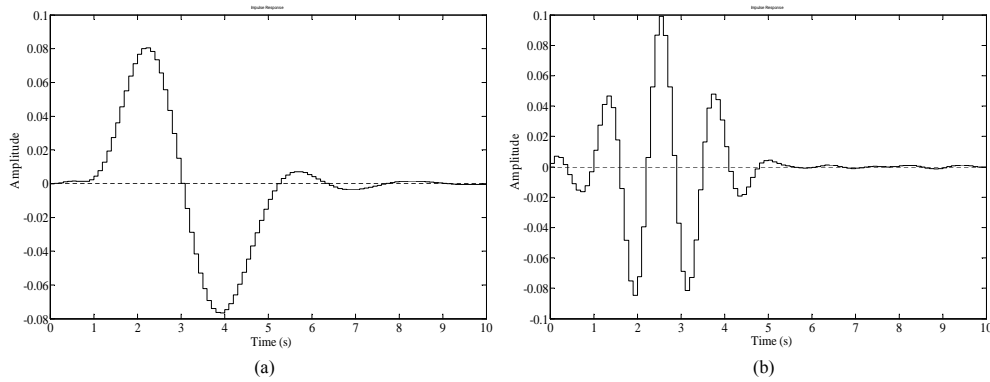


Figure C.2: Discrete-time approximated impulse response for (a) Gaussian and (b) Morlet wavelet bases

$$\begin{aligned} zx &= (A - I)x + Bu \\ y &= Cx + Du \end{aligned} \tag{C.6}$$

which is different from the usual state space description and  $I$  is the identity matrix. As described before, the different coefficients in the state space matrices represent the interconnections and multiplicative factors between the various integrators and the input and output signals. Every coefficient from  $A$  and  $B$  matrices will be realized by means of switched capacitor integrators. The  $C$  matrix scales the output signals from the integrators so it will be realized by using capacitors and adders.

A switched capacitor filter is realized with the use of some basic building blocks such as opamps, capacitors and switches driven by non-overlapping clock signals. The operation of a switched capacitor integrator is as follows. Capacitors are charged and discharged by periodically opening and closing the switches located on either side of the capacitor. This generates a charge transfer that results in a pulsing current flow. The average current can be calculated and, if the frequency is high enough, this current will be equivalent to a current through a resistor. This means than the resistive elements in the circuit can be replaced by capacitors. The amount of current, and thus the equivalent resistance, depends on two variables: the size of the capacitor and the switching frequency, and this means that also the frequency behaviour of the filter will depend on this two parameters.

## Non-inverting and inverting SC integrators

As it has been previously said we implement each of the coefficients of the state-space matrices by means of capacitance ratios in the integrators. As we have positive and negative coefficients it's necessary to choose a different

topology for each kind, being non-inverting and inverting integrators. The circuit diagram of the non-inverting integrator is given in Fig. C.3 which implements the first-order transfer function given by

$$H(z) = \left( \frac{C_1}{C_2} \right) \frac{1}{z - 1} \quad (\text{C.7})$$

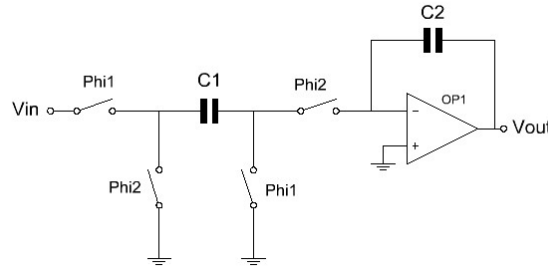


Figure C.3: Non-inverting SC integrator

$\Phi_{i1}$  and  $\Phi_{i2}$  represents the clock phases. The right behaviour of the clocks is essential for the proper function of the switches. The clocks set the time when  $C_1$  and  $C_2$  will be charged and they must be non-overlapping in order to guarantee charge is not inadvertently lost. The term non-overlapping refers to two logic signals running at the same frequency and arranged in such way that at no time both signals are high illustrated in Fig. C.4.a [2]. The rise and fall time in the signals also plays an important roll on the circuit behaviour since an ideal clock signal will induce the switches to drive more charge into the circuit and thus to have clock forethought in the output [16]. A simple circuit to provide these non-overlapping clock signals is shown in Fig. C.4.b.

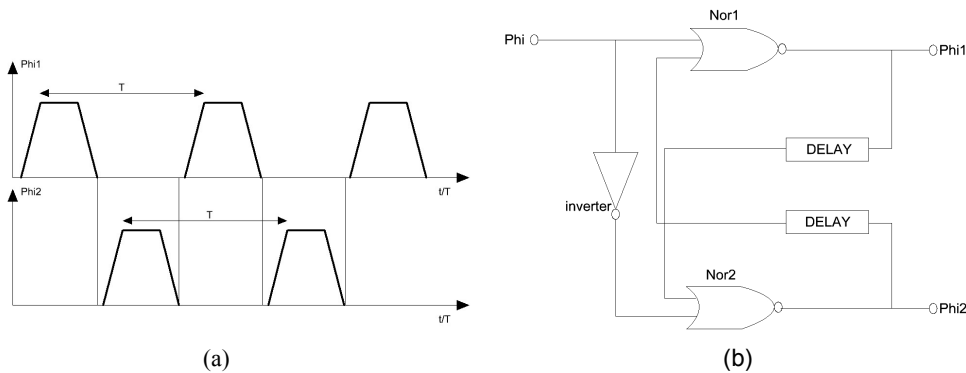


Figure C.4: Non-overlapping clock signals

Finally, to implement the negative coefficients of the state space, Fig. C.5 shows one possible topology for the inverting SC integrator which implements

$$H(z) = -\left(\frac{C_1}{C_2}\right) \frac{1}{z-1} \quad (\text{C.8})$$

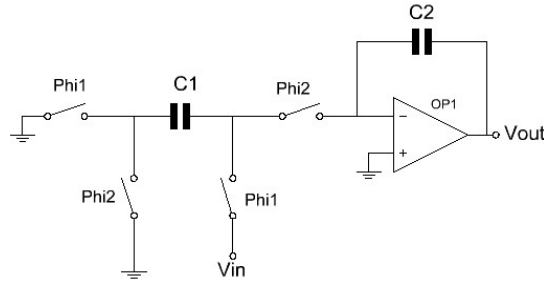


Figure C.5: Inverting SC integrator

The switches of both integrators can be implemented with just simple nmos transistors. The most important characteristics they must fulfil are a very high off resistance (so little charge leak occurs), a relatively low on resistance (so the circuit can settle in less than half the clock period) and introduce no offset voltage when they are turned on [2].

As one can see the nonidealities of the switches lead us to have glitches in the signal. The MOS switch couples the clock transitions to the sampling capacitor through its gate-drain or gate-source capacitance and the effect introduces an error in the output sampled voltage [4]. In order to improve this clock feed-through effect we can use Transmission Gates (TG). A Transmission Gate is a combination of p-MOS and n-MOS transistors as shown in Fig. C.6. For this circuit, ideally the clock feed-through signals at the transistors nodes cancel each other.

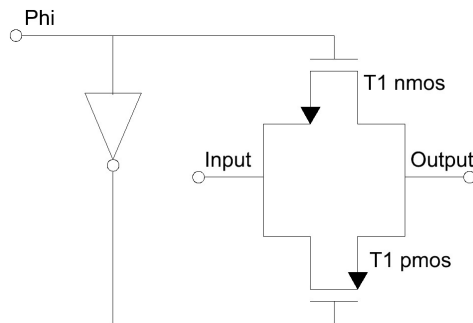


Figure C.6: Transmission Gate

Finally, in order to cancel the effects of charge injection we can use dummy switches. We can assume that the charge deposited by the transistors in the capacitor can be removed by means of another transistor that will absorb it to create a channel.

At last, in order to design the proper operational amplifier (opamp) for a SC filter we must take in account some important aspects as dc gain, unity-gain frequency, phase margin, slew-rate and dc-offset. The opamps can be realized by two stages CMOS amplifier as given in Fig. C.7.

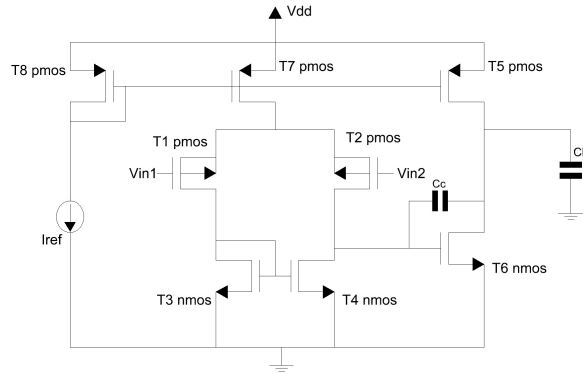


Figure C.7: Two stages CMOS operational amplifier

Simulation results using  $0.35\mu\text{m}$  AMS CMOS IC process is given Fig. C.8. As one can see, the obtained results are pretty close to the ideal impulse response shown in Fig. C.2, which confirms the good performance of the switched-capacitor wavelet filter.

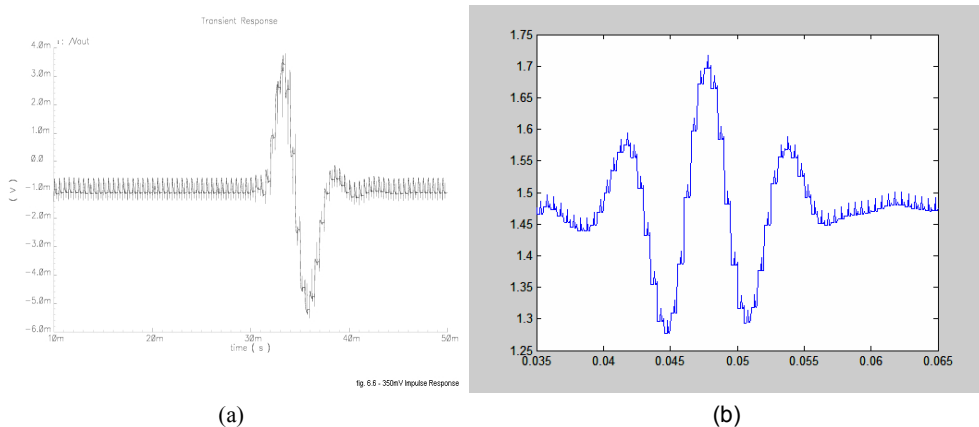


Figure C.8: Impulse response of the SC wavelet filters (a) first derivative of a Gaussian and (b) Morlet

## Appendix D

# Ultra-Wideband Circuit Designs

In today's marketplace for emerging communication technologies, the focal point of attention is ultra-wideband (UWB) radio as it not only promises enhanced data throughput with low-power consumption, but also provides high immunity against electromagnetic interference (EMI) and robustness to fading. It is expected that future short-range indoor ultra-wideband (UWB) telecommunication systems will operate in the frequency band from 3.1-10.6GHz according to the Federal Communications Commission (FCC) mask [7-11]. Ultra-wideband communication offers significant contributions and advantages but simultaneously a number of challenges also need to be addressed.

When implemented as impulse radio (IR-UWB) (i.e., where the information is transmitted by very short EM pulses [7], [12]) this new communication technology may revolutionize the way we think in wireless technology by modulating data in time rather than in frequency with low-power consumption. From the perspective of traditional narrow-band systems, the wideband nature of the front-end architecture employed in UWB systems requires a totally different design methodology of both the UWB front-end architecture and its constituting UWB circuit building blocks. In the following sections we describe some UWB circuit designs using the methodology presented in this thesis.

### D.1 Impulse Generator for Pulse Position Modulator

Pulse Position Modulation (PPM)) is used to encode the binary transmitted data [13], [14]. The waveform to be transmitted is the Gaussian monocycle due to its intrinsic time-frequency resolution product [11], [15], which is important for applications such as positioning and imaging. The impulse generator consists of a cascade of a fast triangular pulse generator and a pulse-shaping network or Gaussian filter (i.e., a filter with the first derivative of a Gaussian

impulse response) [16], [17]. As mentioned in Chapter 4, a Gaussian filter can be implemented by a cascade of complex first-order systems (CFOS). Then the filter is implemented as a cascade of three complex first-order systems (CFOS), which, in turn, consist of gm-C sections that employ differential pairs with partial positive feedback. The entire Pulse Position Modulator block diagram is shown in Fig. D.1. The transmitter is the combination of the modulator with the impulse generator.

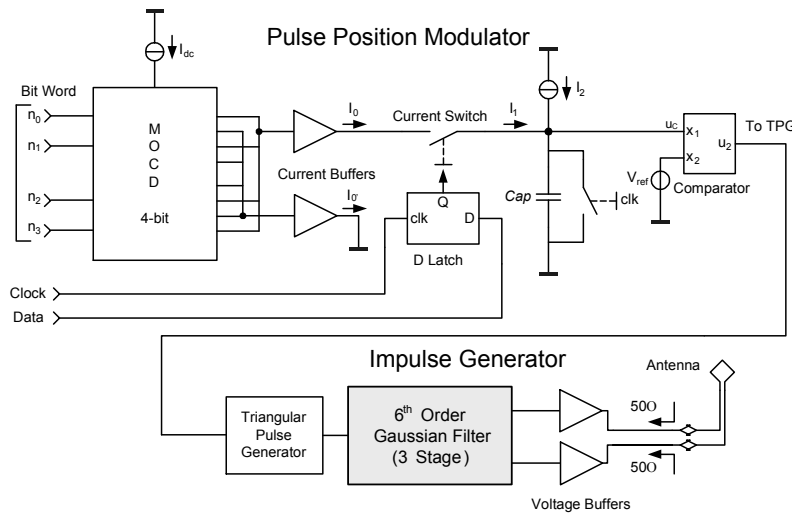


Figure D.1: Block diagram of the Pulse Position Modulator

The chip microphotograph and the layout of the Pulse Position Modulator core is given in Fig. D.2. The circuit has been designed using IBM 0.18 $\mu$ m BiCMOS IC technology.

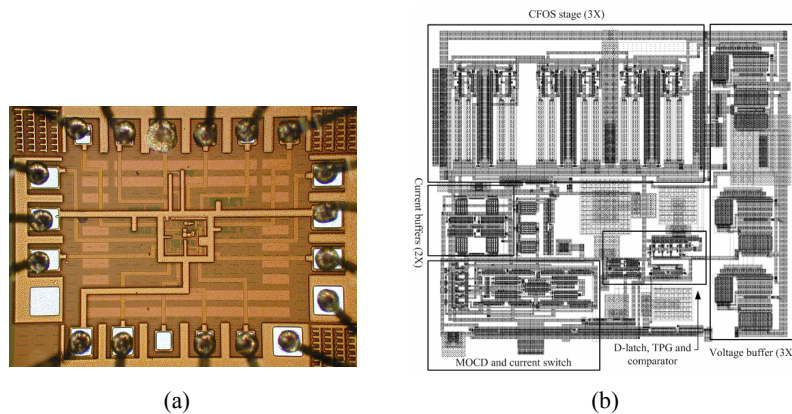


Figure D.2: (a) Microphotography and (b) Layout of the impulse generator and modulator core.

Fig. D.3 shows the measured Gaussian monocycle waveform. There is a 75ps discrepancy in the pulse width as compared to the simulated results. Furthermore, to verify pulse position modulation, a clock signal (15MHz), which acts as the binary input signal, is streamed into the D-latch. A bit code (0001) is chosen to verify that the least significant bit would vary the position of the pulse by approximately 315ps. Finally, Table D.1 highlights the measured parameters of the impulse generator.

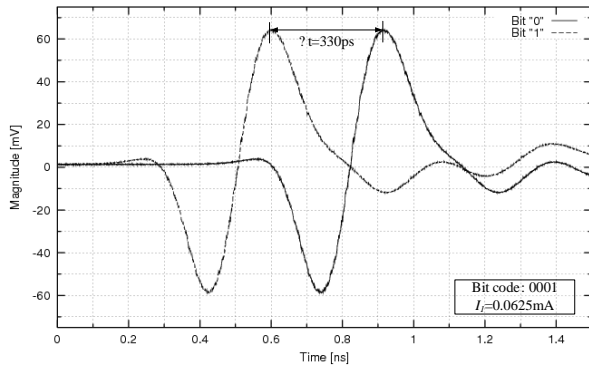


Figure D.3: Measured impulse response of a monocycle Gaussian and pulse position modulation for bit code 0001

Table D.1: Measured Performance of the impulse generator

|   |                          |
|---|--------------------------|
| Technology                                | $0.18\mu\text{m}$ BiCMOS |
| Die area                                  | $1.25\text{mm}^2$        |
| Active area                               | $0.306\text{mm}^2$       |
| Pulse width<br>Gaussian Monocycle         | 375ps - measured on PCB  |
| Time delay<br>Bit code: 0001              | 315ps                    |
| Current consumption<br>of Gaussian filter | 14.4mA @ 1.8 V           |

## D.2 A Delay Filter for an UWB Front-End

A continuous-time analog delay is designed as a requirement for the autocorrelation function in the Quadrature Downconversion Autocorrelation Receiver (QDAR) [1]. Fig. shows a Quadrature Downconversion Autocorrelation Receiver (QDAR) [1], which is designed to operate in the presence of strong narrowband interference, while still being able to detect the incoming UWB signal. Hence, to further reduce the influence of the narrowband interferers, frequency selectivity is introduced in the delay element.

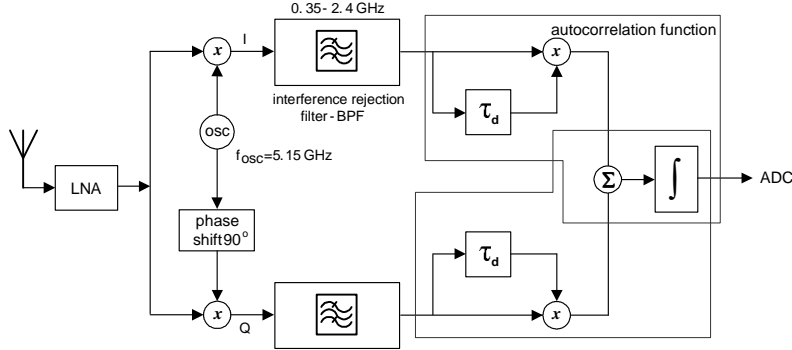


Figure D.4: Quadrature Downconversion Autocorrelation Receiver

Assuming that the incoming waveform at the receiver,  $x(t)$ , is a Morlet given by,

$$x(t) = \cos(\omega_0(t - \tau))e^{-(t-\tau)^2} \quad (\text{D.1})$$

where  $\omega_0$  is the center frequency and  $\tau$  is the time instant at which the Morlet waveform is centered, the impulse response,  $h(t)$ , of the delay filter is chosen to match the incoming signal (i.e.  $h(t) = x(t)$ ) and therefore the output of the time delay,  $y(t)$ , is the convolution of the incoming signal and the impulse response of the filter, given by,

$$x(t) = \cos(\omega_0(t - 2\tau))e^{-(t-2\tau)^2} \quad (\text{D.2})$$

where  $\beta$  is the gain factor of the convolved waveform. On comparing Eq. D.1 with Eq. D.2, one can see the distinct resemblance between the convolved waveform and the incoming Morlet signal. As a result, the Morlet signal is delayed by a time period equal to  $\tau$ .

In regards to the transmit reference scheme and from an implementation point of view, one is drawn to the conclusion that the bottleneck to this concept is the physical realization of an accurate continuous-time delay required to execute the autocorrelation function at high frequencies. Then an eight-order Padé approximation of a Morlet function is selected to implement this delay. Subsequently, the orthonormal state space is adopted due to the same reason described in Chapter 5. Each coefficient in the state-space description of the orthonormal ladder filter is implemented at circuit level using a novel 2-stage gm cell employing negative feedback.

Simulation results in IBM's BiCMOS 0.13 $\mu\text{m}$  technology show that through convolution, the Morlet signal is delayed by a time period equal to  $\tau$ , as shown in Fig. D.5.

This delay filter requires a total current of 70 mA at a 1.6 V power supply. The 1-dB compression point of the delay is at 565 mV and the SNR is 47.5 dB. On performing a Monte Carlo simulation it becomes evident that the response

### D.3 A FCC Compliant Pulse Generator for UWB Communications

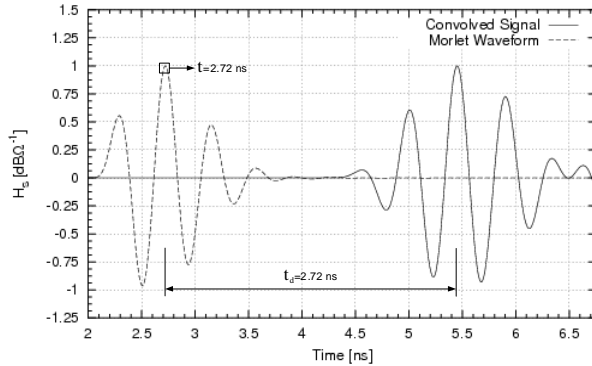


Figure D.5: Time delay between the incoming Morlet waveform and convolved signal

of the frequency selective analog delay does not suffer drastically from neither process variations nor component mismatch.

### D.3 A FCC Compliant Pulse Generator for UWB Communications

In this thesis, we have shown that it is feasible to design filters with arbitrary waveform responses. Therefore we propose an ultra-wideband pulse generator incorporating a filter with a Daubechies' impulse response (i.e. maximally flat over the desired frequency range).

As seen in Fig. D.6, by generating a window-like response in the baseband (i.e. with the Daubechies' filter) and then through upconversion, the energy spectrum of the pulse generator can be matched to that of the FCC frequency mask. For detection in the receiver, the absolute shape of the transmitted waveform is not relevant as seen in [4]. Biphase modulation of the transmitted waveform can be achieved by alternating the polarities of the “impulses” that are used to drive the Daubechies' scaling function filter.

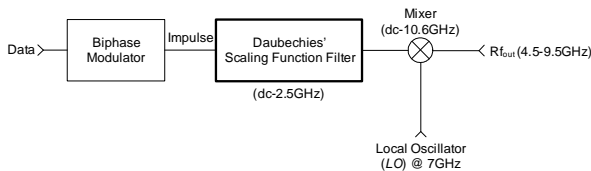


Figure D.6: Proposed pulse generator block diagram

An eight-order Padé approximation of its transfer function is selected to implement the FCC stipulated frequency spectrum. Again, the orthonormal ladder structure has been chosen and the coefficients in the state-space descrip-

tion is implemented at circuit level using a novel 2-stage gm cell employing negative feedback.

From simulation results in IBM's CMOS  $0.13\mu\text{m}$  technology, Fig. D.7 demonstrates that the pulse generator response is closed to the ideal impulse response. The Daubechies filter requires a total current of 25mA from a 1.2V power supply.

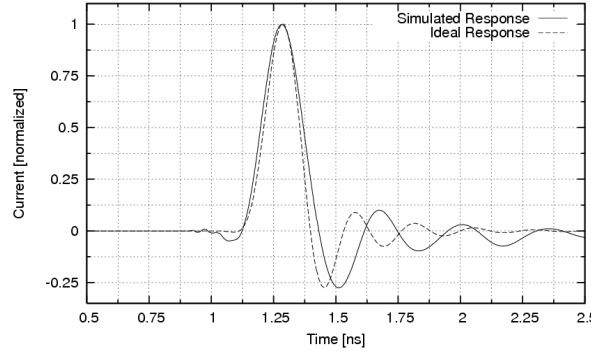


Figure D.7: Impulse response of an 8th order Daubechies' scaling function filter

Finally, Fig. D.8 shows the frequency spectrum of the Daubechies' scaling function upconverted with a 7GHz carrier. As seen in the figure, the pulse generator's performance can now be optimized for maximum energy efficiency. The frequency coverage of the simulated waveform is about 85% of the FCC mask.

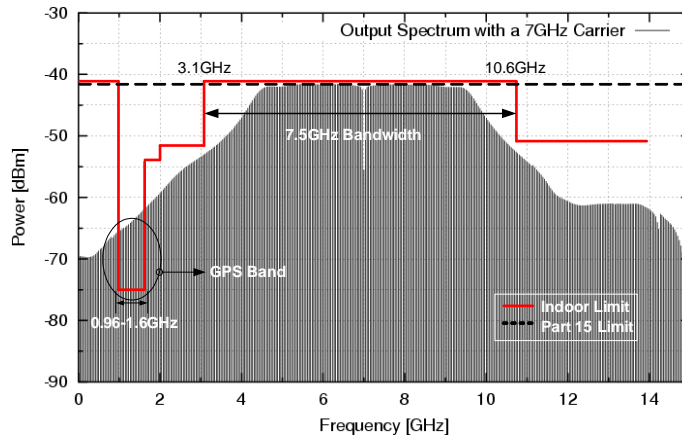


Figure D.8: Frequency spectrum of the Daubechies' scaling function

# Summary

The purpose of this thesis is to describe novel signal processing methodologies and analog integrated circuit techniques for low-power biomedical systems.

Physiological signals, such as the electrocardiogram (ECG), the electroencephalogram (EEG) and the electromyogram (EMG) are mostly non-stationary. The main difficulty in dealing with biomedical signal processing is that the information of interest is often a combination of features that are well localized temporally (e.g., spikes) and others that are more diffuse (e.g., small oscillations). This requires the use of analysis methods sufficiently versatile to handle events that can be at opposite extremes in terms of their time-frequency localization.

Wavelet Transform (WT) has been extensively used in biomedical signal processing, mainly due to the versatility of the wavelet tools. The WT has been shown to be a very efficient tool for local analysis of nonstationary and fast transient signals due to its good estimation of time and frequency (scale) localizations. Being a multiscale analysis technique, it offers the possibility of selective noise filtering and reliable parameter estimation. Signal analysis methods derived from wavelet analysis carry large potential to support a wide range of biomedical signal processing applications including noise reduction, feature recognition and signal compression. The discussion here deals with wavelet techniques for cardiac signals analysis.

Often WT systems employ the discrete wavelet transform, implemented on a digital signal processor. However, in ultra low-power applications such as biomedical implantable devices, it is not suitable to implement the WT by means of digital circuitry due to the relatively high power consumption associated with the required A/D converter. Low-power analog realization of the wavelet transform enables its application *in vivo*, e.g. in pacemakers, where the wavelet transform provides a means to extremely reliable cardiac signal detection.

In this thesis we present a novel method for implementing signal processing based on WT in an analog way. The methodology presented focuses on the development of ultra low-power analog integrated circuits that implement the required signal processing, taking into account the limitations imposed by an implantable device.

From the wavelet definition, we state that the implementation of a wavelet filter is based on the design of a bandpass filter that presents an impulse response equal to a wavelet base. To obtain the transfer function of a particular wavelet filter, mathematical approximation techniques are required. We indicate several methods to obtain good approximations in the time domain of the wavelet bases functions. One important objective of the introduced approaches is that the resulting approximated function should be rational and stable in the Laplace domain. This means that the approximating function must lead to a physically realizable network. Nevertheless, we can notice that due to limitations in chip area, power consumption and coefficient matching, there is a trade-off between the approximation accuracy versus the order of the implemented filter. Thus, the design challenge is to obtain a low-order system while preserving a good approximation to the intended function. Due to their general applicability and excellent accuracy, the Padé and the  $L_2$  approximation were chosen, which generate reasonably low-order and good-fit transfer functions.

Subsequently, there are many possible state space descriptions for a circuit that implements a particular transfer function. The same holds for practical realizations. This allows the designer to find a circuit that fits specific requirements. From two newly defined figure-of merits, we concluded that the orthonormal ladder structure is the optimal state space representation with respect to dynamic range, sparsity and sensitivity, which represent the most important design aspects in low-power low-voltage analog filters.

A promising technique for the design of ultra low power analog integrated circuits is the one of Dynamic Translinear (DTL) circuits. The translinear circuit approach is a current-mode technique, which is inherently non-linear and performs a compression and an expansion on the processed signal. The benefit of a companding (compressing-expanding) system is that a signal with specific DR can be processed in a system block with a smaller DR than the signal, and by this, offer low-voltage and low-power operation. In addition, only transistors and capacitors are required to realize a filter function. Since in conventional ultra low-power designs resistors would become too large for on-chip integration, their superfluity is a very important advantage. Moreover, the DTL principle can be applied to the implementation of functions described by linear and nonlinear polynomial differential equations. Another suitable technique for low-power low frequency filter design is based on CMOS triode strong-inversion  $nA/V$  transconductor for linear  $g_m - C$  filters. In the field of medical electronics, active filters with large time constants are often required to design low cutoff-frequency filters (in the Hz and sub-Hz range), necessitating the use of large capacitors or very low transconductances. To limit capacitors to practical values, a transconductor with an extremely small transconductance  $G_m$  (typically a few  $nA/V$ ) is needed and transistors kept in the triode region benefit from a lower transconductance than the ones operating in saturation or weak-inversion regions.

Finally, the methodology presented is employed in the design of several ultra low-power biomedical systems and analog wavelet filters. The simulated and measured results demonstrate an excellent performance in generating the desired Wavelet Transform and achieving correct cardiac signal detection in an ultra low-power environment.



# Samenvatting

Dit proefschrift beschrijft de ontwikkeling van nieuwe signaalbewerkings-methodologieën en analoge geïntegreerde circuit-technieken voor laagvermogens biomedische systemen.

Fysiologische signalen, zoals het elektrocardiogram (ECG), het elektro-encefalogram (EEG) en het elektromyogram (EMG) zijn voornamelijk niet-stationair. De hoofdmoeilijkheid met betrekking tot biomedische signaalbewerking is dat de relevante informatie dikwijls een combinatie is van kenmerken die goed in tijd gelokaliseerd zijn (b.v. pieken) en andere die meer verspreid zijn (b.v. kleine oscillaties). Dit vereist het gebruik van analysemethoden die voldoende veelzijdig zijn om overweg te kunnen met gebeurtenissen die op tegenovergestelde uitersten in termen van hun tijd-frequentie lokalisatie kunnen liggen.

De Wavelet Transformatie (WT) wordt veelvuldig gebruikt in biomedische signaalbewerking, hoofdzakelijk dankzij de veelzijdigheid van de wavelet-werktuigen. De WT is een heel efficiënt hulpmiddel gebleken voor lokale analyse van niet-stationaire en snel veranderende signalen ten gevolge van zijn goede schatting van tijd- en frequentie- (schaal) lokalisaties. Zijnde een analyse-techniek op meervoudige schaal, biedt het de mogelijkheid van selectief filteren van ruis en betrouwbare parameter-schatting. Signaal-analyse- methoden die van de wavelet analyse afgeleid worden bieden goede mogelijkheden voor ondersteuning van een groot assortiment aan biomedische signaalbewerkings-toepassingen inclusief ruis-reductie, het herkennen van eigenschappen en signaal -compressie. De besprekung hier betreft wavelet-technieken voor de analyse van hartsignalen.

WT systemen wenden dikwijls de discrete wavelet-transformatie aan, gerealiseerd op een digitale signaalprocessor. Echter, in ultra laag-vermogens-toepassingen zoals biomedische implanteerbare apparaten, is het niet mogelijk om de WT door middel van digitale circuits te implementeren als gevolg van de reusachtige hoeveelheid vermogen noodzakelijk voor analoog-naar-digitaal conversie. Een laag-vermogens- analoge realisatie van de wavelet-transformatie biedt de mogelijkheid van toepassing *in vivo*, b.v. in pacemakers, waar de wavelet-transformatie een middel biedt tot het uitermate betrouwbaar detecteren van hartsignalen.

Dit proefschrift beschrijft een nieuwe methode voor het implementeren van signaalbewerking gebaseerd op de WT op een analoge manier. De voorgestelde methodologie richt zich op de ontwikkeling van ultra laag-vermogens- analoge geïntegreerde schakelingen die de noodzakelijke signaalbewerking uitvoeren, rekening houdend met de beperkingen die door een implanteerbaar apparaat opgelegd worden.

Uitgaande van de wavelet-definitie stellen wij dat de uitvoering van een wavelet filter op het ontwerp van een banddoorlaat filter is gebaseerd waarvan de impuls-responsie gelijk is aan een wavelet basis. Om de gewenste overdrachtsfunctie van een wavelet filter te verkrijgen dienen benaderingsmethoden te worden toegepast. Wij geven enkele methoden om goede benaderingen in het tijd-domein van de wavelet basis-functies te verkrijgen. Een belangrijk doel van de voorgestelde benaderingsmethoden is dat de resulterende benaderende functie rationaal en stabiel in het Laplace-domein moet zijn. Dit houdt in dat de benaderende functie tot een realiseerbaar netwerk moet leiden. Desalniettemin kunnen wij opmerken dat, als gevolg van beperkingen in chipoppervlak, vermogensverbruik en de overeenkomst van coëfficiënten, er een afweging bestaat tussen de nauwkeurigheid van de benadering en de orde van het geïmplementeerde filter. Dus, de ontwerp-uitdaging betreft het verkrijgen van systeem van lage orde en tevens een goede benadering van de beoogde functie. Tengevolge van hun algemene toepasbaarheid en uitstekende nauwkeurigheid werden de Padé- en de  $L_2$ -benaderingen gekozen, die overdrachtsfuncties genereren van relatief lage orde en goede overeenkomst.

Vervolgens zijn er vele mogelijke state-space systemen voor een filter dat een bepaalde overdrachtsfunctie implementeert. Hetzelfde geldt voor praktische realisaties. Dit staat ontwerpers toe een filter-topologie te vinden die het best aansluit bij hun eisen. Aan de hand van twee nieuw gedefinieerde maatstaven concluderen wij dat de orthonormale ladder-structuur de optimale state-space-systeem representatie is met betrekking tot dynamisch bereik, spaarzaamheid en gevoeligheid, welke de belangrijkste ontwerpaspecten in laag-vermogens-, laag-spannings- analoge filters vertegenwoordigen.

Een veelbelovende techniek voor het ontwerp van ultra laag-vermogens-analoge geïntegreerde schakelingen is die van Dynamisch-Translineaire (DTL) schakelingen. De translineaire schakelingen benadering is een stroom-modus techniek, die inherent niet-lineair is en een compressie en een expansie verricht op het verwerkte signaal. Het voordeel van een companderend (comprimerend - expanderend) systeem is dat een signaal met specifiek dynamisch bereik (DR) in een systeemblok met een kleiner DR dan het signaal verwerkt kan worden en, hierdoor, laag-spannings- en laag-vermogens-werking mogelijk maakt. Bovendien worden slechts transistoren en condensatoren vereist om een filter-functie te realiseren. Aangezien in conventionele ultra laag-vermogens-ontwerpen weerstanden te groot zouden worden voor op-chip integratie, is hun overbodigheid een heel belangrijk voordeel. Bovendien kan het DTL-principe toegepast worden om functies die beschreven worden door lineaire en niet-

lineaire polynomiale differentiaalvergelijkingen te implementeren. Een andere geschikte techniek voor het ontwerpen van laag-vermogens-, laag-frequente filters is gebaseerd op het gebruik van CMOS triode sterke-inversie  $nA/V$  transconductors voor lineaire  $g_m - C$  filters. Op het gebied van medische elektronica worden dikwijls actieve filters met grote tijdconstanten vereist om filters met lage kantel-frequenties (in het Hz en sub-Hz gebied) te ontwerpen, welke het gebruik van grote condensatoren of heel lage transconductanties noodzakelijk maken. Om condensatoren tot praktische waarden te beperken is een transconductor met een bijzonder kleine transconductance  $G_m$  (typisch enkele  $nA/V$ ) nodig en profiteren transistoren die in het triode gebied gehouden worden van een lagere transconductantie dan diegene die in verzadiging of zwakke inversie worden gebruikt.

Tenslotte is de voorgestelde methodologie aangewend in het ontwerp van enkele ultra laag-vermogens- biomedische systemen en analoge wavelet-filters. De gesimuleerde en gemeten resultaten spreiden een uitstekende prestatie in het genereren van het gewenste Wavelet Transformatie en het bereiken van correcte detectie van hartsignalen in een ultra laag-vermogens omgeving ten toon.



# Acknowledgements

Certainly, this thesis would not have been possible without the support and understanding of many people. Therefore, I would like to thank all of them, including those I may not have chance to mention here.

First of all, I would like to thank my supervisor and friend Wouter Serdijn for his enthusiastic guidance and support, not only in my scientific research, sharing his expertise in circuit designs, but specially and more important carrying constantly about my personal life.

I am obliged to my promotor John Long for his advice and discussions held about IC technology and chip fabrication, which really improved the quality of this work.

I would like to express my gratitude to José Camargo, my former mentor at University of Brasilia, who stimulated me enormously with his enthusiasm and inspiring discussions about microelectronics and for introducing me to the Electronics Research Laboratory.

To all the member of the Electronic Research Laboratory, for providing a good working environment. In special, Marion de Vlieger for her kind and prompt assistance on all kind of administrative and personal issues. Also many thanks to the M.Sc. students who contributed to this work and to Loek van Schie and Will Straver for the technical support.

Special thanks for the members of the Biosens project, Ronald Westra, Ralf Peeters and Joël Karel, for interesting discussions and support; and to Richard Houben, for the valuable and pleasant cooperation with Medtronic.

The financial support of the Dutch Science and Technology Foundation (STW), who funded this Ph.D project under grant no. DTC 6418 is kindly acknowledged.

Thanks to the DIMES Laboratory and IBM Microelectronics for fabrication access.

I am indebted to my room mates, for the cooperative atmosphere and exchange of remarks and thoughts. First, Arturo Sarmiento who helped me at the beginning and later my half-Brazilian friend Sumit Bagga who took essential part in my scientific research as well as in my social life during this period.

I am really thankful to have made so many good friends in Holland. Their friendship was essential, both in joyful and difficult moments of being a foreigner, and I am sure that our friendship will last forever.

I would like to thank all my true friends in Brazil for our great relationship throughout these years and who have shown to me that real friendship does not depend on the distance.

I thank to all my relatives who have cared about me and have supported my decisions during my entire life, uncle, aunts, cousins and family-in-law. Special thanks go to my brother and sister, with whom I am really grateful for our very pleasant relationship.

I am very thankful to my parents who always believed in me, providing all the opportunities to study and develop myself. Their love, dedication and motivation encouraged me to pursue my personal objectives. They certainly are the solid base from which I build my way.

I also would like to thank my son Felipe with love, who still might not be able to comprehend the importance of his presence in my life, he fills every day my life with happiness and inspiration, giving me the strength to never turn back.

Last, but certainly not least, I would like to express my deepest gratitude to my beloved wife Carolina, who unconditionally supported me, in spite of postponing her career and of being away from her family. For sure, this thesis would not have been completed successfully without her love which sustained me and kept me straight towards the end. “Juntos não há estrelas que não podemos alcançar, nem sonhos que não podemos realizar”.

# Biography



**Sandro A. P. Haddad** was born in Anápolis, Brazil, on February 8, 1977. He received his B.Eng. degree from the University of Brasília (UnB), Brazil, in 2000, with honors. He was awarded the best-graduated student of the year, from the Faculty of Electrical Engineering, UnB. In February 2001, he joined the Electronics Research Laboratory, Delft University of Technology (TUDelft), The Netherlands, where he started research towards his Ph.D degree. His project is part of BioSens (Biomedical Signal Processing Platform for Low-Power Real-Time Sensing of Cardiac Signals). His research interests include low-voltage, ultra low-power analog electronics and biomedical systems, and high-frequency analog integrated circuits for UWB communications.

## BioSens project

Around 40% of all human deaths are attributed to cardiovascular diseases. Cardiac pacing has become a therapeutic tool used worldwide with over 250.000 pacemaker implants every year. Cardiac pacemakers include real-time sensing capacities reflecting the state of the heart. Also, continuously monitoring the patient's cardiac status collecting patient data over an extended period of time will improve quality of cardiac care. The main goal of this project is to improve analyzing and recording relevant cardiac activity data via implantable sensors. This will provide a new opportunity for monitoring and managing infarct-threatened patients and post-infarction patients in the out-hospital

setting. One of the major activities is the development of low-power analog integrated circuits that implement the required signal processing, taking into account the limitations imposed by an implantable device.

BioSens is a research project of the Electronics Research Laboratory (ELCA), part of the Delft University of Technology (TUDelft) and the Department of Mathematics (Math), part of the University of Maastricht (UM). At the same time the work is embedded in the Integrated Smart Microsystems (ISM) research theme of the Delft Institute of Microelectronics and Submicron Technology (DIMES). Also, the project's primary user is Medtronic (world leader in medical technology).

# List of publications

## Book chapter(s)

- W. A. Serdijn, **S. A.P. Haddad** and Jader A. De Lima, “Ultra Low-Power Low-Voltage Analog Integrated Filter Design,” in J.H. Huijsing, A.H.M. van Roermund and M. Steyaert (Editors) *Analog Circuit Design*, Kluwer Academic Publishers, February, 2006, ISBN: 1-4020-3884-4.

## Journal papers

- **S.A.P. Haddad**, S.Bagga and W.A. Serdijn, “Log-domain wavelet bases,” *IEEE Transactions on Circuits and Systems - I: Regular Papers*, vol. 52, no. 10, Oct. 2005.
- **S.A.P. Haddad**, R. Houben and W.A. Serdijn, “The evolution of pacemakers: an electronics perspective, from the hand crank to advanced wavelet analysis,” *IEEE Engineering in Medicine and Biology*, vol. 25, no. 3, May/June. 2006.
- **S. A. P. Haddad**, R. Houben and W.A. Serdijn, “The history and development of pacemakers: an electronics perspective,” *Klinische Fysica*, January 2004.
- S. Bagga, A. V. Vorobyov, **S. A. P. Haddad**, A. G. Yarovoy, W. A. Serdijn and J. R. Long, “Co-design of an Impulse Generator and Miniaturized Antennas for IR-UWB,” *IEEE Transactions on Microwave Theory and Techniques - Special Issue on UWB*, vol. 54, no. 4, April 2006.

## Tutorials

- **S.A.P. Haddad**, “Advanced ultra low-power biomedical signal processing based on analog wavelet transform,” *invited presentation, SFORUM-SBMICRO-SBCCI*, Ouro-Preto, Brazil, August 28 - September 1, 2006.

## Conference proceedings

- **S.A.P. Haddad** and W.A. Serdijn, “An Ultra Low-Power Class-AB Sinh integrator”, *proc. Symposium on integrated circuits and systems design*, SBMICRO-SBCCI, Ouro-Preto, Brazil, August 28 - September 1, 2006.
- R.L.M. Peeters, J.M.H. Karel, R.L. Westra, **S.A.P. Haddad** and W.A. Serdijn, “Multiwavelet Design for Cardiac for cardiac signal processing”, *proc. International Conference of the IEEE Enigneering in Medicine and Biology Society* (EMBC 2006), New York, August 30 - September 3, 2006.

- S. Bagga, **S.A.P. Haddad**, W.A. Serdijn and J. R. Long, “An FCC Compliant Pulse Generator for IR-UWB Communications”, *proc. IEEE International Symposium on Circuits and Systems (ISCAS)*, Kos, Greece, May 21-24, 2006.
- S.Kashmiri, **S.A.P.Haddad**, and W.A. Serdijn, “High-Performance Analog Delays: Surpassing Bessel-Thomson by Pade-Approximated Gaussians,” *proc. ISCAS*, Kos, Greece, May 21-24, 2006.
- S. Bagga, **S.A.P. Haddad**, W.A. Serdijn and J. R. Long, “Ultra-Wideband Radio: Unconventional Circuit Solutions for Unconventional Communication,” *invited presentation, proc. Workshop on Advances in Analogue Circuit Design*, AACD, Maastricht, The Netherlands , April 4 - 6, 2006.
- J.M.H. Karel, R.L.M. Peeters, R.L. Westra, **S.A.P. Haddad**, W.A. Serdijn, “Wavelet design for analog implementation”, *25th Benelux Meeting on Systems and Control*, Heeze, The Netherlands, March 13-15, 2006.
- J.M.H. Karel, R.L.M. Peeters, R.L. Westra, **S.A.P. Haddad** and W.A. Serdijn, “An L2-based approach for wavelet approximation”, *proc. CDC-ECC 2005*, Seville, Spain, December 12-15, 2005.
- S.M. Kashmiri, **S.A. P. Haddad** and W.A. Serdijn “Systematic Performance Comparison of Bessel-Thomson vs. Pad Approximated Delay Filters,” *proc. ProRISC*, Veldhoven, the Netherlands, November 17 - 18, 2005.
- Sumit Bagga, **Sandro A. P. Haddad**, Wouter A. Serdijn and John R. Long “A BPM Transmitter for Impulse Radio Ultrawideband Communications,” *proc. ProRISC*, Veldhoven, the Netherlands, November 17 - 18, 2005.
- **S.A.P. Haddad**, J.M.H. Karel, R.L.M Peeters, R.L. Westra and W.A. Serdijn, “Ultra Low-power Analog Morlet Wavelet filter in 0.18m BiCMOS Technology”, *proc. ESSDERC-ESSCIRC 2005*, Grenoble, France, September 12-16, 2005.
- S. Bagga, **S.A.P. Haddad**, W. A. Serdijn, J. R. Long and Erik B. Busking, “A Delay Filter for an ir-UWB Front-End,” in *International Conference on Ultrawideband (ICU)*, Zurich, Switzerland, September 5-8, 2005.
- J.M.H. Karel, R.L.M. Peeters, R.L. Westra, K.M.S. Moermans, **S.A.P. Haddad** and W.A. Serdijn, “Optimal discrete wavelet design for cardiac signal processing”, in *proc. EMBC 2005*, Shanghai, China, September 1-4, 2005.
- J.M.H. Karel, R.L.M. Peeters, R.L. Westra, **S.A.P. Haddad**, W.A. Serdijn, “Wavelet approximation for implementation in dynamic translinear circuits”, *proc. IFAC World Congress 2005*, Prague, July 4-8, 2005.
- **S.A.P. Haddad**, J.M.H. Karel, R.L.M. Peeters, R.L. Westra and W.A. Serdijn, “Analog Complex Wavelet Filters”, *proc. ISCAS*, Kobe, Japan, May 23-26, 2005.
- S. Bagga, **S.A.P. Haddad**, K. van Hartingsveldt, S. Lee, W. A. Serdijn and J. R. Long, “An Interference Rejection Filter For An Ultra-Wideband Quadrature Downconversion Autocorrelation Receiver,” *proc. ISCAS*, Kobe, Japan, May 23-26, 2005.
- **S.A.P. Haddad**, R. Houben and W.A. Serdijn, “Smart pacemakers, from the hand crank to advanced wavelet analysis,” *invited presentation, proc. 3rd DISENS Symposium on Biomedical Sensors*, Delft, the Netherlands, May 19, 2005.

- J.M.H. Karel, R.L.M. Peeters, R.L. Westra, **S.A.P. Haddad**, W.A. Serdijn, “L2-Approximation of Wavelet Functions”, *proc. 24th Benelux Meeting on Systems and Control*, Houffalize, Belgium, March 22-24, 2005.
- **S.A.P. Haddad**, J.M.H. Karel, R.L.M. Peeters, R.L. Westra, W.A. Serdijn, “Complex Wavelet Transform for Analog Signal Processing,” *proc. ProRISC*, Veldhoven, the Netherlands, November 25-26, 2004.
- **S.A.P. Haddad**, N. Verwaal, R. Houben and W.A. Serdijn, “Optimized dynamic translinear implementation of the Gaussian wavelet transform”, *proc. ISCAS*, Vancouver, Canada, May 23-26, 2004.
- **S.A.P. Haddad**, S. Bagga and W.A. Serdijn, “Log-domain wavelet bases”, *proc. ISCAS*, Vancouver, Canada, May 23-26, 2004.
- S. Bagga, G. de Vita, **S.A.P. Haddad**, W.A. Serdijn and J.R. Long, “A PPM Gaussian pulse generator for ultra-wideband communications”, *proc. ISCAS*, Vancouver, Canada, May 23-26, 2004.
- S. Bagga, G. de Vita, **S.A.P. Haddad**, W.A. Serdijn and J.R. Long, “A PPM Gaussian pulse generator for ultra-wideband communications,” *proc. ProRISC*, Veldhoven, 26-27 November 2003.
- N. Verwaal, **S.A.P. Haddad**, R.P. Houben and W.A. Serdijn, “ Optimized dynamic translinear implementation of the Gaussian wavelet transform,” *proc. ProRISC*, Veldhoven, 26-27 November 2003.
- **S.A.P. Haddad**, S. Gieltjes, R.P.M. Houben and W.A. Serdijn, “An Ultra Low-Power Dynamic Translinear Sense Amplifier for Pacemakers”, *proc. ISCAS*, Bangkok, Thailand, May 25-28, 2003.
- **S.A.P. Haddad**, R.P.M. Houben and W.A. Serdijn, “Analog Wavelet Transform Employing Dynamic Translinear Circuits for Cardiac Signal Characterization”, *proc. ISCAS*, Bangkok, Thailand, May 25-28, 2003.
- **S.A.P. Haddad**, R.P.M. Houben and W.A. Serdijn, “First derivative Gaussian Wavelet function employing Dynamic Translinear Circuits for Cardiac Signal Characterization,” *proc. ProRISC*, Veldhoven, 28-29 November 28-29, 2002.
- **S.A.P. Haddad** and W.A. Serdijn, “High-frequency Dynamic Translinear and Log-domain circuits in CMOS technology”, *proc. ISCAS*, Phoenix, Arizona, U.S.A., May 26-29, 2002.
- **S.A.P. Haddad** and W.A. Serdijn, “Mapping the Wavelet Transform onto silicon, “The Dynamic Translinear Approach,” *proc. ISCAS*, Phoenix, Arizona, U.S.A., May 26-29, 2002.
- **S.A.P. Haddad** and W.A. Serdijn, “High-frequency log-domain and dynamic translinear circuits in CMOS technology,” *proc. ProRISC*, Veldhoven, 29-30 November 2001.
- **S.A.P. Haddad** and W.A. Serdijn, “Low-power adaptive bipolar low noise amplifier,” *proc. ProRISC*, Veldhoven, 29-30 November 2001.
- **S.A.P. Haddad** and W.A. Serdijn, “Wavelet transform with dynamic translinear circuits for cardiac signal characterization in pacemakers,” *proc. ProRISC*, Veldhoven, 29-30 November 2001.

- **S.A.P. Haddad** and W.A. Serdijn, “Low-Power adaptive bipolar low noise amplifier”, *proc. SBMICRO-SBCCI*, Pirenopolis, Brazil, September 10-14, 2001.